A DETAILED STUDY OF THE MECHANICAL AND ELECTRICAL ASPECTS OF MICROPARTICLE IMPACT PHENOMENA

by

AMRIT S. BRAH B.Sc (HONS)

A Thesis Submitted for the Degree of DOCTOR OF PHILOSOPHY.

December, 1977.

Abstract

An experimental and theoretical study of the impact behaviour of charged microparticles in a high voltage vacuum gap has been carried to investigate under controlled conditions the role of low velocity mi particles ($\lesssim$ 500 ms^{-1}) in initiating electrical breakdown in such gaps This has involved developing a unique (UHV) low-velocity source of mic sized charged particles to study the underlying mechanical and electri aspects of micro-particle impact on a range of target materials e.g. Pb, Ti, C, stainless-steel and mica etc., having atomically clean or oxidised surfaces. Argon-ion etching and electron-beam heating has b used for in-situ surface treatment and ellipsometry for characterising target surfaces. An associated sphere/plane theoretical model has be developed for detailed analysis of the many complex electrical (in-fli field emission, M.I.M. tunnelling and ohmic conduction) and mechanical (impact dynamics, deformation and heating) phenomena that are involve when a microparticle closely approaches and impacts on a plane target. In each instance the influence of parameters such as particle radius, particle/target impact velocity, surface field, surface condition and material has been determined.

It has been generally established that the "microscopic" mechanica behaviour of the materials studied, as measured by the coefficient of restitution e, follows the same general trend as found with correspondi macro-systems. However, there are considerable differences in the thi velocity of plastic deformation and the amount of scatter obtained whic has been interpreted as being mainly due to the differences in the mech properties of a very small localised volume of a surface and those of a bulk solid. The electrical behaviour as measured by charge reversal response has been shown to be predominantly controlled by electron tunn and that the mechanism is extremely sensitive to the differences in wor functions of the two interacting materials, the surface field, the thi and properties of the contamination films. Finally, these findings ha been shown to have important implications on the behaviour of naturally occurring microparticles in high voltage gaps, with the evidence sugges that the electrical rather than mechanical properties are the decisive factor for initiation of breakdown by the bouncing mechanism.

Microparticle/High-voltage/Impact/Tunnelling/Vacuum-breakdown

A DETAILED STUDY OF THE MECHANICAL AND ELECTRICAL ASPECTS OF MICROPARTICLE IMPACT PHENOMENA

by

AMRIT S. BRAH B.Sc (HONS)

A Thesis Submitted for the Degree of DOCTOR OF PHILOSOPHY.

December, 1977.

Abstract

An experimental and theoretical study of the impact behaviour of charged microparticles in a high voltage vacuum gap has been carried ou to investigate under controlled conditions the role of low velocity mic particles ($\lesssim$ 500 ms^{-1}) in initiating electrical breakdown in such gaps. This has involved developing a unique (UHV) low-velocity source of micr sized charged particles to study the underlying mechanical and electric aspects of micro-particle impact on a range of target materials e.g. C Pb, Ti, C, stainless-steel and mica etc., having atomically clean or oxidised surfaces. Argon-ion etching and electron-beam heating has be used for in-situ surface treatment and ellipsometry for characterising target surfaces. An associated sphere/plane theoretical model has bee developed for detailed analysis of the many complex electrical (in-flig field emission, M.I.M. tunnelling and ohmic conduction) and mechanical (impact dynamics, deformation and heating) phenomena that are involved when a microparticle closely approaches and impacts on a plane target. In each instance the influence of parameters such as particle radius, particle/target impact velocity, surface field, surface condition and material has been determined.

It has been generally established that the "microscopic" mechanica behaviour of the materials studied, as measured by the coefficient of restitution e, follows the same general trend as found with correspondi macro-systems. However, there are considerable differences in the thr velocity of plastic deformation and the amount of scatter obtained whic has been interpreted as being mainly due to the differences in the mech properties of a very small localised volume of a surface and those of a bulk solid. The electrical behaviour as measured by charge reversal response has been shown to be predominantly controlled by electron tunn and that the mechanism is extremely sensitive to the differences in wor functions of the two interacting materials, the surface field, the thi and properties of the contamination films. Finally, these findings ha been shown to have important implications on the behaviour of naturally occurring microparticles in high voltage gaps, with the evidence sugges that the electrical rather than mechanical properties are the decisive factor for initiation of breakdown by the bouncing mechanism.

Microparticle/High-voltage/Impact/Tunnelling/Vacuum-breakdown

A DETAILED STUDY OF THE MECHANICAL AND ELECTRICAL ASPECTS OF MICROPARTICLE IMPACT PHENOMENA

by

AMRIT S. BRAH B.Sc (HONS)

A Thesis Submitted for the Degree of DOCTOR OF PHILOSOPHY.

December, 1977.

Abstract

An experimental and theoretical study of the impact behaviour of charged microparticles in a high voltage vacuum gap has been carried out to investigate under controlled conditions the role of low velocity micro-particles ($\lesssim$ 500 ms^{-1}) in initiating electrical breakdown in such gaps. This has involved developing a unique (UHV) low-velocity source of micron-sized charged particles to study the underlying mechanical and electrical aspects of micro-particle impact on a range of target materials e.g. Cu, Pb, Ti, C, stainless-steel and mica etc., having atomically clean or oxidised surfaces. Argon-ion etching and electron-beam heating has been used for in-situ surface treatment and ellipsometry for characterising the target surfaces. An associated sphere/plane theoretical model has been developed for detailed analysis of the many complex electrical (in-flight-field emission, M.I.M. tunnelling and ohmic conduction) and mechanical (impact dynamics, deformation and heating) phenomena that are involved when a microparticle closely approaches and impacts on a plane target. In each instance the influence of parameters such as particle radius, particle/target impact velocity, surface field, surface condition and material has been determined.

It has been generally established that the "microscopic" mechanical behaviour of the materials studied, as measured by the coefficient of restitution e, follows the same general trend as found with corresponding macro-systems. However, there are considerable differences in the threshold velocity of plastic deformation and the amount of scatter obtained which has been interpreted as being mainly due to the differences in the mechanical properties of a very small localised volume of a surface and those of a bulk solid. The electrical behaviour as measured by charge reversal response has been shown to be predominantly controlled by electron tunnelling and that the mechanism is extremely sensitive to the differences in work functions of the two interacting materials, the surface field, the thickness and properties of the contamination films. Finally, these findings have been shown to have important implications on the behaviour of naturally occurring microparticles in high voltage gaps, with the evidence suggesting that the electrical rather than mechanical properties are the decisive factor for initiation of breakdown by the bouncing mechanism.

Microparticle/High-voltage/Impact/Tunnelling/Vacuum-breakdown

TABLE OF CONTENTS

CHAPTER 1

1.1. INTRODUCTION

1.1.1. Historical Survey of the Subject

The use of vacuum for high voltage insulation is an old and well established technique.Similarly, its breakdown under certain critical conditions is well known and a much investigated limitation. The first description of vacuum arc initiation was published almost a century ago (1), and since then, there has been an increasing interest in the electrical properties of high vacuum insulation. This is a consequence of its wide use in devices such as X-ray tubes, electron optical devices, high power vacuum switches, particle accelerators, to mention but a few and many other applications including those of space research (2)(3).

The initiation of Electrical Breakdown between two electrodes separated by an insulator occurs when there is an adequate charge multiplication in the dielectric. In vacuum, if the mean free path of the charge carriers is sufficiently greater than the gap separation (d), then the collision-induced multiplication of charged particles in the inter-electrode space will be insufficent to create a self-sustaining discharge. On this basis, it can be shown that breakdown should not occur below a pressure (p) where the product (pd) is less than 10^{-4} torr m., since below this value the mean free path is in the order of meters. The fact that breakdown can occur even at the lowest possible values of (pd), suggests that there must be other mechanisms whereby charge carriers are produced and multiplied, at least within limited regions of the inter-electrode space.

Until recently, the sequence of events that finally leads to breakdown of the vacuum gap, under high electrical stress has not been properly understood. However, during the last two decades or so, a large amount

of work has been done in this field. Many aspects of vacuum breakdown are now better understood and the overall problem can be seen in perspective. Nevertheless, it is a complex problem and much work remains to be done. The aim of the present research is to investigate in greater depth a specific mechanism that can initiate vacuum breakdown.

1.1.2. Review of the physical parameters known to influence the onset of breakdown

When an increasing voltage is applied across a vacuum gap, between two metal electrodes, there comes a point when the current flowing across the gap spontaneously increases to a value limited only by the external circuit and is accompanied by the occurance of a luminous arc within the interelectrode space. This transition from gap insulation to conduction is known as vacuum breakdown. The value of the voltage prior to this event is defined as the breakdown voltage for the gap under the given operating conditions.

The initiation of breakdown is a complex phenomenon, depending on a large number of parameters, where the associated physical mechanisms are frequently not precisely understood. The more important of the known influences will now be briefly surveyed, but without attempting to offer any physical explanations.

The breakdown field has been found to be a decreasing function of electrode separation (4). That is, the breakdown field for a very small gap separation (~0.1mm) is found to be quite high (~$10^8 Vm^{-1}$), as compared with the breakdown field (~$10^6 vm^{-1}$) for large gaps (~100mm). This suggests the possibility of at least two different breakdown mechanisms (4) which are discussed in section (1.3). For small gaps, as the applied voltage is increased, relatively steady prebreakdown currents that are predominantly due to electrons are obtained (5). However, with somewhat larger

gaps (~3 mm), millisecond pulses called micro-discharges also occur but these are found to be predominantly ionic in nature (6). The steady prebreakdown current that a gap can withstand is found to be appreciably higher for small gaps. If a gap is continually sparked over, the breakdown voltage increases until it reaches a 'plateau'. This effect is known as conditioning (7)(8)(9).

Electrode material is important, with both anode and cathode materials having an influence. In many cases, the anode material is especially critical. An approximate ranking in order of increasing excellence is (10): C, Be, Pb, Al, Cu, Ni, Fe, SS, Ti, Mo, and W.

The evidence available on the effect of electrode surface finish on the gap insulation is contradictory. Although a substantial improvement was reported by Trump (11), there are other reports (12) suggesting that the surface finish has very little effect on the voltage hold-off capacity. General surface contamination reduces breakdown voltage; a reduction of up to 50 % of the value for clean electrodes has been reported (13)(14). Jedynak (15) investigating the effect of surface coatings has shown that thin dielectric films on the cathode surface, if properly applied, can substantially enhance the insulation of a vacuum gap, although anode coatings were usually found to be detrimental.

The breakdown voltage of a given gap has been found to be significantly dependent on the electrode geometry (16). Firstly, there is an 'area' effect, i.e. the insulation strength is reduced with an increase in electrode area. Secondly, however, the insulation strength is also reduced with a decrease in the electrode curvatures, but this is inspite of a decrease in the exposed area.

Slivkov (17) investigated the effect of electrode temperature on the gap insulation ; no significant difference in the breakdown voltage was observed on heating the electrodes until the transition temperature was

attained. By cooling electrodes to liquid nitrogen temperatures, Maitland (18) however, has reported some improvement in the breakdown value.

Differences in the residual gas pressure for gaps of ~1mm. have been reported to markedly influence the insulation strength (19)(20). For pressures between 10^{-3} and 10^{-4} torr the breakdown voltage was found to read a maximum, almost twice that obtained at very low pressures.

Denholm, (8) investigating the effect of applied voltage, compared the behaviour under direct, alternating and impulse voltages. It was shown that the breakdown voltage for 50 hz a.c. voltage lies between the d.c. and impulse voltage. The rate of rise (21)(22) of the applied voltage has also been found to influence the breakdown voltage which increases with the frequency (23). Under steady state conditions breakdown is quite often unheralded and sporadic so that a given pair of electrodes may support a constant voltage for hours, or even days and then suddenly breakdown; also when an impulse is applied there is a time delay before the onset of breakdown. Rohrbach (24) has conducted extensive studies on these effects and established the existence of the breakdown time lags.

Lastly, by limiting the amount of energy released in the arc on breakdown, even the external circuit of the power supply has been found to influence the breakdown voltage. It has been reported (8) that a large resistance in series with the gap gave rise to erratic and low breakdown voltages, the highest and most consistent results being obtained with zero resistance.

It is clear from above that controlled experiments taking into account all these parameters are almost impractical. Interpretations of the results are complex and disagreement among the different investigators is quite common. Consequently, many different hypotheses have been put forward to explain the various aspects of vacuum breakdown summarised above. A few of the more important hypotheses, that have emerged, are discussed in the following section.

1.2 SURVEY OF THE VACUUM BREAKDOWN HYPOTHESES

Many different mechanisms have been proposed in attempts to explain the phenomena associated with the breakdown of a vacuum gap. There are at least three major hypotheses, all of which are based on semi-empirical fact but none of which are complete either qualitatively or quantitatively. In view of recent experimental results, the present consensus among the investigators is that breakdown could result from any or all of the following three fundamental processes:

(i) Elementary particle exchange

(ii) Field emission

(iii) Clump or Microparticle exchange

1.2.1 Particle Exchange Hypothesis

Van atta et al (25) first proposed a mechanism based on the regenerative interchange of charged atomic particles between the two electrodes. That is, a chain reaction in which particles ejected from one electrode produce upon impact at the other electrode surface, particles of opposite sign, which in turn produce more particles of the first kind, etc. Breakdown occurs when the regeneration coefficient (i.e. the product of the yields for the generation of secondary particles at the respective surfaces) exceeds unity.

The particles postulated include positive ions, negative ions, electrons and photons. Particle exchange processes have been the subject of experimental and theoretical investigation for several decades and various refinements and variations of the basic model have been proposed, particularly in respect of the processes associated wit the initial emission of charged particles. For instance, Ionov (26) has proposed field-enhanced thermionic emission of positive and negative ions from the contamination layers at the electrode sufaces. Mansfield (27) and Arnal (28) have more specifically proposed the exchange of positive and negative hydrogen ions originating from contamination layers due to oil from the vacuum system, and more recently Tarasova (29) has shown that not only hydrogen ions but heavier ions and micro-particles can participate in the process.

In general, particle exchange theories seem inadequate to explain vacuum breakdown between clean electrodes, since in that case secondary emission yields are much too low to sustain a chain reaction (30)(31). Nevertheless, they provide a reasonable mechanism for explaining the very low steady state current and the repeated microdischarges between contaminated electrodes which have been observed by a number of investi gators, particularly Germain and Rohrbach (32). Hence, they are very useful in explaining, at least qualitatively, an important aspect of prebreakdown phenomena in poor vacuum. However, even for contaminated surfaces it is not clear that particle exchange theories can explain the transition from microdischarges to full voltage breakdown.

1.2.2 Field Emission Hypothesis

The basic model for the field emission breakdown hypothesis can be summarised as follows. At low gap voltages, stable field emission occurs, originating as isolated emitters on the cathode surface. As the gap voltage is increased, the prebreakdown current increases exponentially and causes local heating at both the cathode and anode. When the voltage reaches a critical value, regenerative thermal instabilities develop either at the cathode or anode, leading to breakdown by local evaporation and subsequent ionization of the electrode material.

The field emission current density is governed by the Fowler-Nordheim law (33) and can be put in the simplified form:

$$J = 8.0 \times 10^{-5} \frac{E_o^2}{\phi} \exp\left(-6.12 \times 10^8 \frac{\phi^{3/2}}{E_o}\right) \quad \ldots\ldots (1.1)$$

Where J = emmitted current density in ampere/cm^2,

E_o = the macroscopic applied field in V/cm

and ϕ = work function of the electrode in eV.

For the nominal macroscopic breakdown fields obtained in practice, equation 1.1, yields very insignificant amounts of current (less than an electron per second), which suggests that the field emission processes would be unlikely to play an important role in vacuum breakdown. However, this dilemma was overcome by postulating field-enhancing protrusions (34) with field enhancement factors β of ~ 200, on the cathode: the microscopic field being given by the expression $E_{mic} = \beta E_o$

Subsequently, many authors (35) (36) have observed protrusions on electrode surfaces, and mathematical expressions have been derived for the field enhancement factor of certain idealised geometries(37).

Introducing $Eo = V/(kd)$, where $k = 1$ for plane parallel electrodes, the field emission current density may now be written as

$$J = 8.0 \times 10^{-5} \beta \frac{V^2}{kd} \phi^{-1} \exp\left(-6.12 \times 10^{8} \phi^{3/2} \beta \left(\frac{V}{kd}\right)^{-1}\right) A / cm^2 \quad \ldots.(1.2)$$

where V is the applied voltage and d the gap spacing for an effective emitting area A, the measured emission current will therefore be given by

$$I = J.A \text{ Amps.} \quad \ldots.(1.3)$$

By recording emission currents, for a range of voltages at a given electrode spacing, it follows from equation (1.2) that the plot of log I/V^2 verses $1/V$ should produce a linear graph. From the slope it is possible to obtain an estimate of the enhancement factor β, and from the intercept an estimate for the emitting area A. Such Fowler-- Nordheim plots have been obtained by many authors (38) (39) (40), thereby strongly suggesting that the prebreakdown conductivity, at least for gaps less than a few millimeters, is due to field emission. There are also reports (41) (42) however, that experimental observations on the emission from metal surfaces in vacuum are best described in terms of Schottky emission (43). Morrant (44) has shown that results which gave straight lines for field emission plots, should also give straight lines for Schottky plots.

Depending on the nature of a protrusion, various theoretical models have been proposed (45)(46)(47) predicting either a cathode or an anode initiated breakdown. In the case of <u>cathode - initiated voltage breakdown,</u> first proposed by Dyke and Trolan (34), the instability is believed to be due to its own emitted current. The rate of temperature rise of the emitter tip is controlled by three separate energy exchange phenomenon - viz :

i) Resistive or Joule heating of the emitter due to current flow through the emitter.

ii) Nottingham Effect (48), which is due to the energy difference between the mean energy of emitted electrons and mean energy of those within the conduction band. This effect predominates at low temperatures and is primarily responsible for raising the emitting tip to the high temperature where its resistivity becomes large and Joule heating normally takes over. In contrast at higher temperatures the effect becomes negative and cooling occurs, thus exerting a stabilizing influence on the Joule heated protrusion. In general, the effect is most important for low melting point materials.

iii) Thermal conduction and radiation cooling of the emitter. An analysis by William and Williams (49), which allowed for both the variation of resistivity with temperature and Nottingham effect, has shown that radiation cooling is about three orders of magnitude smaller than conduction cooling and hence may be neglected.

In the case of anode induced breakdown first proposed by Boyle (50), the instability is supposed to be the result of vaporisation of the anode material from localised anode spots, that have been subjected to electron bombardment by electron beams originating from cathode protrusions.

This mechanism was later refined and developed more quantitatively by a number of researchers (45)(46)(47). The main conclusion of this work was that a criterion could be formulated which predicted whether thermal instabilities developed at the cathode or anode. This criterion could be tested by analysis of the stable prebreakdown currents. The main parameters determining whether thermal instabilities originate at the cathode or anode is the local field enhancement factor β of the emitting cathode protrusions. Large β values lead to cathode initiation

and small β-values lead to anode initiation. This suggests anode initiation may be fairly common for relatively smooth cathodes.

In general therefore, the phenomena of regenerative thermal instabilities arising from excessive field emission is well understood and established as a basic process responsible for vacuum breakdown; at least for short gaps ($\sim$1mm) in high vacuum. However, there is no clear experimental confirmation with regard to whether breakdown is either cathode or anode induced. Furthermore, it has been argued (40) that steady evaporation of material from either electrode, due solely to local heating by pre-breakdown currents, does not produce metal vapour of sufficient density in the gap for any significant avalanche process to occur.

Hence, the sequence of events that are happening after the onset of field emission need to be clarified experimentally. Another paradoxical situation in the field emission hypothesis concerns the presence of protrusions themselves. There is some evidence (51) to suggest that these protrusions are formed on the electrode surface after application of the voltage. In further support Van Oostrum (52), in more recent work, has shown that the microscopic surface conditions are subject to changes with time, particularly at gap voltages high enough to induce prebreakdown currents. If this is indeed the case then the mechanisms that are responsible for the growth of these protrusions and other microscopic changes need to be better understood.

1.2.3 Clump or Microparticle Hypothesis

Cranberg (53) was the first to propose that charged aggregates of material, clumps or microparticles loosely attached to the surface of the electrode, are torn away by electrostatic forces and are accelerated to the opposite electrode by the applied electrostatic field, thereby gaining kinetic energy during transit.

Breakdown is assumed to occur when the energy per unit area (W) delivered to the target electrode exceeds the critical value C', a constant for a given pair of electrodes. The quantity W is the product of the gap voltage (V) and the charge density on the clump; the latter being proportional to the electric field at the electrode from which the clump originates. The criterion for breakdown is,

$$VE = C' \qquad \text{.....(1.4)}$$

For plane electrodes $E = V/d$, where d is the interelectrode spacing and C is another constant involving C', so that the above criterion may be re-expressed as

$$V = (Cd)^{0.5} \qquad \text{.....(1.5)}$$

By plotting the breakdown voltage (V) for a range of gaps ($d=10^{-3}$-10 cm), using the experimental data from a number of different investigators, Cranberg obtained a plot showing good agreement with his hypothesis. He has also obtained an estimate of the temperature rise (53) of the target area The energy (W) delivered by the clump per atom struck on the target electrode is

$$W \simeq Ca^2/4 \qquad \text{.....(1.6)}$$

where a is the interatomic spacing. If n^* is the penetration depth in to the electrode, expressed in atomic layers of the electrode receiving the energy of the clump, the local temperature (T) attained is given by,

$$T = Ca^2/4\pi n^* k \qquad \text{.....(1.7)}$$

where k = Boltzmann's constant.

Using this expression Cranberg has shown that a temperature well in excess of the metallic boiling point could be expected for penetrations of several hundred atomic layers of the electrode. Subsequently, there have been many refinements and developements of this basic idea of Cranberg's and these are discussed in section (1.4).

1.3 The Dependence of the Breakdown mechanisms on the Experimental Regime

From the foregoing discussions outlining the various vacuum breakdown hypotheses, it seems that a number of breakdown mechanisms could occur either singly or simultaneously in any given vacuum gap. Nevertheless, it is possible to separate the various physical models and to characterise them in terms of different gap regions. This is illustrated in figure1.1, where the curves show the breakdown threshold as a function of the initiating mechanism.

In region A(Fig.1.1), with gaps $\lesssim$1mm and voltages up to $\sim$50KV, where both the limits are approximate and depend onsurface conditions, field-dependent electron currents are observed prior to breakdown and this region is clearly dominated by field-emission breakdown.

For gaps $\gtrsim$1mm corresponding to region B (Fig.1.1), an increase in voltage is associated with the appearance of ionic microdischarges which occur at a distinctive voltage-threshold, dependent on the gap spacing and the state of electrode surface. There is however, no definite proof that these microdischarges can lead to breakdown.

For even larger gaps corresponding to region C(Fig.1.1), it is clear that the microparticle-initiated breakdown dominates.

There is however, a great deal of overlap of these regions A,B and C(Fig.1.1), particularly in the transition region B. For example at small gaps and low voltages the microparticle velocities can reach the limit of elastic deformation by an energy enhancing mechanism, resulting from multiple bouncings between the electrodes under the condition of efficient charge reversal during impact (54). Even if breakdown is not

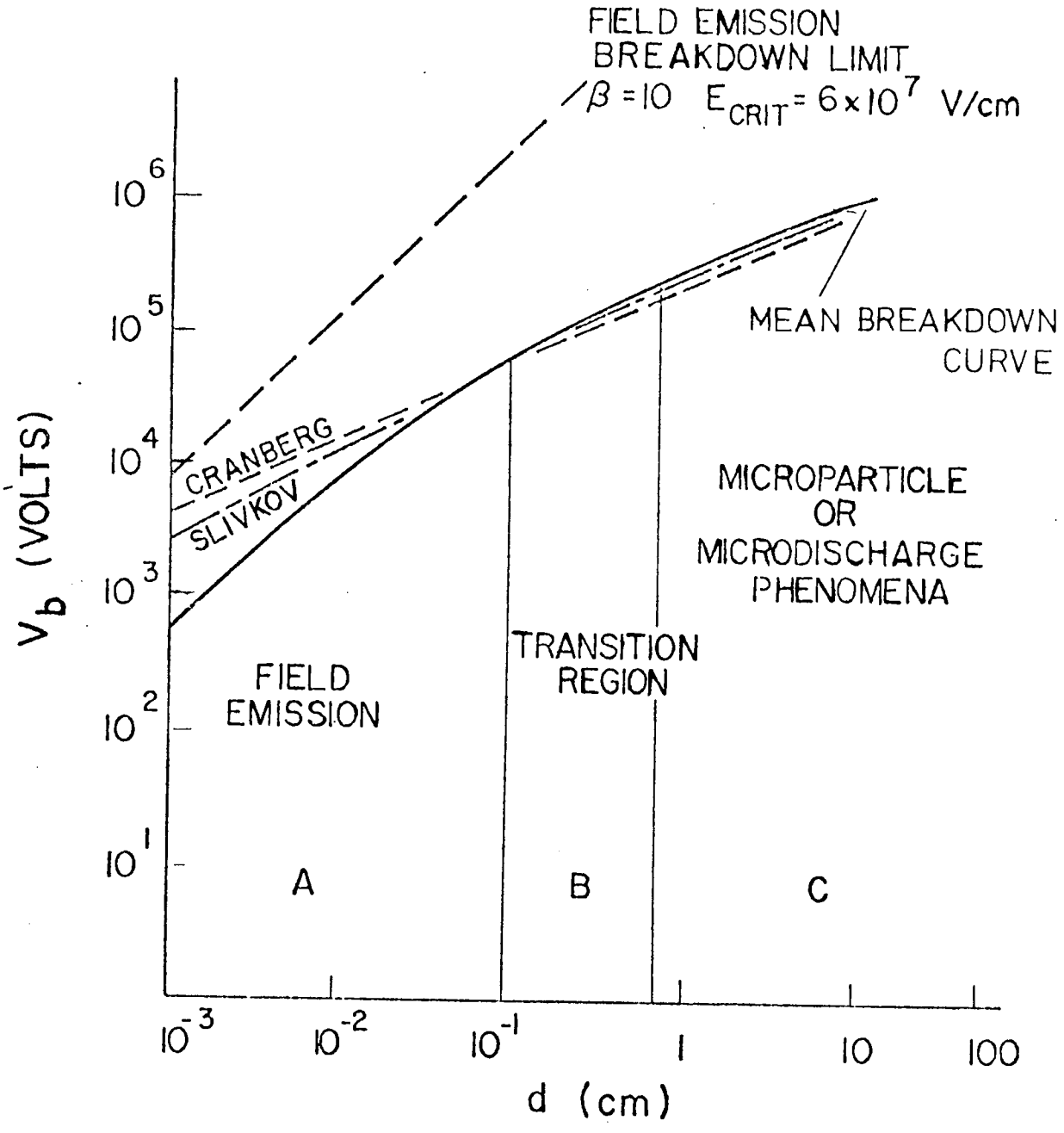
FIELD EMISSION
BREAKDOWN LIMIT
β = 10 E_CRIT = 6 x 10^7 V/cm
MEAN BREAKDOWN
CURVE
CRANBERG
SLIVKOV
MICROPARTICLE
OR
MICRODISCHARGE
PHENOMENA
TRANSITION
REGION
FIELD
EMISSION
A
B
C
V_b (VOLTS)
10^6
10^5
10^4
10^3
10^2
10^1
10^-3
10^-2
10^-1
1
10
100
d (cm)

Figure 1.1

directly initiated by impact generated plasma, the local damage so caused can give rise to field emission sites and the subsequent possibility of cathode or anode instabilities (35).

This could also happen in the case of larger gaps, where the higher voltages can result in the particle velocities exceeding the limit of elastic deformation for a single transit of the gaps, leading to a sudden breakdown, without any measurable pre-breakdown current. Thus a $\sim$0.01mm gap can withstand currents up to a few milliamps without voltage collapse, whilst currents of few nanoamps are all that flow through a $\sim$30mm gap before breakdown (4). This also suggests that here the mechanism of breakdown is something other than due to field emission, probably microparticle induced.

In conclusion therefore, an explanation of breakdown on the basis of field emission could be given when the gaps are the order of few millimeters or less, if one assumes field enhancing protrusions with reasonable enhancement factors ($\geq$100). For larger gaps however, a mechanism based on field emission alone does not satisfactorily explain the observed phenomenon, unless the existence of protrusions with unrealistically large field enhancement factors ($\geq$1000) (55) is assumed. But any such explanation based on large enhancement factors will also be unsatisfactory, since the enhancement factors are a decreasing function of electrode spacing (for gaps$\sim$1mm). Thus, for gaps greater than few mm., the experimental results can only be explained by resorting to an alternative mechanism, the most likely of these is some form of microparticle process.

1.4 MICROPARTICLE PHENOMENA

Since Cranberg's original proposal in 1952 (see section 1.2.3), there have been many discussions in the literature concerning the possibility of microparticle induced breakdown. In this time, little has emerged that makes the application of microparticle theories either convenient or compelling. Nevertheless, in the last decade or so, many experimental observations and improved theories have paved the way for a better understanding of how they may be important. This evidence of their existence and current theories are discussed below.

1.4.1 Experimental evidence for the existence of naturally occuring microparticles in high voltage vacuum gaps.

1.4.1a Material Transfer

Observation of material transfer in the form of clumps or micoparticles from one electrode to the other in the prebreakdown phase has been reported by a number of research workers. Most of the earlier investigations were carried out using two basic techniques, namely, the radio-active tracer techniques(56)(57)(58) and microscope techniques(59)(60)(61)(62) for the topographical examination of electrode surfaces. In the majority of cases the rate of transfer of the anode material was found to be one or two orders of magnitude greater than the cathode material.

Razin et al (62), using a cinemicrophotography technique, studied the way the topography of electrode surfaces changes in the presence of applied electric fields. In agreement with later workers (60) (61), they observed the removal of particles from the anode under the action of high electrical stresses ($\gtrsim 2.10^7$ V/m), but on traversing the gap these particles failed to cause breakdown. Nevertheless, they observed

ucleation and growth of microtips on the anode surface, which when uptured due to further increase in the applied field, resulted in the reakdown of the vacuum gap. It also appears from this and other work 65), that electrode impurities are often a cause of the observed aterial transfer.

Rohrbach (63) and Piuz (64) have demonstrated a Laser-scattering echnique whereby it is possible to make inflight detection of microparicles of sizes greater than 3μm. Puiz observed several events which ould be identified as microparticles, but the frequency of observations as too low to account for the many breakdowns that occured which had he characteristics of a microparticle induced event. A possible xplanation of this result could be that the important regime of the micron submicron particle was not explored due to the noise - imposed detection limit of the instrument used.

A more direct approach to confirm material transfer was adopted by Hurley and Parnel (65), where a plastic film was interposed between electrodes in the prebreakdown phase. On examination the film showed presence of trapped particles 3-40μm in diameter which, after analysis, were shown to be impurities.

More recently, Menon and Srivastava (66), using a shielded collector placed behind perforated (50% transparency) cathodes of differing materials, have observed the release of micron and submicron particles in large numbers ($\sim 10^6/m^2$). This occured at voltages as low as 30% of the breakdown voltage. These particles which were in the main of anode material were produced simultaneously to the observation of low level light flashes in the gap. Large microparticles, greater than 10μm, were not generated during the normal prebreakdown phase, thus suggesting that the breakdown is predominantly due to micron-submicron particles.

In a recent experiment to investigate the effect of micro - particle and ion bombardment on electrical breakdown in a broad area vacuum gap, Beukema (67) has shown that the microparticles originate from both the anode and the cathode. Also in agreement with Menon and Srivastava, an abundance of micron-submicron particles were found to be released in the prebreakdown voltage range. However, similar numbers of small particles ($\sim 10^6$/m.) were not observed in the experiments of Chatterton and Biradar (68) or those of Hurley and Parnel (65). A possible explanation for these cases could be that the collecting surfaces were exposed to electric fields and so that many of the weakly attached particles may have been removed and lost from the gap. Also in the case of Hurley and Parnel, the detection of particles was done by optical microscopy, which suggests that the small submicron particles would not have been observed.

1.4.1b Electrical inflight detection

Boulloud (69), while considering the charge transfer due to microparticles, estimated that this would be difficult to detect against the normal breakdown currents. Instead, the charge flow was estimated using averages, no consideration being given to the expected pulse shape. In the case of multiple bouncing (i.e. for particle velocities below the elastic limit) it was shown that the mean current - i after large number of impacts was

$$i = Qv/d \qquad \ldots\ldots(1.8)$$

where Q = charge on the particle

v = mean velocity

d = interelectrode spacing

For typical conditions Boulloud found that $i = 10^{-8}$ Amps., for a micron

In a recent experiment to investigate the effect of micro - particle and ion bombardment on electrical breakdown in a broad area vacuum gap, Beukema (67) has shown that the microparticles originate from both the anode and the cathode. Also in agreement with Menon and Srivastava, an abundance of micron-submicron particles were found to be released in the prebreakdown voltage range. However, similar numbers of small particles ($\sim 10^6$/m.) were not observed in the experiments of Chatterton and Biradar (68) or those of Hurley and Parnel (65). A possible explanation for these cases could be that the collecting surfaces were exposed to electric fields and so that many of the weakly attached particles may have been removed and lost from the gap. Also in the case of Hurley and Parnel, the detection of particles was done by optical microscopy, which suggests that the small submicron particles would not have been observed.

1.4.1b Electrical inflight detection

Boulloud (69), while considering the charge transfer due to microparticles, estimated that this would be difficult to detect against the normal breakdown currents. Instead, the charge flow was estimated using averages, no consideration being given to the expected pulse shape. In the case of multiple bouncing (i.e. for particle velocities below the elastic limit) it was shown that the mean current - i after large number of impacts was

$$i = Qv/d \qquad \ldots\ldots(1.8)$$

where Q = charge on the particle

v = mean velocity

d = interelectrode spacing

For typical conditions Boulloud found that $i = 10^{-8}$ Amps., for a micron

sized particle undergoing continuous bouncing. This value of current is of the same order of magnitude as the prebreakdown currents observed in practice that are accompanied by evidence of material transfer (68) (59) (56). Schwabe (59), also found that the amount of mass transferred increased with an increase in the prebreakdown current density and concluded that the quantity of material transferred was proportional to the charge transferred. More recently, Chatterton (68), by measuring the prebreakdown currents while the field emission currents were suppressed by heat conditioning, showed that they compared favourably in shape and size with those corresponding to microparticle motion within the inter-electrode space.

In addition, the charge flow resulting from the motion of microparticles which were artificially introduced into the vacuum gap, has been observed by Razonova (71) and Olendzkaya (72), and more recently confirmed by Hurley (73) and Cornish et al (74).

1.4.1c Impact Ionisation

Apart from investigations of charge flow due to the microparticle motion, a number of micrometeriod simulation studies (75) (76) (77) (78) have shown that plasma can be generated during the impact of high velocity microparticles on metal targets. In relation to vacuum breakdown, that is, for the energy range of microparticles normally found in vacuum gaps, Menon and Srivastava (83) have made a comparison between the two phenomena based on the recent work of Smith and Adams (75) and shown that charge transfer should dominate over charge generation in most experimental situations except perhaps at the highest voltages.

1.4.1d Impact Damage

Topographical studies using electron optical techniques to investigate the presence of impact damage resulting from microparticles have been carried out by a number of research workers. Little and Smith (51), in their experiments with plane parallel aluminium electrodes, were the first to report that the particles ejected from the anode cause craters and associated sharp field enhancing protrusion on the cathode surface, which can subsequently act as field emitters leading to breakdown (see section 14.2 ii); the anode sites from which the microparticles originated were located along or near the grain boundaries. This important conclusion has received additional support from a number of later studies: Latham and Braun (54) observed extensive microcratering with assoicated sharp field enhancing protrusions on a tungsten hairpin cathode used in conjunction with plane anodes of various materials. Biradar and Chatterton (36), using a cylindrical geometry observed similar impact damage on the smooth surface of the central tungsten wire that had been preheated to $>2000^{\circ}C$. Menon and Srivastava (66), using a range of differing electrode material combinations, in plane-anode perforated cathode configuration, found that the collector placed behind the cathodes showed evidence of impact craters with sharp protruding edges; examination of the electrode surfaces also revealed evidence of the possible sites of formation of microparticles. More recently, Buekema (67) using stainless-steel and titanium broad area, plane electrod has shown that microparticles originating from both anode and cathode can cause impact damage on the cathode surface, resulting in an increase in the measured field enhancement factor. The latter observation of microparticles originating from cathode returning and impacting on the cathode, indirectly supports the 'bouncing' hypothesis, (55), (68), (72), (see section 14.2 (iv)); which incidentally is

also supported by the earlier work of Fabiniak, (80). Where, in a series of topography studies with plane electrodes of various materials, a number of sites on both electrode surfaces, of groups of craters similar in shape but increasing in depth were observed, indicating successive bouncing to have taken place.

1.4.1e Origin of Microparticles

A great deal is still to be learnt about the details of the origin of microparticles, especially in the case of 'microsparks' observed by Menon and Srivastava (66), which appear to herald particle generation. Suggestions for their possible origin include weakly attached regions (81), impurities (62) (66), thermally produced anode protrusions (35) and debris from previous breakdown (all arcs emit droplets (83)), can all play a part in microparticle production. However, their size distribution, detailed frequency of occurrence and relation to electrode surface properties still requires further investigation. In any event, the likelihood of large microparticles ($\geqslant 5\mu m$) occurring in large numbers now seems unlikely.

1.4.1f Deliberate insertion of microparticles into a high voltage gap

The effect of the deliberate introduction of artificially generated microparticles into a vacuum gap has been investigated by a number of research workers. Slattery et al (84), using carbonly-iron spheres (1-2μm in diameter), which were accelerated in a hypervelocity accelerator to velocities $\geqslant$ 2km/s, have shown that by firing these particles into a high voltage vacuum gap it was possible to initiate breakdown; the probability of breakdown was found to be greater when they were fired at the cathode.

In another type of experiment, Rozanova (85) introduced artificial (5-40μm dimeter) particles of W,Ni, and graphite onto the electrode surfaces and on application of high voltage it was found that these particles which were weakly bound to the electrode surface, could initiate vacuum breakdown. From the study of time lags, it was inferred that breakdown is initiated when a positively charged microparticle was incident on the cathode. Similarly, Poshekhonov and Progorelski (87) by using somewhat larger (20-80μm dimeter) molybdenum particles, have also observed the resulting initiation of vacuum breakdown; the breakdown delay time was found to correspond to the interelectrode transit time. Olendzkaya (72) and Udris (86), in experiments using even larger particles (0.5-09mm) of steel and mercury have shown that breakdown can be initiated by the process of trigger discharge (see section 14.2,iii). Martynov and Ivanov (88) whilst studying this mechanism by using millimeter sized insulating particles found that the breakdown voltage increased almost linearly with particle size.

1.4.1g Velocity of Microparticles

The direct experimental evidence for the velocities of naturally occurring microparticles is somewhat meagre. Artificial microparticle velocities have been estimated by observing the pre-breakdown pulse structure (68) and by measuring time delays to breakdown (71) (87); in all of these cases particle velocities lay in the range 1 - 20ms^{-1} (68). Similarly, naturally occurring particles, in the very few instances observed, were found to have velocities of ~1ms^{-1} (68), for mainly large (>10μm) particles. This however, is not in agreement with the observations of Piuz (64), who found (6-10μm) sized particles with velocities of approximately 400ms^{-1}. On the other hand, impact damage studies, whilst imprecise, indicate velocities at impact of $\geq$500ms^{-1} (70). This suggests that the subject of particle velocities requires further investigation both experimentally and theoretically.

1.4.2 Microparticle - induced Breakdown Theories

From the experimental evidence of microparticle properties described above, it is clear that the most important parameters in deciding the mechanism of breakdown are the particle size and impact velocity. Consequently, of the many microparticle breakdown theories put forward, four basic types have emerged which in essence depend upon particle size and impact energy for their relevance. All of course, are developments of Cranberg's early idea that when clump energy reaches a certain fixed value breakdown can be initiated. This simple idea however, does not involve any discussions of the energy transfer process or of the breakdown development.

(i) For ultra high velocity, small (mainly submicron) particles. Slivkov (89) has developed Cranberg's model by putting in two constraints that are related to energy exchange and breakdown development.

(a) The particle must have sufficient velocity to vaporise itself. This implies that for a given value of the gap voltage (V) and field (E), the particle radius must be less than certain critical value r_{max}.

(b) Sufficient vapour must be produced so that at some stage the (pd) product of the expanding gas pocket coupled with the voltage across the pocket should allow a gas discharge to be initiated, which implies that the microparticle radius exceed a certain critical value r_{min}.

These considerations lead to gap / breakdown voltage law of the form

$$V \propto d^{0.625} \qquad \ldots\ldots(1.9)$$

This expression although derived quite differently is similar to Cranberg's original expression for breakdown (see eq. 1.5). The Slivkov (89) model is essentially a high velocity one, since it is known from

a number of micrometeroid simulation studies (75) (76) (77) that particle velocities exceeding 6 km/sec appear to be necessary to completely vaporise particles.

Germain and Rohrbach (90) made similar calculations to Slivkov's to explain their breakdown results for large gaps (1-10cm) and voltages up to ~700kV ; in order to give a high charge/mass ratio they considered a semi-ellipsoidal microparticle with its elliptical end pointing along the electric field lines. Experimentally however, breakdown was observed by Slattery et al (84) at velocities between 2-4 km/sec, which implied that Slikov's simple model required some modifications to allow for the possibility of partial evaporation of the larger microparticles and gas desorption from electrode surfaces. To meet this limitation Slivkov (91) subsequently extended his basic model.

(ii) For micron and submicron sized particles travelling at intermediate velocities (0.5 - 2km/sec), that are somewhat in excess of tne elastic limit of commonly used electrode materials, the microparticles can stick or cause extensive damage in the form of craters with sharp edges (see section 1.4.1d) giving rise to field emission sites on the target electrode. It is thus possible to imagine that in this case, breakdown could be caused by the sudden creation of these sites on the cathode, which immediately go unstable through conventional field emission processes. The observation of the formation of such craters and associated field emission sites was first reported by Little and Smith (51) and has later been confirmed by others (55) (68) (66) (67).

(iii) When particles are large (>10μm), their impact velocities are usually too low to cause breakdown resulting from electrode surface damage. However, they can still initiate breakdown (71)(72)(87), by

the process of trigger discharge - first proposed by Olendzkaya (72) and Udris (86), who suggested that as the particle approaches an electrode, the enhancement of field between the charged particle and the electrode causes a discharge between them. This discharge could then trigger the breakdown of the main gap. However, the details of the energy exchange mechanism leading to such a discharge were not discussed by the authors.

To account for this, Martynov (88) (92) and Chatterton et al (93) (95) independently refined the basic model in two slightly different ways. Both proposed that the trigger discharge is caused by field emission in the particle - electrode interspace, due to the presence of the conducting sphere and its charge causing field enhancement, just prior to impact. However, they are at variance on how the breakdown of the main gap is triggered. Martynov (92) proposes that after the trigger discharge, the plasma produced extends beyond the interspace, so as to form a positive ion - sheath which enhances the field locally allowing a conventional field emission breakdown to occur in the main gap. Whereas in Chatterton et al's model (93), which basically is a development of an earlier idea of Poshekhonov and Pogorelskii (87), it is proposed that the trigger discharge melts regions on the particle and electrode, so that when the particle bounces back an emission site is formed, which could go unstable immediately or at some time later. Although it is probably too early to decide between these two models of breakdown development, it is however clear that particles exceeding (30-50μm) in size are necessary for the trigger process to operate. In a more recent work, Chakrabarti (94) has extended this limit to particles ($\geqslant$50μm) in radius, thus suggesting that this process is only likely to be important in the very rare cases when such large particles exist in the interelectrode gap.

Another version of trigger discharge process has been proposed by Poshenkhonov and Solovyev (96) to explain short time-lag breakdown in the presence of conducting metal particles. They have considered the possibility of breakdown initiation by the detachment of a microparticle from the cathode surface in the rising part of an impulse waveform. Their experimental and theoretical analysis of the field under these conditions showed that trigger discharge initiated breakdown can also occur as the particle leaves the electrode surface, whereas previously, the mechanism is dependent on the particle size and the rate of voltage rise (95). Particles of sizes less than 80μm appear unlikely to undergo this form of breakdown.

(iv) For smaller sized particles (say $\lesssim$ 5um), that occur abundantly (66) (67) at velocities below the elastic limit, initiation of breakdown is only possible if the existence is assumed of some intermediary mechanism by which the energies of these particles may be enhanced. To date , two different mechanisms by which particle energy may be increased have been proposed; (a) inflight charge enhancement (65) and (b) energy enhancing bouncing impacts (55) (68) (72).

Hurley and Parnel (65) have considered the case of a particle which is itself field emitting during its interelectrode flight. By using computer simulation techniques, it was shown that a positive particle, originating at the anode, can, as a result of inflight field emission, increase its charge on approaching the cathode. The kinetic energy upon arrival at the cathode will thus be correspondingly increased. The reverse of this process will operate on particles originating at the cathode, where the initial negative charge will be decreased by inflight field emission, and under favourable conditions it may even be

completely neutralized and subsequently reversed in sign. There is however, no direct experimental evidence available to support the existence of this effect.

Latham and Braun (55) have suggested that particles with velocities below the elastic limit, can undergo, at least one intermediate low - velocity bouncing impact during their life cycle, which, under favourable conditions of momentum and charge reversal, can result in kinetic energy enhancement sufficient to give the high impact velocities necessary to produce local melting evident as microcraters and field emission sites and finally leading to breakdown. It was also suggested, that the molten material produced in this process may provide a source of spherical 'Secondary' microparticles which are similarly accelerated from the anode to give further cathode microcratering and a second generation of secondary microparticles. The profusion of craters following a single 30μs field pulse (97) illustrates the catastrophic progress of this chain reaction type electrode damaging process. This concept of particle bouncing has also been mentioned by Chatterton and Biradar (68), as a possible explanation for energy enhancement. Originally however, this mechanism was considered by Olendzkaya (72), but his experimental evidence for occurrence of the phenomena was somewhat inconclusive. Nevertheless, since then, there have been many experimental observations which indirectly support this process.

A number of electrical detection studies (see Section 1.4.1b) involving the analysis of the prebreakdown current structure, have found evidence of particle bouncing. For example, Martynov (88), by introducing artificial microparticles in a plane parallel electrode arrangement, has shown that the resultant prebreakdown current structure (approx. sinusoidal) to be due to

the particle bouncing to and fro between the electrodes. This bouncing process is also particularly important in explaining the observed time lags (63) (71) (99). Razonova (71) found that the time delay to breakdown was doubled when artificial microparticles were placed on the cathode, thus suggesting that the cathode originating microparticles with velocities below the elastic limit can, after an energy enhancing bounce, initiate breakdown by impacting on the cathode. In further support, topography studies carried out by Fabiniak et al (80) and more recently, by Buekema (67) (see section 1.4.1d) have also found evidence indicating particle bouncing.

In a more recent work Latham (81), has extended this model by suggesting that the microparticle charge reversal efficiency may be governed by the differences in the mechanical and electrical properties of the equilibrium oxide layer (98) found on most of the commonly used electrode materials and has thus attempted to explain the observed differences in the breakdown voltage for different electrode materials (see section 1.1.2); especially the influence of the anode material (54) as the controlling parameter of the microcratering mechanism. This suggestion is also supported by the earlier work of Jedynak (15), where the application of a thin dielectric coating to the electrode surfaces was found to quite significantly influence the breakdown voltage.

1.5. Status of Problem

In conclusion therefore, it is well established that electrical breakdown for small interelectrode gaps ($\lesssim$ 1mm) is due to the field emission process and for large gaps ($\gtrsim$ 6mm) it is the result of the impact of high energy microparticles. Whereas, for the intermediate range of gaps (2-5mm) some further clarification is needed, since it is difficult to justify the high field enhancement factors necessary for purely a field emission induced breakdown and the single transit particle energies are too low to cause the formation of emission sites on the target or the vaporisation of the particle or target. Electrical breakdown can be initiated by low energy particles by trigger discharge, but this mechanism requires large particles ($\gtrsim$ 50μm) which are rarely observed in practice. Whereas large numbers of micron - sub-micron sized particles have been commonly observed, it is however difficult to justify the initiation of breakdown by such particles without postulating the existence of some intermediary energy enhancing mechanism. The most promising of these is the energy enhancement of a microparticle following a bouncing impact with efficient momentum and charge reversal. The aim of this work is to carry out a detailed study of this proposed mechanism both theoretically and by direct experimentation.

CHAPTER II

THEORETICAL CONSIDERATIONS

The theoretical expressions and conclusions derived in this chapter will be later used in Chapter V for interpretation of the experimental data obtained from a series of simulated impact and ellipsometric studies described in Chapter III.

2.1 MICROPARTICLE IMPACT PHENOMENA

2.1a Introduction

It is clear from the foregoing discussion of Chapter I that the initiation of electrical breakdown in vacuum by high energy microparticles (53) is a well established concept. However, more recent theoretical work dealing with the mechanism of microparticle formation, charge acquisition, motion and impact energy exchange (68) (55) (72) (99) indicates that it is difficult to correlate the range of impact energies obtained experimentally (36) (54) (66) with those predicted theoretically, for a single transit impact. To overcome this dilemma, it has been suggested (55) (68) (72) that a microparticle may undergo an intermediate bouncing impact which under the conditions of efficient momentum and charge reversal would represent an energy enhancing mechanism.

The aim of this section is to establish a detailed theoretical analysis of this proposed hypothesis; i.e. the underlying interactions that take place as a result of a charged microparticle closely approaching, impacting and finally under certain favourable conditions bouncing off a plane charged surface will be considered. Specifically, this will involve a detailed analysis of various electrical phenomena (e.g. in-flight Field Emission, Metal-Insulator-Metal tunnelling and contact charging etc.) and mechanical (impact kinetics - damage, restitution factor, contact area and contact time etc.) impact processes,

under a number of experimental conditions. One in particular being the presence of equilibrium oxide layers on the interacting surfaces.

2.1b Theoretical model

Consider figure 2.1, which schematically illustrates a plane parallel high voltage vacuum gap. A spherical microparticle is assumed to be initially lying in contact with the plane electrode (anode in the present case). This microparticle will detach itself from its parent electrode at some critical voltage V, determined by a balance between cohesive/adhesive attractive forces and the repulsive electrostatic forces.

On detachment from this electrode it will acquire a charge given by (100)

$$Q_o = Z\pi\epsilon_o E_o r^2 \quad \ldots\ldots\ldots \quad 2.1$$

where r = particle radius

Z = charge factor which depends on the particle and plane geometries (65), i.e. for a microsphere resting on a plane Z = 6.58 and if it is half embedded Z = 3.

ϵ_o = Permittivity of free space

E_o = Macroscopic field = V/d

V = applied voltage

d = interelectrode gap

Due to its finite charge, it will then be accelerated to the opposite electrode (cathode) and as a result of a single transit across the interelectrode gap, assuming no inflight charge losses (see later) it will acquire a (theoretical) terminal velocity (u_o) given by

$$u_o = \left(\frac{2Q_oV}{m}\right)^{\frac{1}{2}} \quad \ldots\ldots\ldots \quad 2.2$$

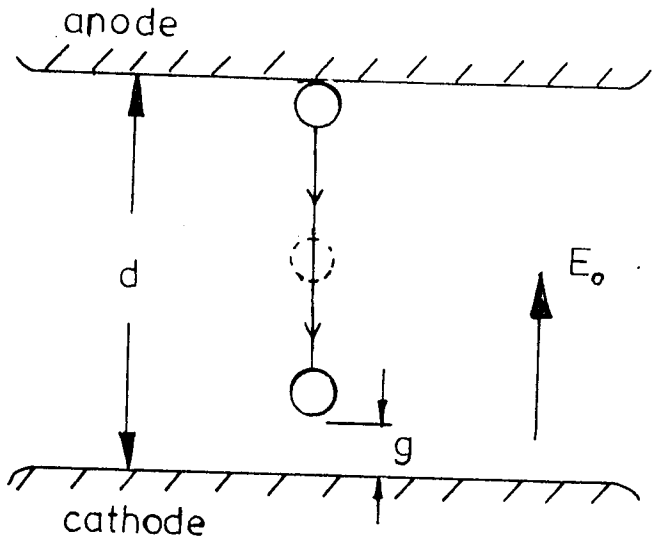

Figure 2.1

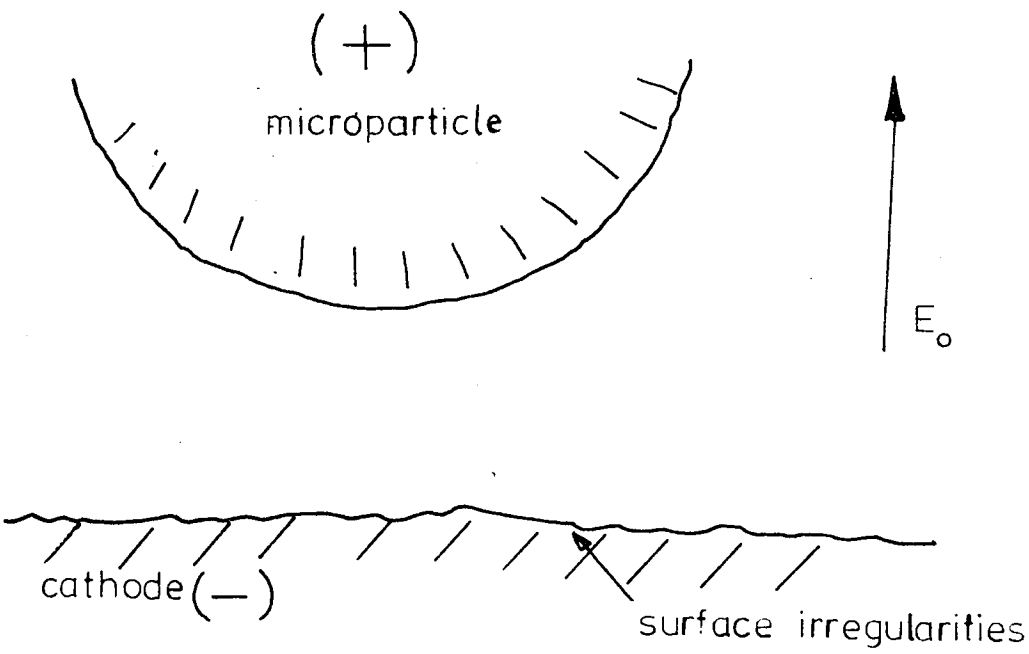

Figure 2.2

where m = mass of the particle.

Nearing the end of its flight, a few μm away from the opposite electrode, it is further assumed that the microparticle travels with a constant velocity equal to its terminal velocity (u_o).

As it closely approaches the opposite electrode (cathode), a new situation arises where on the microscopic scale, the microsphere itself startes to act as an 'anode' to the cathode protrusions (see Figure 2.2). From this stage onwards, as the 'microgap', the gap between the particle and cathode narrows, a number of complex processes can occur, which depend on a variety of parameters such as the particle mass, geometry, position and velocity, the microgap field, the interelectrode gap, its geometry and field as well as the particle and electrode materials and their surface conditions.

(i) At distances of few times the particle radius, the microscopic field E_o across the 'microgap' begins to rise and this may lead to initiation of in-flight field emission (65). As a result, the electron bombardment of the particle may cause: (a) its positive charge to decrease or even be completely neutralised, (b) a localised temperature rise at 'hot spots' on the particle, (c) a temperature rise of the field emitting protrusions on the cathode, (d) a pressure rise in the microvolume between the particle and the cathode due to desorption of adsorbed gas layers and in an extreme case partial evaporation of the particle itself. Under favourable conditions, the cooperative action of all the above mentioned factors could eventually lead to a discharge across the main gap.

(ii) For even closer approach, e.g. few hundred Angstroms away, there is a possibility of metal-vacuum-metal tunnelling (101) which can

further contribute in neutralising the charge on the particle.

Moreover, at this stage it should also be mentioned that the decrease in the initial charge of the particle by these inflight processes may under certain critical conditions be quite large, and as a result could lead to a significant reduction in velocity of the particle, especially in the case of inflight field emission (65), where the process can start to operate at comparatively large approach distances.

(iii) When the particle finally impacts onto the plane electrode, there are two possible mechanisms by which the charge transfer can take place between these bodies; Close -proximity tunnelling (101), field assisted or otherwise (see section 2.1.2) and or Ohmic conduction (103), i.e. charge flow via a total contact resistance R, consisting of bulk resistance R_b, constriction resistance R_c and if oxide film is present, film resistance R_f, formed between the impacting surfaces. Firstly, this will neutralise any charge remaining on the particle and then possibly give it a reverse charge. The relative importance of the two mechanisms in governing the magnitude of the reverse charge will depend on the surface conditions of the impacting surfaces and the condition under which the impact occurs e.g. surface-conductivities, contact area and possibly contact time etc. For instance, the charge acquired by a particle on detachment from a parent electrode under steady state conditions is given by equation 2.1 above, this however may not be strictly applicable to the present 'dynamic situation' i.e. bouncing impacts where limited (very short) 'contact times' may be involved.

Furthermore, depending on the incident energy of the particle and its mechanical properties e.g. hardness, density, Young's Modulus etc. and those of the target material, many different types of

impacts ranging from fully elastic, semi-elastic to inelastic can occur (104) (see section 2.1.5). The type of impact in turn will govern the contact time and the effective 'contact area' between the colliding surfaces, through which the electronic conduction takes place. In addition, a major portion of the kinetic energy available from the impact will be consumed in causing deformation and heating of the impacting surfaces and at higher energies it can also cause charge release (75) (76) (77) (see section 2.1.6). Both the heating and stress effects due to impact can influence the effective contact resistance (103), (105) and hence the conduction process taking place through it.

Furthermore, the type of impact the particle undergoes is also dependent on its pre-impact state, for instance it may have suffered considerable pre-heating by the inflight charge transfer processes, which in an extreme case can cause partial melting possibly leading to formation of a microweld on impact.

Therefore, clearly there are a multiplicity of factors which operating individually or cooperatively can significantly influence the conditions under which the collision occurs, the final state of the particle, the target impact area (e.g. type of crater, if any, produced), the reverse charge acquired by the particle and its rebound velocity.

(iv) Assuming that the microparticle is able to acquire a reverse charge equal to the equilibrium charge (given by equation 2.1) after impacting onto the oppositely charged plane electrode it will then detach itself from this electrode under the action of a repulsive electrostatic force given by (63):

$$F = 1.37\, E_o r^2 \qquad \ldots\ldots\ldots \qquad 2.3$$

and be accelerated back to the 'original'electrode under the action of the macroscopic field E_o. Moreover, if the particle had impacted onto the plane electrode with an incident velocity below the elastic limit of deformation it will 'bounce' back with a rebound velocity that is dependant on the restitution factor of the impacting solids (see section 2.1.5b). Thus, the re-acceleration due to efficient charge reversal and the elastic reflection are additive and hence under favourable conditions would represent an energy enhancing mechanism.

2.1c Possible influences of thin surface films

As discussed in section (2.2), most metal surfaces which have been exposed to atmosphere tend to carry thin protective surface films (103) (106) made up mainly of an oxide layer, possibly adsorbed layer and if diamond polished, even a Bielby layer (107), but the thickness and the properties of these films e.g. mechanical strength, electrical conductivity and dielectric constant, etc. may vary considerably from metal to metal. In addition, the vacuum breakdown voltage is also found to vary quite significantly with electrode material (see section 1.4.1), especially the anode material; it has been reported (54) that the onset of cathode microcratering may be significantly suppressed by the choice of anode material. For example, under identical experimental conditions, stainless-steel electrodes which support a $\backsim$30Å thick mechanically strong dielectric layer has a breakdown voltage almost three times higher than copper electrodes that have a $\backsim$ 20Å thick mechanically weak and semi-conducting oxide layer. Stainless-steel has also been found to be outstandingly more favourable in suppressing microcratering and hence stable conditions, than other commonly used anode materials

e.g. Al., Cu., Ni., and W. Accordingly, it has been suggested (15) (81) (184) that the presence of these equilibrium oxide layers on metal electrodes could be a crucial factor in influencing the initiation of electrical breakdown. The precise nature of this influence is however quite complex and requires a great deal of further investigation. Some of the ways in which the presence of the oxide layer may be important are outlined below.

(i) There can be a change in the accelerating macroscopic field E_o, experienced by the particle, in the same way that the field between a parallel plate capacitor is decreased when a dielectric slab is interposed between the plates (see section 2.1.4). This change, however is likely to be quite small, almost negligible, because of the very small thickness of the equilibrium dielectric oxide films (max. $t_f \backsim 50\text{Å}$) as compared to the interelectrode spacing (d) (which is the order of $\backsim$ mm's) e.g. giving a very small value for the ratio t_f/d $10^{-6} - 10^{-7}$.

(ii) In contrast, for the case of the microscopic field E_g between the particle and the plane the presence of the protective film could well be more significant, especially at small approach distances i.e. few hundred Å away, (see section 2.1.2). Thus, if E_g is significantly affected by the presence of these surface films then processes like inflight field emission (65) and m.v.m. tunnelling (101) which are predominantly dependant on E_{mic} will also be influenced.

(iii) Also, if a field emitting particle (65) approaches an anode with poorly conducting surface layer there is a possibility of local electron surface/space charge build-up (108). This mechanism becomes important when the interelectrode-transit time of the particle T_r is less than or comparable to the dielectric relaxation time (T) of the oxide layers and hence may cause repulsion of the emitting particle

with an effective 'cushioning' of the impact.

(iv) Finally, when the particle impacts onto the plane electrode the presence of a mechanically strong and poorly conducting dielectric surface films may prevent efficient electrical conduction between them. This is because the dielectric films introduce a highly resistive path between the two conductors and thus affect the efficiency of the charge transfer both by the ohmic (103) and tunnelling conduction processes (see later).

The efficiency of the tunnelling processes may also be influenced by the changes introduced in the work functions of the contacting surfaces due to the presence of the contamination film (109) (221) (222) (see section 2.2). In addition, the resulting deterioration in the charge transfer rates due to the surface films may well be more significant in the case of bouncing impacts where very short contact times ($\sim 10^{-8}$S) (55) are involved.

Furthermore, these films can also affect the mechanical interactions that is, make the impacting surfaces harder (110) and thus influence the restitution factor (see table 2.1)

Table (2.1)

Hardness and coefficient of friction of atomically clean and oxided Metals (110)

Material	Hardness $^{g}/_{m}$		Load at which appreciable Metal contact occur (g)	Coeff. of Friction μ	
	Metal	Oxide		Metal on Metal	Oxide on Oxide
Gold	20	--	0	2	1
Silver	26	--	0.003	1	0.8
Tin	5	1650	0.02	1	1
Aluminium	15	1800	.02	1.2	0.8
Zinc	35	200	.05	0.8	1.2
Copper	40	130	1	1.6	0.8
Iron	120	150	10	0.6	1.0
Chromium	800	--	1000	--	0.4

2.1.1 Electrical Interactions

2.1.1a Electronic conduction through small vacuum and dielectric insulated gaps

Electronic states in a metal are filled up to some maximum energy the 'Fermi level' (ℓ_f), whilst electrons in vacuum have a certain minimum energy, the rest energy or the vacuum level (ℓ_o). In terms of energy diagrams, generally for all known metals the Fermi level lies below the vacuum level and thus a barrier is defined at the metal-vacuum interface which prevents electrons escaping from the metal surface. In other words, it requires energy to remove an electron from a metal into vacuum.

Consider the case of two identical metal electrodes separated by a small vacuum gap (g) as shown in figure 2.3. In the absence of applied voltage between these electrodes, their Fermi levels match (i.e. $\phi_a = \phi_b$) and the surface barriers of each metal extend into the gap to form a rectangular potential barrier of height equal to the work function. In addition, the effect of the image force set up in the interspace is to round off the corners of the rectangular potential barrier effectively reducing it's thickness.

Suppose an electron of mass m, charge e and zero potential energy is moving in x-direction with velocity v_o in metal (a), it will approach the barrier with a total energy W given by:

$$W = \tfrac{1}{2} m v_o^2 = eV_x \qquad \ldots\ldots\ldots \qquad 2.4$$

V_x is measured in volts and W is the total energy of a V_x-volt electron. If metal (a) is heated to sufficiently high temperatures its electrons will be thermally excited, some may attain energies (i.e. V_x) larger than the barrier height and so will surmount the barrier into metal (b), thus giving rise to the phenomenon of 'Thermionic Emission' (138). If in addition, an electric field

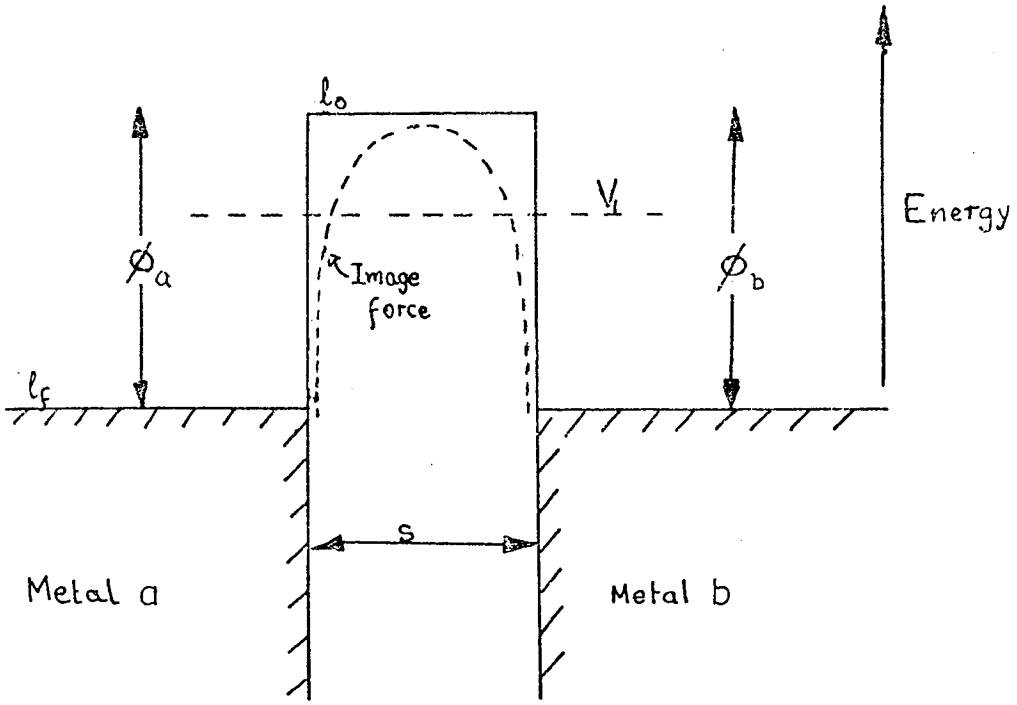

Figure 2.3

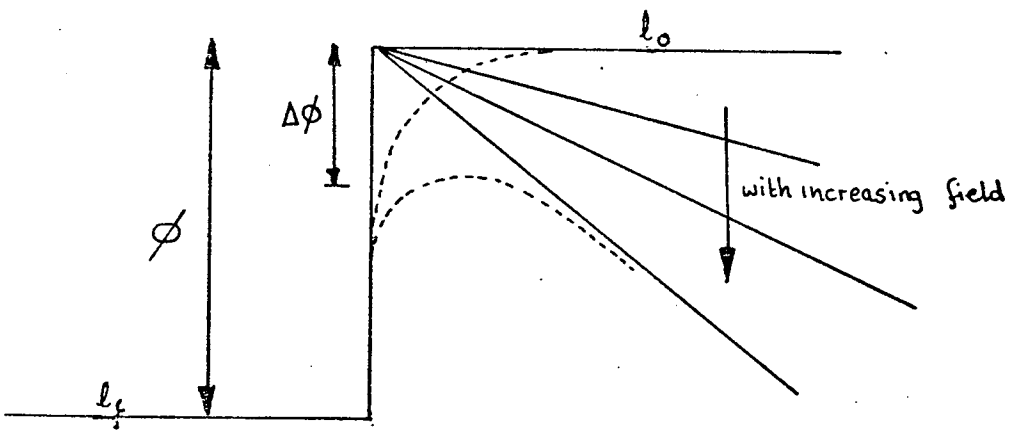

Figure 2.4

is applied to surface of metal (a), in directon which assists electrons to escape, the surface barrier will be changed as shown in figure 2.4 For moderate applied fields the barrier now has a maximum height less than ϕ and this has the effect of increasing thermionic emission - Schottky Effect (139).

For electrons which are not thermally excited and which have energies smaller than the height of the potential barrier, classical physics precludes finding such electrons in the interspace and predicts reflection with certainty. However, because of the wave-nature of electrons, i.e. electrons behaving as deBroglie Waves, Quantum theory states otherwise. The Schrodinger function $\Psi(x)$, has finite values in the interspace even though the barrier may be higher than V_x. So that, although the wave function decays rapidly with depth of penetration of the barrier from the electrode/vacuum interface and for barrier of macroscopic thickness is essentially zero at the opposite interface, indicating zero probability of finding an electron there, however if the barrier is thin ($< 100\text{Å}$) the wave function has non-zero values at the opposite interface. For this case then there is a finite probability of finding an electron from metal (a) in metal (b) and is given by the well known WKB approximation in terms of the transmission coefficient $D(V_x)$;

$$D(V_x) = \exp\left[\frac{-4\pi}{h}\int_g \left\{2m\left[\phi(x) - V_x\right]\right\}^{\frac{1}{2}} dx\right] \quad \ldots\ldots\ldots \quad 2.5$$

where (h) is Plank's constant.

Thus, the transfer of an electron having V_x smaller than the barrier height between the two electrodes is by penetration rather than jump over the potential barrier i.e. by the Tunnel Effect (101) For the case shown in figure 2.3 where $\phi_a = \phi_b$ and applied voltage $V = 0$, electrons tunnel just as often in either direction with no observable net current flow. If however, the Fermi-levels of the two

metal electrodes differ (see figure 2.5) and this can be either due to their work functions originally being different i.e. different metals or more importantly as a result of applied voltage, then an observable tunnel current will flow from the more negative metal to the more positive one.

Furthermore, it is possible to separate the tunnelling process into two distinct types namely Field emission (33) and Metal-Vacuum-Metal (101) tunnelling, by the different gap regions and applied voltages at which they occur. There is also a third intermediate type, but this is essentially a combination of two main types.

Field emission or Fowler-Nordheim tunnelling (33) can occur at relatively large interelectrode gaps and large applied voltages. The effect of the high applied field is to drastically alter the shape of the barrier (see figure 2.6), enabling the electrons to tunnel through the reduced thickness of the barrier. The tunnelling from metal (a) proceeds above the vacuum level of metal (b) and hence all the energy states on the vacuum side are available for occupation. The F.E. current density (j) varies exponentially with the applied field and was first derived for a rectangular potential barrier by Fowler-Nordheim (33) and later completed for the image force by others (153), see section (1.2.2.) for further details.

In contrast, metal-vacuum-metal tunnelling is characterised by small interelectrode gaps ($\leq 200\text{Å}$) and small applied voltages i.e. $V \gtrsim 0$. The presence of an applied field causes a difference in the Fermi levels as shown in figure 2.5. (N.B. as mentioned above the Fermi levels can originally, that is with $V = 0$, be at different levels if the two metal electrodes have differing work functions). The electrons from metal (a), having the higher Fermi-level will tunnel through the barrier to fill up the available energy states in metal (b) which has the lower Fermi level. The number of such

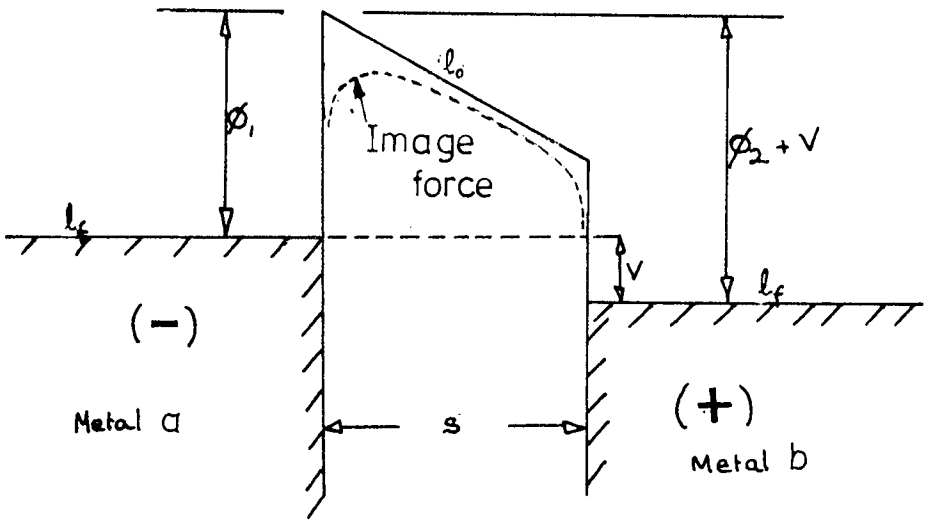

Figure 2.5 Low Bias

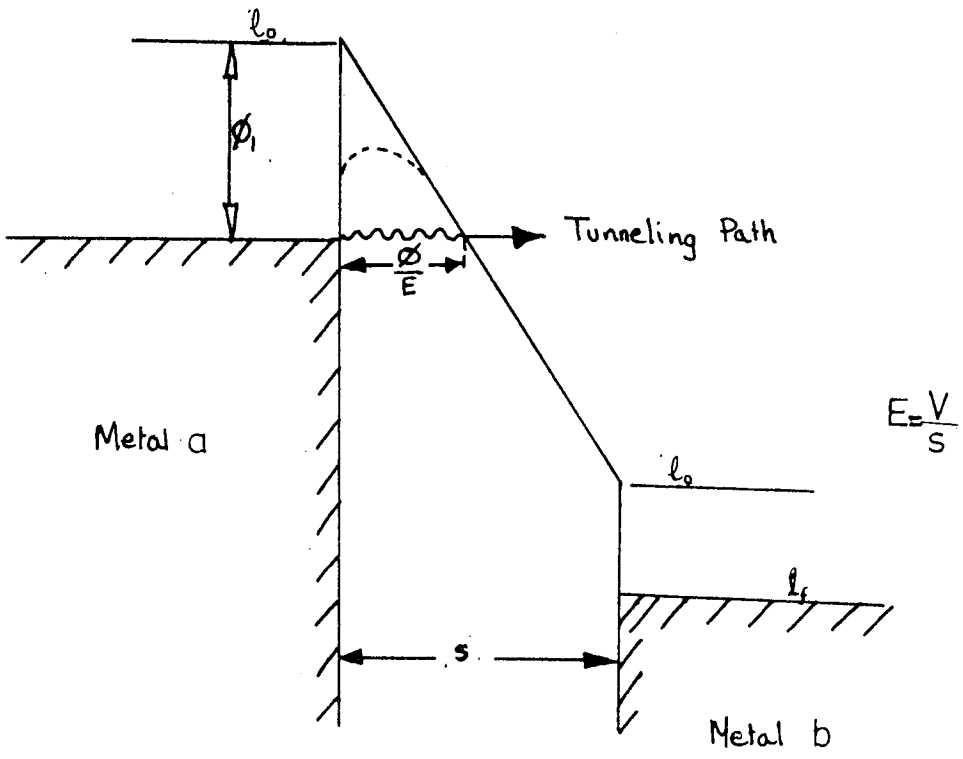

Figure 2.6 High Bias

energy states in metal (b) are limited and dependent on the applied voltage, and an increase in applied voltage results in an increase in the number of available states. The current density (J) increases linearly with applied voltage and the changes in the shape of the barrier have little effect. In fact, the M-V-M tunnel effect can be regarded as being 'ohmic' since the current density (J) is proportional to V and the concept of tunnel resistivity σ ($=\frac{V}{J}$) can be used. Where σ is a function of the interelectrode gap (g), the work functions of metal electrodes (ϕ_a and ϕ_b), the applied voltage (V) and relative permittivity (ϵ_r) of the dielectric, hence $\sigma = \sigma (g, \phi, \epsilon_r, V)$.

2.1.1b Conduction through thin dielectric films

In a dielectric, an energy gap (or forbidden gap $\gtrsim$ 2ev) separates a full allowed band (valence band) and a conduction band (of width (χ) - called the activation energy) and generally the Fermi level (ℓi) of a pure dielectric bisects the forbidden band. If impurities are present they introduce allowed levels in the forbidden band moving the Fermi-level up or down. In addition, the well defined boundaries of a forbidden band separating the conduction and valence bands are only true for a crystalline solid and are not strictly applicable to polycrystalline or amorphous insulators as in the present case of oxide films on metals. However, it can be shown that the essential features of the band structure of a solid are determined by the 'short-range' order within the solid and that the properties of the band structure of a crystalline state are carried over to a polycrystalline state. Thus, in the study of thin oxide films, the inherent smearing of conduction and valence band edges obtained because of the lack of long range order, can to a first-order approximation be represented by a well defined energy gap which is

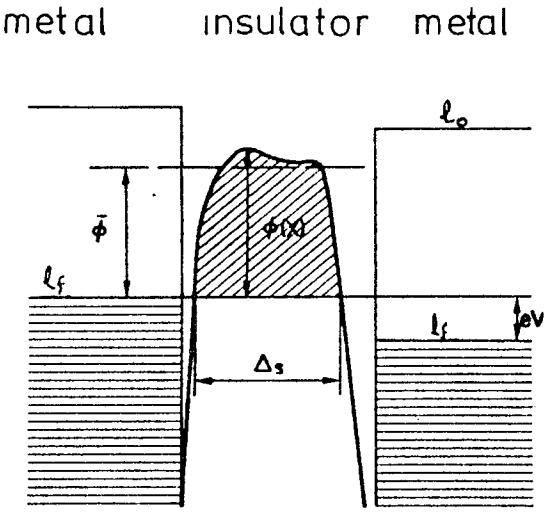

General barrier in dielectric film between two metal electrodes

FIGURE 2.7

representative of perhaps an average value of the non-discrete energy gap.

When two metal electrodes are separated by a dielectric film, the equilibrium conditions require that the top of the forbidden gap of the insulator be positioned above the Fermi-levels of the electrodes as shown in Figs.2.7-11(134). Thus, the action of the insulating film is to introduce a potential barrier between the electrodes effectively impeding any charge flow between them. However, if the mobility in the dielectric film is reasonably high and the density of donors (or acceptors) and traps is low enough for band bending over the thickness of the film to be negligible (134) then a situation conceptually identical to that encountered in the vacuum insulated gaps of the preceeding section is obtained. In principle, the only change is that the work functions of the electrodes are replaced by the energy barrier from the Fermi-level of the metal to either the conduction or the valence band of the dielectric, whichever is the lower. So that, electronic conduction can similarly take place between dielectric insulated electrodes by the thermal excitations of electrons over the barrier and or by quantum mechanical tunnelling provided the barrier is sufficiently thin to permit penetration. The latter phenomenon of tunnelling through thin semi-conducting and insulating films, (or metal-semiconductor and metal-insulator barrier) is a highly refined topic in its own right and has accumulated a large amount of literature in the past few decades (101) (131) (132) (133) (136).

The type of contact that exists at the metal-dielectric interface is determined by the relative magnitudes of the metal-insulator work functions (ϕ) and (ϕ_i) respectively and falls into three categories: (i) Ohmic or Mott-Gurney contact ($\phi < \phi_i$), (ii) blocking-contact or

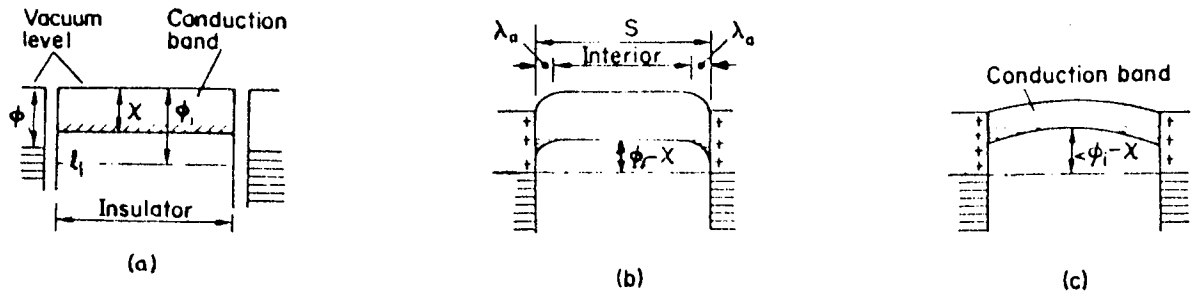

Figure 2·8 $\phi < \phi_i$

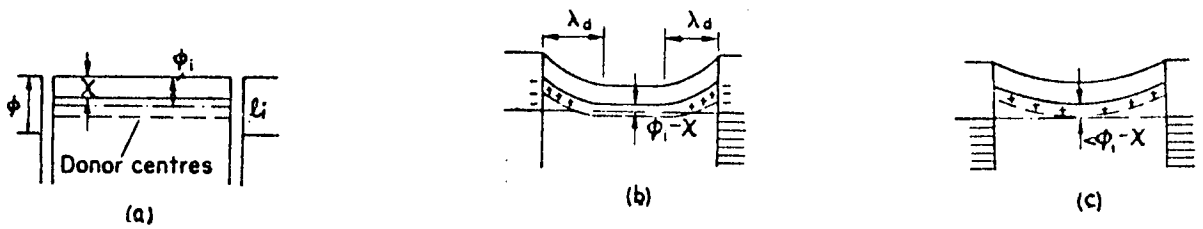

Figure 2·9 $\phi > \phi_i$

Figure 2·10 $\phi = \phi_i$

Schottky barrier ($\phi > \phi_i$) and (iii) neutral contact ($\phi = \phi_i$).

(i) When $\phi < \phi_i$ as shown in figure 2.8a, to satisfy the equilibrium conditions, electrons are injected from the electrode into the insulator conduction band, thus giving rise to space-charge induced field. This field causes the bottom of the conduction band to curve upwards away from the interface (see figure 2.8b) so that it lies ($\phi_i - \chi$) above the Fermi level but the space-charge region or the accumulation region (λ_a) screens the interior of the insulator keeping the middle of the conduction band flat. However, if the film is thin, then overlapping of the accumulation regions (λ_a) will occur and since there is insufficient change within these regions to screen the interior effectively from the conditions at the interfaces it will cause space-charge to extend throughout the insulator making the height of the conduction band greater then ($\phi_i - \chi$) above the system Fermi-level (see figure 2.8c). Thus, in this type of contact, there is a reservoir of charge which is capable of supplying electrons to the insulator as required by bias conditions and hence the conduction process is limited by the rate at which electrons can flow through the bulk of the insulator rather than the rate at which they are supplied by the electrode (137).

(ii) For $\phi > \phi_i$, as shown in figure 2.9a, electrons flow from the insulator into metal to establish equilibrium conditions. A space charge region of positive charge or a depletion region (λ_d) is thus created in the insulator and an equal negative charge resides on the metal electrodes. With the effect that a local field exists within the surface of the insulator which causes the bottom of the conduction band to bend downwards until it lies in an energy ($\phi_i - \chi$) above the Fermi-levels (see figure 2.9b), but the interior of the insulator is field free because the depletion regions effectively screen the interior

from the surfaces. However, if the depletion regions overlap ($s < 2\lambda d$) as shown in figure 2.9c, and they do not contain sufficient charge to screen the interior from the surface then the conduction band will be bent throughout it's length concaving upwards so that the bottom of the conducting band is higher than (ϕ-x) above the Fermi-level at the centre of the insulator. Thus, the free electron density at the interface is much lower than that in the insulator, and hence the rate of flow of electrons through the system is limited by the rate at which they flow over the interfacial barrier.

(iii) Lastly, when $\phi = \phi i$ due to absence of space-charges there is no band bending present and the resultant conduction band is flat as shown in figure 2.10a. Similar type of contact is also obtained when ($\phi << \phi i$) and the trap levels, if any are positioned more than ~lev above the Fermi-level, so that the band bending is negligible. These neutral type of contacts represent a transitional stage between ohmic and blocking contact, because for an initial voltage bias, the cathode supplies sufficient current to balance current flow through the insulator and the conduction process is ohmic, but then a current limit is reached (saturated thermionic-Richardson (iii)) and process ceases to be ohmic and becomes blocking.

Furthermore, when dissimilar electrodes of work functions ϕ_a and ϕ_b (assuming $\phi_b > \phi_a$) are connected to the dielectric film (see figure 2.10b), the interfacial potential barriers differ in energy by an amount.

$$(\phi_b - x) - (\phi_a - x) = \phi_b - \phi_a \quad \ldots\ldots\ldots \quad 2.6$$

As a result the conduction band slopes downwards from the higher barrier with a gradient $(\phi_b - \phi_a)/g$, and an intrinsic field E_i $(=(\phi_b - \phi_a)/eg)$ exists within the insulator. The origin of this zero bias intrinsic field is a consequence of electrons transferring from

the metal (a) with lower work function (ϕ_a) to metal (b) the higher work function ϕ_b, so that the positive and negative surface charge appear on metals (b) and (a) respectively. The amount of charge Q_i transferred between the electrodes depends on contact potential $(\phi_b - \phi_a)/e$, and the capacitance C of the system,

$$Q = C\,\frac{(\phi_b - \phi_a)}{e} = \frac{A\,\epsilon_o\,\epsilon_r(\phi_b - \phi_a)}{eg} \qquad \ldots\ldots\ldots \qquad 2.7$$

where A is the contact area.

For a very thin insulator the field E_i across the film can be quite large e.g. $E_i \backsim 5\times10^6$ for a 20Å film and $\phi_b - \phi_a \backsim$ lev. Now if external bias is applied, and metal (a) is positively biased, then E_i augments the applied field but when it is negatively biased E_i acts to reduce the applied field.

Tunnelling through dielectric films. As mentioned above, charge transfer through dielectric insulated gaps can take place by the Tunnel effect. The electron tunnel currents flowing between two metal electrodes separated by thin dielectric films have been considered in several studies (132) (133) (134) (136). A generalised formula for the tunnel current density (J) as a function of applied voltage (V) for a barrier of any arbitrary shape, which is currently and most commonly used is given by (133) (134)

$$J = J_o\left\{\underline{\phi}\exp\left(-N\underline{\phi}^{\frac{1}{2}}\right) - (\underline{\phi} + eV)\exp\left[-N(\underline{\phi} + eV)^{\frac{1}{2}}\right]\right\}\ldots. \qquad 2.8$$

where $J_o = \dfrac{e}{2\pi h\,(\beta\,\Delta_g)^2}$ and $N = \dfrac{(2m)^{\frac{1}{2}}\,4\pi\,\Delta_g}{h}$;

Δ_g = width of the barrier at the Fermi-level of the negative electrode.

$\underline{\phi}$ = mean barrier height above Fermi-level of the negative electrode.

m = mass of electron.

e = unit electronic charge, and

β = a function of barrier shape, usually ~ 1. Expressing (Δ_g) and ($\underline{\phi}$) in angstroms and electron volts respectively and J in Acm^{-2} equation 2.15 reduces to (134) (135),

$$J = \frac{6.2 \times 10^{10}}{(\Delta_g)^2} \left\{ \underline{\phi} \exp\left(1.025\, \Delta_g\, \underline{\phi}^{\frac{1}{2}}\right) - (\underline{\phi} + V) \exp\left[-1.025 \Delta_g (\underline{\phi}+V)^{\frac{1}{2}}\right] \right\} \quad 2.9$$

The above expressions apply to the barriers of the simplest forms as shown in figures 2.10a and b. They assume a parabolic energy momentum relation with free electron mass (m) in all regions and electronic energy distributions corresponding to absolute zero temperature. Since the current density is only slightly temperature dependant i.e. there is slight quadratic temperature dependance (133) given by $J(V,T) = J(V,0)(1 + 6 \times 10^{-7} T^2)$, then these equations may safely be used at higher temperatures and are quite suitable for predicting the salient features of tunnelling J-V characteristics. However, there have been several other studies of a more detailed nature, which have considered the effect of space charge (140) (141), traps and ions in the insulator (142) (143) the effect of the shape of the forbidden band (144), representation of an insulator by a series of potential wells (145), electric field penetration of electrodes (146) diffuse reflection (147), and time dependent tunnelling (148).

Furthermore, when the electrodes are dissimilar i.e. $\phi_1 \neq \phi_2$, then assymetric junction or trapezoidal barriers (see figure 2.10a,b) are obtained and J-V characteristics are found to be polarity dependant. Assuming $\phi_2 > \phi_1$ the current densities for the forward bias (= J_1, when the electrode with work function ϕ_1 is positively biased) and reverse bias (= J_2 when the electrode with work function ϕ_1 is negatively biased) conditions can be derived from equation 2.9. Two distinct applied voltage are obtained. (i) In the voltage range

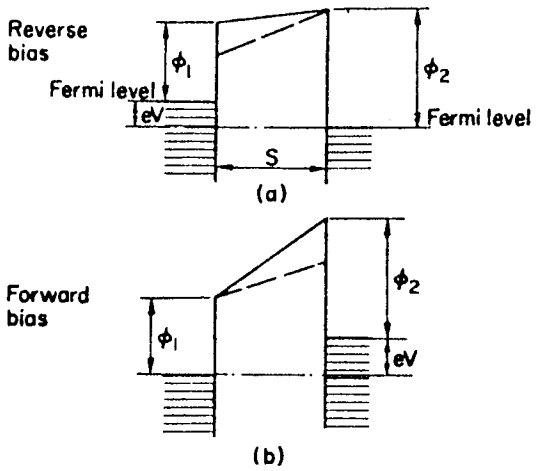
Reverse bias
ϕ_1
Fermi level
eV
ϕ_2
Fermi level
S
(a)
Forward bias
ϕ_1
ϕ_2
eV
(b)

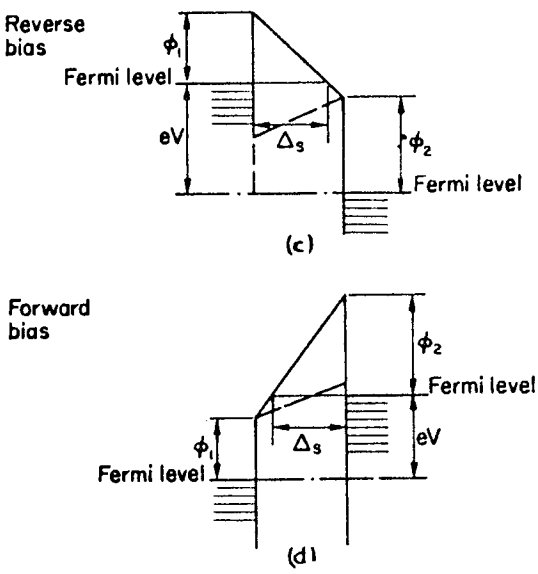
Reverse bias
ϕ_1
Fermi level
eV
Δ_s
ϕ_2
Fermi level
(c)
Forward bias
ϕ_2
Fermi level
ϕ_1
Δ_s
eV
Fermi level
(d)

Figure 2·11

$0 \leq V \leq \phi$, figure 2.11a and b, illustrate the energy diagrams for the reverse and forward direction of polarity respectively and current densities are given by,

$$J_1 \simeq J_2 \simeq \frac{3.1\times10^{10}}{g^2}\left\{ (\phi_1 + \phi_2 - V)\exp\left[-0.725g(\phi_1 + \phi_2 - V)^{\frac{1}{2}}\right] - (\phi_1 + \phi_2 + V)\exp\left[-0.725g\,(\phi_1 + \phi_2 + V)^{\frac{1}{2}}\right]\right\} \quad \ldots\ldots \quad 2.10$$

Since $J_1 \simeq J_2$, the J-V characteristic is symmetric with polarity of bias.

(ii) In the voltage range $V > \phi_2/e$, for the reverse bias condition as shown in Figure 2.11c

$$J_1 = \frac{3.38\times10^{10}(V-\Delta\phi)^2}{\phi_1 g^2}\left\{\exp\left(\frac{-0.69g\phi_1{}^{3/2}}{V-\Delta\phi}\right) - \left(1+\frac{2V}{\phi_1}\right)\exp\left[-\frac{0.69g\,\phi^{3/2}(1+2V/\phi_1)^{\frac{1}{2}}}{V-\Delta\phi}\right]\right\} \quad \ldots \quad 2.11$$

and for the forward bias condition as shown in figure 2.11d

$$J_2 = \frac{3.38\times10^{10}(V+\Delta\phi)^2}{\phi_2 g^2}\left\{\exp\left(-\frac{0.69g\phi_2{}^{3/2}}{V+\Delta\phi}\right) - \left(1+\frac{2V}{\phi_2}\right)\exp\left[-\frac{0.69g\,\phi^{3/2}\,(1+2V/\phi_2)^{\frac{1}{2}}}{V+\Delta\phi}\right]\right\} \quad \ldots\ldots \quad 2.12$$

In this case equation 2.11 and 2.12 are not equivalent. It follows then, that the J-V characteristics is asymmetric in this range. In fact not only is the J-V characteristic asymmetric with polarity, but the direction of rectification reverses at some particular voltage as shown in figure 2.12, after Hartman (136).

At high voltages when $V > \frac{\phi_2}{e}$, both equations 2.11 and 2.12 reduce to familiar Fowler-Nordheim equation.

Figure 2.13, shows the tunnel resistance (V/J) as a function of (V) for g = 20,30, and 40Å, ϕ_a = 1ev and ϕ_b = 2ev ($\Delta\phi$ = 1ev). The

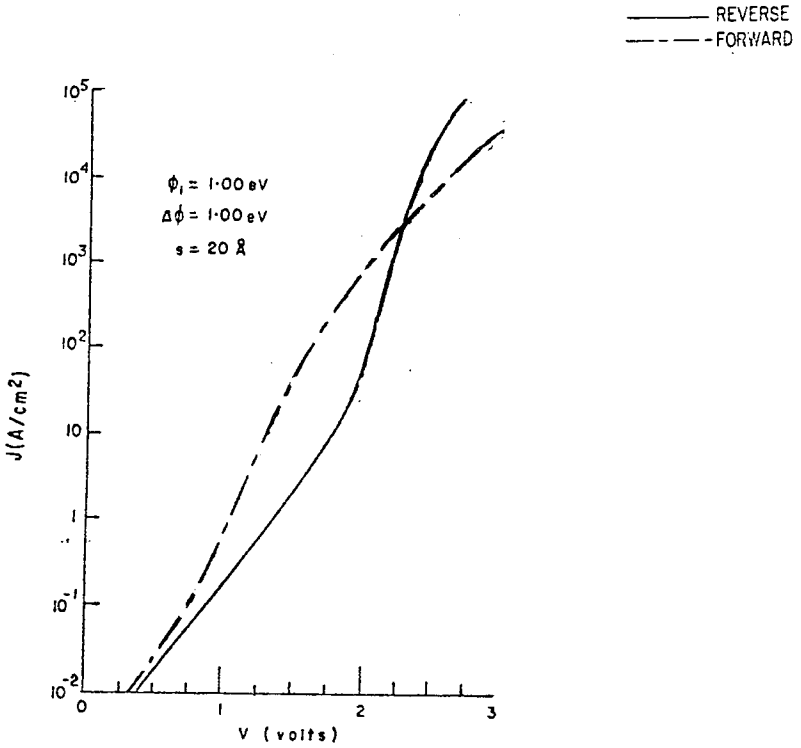

Figure 2·12

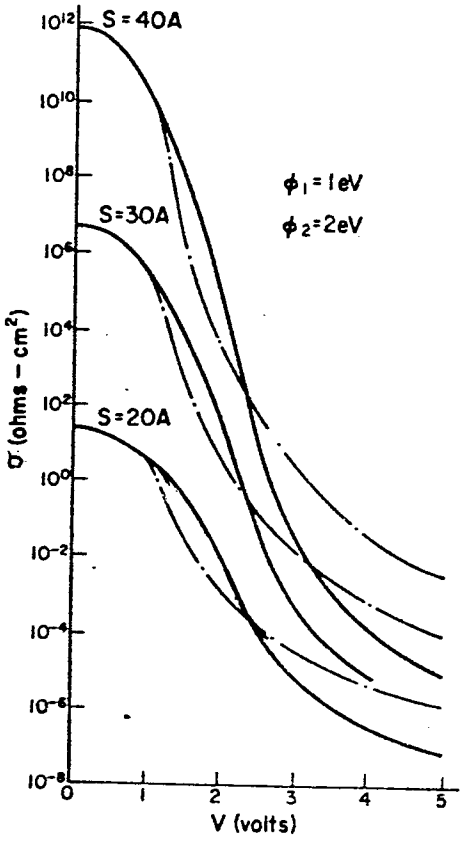

Figure 2·13

reverse and forward direction are depicted, respectively by the full and dotted curves. Several features of curves will be immediately apparent: at very low voltages the curves are horizontal which means that the junction resistance is ohmic. The junction resistance falls off rapidly with increasing voltage bias, and the effect is more pronounced the thicker the film. The junction characteristics are symmetric as noted above; thereafter they are asymmetric reversing with the direction of asymmetry at a voltage ($V \sim 2.5v$) which is practically independent of insulator thickness.

Although the above results apply to an ideal barrier, however several experimental confirmations, for variety of junctions exist that support these theories (149) (150) (151).

2.1.2 Field Calculations

Since the charge transfer processes, like inflight field emission and metal-insulator-metal tunnelling are predominantly dependent on the microscopic field E_g between the microsphere and the plane electrode it is therefore necessary to compute this field as a function of such parameters as the particle radius, charge, position, and the macroscopic field E_o. Such field calculations have been carried out by a number of research workers (88) (83) (67) and are discussed below. Most of these however, have been restricted to the special conditions operating with the trigger discharge mechanism, where large particles ($r \geqslant 10\mu m$) and hence large approach distances were only considered. Also, no consideration was given to the presence of dielectric oxide films commonly found on metal surfaces which have been exposed to the atmosphere (see section 2.2). The present work, in contrast, is concerned with extending the analysis to micron-submicron sized particles and approach distances of the order of tens of Angstroms. In addition, the effect

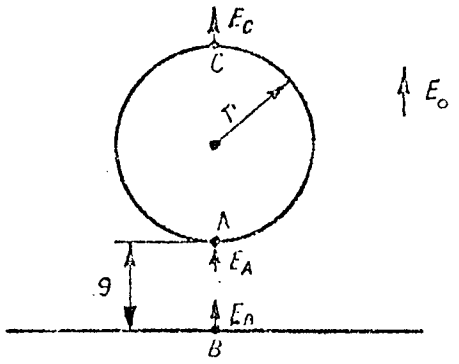

Fig. 2.14

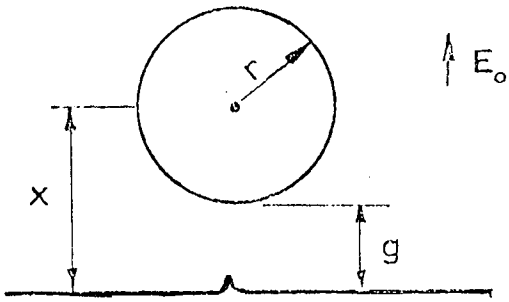

Fig. 2.16

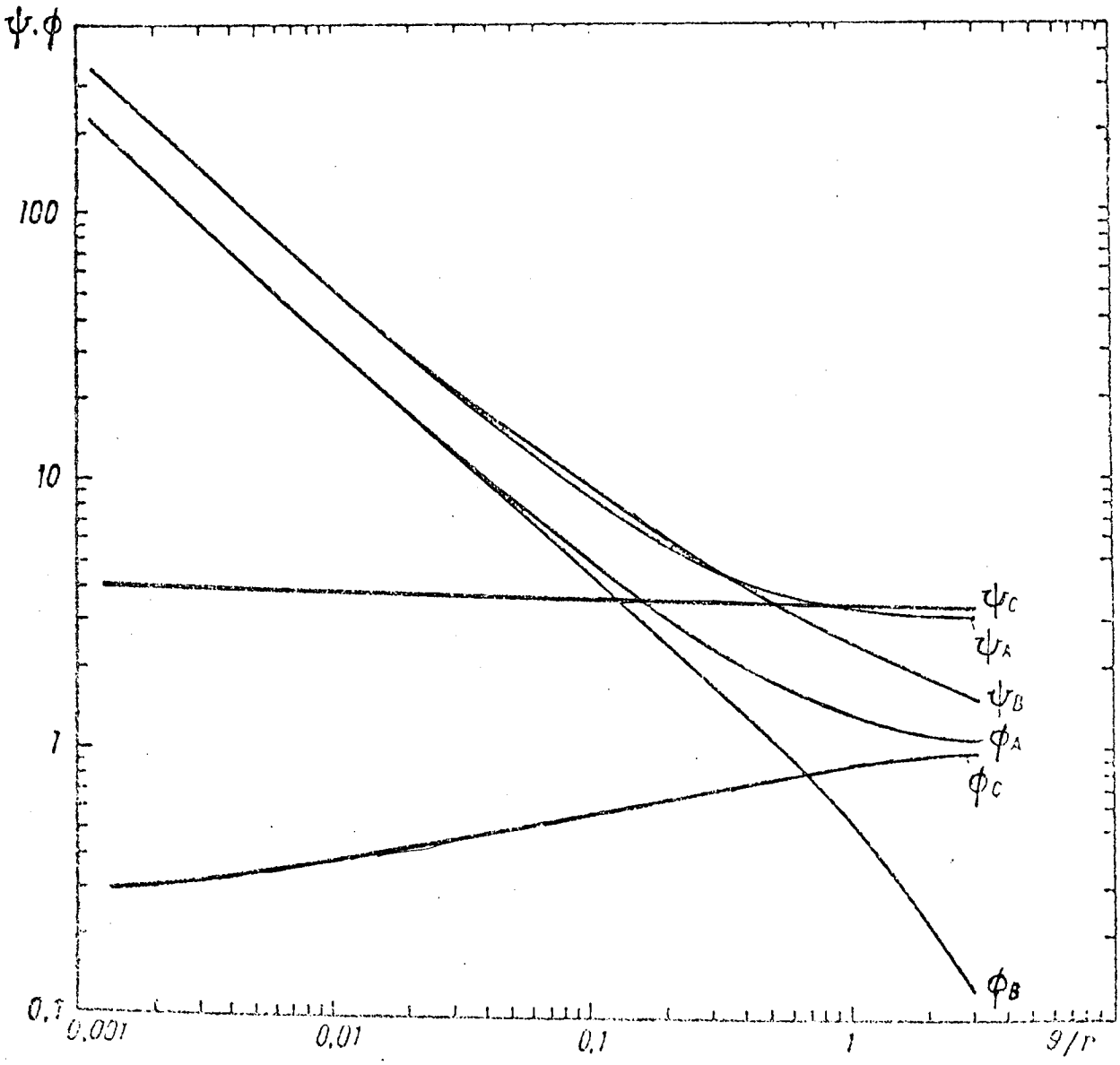

Fig. 2.15

of equilibrium oxide layers will also be investigated, especially at very small approach distances where it is likely to be most significant.

The microscopic field (E_g) can essentially be taken to be composed of three main components which are associated with the three charge distributions; (i) the initial charge on the particle, (ii) the charge which produces the macroscopic field intensity E_o residing on plane electrodes and (iii) the charge induced on the surface of the sphere. Using this approach, there are a number of ways of obtaining E_g, but they all entail using one of two basic techniques, the analytic solution of Laplaces equation and the method of images.

The first, and incidentally the most rigorous microscopic field calculations, were carried out by Martynov (79). Figure 2.14, shows a conducting charged sphere which is in close proximity to a conducting charged plane and in a uniform field E_o. Evidently, the fields that are of interest are at A, B and C as shown. In order to arrive at the expressions for these fields, it is first necessary to consider the case of two conducting spheres of radii r and R at potentials V_2 and V_1 respectively for which the resultant fields can be obtained. One of the spheres is then allowed to increase its radius to infinity (e.g. say $R \longrightarrow \infty$) and becomes a plane, so that the technique may be applied to the present sphere - near -plane problem.

The resultant field $\hat{E}$ between the two spheres can be found by the superposition of two fields viz, E_1 produced by sphere R at potential V_1 when sphere r is earthed, and E_2 produced when sphere r is at potential V_2 and sphere R is earthed. Hence:

$$\hat{E} = E_1 + E_2 \qquad \ldots\ldots\ldots \qquad 2.13$$

It can be shown that the above fields are given by (152)

$$E_{1A} = \frac{V_1}{r} \sum \frac{\operatorname{sh}\theta\left(1+k+\frac{hp}{r}+p\right)}{\operatorname{sh}(n+1)\,\theta\,(1-k+\frac{h}{r}\,p-p)^2} = \frac{V_1}{r} \sum {}_{1A} \qquad \ldots\ldots\ldots \qquad 2.14$$

and

$$E_{2A} = \frac{-V_2}{r} \operatorname{sh}\theta \left[\sum \frac{pk + 1}{\operatorname{sh}(n+1)\theta \left\{1-k-\left(\frac{h}{r} - 1\right)pk\right\}^2} \right.$$

$$\left. \sum \frac{h/rp + 1}{\operatorname{sh}(n+1)\theta\left\{2h/r-1-k+h/r\left(h/r-1\right)p\right\}^2} \right] = \frac{V_2}{r} \sum 2A \qquad \ldots\ldots \qquad 2.15$$

$$E_{1B} = \frac{-V_2}{r} \operatorname{sh}\theta \sum \frac{2 + kp + \frac{hp}{r}}{\operatorname{sh}\ (n+1)\theta\ \left(\frac{h}{r} - k\right)^2} \qquad \ldots\ldots\ldots \qquad 2.16$$

$$E_{2B} = \frac{-V_1}{r} \operatorname{sh}\theta \left[\sum \frac{k + p}{\operatorname{sh}\ (n+1)\theta\ \left(k\frac{h}{r} -1\right)^2} \right.$$

$$\left. + \sum \frac{1 + h/r\ p}{\operatorname{sh}\ (n+1)\theta\left\{h/r-k+p^2\left(h^2/r^2 -1\right)\right\}^2} \right] \qquad \ldots\ldots\ldots \qquad 2.17$$

$$E_{1C} = \frac{V_1}{r} \sum \frac{\operatorname{sh}\theta\left(p+k+\frac{h}{r}p -1\right)}{\operatorname{sh}(n+1)\theta\ \left(1+k+p+\frac{h}{r}p\right)^2} \qquad \ldots\ldots\ldots \qquad 2.18$$

$$E_{2C} = \frac{V_2}{r} \operatorname{sh}\theta \left[\sum \frac{1 + pk}{\operatorname{sh}(n+1)\theta\ \left\{1+k+\left(\frac{h}{r} +1\right)pk\right\}^2} \right.$$

$$\left. - \sum \frac{1 + \frac{h}{r}}{\operatorname{sh}(n+1)\theta\left\{1-k+p\frac{h}{r} + \frac{h}{r}\left(\frac{h}{r} + 1\right)p\right\}^2} \right] \qquad \ldots\ldots\ldots \qquad 2.19$$

Where, $\operatorname{ch}\theta = \dfrac{h_o^2 + R^2 - r^2}{2Rr} = \frac{1}{2}p\left[\dfrac{h^2}{r^2} - 1\right] + \dfrac{h}{r}$ $\qquad \ldots\ldots\ldots \qquad 2.20$

$$k = \frac{\operatorname{shn}\theta}{\operatorname{sh}(n+1)\theta} \qquad \ldots\ldots\ldots \qquad 2.21$$

$p = \frac{r}{R}$, $h_o = R+h$, and $h(=g+r)$ is the distance from centre of the sphere radius r to the surface of sphere radius R. Also note from equations (2.1) and (2.5) that $0 < \theta < \infty$ and $K < 1$.

Now, if the charge (Q_o) on the small sphere is expressed in terms of capacity coefficients (152) i.e.,

$$Q_o = C_{11}V_2 + C_{12}V_1 \qquad \ldots\ldots\ldots \qquad 2.22$$

where

$$C_{11} = 4\pi\epsilon_o r \sum \frac{sh\theta}{sh\,(n+1)\theta\,(1+pk)} \qquad \ldots\ldots\ldots \qquad 2.23$$

and

$$C_{12} = -\frac{4\pi\epsilon_o r}{(1+\frac{hp}{r})} \sum \frac{sh\theta}{sh\,(n+1)\theta} \qquad \ldots\ldots\ldots \qquad 2.24$$

The resultant field E_A can be written as:

$$\tilde{E}_A = -\frac{Q_o}{rC_{11}} \sum 2A + \frac{V_1}{\rho R}\left[\frac{C_{12}}{C_{11}} \sum 2A + \sum 1A\right] \ldots\ldots\ldots \qquad 2.25$$

In order to get results that are of interest for this analysis let $R \to \infty$ for finite h; then $p \to o$, $ch\theta \simeq \frac{h}{r}$, $\frac{hp}{r} = \frac{h}{R} \to o$ and $\frac{V_1}{R} = E_o$, also from above $k > 1$ and $o < \theta < \infty$ This enables equation 2.2 to be written as,

$$E_A = \lim_{\rho \to o} E_A = \frac{Q_o}{4\pi\epsilon_o r^2}\,\phi_A\left(\frac{h}{r}\right) + E_o\,\psi_A\left(\frac{h}{r}\right) \qquad \ldots\ldots \qquad 2.26$$

where

$$\phi_A\left(\frac{h}{r}\right) = \frac{1}{a} \sum A' \qquad \ldots\ldots\ldots \qquad 2.27$$

$$\psi_A\left(\frac{h}{r}\right) = 3 - ch\theta - sh^3\theta \sum A + sh\theta\,(ch\theta - \frac{b}{a}) \sum A' \qquad \ldots\ldots \qquad 2.28$$

$$\sum A = \sum \frac{ch(2n+1)\theta - 3}{\{sh(n+1)\theta - shn\theta\}^3} \quad ; \quad a = \sum \frac{1}{sh(n+1)}$$

$$\sum A' = \sum \frac{sh(n+1)\theta + shn\theta}{\{sh(n+1)\theta - shn\theta\}^2} \quad ; \qquad b = \sum \frac{shn\theta}{sh^2(n+1)\theta}$$

Applying boundary conditions to equation 2.26. When the particle is an infinite distance from the plane $\theta \to \infty$, thus

$$\lim_{\theta \to \infty} E_A = - \frac{Q_o}{4\pi \epsilon_o r^2} + 3E_o \qquad \ldots\ldots\ldots \qquad 2.29$$

This is well known expression for the resultant field on a particle at large sphere-plane gaps (155) (156) (157). For a particle closel approaching the plane, $\theta \to o$ and $ch\theta = \frac{h}{r} \to 1$, then $E_A \to \infty$ as expected. For intermediate gaps equation 2.26 has to be evaluated using computer techniques, however some further simplifications are possible which enable a final expression to be written in a more concise form.

Using the standard expression (eq. 2.1) for the charge acquired by a microsphere in contact with a plane viz, $Q_o = \frac{2}{3} \pi^3 \epsilon_o E_o r^2$ equation 2.26 can be written as,

$$E_A = (\pm \frac{\pi^2}{6} \phi_A + \psi_A) E_o \qquad \ldots\ldots\ldots \qquad 2.30$$

By following similar procedure for the other fields at the positions B and C (see figure 2.14.) we get,

$$E_B = (\pm \frac{\pi^2}{6} \phi_B + \psi_B) E_o \qquad \ldots\ldots\ldots \qquad 2.31$$

and

$$E_C = - \frac{(\pm \pi^2}{6} \phi_B + \psi_B) E_o \qquad \ldots\ldots\ldots \qquad 2.32$$

The physical significance of the terms in these field expressions can be accounted for as follows. The term $\frac{\pi^2}{6} E_o$ is the field intensity

at the surface of the microsphere due to its charge, and the functions ϕ's and ψ's describe the effect of the conducting plane. On plotting these functions for a range of $\frac{g}{r}$ ($= \frac{h}{r} - 1$) values as shown in figure 2.15, the functions suffixed A and B are found to increase rapidly at distances comparable to the particle sizes and when $\frac{g}{r} \leq 0.3$, then the relation,

$$\frac{\pi^2}{6} \phi_A \simeq \psi_A = 1.29 \left(\frac{r}{g}\right)^{0.8} \quad \ldots\ldots\ldots \quad 2.33$$

is satisfied. It can also be seen that

$$\phi_A = \phi_B$$

Hence,

$$E_A \simeq 2\psi_A E_o = E_B \quad \ldots\ldots\ldots \quad 2.34$$

This suggests that for small $\left(\frac{g}{r}\right)$ values the fields at positions A and B shown on figure 2.14 are equal and which is not entirely unexpected result. Thus, the microscopic field between a microsphere and plane for close approach ($\frac{g}{r} \leq 0.3$), in its simplified form can be written as (79),

$$E_g = 2.6 E_o \left(\frac{r}{g}\right)^{0.8} \quad \ldots\ldots\ldots \quad 2.35$$

Subsequently, Chatterton et al (93) have carried out field calculations for a model consisting of a sphere-near - plane with a small protrusions (see figure 2.16). The field was assumed to be composed of two potential components due to:

(i) The charge on the particle $= \frac{Q_o}{4\pi \epsilon_o r}$

(ii) The distortion of originally uniform field by the conducting sphere $= V \left(\frac{x}{d}\right)$

The combined field at the protrusion tip is then given by,

$$E_p = \beta \frac{1}{g}\left[\frac{Q_o}{4\pi\epsilon_o r} + V\left(\frac{x}{d}\right)\right] \quad \ldots\ldots\ldots \quad 2.36$$

where g = sphere - plane gap

r = sphere radius

$x = g + r$

d = distance between the parallel electrodes

V = applied voltage between the electrodes

β = field enhancement factor due to protrusions on cathode (taken to be $\lesssim 10$)

Q_o = initial charge on the sphere, derived from standard, sphere-in contact with-plane expression (100)

The above expression however does not take account of the effect due to induced charge distribution and is only applicable to large ($g > r$) particle plane distances.

More recently, Chakrabarti (94) (95) using a similar basic model of a conducting sphere approaching a plane with a small protrusion, extended the above approximate analysis by taking account of the induced charge distributions, so that the field calculations were applicable to the case of a charged conducting sphere in a uniform field and valid for $g/r \lesssim 1$.

The procedure adopted (94)(95)(155), was first to calculate a series of point charges and their images which will allow the sphere and plane to be at a zero potential. This results in a charge $(-Q_1)$ induced on the sphere, given by,

$$Q_1 = -8\pi\epsilon_o E_o (g+r)^2 n (1 + \ldots\ldots) \quad \ldots\ldots\ldots \quad 2.37$$

Then using Lorraine and Carson's (155) calculations for the capacitance (C) of a charged conducting sphere near an earthed plane; the total

potential (V_t) of the sphere relative to the plane can be obtained, i.e.,

$$V_t = \left(\frac{Q_o + Q_1}{C}\right) \quad \ldots\ldots\ldots \quad 2.38$$

The induced charge and capacitance may alternatively be obtained by solving the charged sphere-near-plane problem using method of images via the Atkins' technique (156) or analytically by solution of Laplace's equation using bispherical polar co-ordinates (157). Nevertheless, all these techniques despite their different approaches and differing final expressions after evaluation for a range of (g/r) values give very similar results.

Finally the field between the sphere and the plane for small g/r is given by,

$$E_p = \left(\frac{Q + Q_1}{Cg}\right) \quad \ldots\ldots\ldots \quad 2.39$$

$$= \left(\frac{2\,E_o}{10^{-10}}\right) \left(\frac{r}{g}\right) \frac{2/3 - 4\,(1+g/r)^2 n\,(1+\ldots)}{[1.13 - 1.235 \log\,(g/r)]} \quad \ldots\ldots \quad 2.40$$

This expression is an infinite series which however converges rapidly and may be evaluated to good accuracy on a computer.

Evaluation of the three microscopic field calculation methods outlined above:

Figure 2.17, compares the three techniques in terms of the field enhancement ratio $\mu \left(=\frac{E_c}{E_o}\right)$ for a range of g/r - values. It can be seen that in all the cases the enhancement ratio μ increases rapidly with decreasing g/r ; in other words, the microscopic field increases rapidly with the decreasing particle/plane gap (g). It can be further seen that Chatterton et al's (93) approximate method, curve (a), which as previously mentioned is not really valid for $g/r < 1$, gives much larger and more rapidly increasing μ-values for all g/r than the other two methods and this even when using the lowest field enhancement factors $(\beta = 1)$. Whereas, Martynov's (78) calculation, curve (b), which is valid for $10^{-5} \leq g/r \leq 0.3$, apparently, gives a linear relationship on this log - log scale for μ throughout the range of g/r - values. Meanwhile Chakrabarti's (94) method, curve (c), which is also valid over a similar range of g/r - values, closely follows the latter linear plot giving identical μ's for g/r - values up to 10^{-2}, but then tends to gradually curve upwards, giving slightly higher μ's for the smaller g/r - values i.e. 10^{-3} - 10^{-4}. In conclusion therefore, both these rigorous techniques, despite their different approaches give remarkably similar results thus confirming the validity of these calculations. However, Martynov's method is preferred because of its more explicit basic assumptions and a final expression which is more convenient to evaluate, especially at small g/r-values and hence will be used in this work.

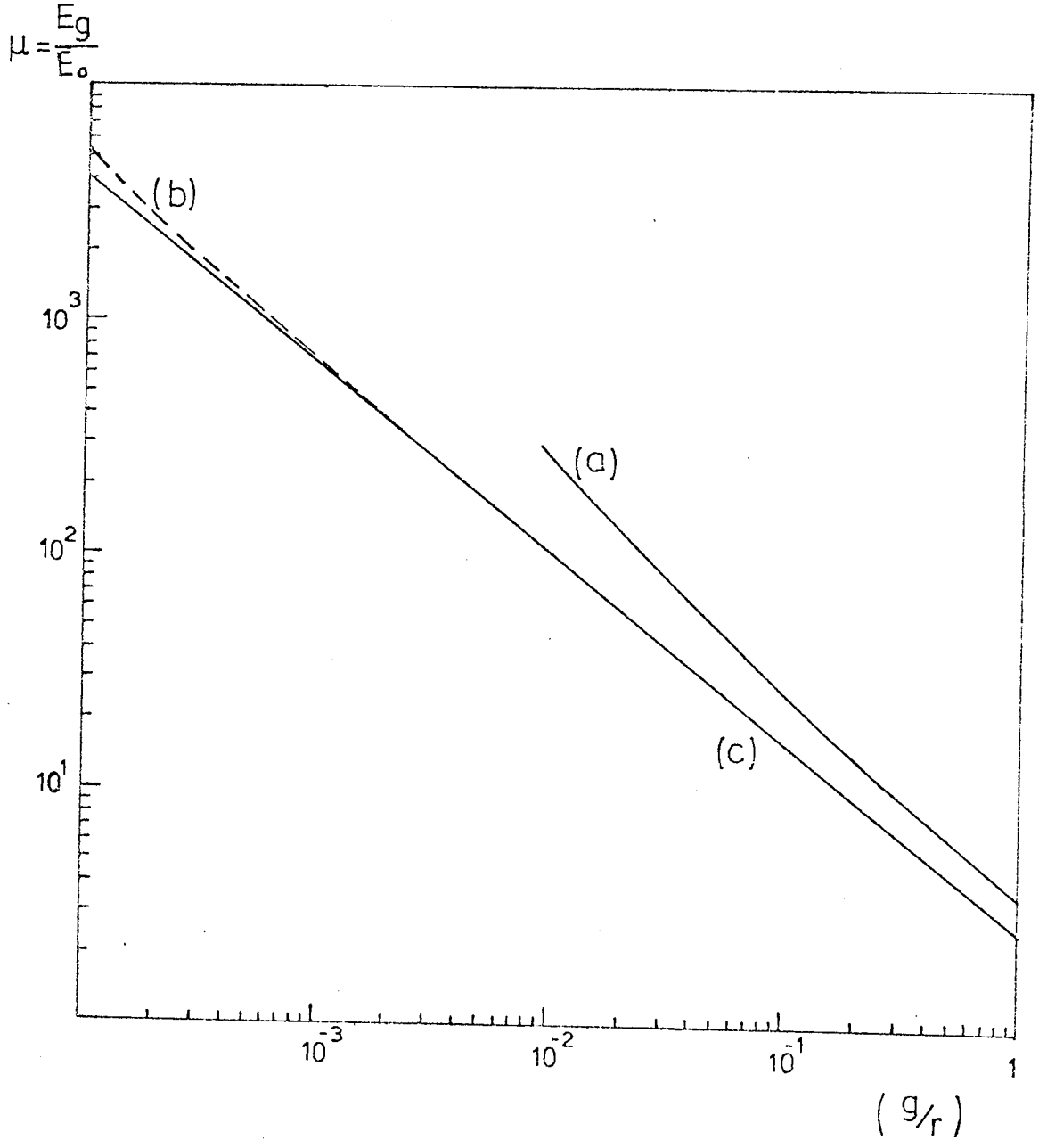

Figure 2.17

2.1.3 Microscopic field with both the sphere and plane supporting thin dielectric surface films

In the preceeding discussions, the presence of thin dielectric films on the sphere-plane surfaces has been neglected in the microscopic field calculations. In order to determine the effect and hence the importance of these surface films on E_g, consider the modified basic model of sphere-near-plane as shown in figure 2.18. Both sphere and plane are assumed to be smooth and supporting thin isotropic dielectric films of uniform thickness (t_s and t_p) with dielectric constants (ϵ_s and ϵ_p) respectively, and separated by a vacuum gap (t_v) so that ($t_v + t_s + t_p = g$), where g is the 'microgap' Then, if the end effects are neglected, this simple model can be approximated to a parallel plate condenser (see figure 2.18b). Thus, using the boundary properties of dielectrics, that is, the normal components of polarisation have the same values and V is continuous (see later), the effective sphere plane capacitance (C) can be written as,

$$\frac{1}{C} = \frac{1}{\epsilon_0 A}\left(\frac{t_s}{\epsilon_s} + t_v + \frac{t_p}{\epsilon_p}\right) \qquad \text{.....} \qquad 2.41$$

where A is the electrode contact area. The 'mean' dielectric constant ($\bar{\epsilon}$) is then given by,

$$\bar{\epsilon} = \frac{g}{\left(\frac{t_v + \epsilon_s t_p + \epsilon_p t_s}{\epsilon_p \epsilon_s}\right)} \qquad \text{.....} \qquad 2.42$$

From equation 2.39, the microscopic field intensity for this modified model then can be written as

$$E_g' = \frac{Q_{tot}}{\bar{\epsilon} C g} = \frac{E_g}{\bar{\epsilon}} \qquad \text{.....} \qquad 2.43$$

From Gauss's law, the charge of the modified sphere in this expression can still be taken to be at its centre although the charge density is not uniform. But if the standard Images technique

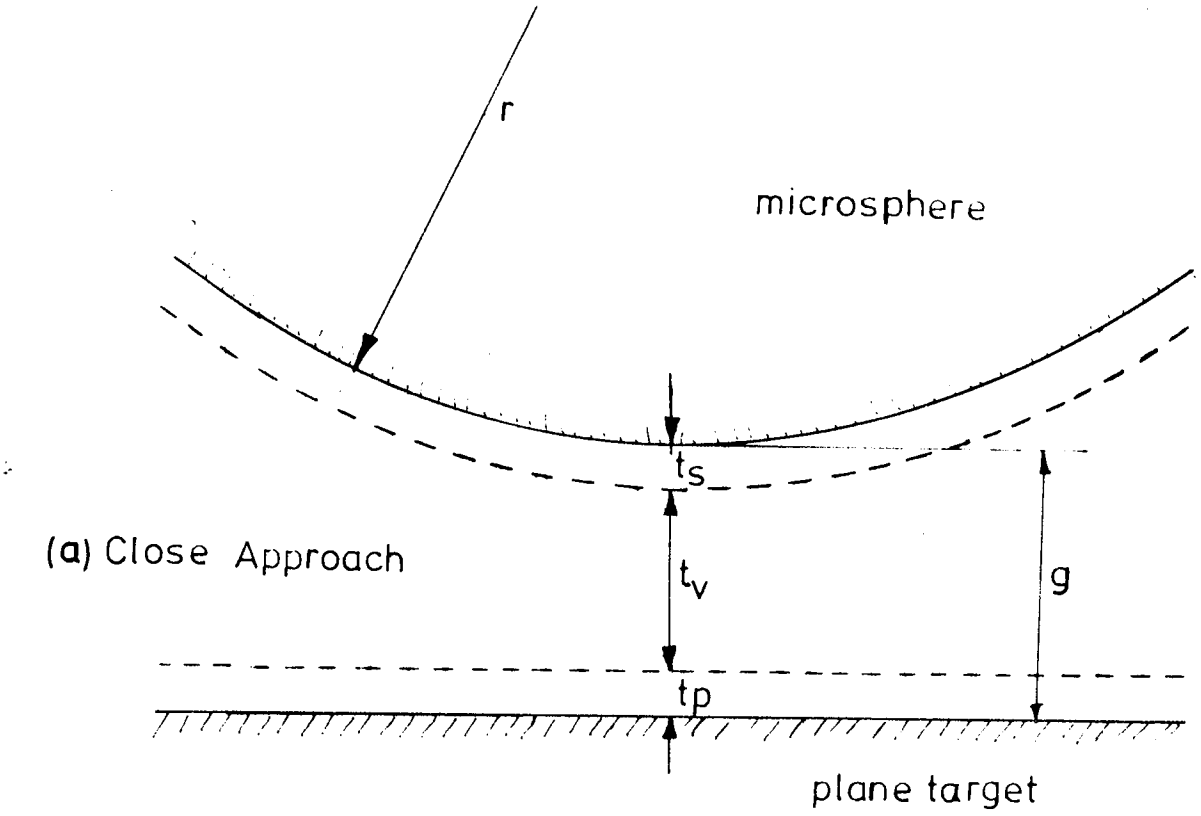

(b) Impact

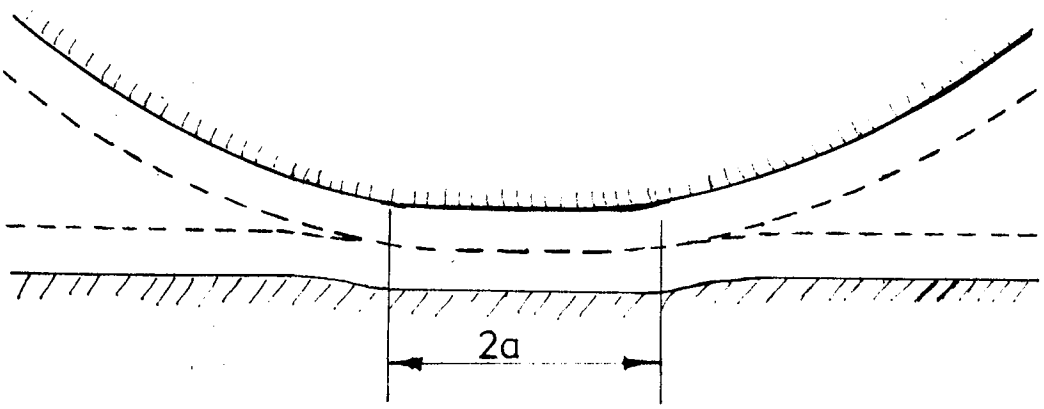

FIGURE 2.18

(94) is only used to obtain the induced charge on the microsphere then the result will be approximate, since the charges induced in the dielectric layer would have been omitted. Nevertheless, this is still a valid assumption provided $t_s \ll R$.

Applying boundary conditions; if g is large, $t_v \gg (t_p + t_s)$, $t_v \to g$, which gives,

$$\bar{\epsilon} \lim_{t \to \infty} \backsimeq 1$$

when g is small, $g \to (t_s + t_p)$ (i.e. in contact, as shown in figure 2.20b), this gives

$$\bar{\epsilon} \lim_{t \to o} \backsimeq \frac{\epsilon_s \epsilon_p (t_s + t_p)}{(\epsilon_s t_p + \epsilon_p t_s)} \qquad \ldots\ldots\ldots \qquad 2.44$$

and if $t_s \backsimeq t_p$, then

$$\bar{\epsilon} = \frac{2 \epsilon_s \epsilon_p}{\epsilon_s + \epsilon_p} \qquad \ldots\ldots\ldots \qquad 2.45$$

Clearly then, at large microgaps the effect of surface oxide films on E_g is negligible and the presence of the surface oxide films can be neglected. But at very small gaps $g \to (t_s + t_p)$, E_g will be predominantly governed by the dielectric film properties and depending on the magnitude of the dielectric constants of the surface films there can be a significant decrease in E_g. Therefore, indicating that it is important to consider their presence at small g/r.

2.1.4 The effect on the electric field intensity E due to the presence of a dielectric layer. (a qualitative approach)

Firstly, consider Gauss's Law which relates the flux of the electric field intensity (E) through a closed surface to the total net charge (Q) enclosed within that surface.

$$\int_{\text{surface (s)}} E.d_a = \int_{\text{volume (v)}} \nabla.E \, dv = \frac{Q}{\epsilon_o} \qquad \ldots\ldots\ldots \qquad 2.46$$

For dielectrics (Q) includes both the bound (P_b) and free (P_f) charges.

$$= \int_v \left[P_f + P_b \right] dv \qquad \ldots\ldots\ldots \qquad 2.47$$

Where the integration is intended to cover both surfaces and volume distribution of free and bound charges. On equating the volume integrals of equations (2.46) and (2.47) gives:

$$\nabla.E = \frac{P_t}{\epsilon_o} \qquad \ldots\ldots\ldots \qquad 2.48$$

$$\text{where } P_t = P_f + P_b \qquad \ldots\ldots\ldots \qquad 2.49$$

Since $P_b = -\nabla.P$, where P is Polarisation, then for any dielectric,

$$\nabla.E = \frac{1}{\epsilon_o} (P_f - \nabla.P) \qquad \ldots\ldots\ldots \qquad 2.50$$

$$\text{or, } \nabla.(\epsilon_o E + P) = P_f \qquad \ldots\ldots\ldots \qquad 2.51$$

but the electric displacement,

$$D = \epsilon_o E + P \qquad \ldots\ldots\ldots \qquad 2.52$$

$$\text{hence } \nabla.D = P_f \qquad \ldots\ldots\ldots \qquad 2.53$$

which implies that divergence of electric displacement (D) depends only on free charges. Rearranging equation 2.52, we have

$$E = \frac{D}{\epsilon_o} - \frac{P}{\epsilon_o} \qquad \ldots\ldots\ldots \qquad 2.54$$

This suggests that the electric field intensity is the sum of two

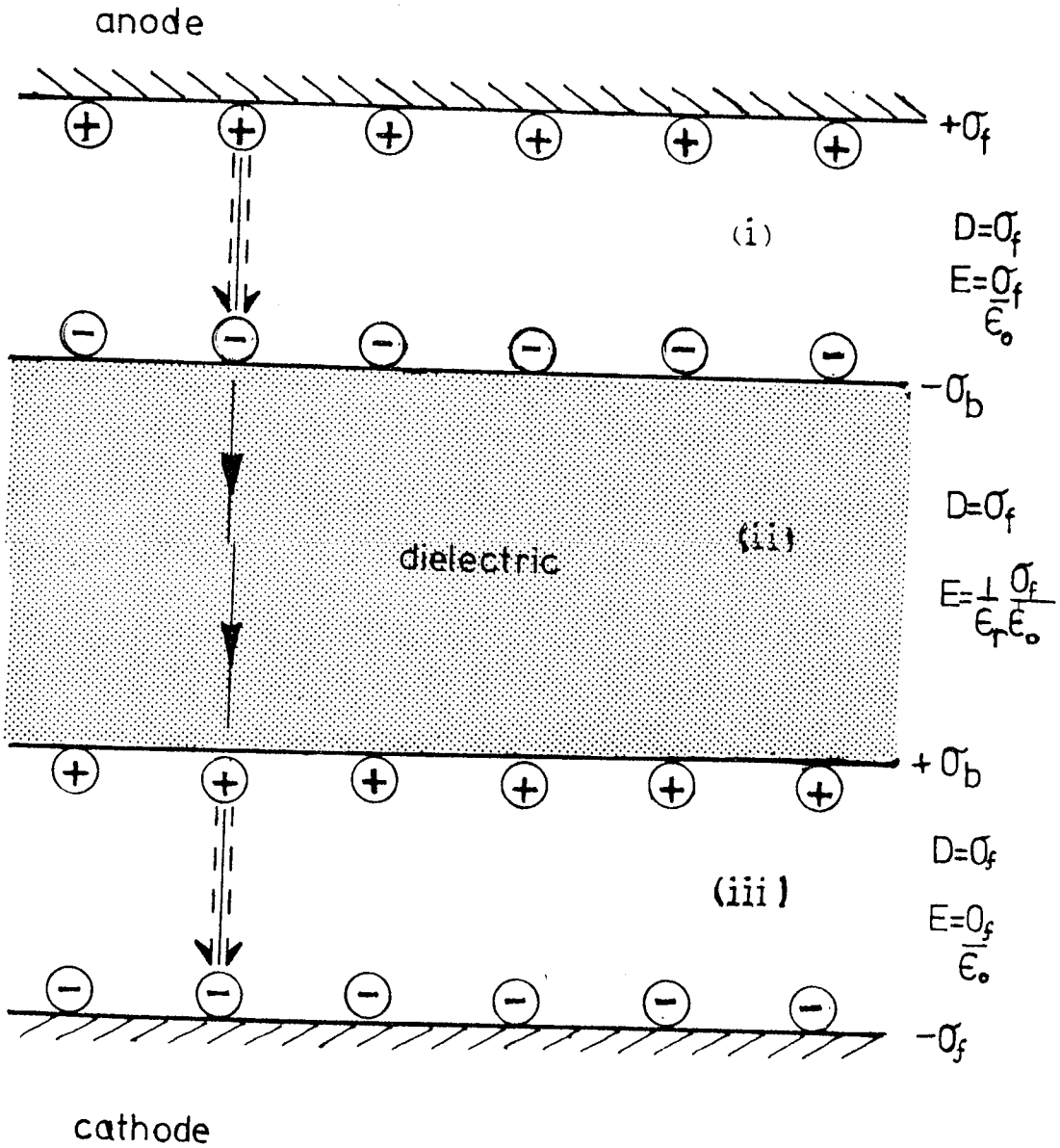
anode
$+\sigma_f$
(i)
$D=\sigma_f$
$E=\frac{\sigma_f}{\epsilon_o}$
$-\sigma_b$
dielectric
(ii)
$D=\sigma_f$
$E=\frac{1}{\epsilon_r}\frac{\sigma_f}{\epsilon_o}$
$+\sigma_b$
(iii)
$D=\sigma_f$
$E=\frac{\sigma_f}{\epsilon_o}$
$-\sigma_f$
cathode

Figure 2.19

fields: $\frac{D}{\epsilon_o}$ associated with free charges and $\frac{-P}{\epsilon_o}$ associated with bound charges.

Applying the above results to situation illustrated in Figure 2.19 in region (i)

$$D = \sigma_f, \quad E = \frac{\sigma_f}{\epsilon_o} \qquad \ldots\ldots\ldots \qquad 2.55$$

and similarly in region (iii)

$$D = \sigma_f, \quad E = \frac{\sigma_f}{\epsilon_o} \qquad \ldots\ldots\ldots \qquad 2.56$$

However, in region (ii), the dielectric region, although $D = \sigma_f$, but

$$E = \frac{D}{\epsilon_o} - \frac{P}{\epsilon_o} = \frac{D}{\epsilon_o} = \frac{\sigma_f}{\epsilon} = \left(\frac{1}{\epsilon_r}\right)\left(\frac{\sigma_f}{\epsilon_o}\right) \qquad \ldots\ldots\ldots \qquad 2.57$$

where $P = N\rho$ and $\sigma_b = P$, Hence, there is decrease in the field by amount $\frac{1}{\epsilon_r}$. This can be explained as follows: Each molecule of the dielectric has a dipole moment p leading to polarisation P. The electric displacement D depends only on free charges $\pm \sigma_f$ and is the same inside and outside the dielectric field. The electric field intensity (E) on the other hand, is reduced inside the dielectric because of polarisation changes $\pm \sigma_b$ which produces a field in opposite direction.

2.1.5 Mechanical Interactions

Solid - Solid Interactions

When two solid bodies collide, a number of complex interactions ranging from deformation, propagation of elastic, plastic, stress and shock waves, heating due to friction and deformation processes, to plasma generation can take place at the point of impact. The relative importance of any one of these interactions, i.e. the fraction of available kinetic energy dissipated in a given process, is predominantly governed by the impact velocity and the mechanical and thermal properties such as Young's Modulus, density, restitution coefficient, melting point, specific heat; geometries and surface conditions of the colliding bodies.

For the present microsystem of a spherical microparticle impacting on a plane metal target Bjork (104) has suggested that it is further possible to distinguish between three physically different processes, mainly by the range of impact velocities at which they occur. The first region is the low-velocity region below a minimum velocity of $0.5 kms^{-1}$, no crater is formed and no plasma released (see section 2.1.6) The second region is transition region where plastic deformation can occur (the plastic stress strain behaviour). The third region is the hypervelocity region $\geqslant 2 kms^{-1}$, this is governed by the hydrodynamic flow theory, i.e. shock wave propagation in solids, where the medium under consideration is treated as a compressible fluid and the Rankine-Hugoniot equations (115) apply. The above conclusions are based on and supported by many experimental observations carried out in connection with micrometeroid simulation studies, where micron-sized spherical iron micro-particles were impacted on plane metal targets at a range of velocities.

Auer et al (76), in a systematic investigation using 0.5 to $10 kms^{-1}$

particles, on several different metal targets e.g. Al, Ag, Au, Cu, Cd, Pb, Ni, and Ti etc, found a relationship between the crater diameter D and the particle velocity (v) given by $D \propto V^{2/3}$, also the crater volume was found to be proportional to the particles energy at higher velocities. Whilst Rudolph (116) in his experiments, using copper targets observed crater formation at impact velocities of only $0.5 kms^{-1}$, the 1μm iron microsphere although itself unaltered was found to be lying $\sim 0.7\mu m$ beneath the surface. In a more recent study Dietzel et al (77) using several different metal targets e.g. Al, Cu, Cd, Sn and W, observed that at velocities below $500ms^{-1}$ the particles were semi-elastically reflected; the crater formation began at around $800ms^{-1}$ and it was between 1-1.5 kms^{-1} when a crater formed with a particle lying within it, but completely unaltered, at higher velocities up to $10kms^{-1}$ the particle was found deformed to almost a coherent layer inside the crater.

Furthermore, there have also been two theoretical predictions of the threshold velocity of plastic deformation (V_c). Latham and Braun (55) using combined results of Tabor (117), Andrews (118) and Taylor (119) for the impact of macrospheres on plane targets obtained an expression for the limiting velocity of elastic impact, given by:

$$V_c = 0.8 \frac{y}{\rho} \quad \ldots\ldots\ldots \quad 2.58$$

Where y is Young's Modulus and ρ is the density of the material respectively. Both for stainless steel and Titanium, this expression gives $V_c = 4kms^{-1}$ and for Tungsten $V_c = 2kms^{-1}$. Whilst, Cook (120) using an entirely different approach of the hydrodynamic theory for impact pressures of fluid jets to the situation of a continuous stream of spherical particles has obtained another expression for v_c, given by:

$$V_c = 2.7 \left(\frac{\sigma}{\rho}\right)^{\frac{1}{2}} \quad \ldots\ldots\ldots \quad 2.59$$

Here, σ is the yield strength of the material. This expression predicts much lower values for v_c than equation 2.58 throughout the range of materials. For example, $v_c \simeq 1 Kms^{-1}$ for tungsten in this case as compared to double the value of $V_c = 2Kms^{-1}$ in the above case.

Clearly then, in a micro-system consisting of a microsphere impacting on plane metal targets, any severe permanent deformation e.g. crater formation for commonly used materials at velocities below $500\ ms^{-1}$ is to be unlikely.

As the present study is concerned with low velocity, essentially elastic or quasi - elastic phenomenon, it is possible to use classical theories of impact, especially the Hertz theory of elastic impact to the present situation.

The main restrictions of this theory are that it is confined to treatment of impact situations where plastic flow, if any, extends only in the vicinity of contact, i.e. it does not permeate throughout the cross-section and it assumes that negligible fraction of the initial kinetic energy is transformed into vibration of the colliding bodies. Neither of these limitations should prove critical for the present arrangement. Firstly, in low velocity impacts any permanent deformation is likely to be localised around the contact point and secondly, the geometry of the microsphere - plane system is such that negligible amount of initial impact energy is removed from the contact region by the propagation of stress waves (121).

2.1.5a Hertz theory of Elastic impact (122)

When two solid surfaces come into contact, the initial contact occurs at isolated tips of peaks, since even the smoothest surfaces are rough on an atomic scale. For the present case, if we assume that the microsphere has a smooth surface and is small compared to the undulations on the target (see figure 2.20) then the microparticle may be treated as an asperite - radius r coming in contact with a surface which is locally flat. Under these conditions it is possible to apply the Hertz theory of elastic impact and obtain three important parameters, namely, the contact area (A), distance of maximum approach (α) and the contact time, which are all vital for better understanding of electrical interactions (see section 2.1.2). In the present case of a sphere impacting on a plane, the area of contact ($A = \pi a^2$) is a circle of radius (r) (see figure 2.21) is given by:

$$a = 0.75\pi r_p (\delta_p + \delta_T)F \quad \ldots\ldots\ldots \quad 2.60$$

where $F = \left(\frac{2mv_i}{t_c}\right)$ is the mean compressive force, r, m, and v_i are the radius, mass and initial velocity of the microsphere;

$\delta_p = \frac{1 - \nu_p}{\pi y_p}$ and $\delta_T = \frac{1 - \nu_T}{\pi y_T}$ are the material properties

i.e. ν's and y's are the Poissons ratio and Young's Modulus of the microsphere and target respectively. The maximum approach (α) is taken as the maximum compression at zero relative velocity and usually the deformation predominantly tends to take place in the softer of the two bodies. In figure 2.21 the microsphere is of harder material than the target:

$$\alpha = \left[\frac{.55\pi v_i^2 (\delta_p + \delta_T)m}{\sqrt{r}}\right]^{2/5} \quad \ldots\ldots\ldots \quad 2.61$$

In the case of elastic impacts α occurs at a time corresponding to one-half of the total contact time (t_c) where:

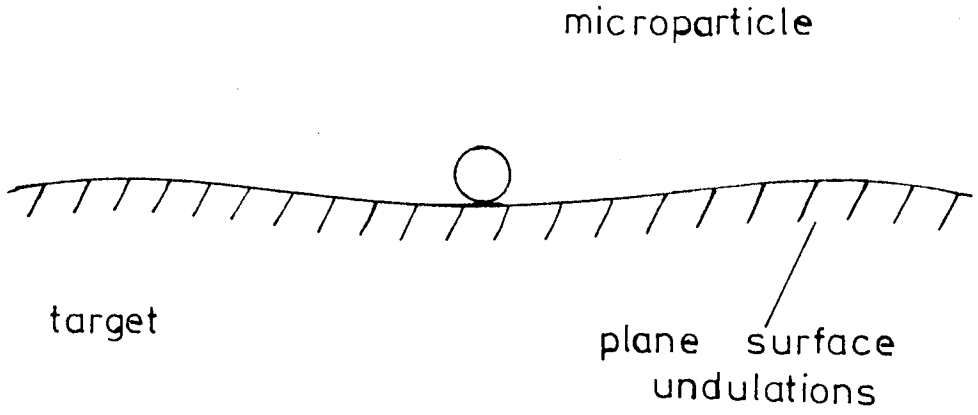

Figure 2·20

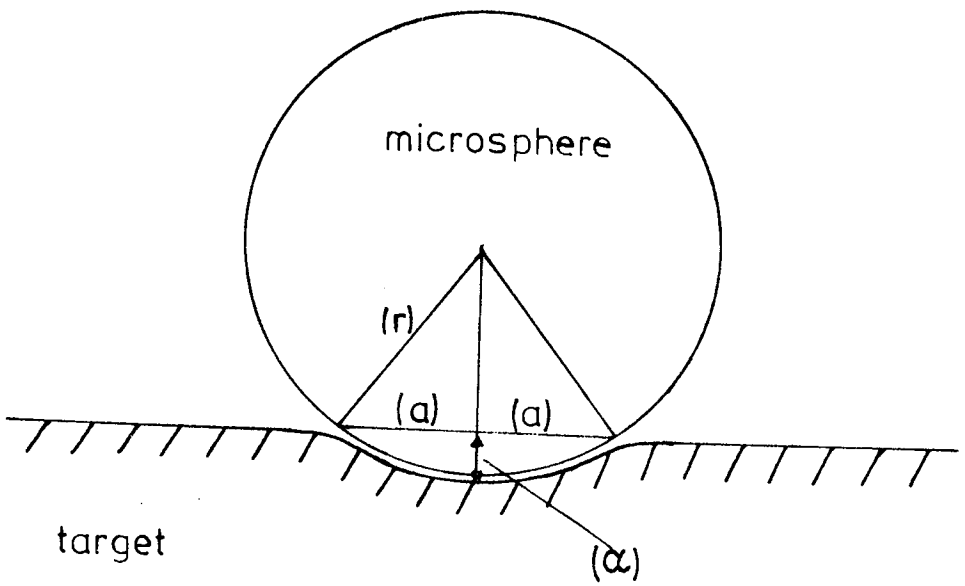

Figure 2·21

$$t_c = 4.53 \left[\frac{(\delta_1 + \delta_2)mp}{\sqrt{r v_1}} \right]^{2/5} \quad \ldots\ldots\ldots \quad 2.61$$

Since the value of Poisson's ratio does not vary significantly among commonly used metals it may be conveniently given a mean value, i.e. $\nu_P = \nu_T = 0.3$, and also if Young's Modulus of the two materials is represented by a mean value $\bar{Y} = \frac{Y_P + Y_T}{Y_P Y_T}$. Then for substitution of these mean values for the material properties δ_P and δ_T, the above expressions can be simplified as follows:

$$a \simeq (1.05)^{1/3} (2.2m\, \bar{Y}\, v_1^{\,2} r^2)^{1/5} \quad \ldots\ldots\ldots \quad 2.62$$

$$\alpha \simeq \frac{a^2}{r} \simeq (1.05)^{2/3} \frac{2.2m\bar{Y}v_1^{2/5}}{\sqrt{r}} \quad \ldots\ldots\ldots \quad 2.63$$

and $$t_c \simeq 4.53 \left(\frac{2.2m\bar{Y}}{\sqrt{r v_1}} \right)^{2/5} \quad \ldots\ldots\ldots \quad 2.64$$

Neglecting the presence of the surface films (since $t_{s,p} \ll \tau$), and substituting appropriate bulk values in equations (2.62) - (2.64), one finds $t_c \sim 2\text{x}10^{-9}$ S. and $a \sim 2\text{x}10^{-8}$ m. Finally, if a uniform decelerat of the particle during the time interval $t_c/2$ is again assumed, from eq. 2. maximum elastic indentation (α) of the target would be $\sim 4\text{x}10^{-9}$ m., i.e. $\alpha \ll r$.

2.1.5b Coefficient of Restitution

For a perfectly elastic impact between the microsphere and plane, the law of conservation of mechanical energy gives the second relation to unequivocaly determine the rebound velocity of the microsphere. However, if the impact produces a permanent deformation then this relation has to be replaced by introduction of a coefficient of restitution e, for the process. This coefficient attempts to describe the degree of plasticity of the collision and is defined as the ratio of final to initial velocity components of the microsphere in direction normal to the contact surfaces e.g.

$$e = \frac{V_{rebound}}{V_{initial}} = \frac{u_2}{v_1} \qquad \ldots\ldots\ldots \qquad 2.65$$

Values of e = 1 and e = 0 denote idealized concepts of perfectly elastic and plastic. Hence, from the mechanical point of view, the materials with higher e-values preferably approaching e = 1, should prove more promising in relation to the mechanism of energy enhancement by charge reversal (see section 5.7).

2.1.5c Impact Heating

As has been previously mentioned, even in low velocity impacts an appreciable amount of the available kinetic energy is expended in causing deformation, this portion of energy however, is eventually dissipated as heat. In addition, a portion of the impact energy may directly be transformed into heat by friction. Thus, depending on the magnitude and the rate of release of the available kinetic energy and the thermal properties e.g. thermal diffusivity, melting point etc. of the colliding bodies, a situation could arise where high temperatures may be generated at the contact surfaces, leading to melting especially if the heating is concentrated to a small volume of the material.

Several experimental and theoretical investigations have attempted to determine the temperature rise for low velocity impacts. Bowden and Tabor (124), measured temperature rises of only a few degrees during normal impact of spheres, with slightly higher temperature rise e.g. 5-10 °C , for a sphere impinging on a sharp spike. Bowden and Yoffe (124) obtained a greater temperature rise of the order of $\backsim 300^{o}C$ by deforming points of hard needles on even harder anvil. On the other hand, Bowden and Pearson (125) and Danson (126) have found that impacts which involve high sliding velocities can result in temperature approaching the melting point of the materials concerned.

More recently, Powell and Quince (127) by applying classical theory of impact to observations of temperature rise and deformation by impact of cylinders on rigid inclined planes, have obtained a satisfactory correlation between the energy dissipated by friction and the heating produced by impact and, also between the energy dissipated by normal impulse and the work done in producing permanent deformation. Given the physical parameters of two solid bodies undergoing impact, it is possible to forecast the heat energy dissipated at the surfaces in contact and the resulting surface temperature. These results were subsequently used (94) in the treatment of impact of microspheres (30 - 100μm rad) on rigid inclined planes and estimation of the temperature rise for both perfectly elastic and quasi-elastic low velocity ($< 100 ms^{-1}$) impacts. It was however found that the temperature rise even for the worst possible case (i.e. 100μm sphere impacting at 45^{o} with a $100 ms^{-1}$ velocity, $e, \mu = 0.5$) was below $\sim 250^{o}C$ and under identical conditions it decreased to below $\sim 100^{o}C$ for a 30μm-rad sphere, there is a further decrease with increasing value of the coefficient of restitution and more noticably with fall in the incident velocity

e.g. at 50 ms^{-1} temperature rise is below $\sim 50^{o}C$. Hence, for the present system with particle radii in the micron-submicron range and near-normal impacts the contribution in temperature rise due to the impact processes is unlikely to be significant.

2.1.5d Solid surfaces Polishing

Mechanical polishing of solid metal surfaces usually involves rubbing them against fine powders e.g. carborundum, corrundum, diamond etc., on a rotating wheel in the presence of a liquid medium i.e. water, oil.

By using successively finer grades of powder a rough surface having marked irregularities may be changed into a very smooth mirror surface with no visible irregularities. Contrary to beliefs of many early workers including those of Newton, Herchel and Rayleigh, this change is not merely the result of diminishingly finer abrasion but a much more complex process as suggested by Bielby (128). At points where rubbing occurs, high localised temperatures that play a fundamental part in the polishing process are generated. The presence of the liquid medium does not prevent the occurrence of the localised hot spots but limits the heat from spreading, preventing large scale surface melting. The high temperatures at the 'hot spots' produce local softening or melting and the plastic material is smoothed over the cooler areas by action of surface tension forces where it quickly solidifies to form a layer which is different in structure to the underlying material - the Bielby layer. Although the exact nature of this polish layer is still a subject of considerable discussion, it is however known that it possesses a very fine grain size corresponding almost to an amorphous structure. In addition, recent electron diffraction studies (129) have shown that the layer

is a fudge of metal and metal oxide, in some cases also the constituents from the polishing medium itself.

Furthermore, the microtopography of an optically flat polished surface, when examined under electron microscope of high magnification, shows 'ups'and 'downs' which are large compared with the size of a molecule. If two such solids are placed in contact, the upper surface will be supported on the summits of the irregularities and the large areas of the surfaces will be separated by a large distance between the peaks. It is difficult to get a surface which is flat within 100 to 1000Å (158) (159).

2.1.6 Plasma generation accompanied by microparticle impact

Investigations carried out in conjuction with micrometeroid simulation studies on the phenomenon of high velocity impact by micron sized particles on metallic targets have shown that impact is followed by production of plasma (75) (76) (77). The total charge released (Q_r) contains equal numbers of electrons and positive ions and may be described empirically in terms of mass (M) and velocity (v) of the particle by a simple power law relationship, given by:

$$Q_r = k\, m^{\alpha} v^{\gamma} \quad \ldots\ldots\ldots \quad 2.66$$

where k, α and γ are constants.

Smith and Adams (76) using spherical carbonyl-iron particles in the mass and impact velocity ranges of 10^{-16} - 10^{-12}kg and .05 - 10kms^{-1} respectively, have obtained values for α and γ as

$$Q_r = km^{1.33} v^{3.2} \text{ for } v < 1 \text{ kms}^{-1} \quad \ldots\ldots\ldots \quad 2.67$$

and

$$Q_r = km^{0.85} v^{3.2} \text{ for } v > 1 \text{ kms}^{-1} \quad \ldots\ldots\ldots \quad 2.68$$

For $v > 1 kms^{-1}$ the constant K was found to have value of $(4\pm1)x10^{-3} C\ kg^{-0.85}\ (kms^{-1})^{-3.2}$. But for $V < 1 kms^{-1}$, as result of very small amounts of plasma produced, they obtained a large scatter in their data and value of K was not given. In agreement, Dietzel et al (77), similarly found that below $.8 kms^{-1}$, vanishingly small amounts of plasma were produced. Thus, indicating that this process is not important for the present application where low velocity $\lesssim 500 ms^{-1}$ impacts are being considered. Furthermore, an analysis by Menon and Srivastava (83) using the above results (76) for velocities up to $2 kms^{-1}$ has shown that the plasma generation process is unlikely to be important in initiating a breakdown.

Part 2

2.2 METAL SURFACES

2.2.1 Introduction

From the discussion in previous sections, it clearly emerges that the mechanical and electrical aspects of microparticle impact behaviour predominantly depend upon the impact energy and bulk properties of the particle/target, additionally however, they can also be considerably influenced by their surface properties. The properties of metal surfac in general are known (see table 2.1) to be significantly affected by the presence of contamination layers, which tend to deposit rapidly on these surfaces (162) on exposure to atmosphere and or are introduced by the method of preparation of the surface (see section 2.1.5d).

Contamination in the form of thin films arising particularly from oxygen deposits are of two kinds: physisorbed and chemisorbed, however contamination can also result from adsorption of other gases, e.g. hydrogen, nitrogen hydrocarbons and rare gases. Physisorbed particles (atoms and molecules) are bound to the metal by means of van der Waal's forces with feeble bonds of the order of 0.05eV. They are easily rubbed away at contact, are to some degree volatile and so can be pumped away at room temperature or after low temperature ($\sim 250^{\circ}$ bakeout. Whereas chemisorbed atoms are bound to valence electrons of the metal surface atoms by covalent bonds. However, the atoms may carry charges and be ionically bound. Of these two types of chemisorption, the latter has a more stronger bonding with typical bond strength of $\sim$ 8eV. The difference is obviously caused by different sites on the pattern of the surface lattice. A theoretical approach to the formation of oxide films on metals has been given by Cabrera and Mott (160) and experimental support for the theory has been found by Bloomer (161).

Once generated, clean metal surfaces may be tested for contamination by measuring a surface-sensitive property of the material. There are a number of approaches which have been used with varying degrees of success. These surface sensitive phenomena include field emission of electrons, field ionization of a gas like helium (163), work functions (164), scattering of low (165) and high energy electrons (166), Auger electron emission (168) and Ellipsometry (169) The latter technique of ellipsometry was used in present studies and the details of this technique are outlined below.

2.2a ELLIPSOMETRY

Ellipsometry is a technique which is eminently suitable for examination of surface layers in the form of thin films. Essentially, it involves the measurement of the optical properties of the reflecting surface film, which in turn enables the thickness of a film on substrate to be determined. This is achieved by measuring the ellipticity, after reflection from a surface, of light which is initially plane polarized. For absorbing materials, the limit of depth from which information is available obviously depends on the penetration of the electromagnetic radiation. The appropriate theoretical approach giving equations relating to the reflection of electromagnetic radiation has been given by Drude (170) and more recently by Ditchburn (169). The significant advantage of the technique is that it is non-destructive and can be used on a specimen in situ, i.e. enclosed inside a vacuum system. The sensitivity is high in that, for example, the detection of the presence of a very thin film a few angstroms thick on a surface is relatively easy. Collectively therefore, all these favourable aspects make this technique highly suitable for the present application, involving the investigation of oxide films on metal surfaces.

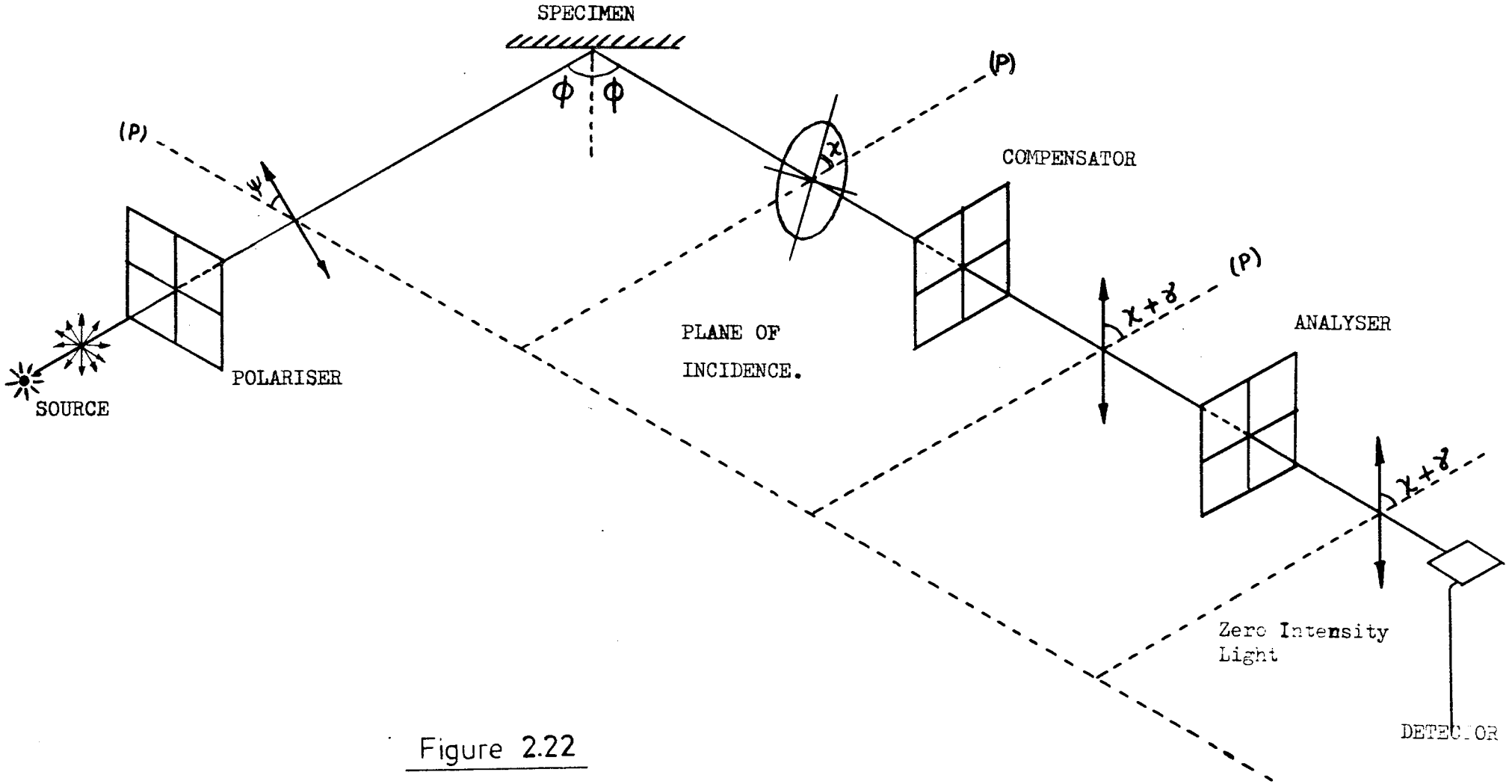
SPECIMEN
(P)
ϕ ϕ
(P)
ψ
χ
COMPENSATOR
PLANE OF
INCIDENCE.
χ+δ
(P)
ANALYSER
SOURCE
POLARISER
χ+δ
Zero Intensity
Light
DETECTOR

Figure 2.22

2.2.1 Basic Instrument Equations

The basic equations relating to the instrument can be obtained from classical theories of light. One must first consider a film free surface with plane polarised light incident on it, where the plane of polarisation is neither perpendicular nor parallel to the plane of incidence. In practice the angle is usually taken at 45^{o} to the plane of incidence so that the amplitude and ratio of components parallel and perpendicular to the plane of incidence is unity. The two media involved are assumed to be isotropic and homogeneous. Reflection produces phase differences between the parallel and perpendicular components of the incident light and changes the amplitude ratio.

The Fresnel reflections are given by:

$$r_{01(p)} = \frac{n_o \cos \phi_1 - n_1 \cos \phi_o}{n_o \cos \phi_1 + n_1 \cos \phi_o} \qquad \ldots\ldots\ldots \qquad 2.69$$

$$r_{01(s)} = \frac{n_o \cos \phi_o - n_1 \cos \phi_1}{n_o \cos \phi_o - n_1 \cos \phi_1} \qquad \ldots\ldots\ldots \qquad 2.70$$

for light travelling from medium 0 to medium 1 having angles of incidence and refraction ϕ_o and ϕ_1, and with the non-absorbing medium refractive indices n_o and n_1 respectively. For absorbing media both n_o and n_1 would be complex. Suffixes (p) and (s) refer to vectors parallel and perpendicular to the plane of incidence respectively. Similar expressions are obtained for the transmission coefficients. The relationship of these reflection coefficients to the instrument reading Δ and ψ is given by the basic ellipsometry equation:

$$\frac{r_p}{r_s} = \tan \psi \; e^{i\Delta} \qquad \ldots\ldots\ldots \qquad 2.71$$

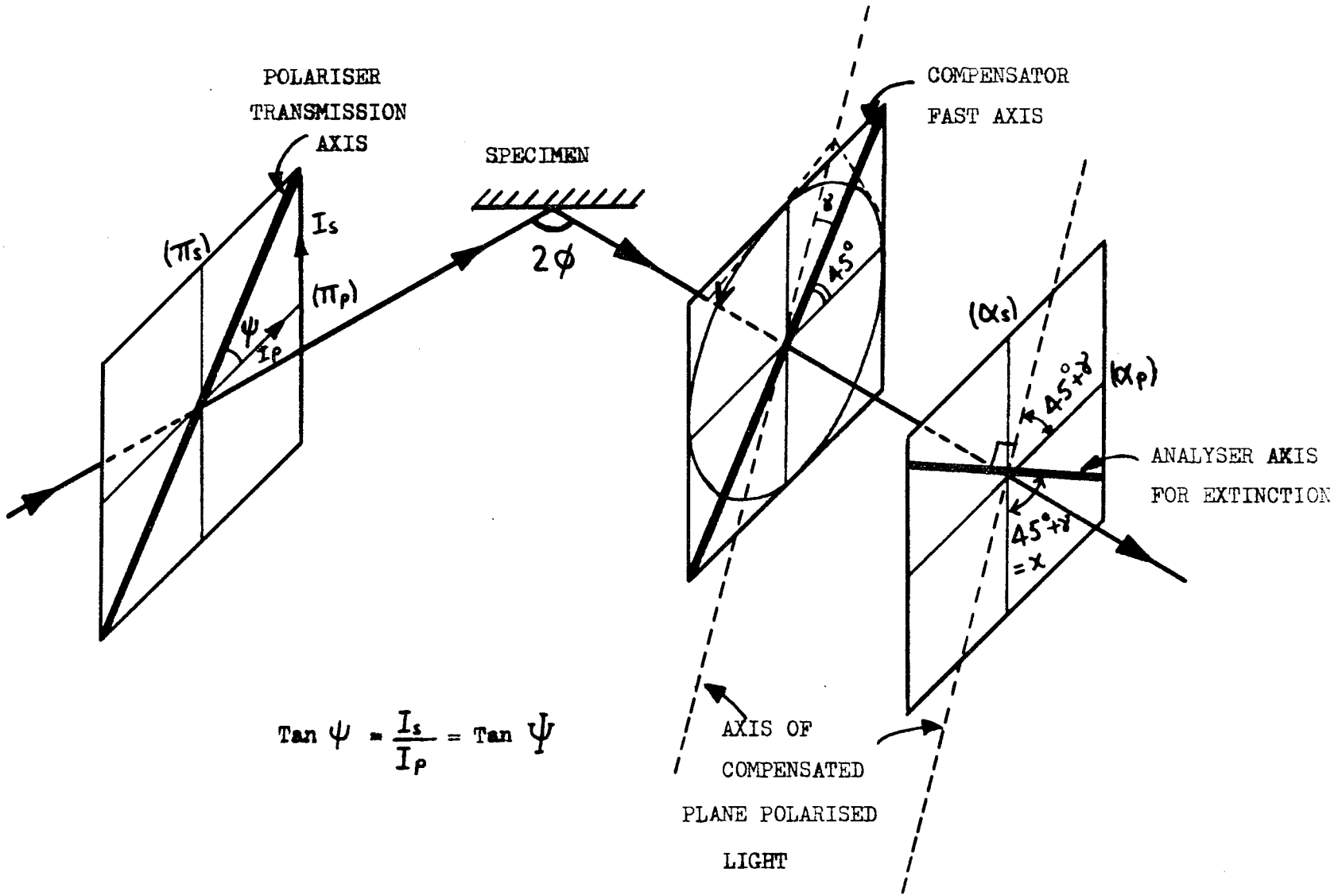
POLARISER
TRANSMISSION
AXIS
SPECIMEN
COMPENSATOR
FAST AXIS
(π_s)
I_s
(π_p)
ψ
I_p
2ϕ
γ
45°
(α_s)
(α_p)
$45°+\gamma$
ANALYSER AXIS
FOR EXTINCTION
$45°+\gamma = x$
$\text{Tan } \psi = \frac{I_s}{I_p} = \text{Tan } \Psi$
AXIS OF
COMPENSATED
PLANE POLARISED
LIGHT

Figure 2.23

The angles ψ and Δ respectively are determined from the polariser and analyser readings of the instrument and represent the amplitude and phase retardations of the reflected light.

2.2.1a Non-absorbing material

For a non-absorbing surface film of refractive index n_1 on a substrate of refractive index n_2 the Fresnel reflection coefficients are written as:

$$r_p = \frac{r_{o1}\,(p) + r_{12}\,\exp D}{1 + r_{o1}(p)\, r_{12}\,(p)\,\exp D} \qquad \ldots\ldots\ldots \qquad 2.72$$

with a similar expression for r_s, where

$$D = \frac{4\pi n_1 \cos \phi_d}{\lambda} \qquad \ldots\ldots\ldots \qquad 2.73$$

d, is the film thickness and λ, is the wavelength of light.

2.2.1b Absorbing media

For absorbing media a complex refractive index $N = n - ik$ replaces the refractive index n so that the Fresnel coefficients also become complex, as does the value of D which is given by:

$$D = 4\pi i\, Ni \cos \phi_1 \frac{d}{\lambda} \qquad \ldots\ldots\ldots \qquad 2.74$$

For an opaque film-free surface, n and k are related to the instrument readings ψ and Δ through the equations (2.69), (2.70), (2.71), and are given in a form suitable for computations by Ditchburn(169).

$$n^2 - k^2 = \frac{\sin^2\phi_o \tan^2\phi_o \,(\cos^2 2\psi - \sin^2 2\psi \sin^2 \Delta\ ) - \sin^2\phi_o}{(1 + \sin 2\psi \cos \Delta\ )^2}$$

and

$$2nk = \frac{\sin^2\phi_o \tan^2\phi_o \sin 4\psi \sin \Delta}{(1 + \sin 2\psi \cos\Delta)^2} \qquad \ldots\ldots\ldots \qquad 2.75$$

2.2.2 Oxidation Studies

In cases where one is considering a chemical reaction at an interface, i.e. oxidation, leading to the formation of a film (see section 2.2.1), an initially clean surface has to be prepared, in which case the equations (2.75) and (2.76) can be applied. The optical constants of the film free surface are first obtained from the appropriate instrument angles ψ and Δ . From the subsequent changes in these angles as the oxide film is formed, in general one can obtain the thickness if the optical constants of the oxide layer are known. Alternatively, they an be determined experimentally by various methods (171).

2.2.3 Compensator Method of Ellipsometry (188)

Figure 2.22, schematically illustrates the basis of the compensator method used in the present work. A monochromatic (549nm), parallel beam of light from a high intensity source is plane polarised after passing through the polariser and is incident on the specimen with an azimuth ψ (the angle of the plane of polarisation with respect to the plane of incidence) and an angle of incidence ϕ. On reflection from the specimen, the plane polarised light beam suffers an amplitude reduction and a phase change between its parallel (p) and perpendicular (s) components and is thus, elliptically polarised i.e. the tip of the electric vector moves in an ellipse with ellipticity (δ) the ratio of minor to major axis and azimuth (α) of the major axis. It then passes through the quarter wave plate compensator (a bi-refringent mica-sheet that produces a 90° phase change between the ordinary and extraordinary rays), which is arranged such that its fast axis is parallel to the major axis of the ellipse so that the vibrations along the major and

minor axis of the ellipse (originally 90° out of phase) are brought into phase again, and plane polarised light restored. Finally, the 'compensated' light then passes through the analyser and its azimuth (γ) is determined by adjusting the analysing polaroid until minimum ($\longrightarrow$ zero) light intensity is received by the photomultiplier detector. This condition is satisfied only when the transmission axis of the analyser is perpendicular to the plane of polarisation of the compensated light.

In order to simplify the experimental procedure, the compensator is initially set with the fast axis at 45° to the plane of incidence, the polariser and analyser are then adjusted for minimum light intensity transmitted to the detector (see figure 2.23). Under this condition, the azimuth of the reflected ellipse is always 45°, i.e. the amplitude of the reflected (p) and (s) components are equal e.g. $I_p^- = I_s^-$. It follows then that the azimuth (ψ) of the polariser is equal to the parameter (Ψ) (see section 3.4.2), since from figure 2.23,

$$\tan \psi = \frac{Is^+}{I_p^+} \qquad \cdots\cdots\cdots \qquad 2.77$$

But,

$$\text{Tan}\,\Psi = \frac{J_p}{J_s} = \frac{\frac{I_p^-}{I_p^+}}{\frac{I_s^-}{I_s^+}} = \frac{\frac{I_p^-}{I_s^-}}{\frac{I_p^+}{I_s^+}} \qquad \cdots\cdots\cdots \qquad 2.78$$

and from above $\frac{I_p^-}{I_s^-} = 1.0$, so that

$$\text{Tan}\,\Psi = \frac{I_s^+}{I_p^+} \qquad \cdots\cdots\cdots \qquad 2.79$$

Comparing equations 2.77 and 2.79 gives $\text{Tan}\,\Psi = \tan \psi$ and hence $\Psi = \psi$.

In addition, the ellipticity (γ) is related to the phase difference (Δ), between the (p) and (s) components and it may be shown that:

$$\tan \Delta = \frac{\tan 2\gamma}{\sin 2x} \quad \ldots\ldots\ldots \quad 2.80$$

Since from above $x = 45^{\circ}$, $\sin 2x = 1.0$, then

$$\tan \Delta = \tan 2\gamma$$

$$\Delta = 2\gamma \quad \ldots\ldots\ldots \quad 2.81$$

Thus, the phase difference (Δ) may be determined from the analyser azimuth since it is a measurement of the ellipticity (γ). As shown in figure 223, the azimuth of the compensated light is ($45 + \gamma$), thence the azimuth of the analyser in its extinction position will be ($45 + \gamma$) with respect to (α s), the perpendicular to the plane of incidence. It is this angle marked χ which is measured experimentally. Since,

$$\chi = 45 + \gamma = 45 + \frac{\Delta}{2}, \quad \ldots\ldots\ldots \quad 2.82$$

it follows that,

$$\Delta = 2\chi - 90 \quad \ldots\ldots\ldots \quad 2.83$$

In general, pairs of polariser and analyser azimuths for extinction occur, falling into four zones. In all, there are 32 such pairs of extinction positions and these can be understood better after representing the state of polarisation of light by means of the Poincaré sphere (172). This is fully discussed in appendix A. Several workers have reported an obscure effect which tends to make some pairs of readings consistently higher than average and some lower, this effect is discussed in detail by McCrackin (173). It is however, not always convenient to measure all the 32 pairs of positions, as in the present experiments where time would not allow this and hence great care must be taken in the choice of measurements (at least 4 pairs) to be taken.

Chapter III

EXPERIMENTAL DETAILS

3.1 Introduction

The discussions of previous chapters have shown that there is considerable speculation as to the role of micronsized particles, in a high voltage vacuum gap and the precise mechanism by which they initiate electrical breakdown. In particular, there is significant amount of indirect evidence to suggest that they undergo at least one low velocity ($\leq$ 500m/s) bouncing impact during their lifecycle which, under favourable conditions of momentum and charge reversal, can result in kinetic energy enhancement sufficient to give the high impact velocities ($\geq$ 1Kms^{-1}) necessary to produce microcraters that are observed on electrode surfaces following electrical breakdown.

The aim of the experimental work described in this chapter is to make an attempt towards a more direct investigation of the underlying mechanical and electrical aspects of microparticle impact, by studying the behaviour of artificially generated microparticles, in a simulated high voltage vacuum gap. Particularly, with the view of directly observing microparticles undergoing bouncing impacts with efficient momentum and charge reversal to verify the existence of energy enhancing mechanism. Specifically, this has involved: (i) Development of a UHV, velocity and charge calibrated microparticle source, capable of delivering single positively or negatively charged, micron-sized particles at a range of velocities. (ii) Use of this facility to study microparticle impact in a specially designed high-field test gap and demonstrate the occurrence of charge reversal following a bouncing impact. (iii) Determination of the dependency of the charge and momentum reversal efficiency on electrode material e.g. Cu, stainless-steel and Ti etc. (iv) Determination of the effect

Chapter III

EXPERIMENTAL DETAILS

3.1 Introduction

The discussions of previous chapters have shown that there is considerable speculation as to the role of micronsized particles, in a high voltage vacuum gap and the precise mechanism by which they initiate electrical breakdown. In particular, there is significant amount of indirect evidence to suggest that they undergo at least one low velocity ($\leq$ 500m/s) bouncing impact during their lifecycle which, under favourable conditions of momentum and charge reversal, can result in kinetic energy enhancement sufficient to give the high impact velocities ($\geq$ 1Kms^{-1}) necessary to produce microcraters that are observed on electrode surfaces following electrical breakdown.

The aim of the experimental work described in this chapter is to make an attempt towards a more direct investigation of the underlying mechanical and electrical aspects of microparticle impact, by studying the behaviour of artificially generated microparticles, in a simulated high voltage vacuum gap. Particularly, with the view of directly observing microparticles undergoing bouncing impacts with efficient momentum and charge reversal to verify the existence of energy enhancing mechanism. Specifically, this has involved: (i) Development of a UHV, velocity and charge calibrated microparticle source, capable of delivering single positively or negatively charged, micron-sized particles at a range of velocities. (ii) Use of this facility to study microparticle impact in a specially designed high-field test gap and demonstrate the occurrence of charge reversal following a bouncing impact. (iii) Determination of the dependency of the charge and momentum reversal efficiency on electrode material e.g. Cu, stainless-steel and Ti etc. (iv) Determination of the effect

of passive oxide films on the momentum and charge reversal efficiencies by setting up suitable apparatus for producing/monitoring 'atomically' clean and oxided electrode surfaces. Argon-ion etching / electron-beam heating being used for in-situ surface preparation, and ellipsometry for monitoring the atomic state of the surface.

3.2 Basic Principle

Figure 3.1 is a schematic representation of the experimental principle showing the simulated high field test-gap (d) and the drift tube detector (D). This test-gap consists of an earthed grid (G)/plane target electrode (T) arrangement and has been shown (see section 4.25) to faithfully simulate the field conditions existing in a plane parallel high-field gap, between two plane electrodes.

A spherical microparticle of known charge, say, $+q_1$ velocity u_1 ($\leq 10 ms^{-1}$) and mass m_1 is recorded as a trapezoidal charge transient (figure 3.1) of height H_1 and duration T_1, as it passes paraxially through the particle detector on its initial excursion. It then enters the high-field test region ($\backsim 10^6$ - $10^7 Vm^{-1}$) through the earthed grid and is accelerated normally towards the negatively biased target.

For the range of target voltages used ($V_T \backsim 0$ - 15kV), the particle undergoes a semi-elastic impact, accompanied by charge reversal so that it is re-accelerated across the gap and recharacterised from the sequential negative going trapezoidal signal of height $-H_2$ and duration T_2, during its return transits of drift tube.

Assuming conservation of particle charge q_1, during its initial acceleration through voltage V_0, one has:

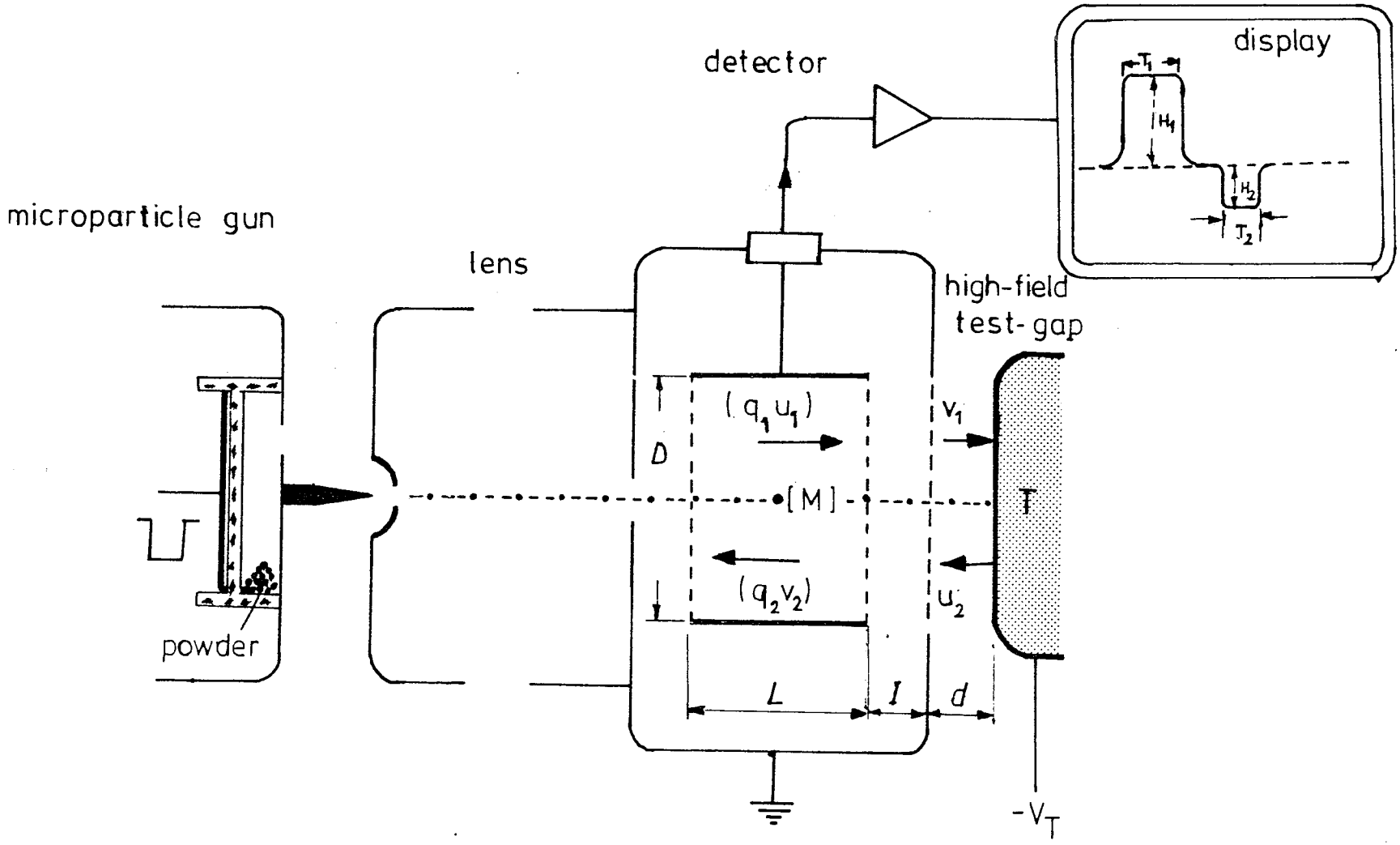
detector
display
microparticle gun
lens
high-field
test-gap
powder
D
(q1 u1)
(q2 v2)
[M]
V1
u2
T
L
I
d
-VT
T1
H1
H2
T2

Figure 3·1

$$\tfrac{1}{2} Mu_1^2 = q_1 V_0 \qquad \ldots\ldots \qquad 3.1$$

where from figure 3.1,

$$u_1 = L/T_1 \qquad \ldots\ldots \qquad 3.2$$

$$q_1 = kH_1 \qquad \ldots\ldots \qquad 3.3$$

k being the charge sensitivity of the detector (see section 4.2.4). Thus, equation 3.1 may be used to calculate the mass M of the particle.

After being accelerated through potential V_T, applied across the high-field gap the particle will impact on the target with a velocity v_1 given by

$$v_1 = u_1 (1 + V_T/V_0)^{\frac{1}{2}} \qquad \ldots\ldots \qquad 3.4$$

The classical impact theories then give the rebound velocity in terms of the coefficient of restitution e (see section 2.15b), that is

$$u_2 = ev_1 \qquad \ldots\ldots \qquad 3.5$$

If the particle charge has been reversed to a value $q_2 = kH_2$ during impact, it follows that the final velocity acquired by the particle will be

$$v_2 = \frac{L}{T_2} = (u_2^2 + 2q_2 V_T/M)^{\frac{1}{2}} \qquad \ldots\ldots \qquad 3.6$$

then from equations 3.1 - 3.6 we have the charge ratio

$$\bar{q} = \frac{q_1}{q_2} = \frac{H_1}{H_2}$$

and the velocity ratio or the coefficient of restitution,

$$e = \frac{u_2}{v_1} = \left\{ \left[\left(\frac{L}{T_2} \right)^2 - \frac{h_2 V_T}{h_1 V_0} \left(\frac{L}{T_1} \right)^2 \right] \left[\left(1 + \frac{V_T}{V_0} \right) \left(\frac{L}{T_1} \right)^2 \right]^{-1} \right\}^{\frac{1}{2}} \qquad 3.7$$

The only difference between the above simulated arrangement and the natural case (see section 3.2) is that for the latter case,

the particle has a zero initial velocity, whereas in the present case it has a finite value. Nevertheless, this can be made a suitably low value, i.e. $u_1 \leq 10ms^{-1}$ compared with $v_i \rightarrow 200ms^{-1}$. Apart from this all the other important conditions, such as the macroscopic field distribution and the microscopic field between the particle and plane electrode should be identical. Thus, the particle/target interactions which are of prime importance to the present work and which take place as the particle closely approaches and impacts onto plane (see section 2.1b) remote from the grid and any of its disturbing influences should also be identical.

Furthermore, the use of metallic microparticles is an automatic pre-requisite for a simulation study of the impact phenomena occurring in a metal-electrode, high voltage vacuum gap. The choice of an appropriate particle size-range for the investigation rests on two considerations. Firstly, as shown by Boulloud (181), the lower limit of the particle diameter (2r) is set by the requirement that the forces arising from the externally applied electric field E_o, are sufficient to overcome the van der Waals adhesive forces and detach the particle from the parent electrode. Following these analysis, for a metallic contact the detachment force is given by;

$$F_d = 4\pi\epsilon_o r (\gamma - 1) E_o^2 \quad \ldots\ldots \quad (1)$$

where γ is the field enhancement factor and the adhesive force is given by,

$$F_a = 2Ar \quad \ldots\ldots \quad (2)$$

where A is a force constant.

The condition of detachment then is $F_d > F_a$, or

$$r \geq r_d = \frac{A}{2\pi\epsilon_o(r-1)E_o^2} \simeq \frac{4}{\beta - 3}\mu m \quad \ldots\ldots \quad (3)$$

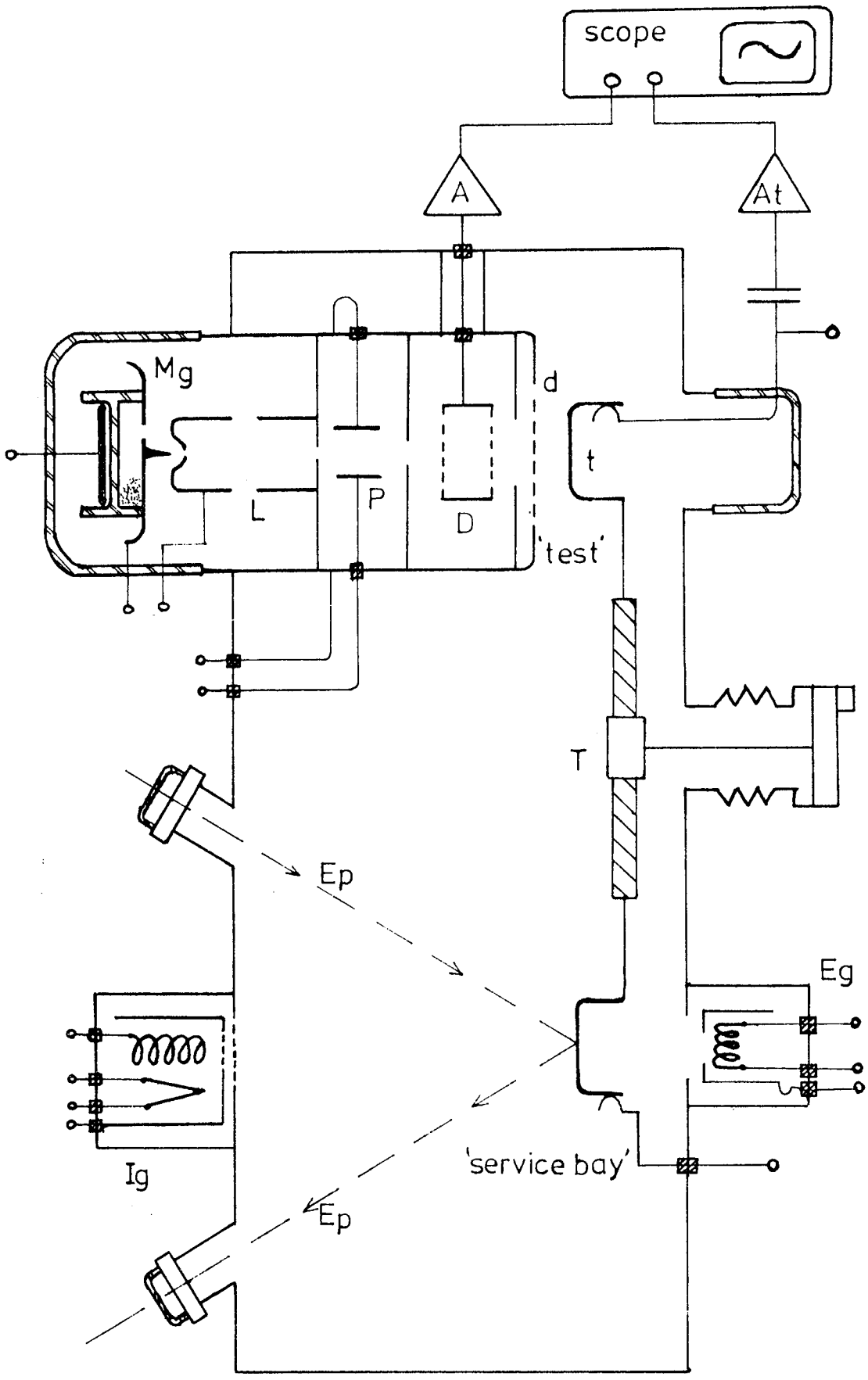

Figure 3.2 EXPERIMENTAL APPARATUS

For $E \cong 3 \times 10^{7}$ V m^{-1} and $\beta = 10$ it can be shown that, r cannot be less than some tenths of μm. Secondly, the upper limit is fixed by the necessity to faithfully simulate the interactions which take place in a natural high voltage vacuum gap. Accordingly the 5μm diameter upper limit is based on a considerable amount of evidence (66), (67), which indicates that sizes of naturally occurring microparticles which initiate electrical breakdown are below 10μm in diameter.

In the present experiments 0.1μm to 5μm diameter (186) carbonyl-iron (99.9% iron) has been used because of its ready availability in the right size range especially in a spherical form, which greatly facilitates the mathematical analysis of experimental data.

3.3 Experimental Apparatus

Figures 3.2, 3.3, and 3.4 show the complete layout of the experimental apparatus used in this study. The specially designed UHV experimental chamber is mounted on a standard Vacuum Generator (DPUHV-2/4) pumping system and is fitted with a number of facilities

The microparticle facility incorporating the dust source gun (M_g) together with its electrostatic focusing/decelerating (L) and positioning (P) elements, the drift tube detector (D) and its associated Fet-amplifier (A) and storage oscilloscope recording/display system. The target assembly, consisting of U.M.D. mounted (i.e. externally adjustable) multi-target holder, capable of carrying up to 8 diamond polished targets on the ends of its - 8 spoke-like high voltage/temperature insulated arms. Apart from enabling several specimens to be studied at each system evacuation, this arrangement permits a chosen target to be positioned either in its 'test' location, i.e. in line with microparticle flux, where

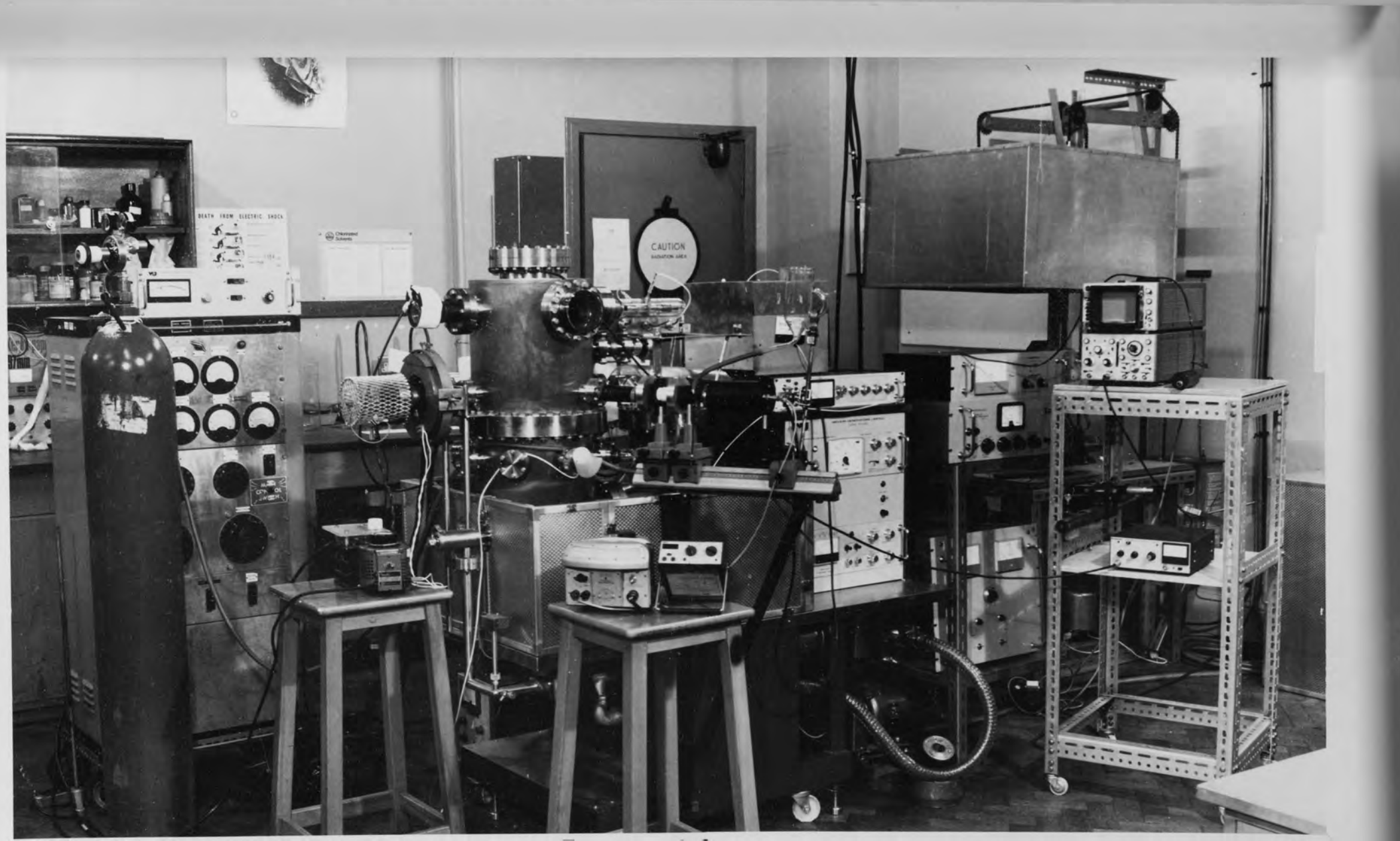
DEATH FROM ELECTRIC SHOCK
CAUTION

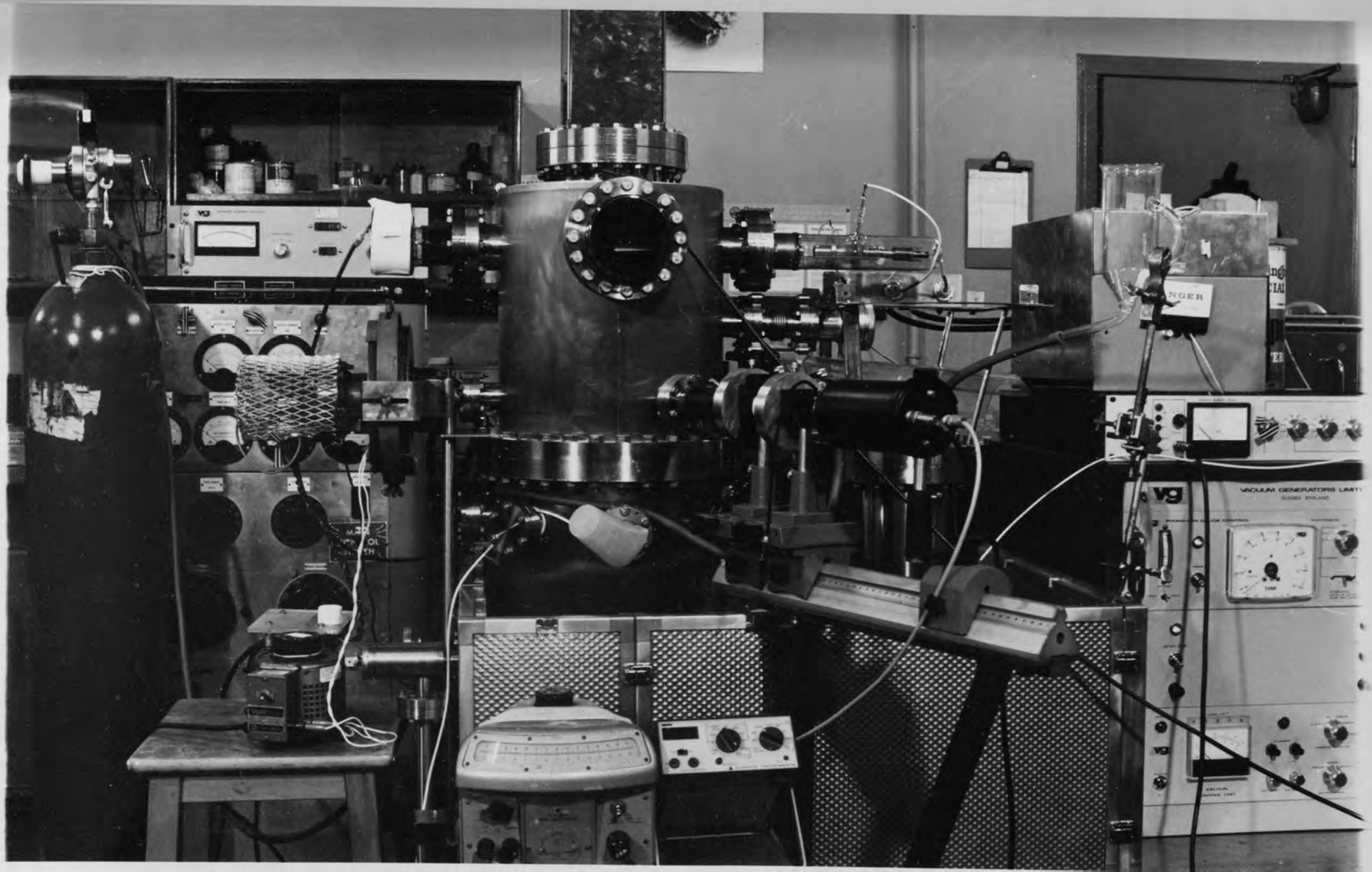
VACUUM GENERATORS LIMITED

further fine adjustments of electrode separation and the parallelity of the high-field gap (T) may also be carried out, or alternatively in its 'service' bay location, i.e. in line with the argon-ion (I_g) and electron gun (E_g) facilities for in-situ surface treatment. In addition, there are optical ports for an external ellipsometry assembly (E_p) for monitoring the state of oxidation of target surfaces.

3.31. Vacuum System

Vacuum environment is an automatic pre-requisite for any experiments concerned with vacuum breakdown. In addition, any experiment designed to study the physical properties of surfaces requires the preparation of a surface free of contamination and the maintenance of cleanliness for a time which is sufficient to perform the experiment. If the time is only a few seconds, then a vacuum of about 1×10^{-6} torr is enough. If however, the time required is in order of several minutes or hours then the surface must be prepared and mounted in a UHV of $\lesssim 1 \times 10^{-9}$ torr.

Figure 3.5 shows the layout of various components which make up the complete vacuum system (see also Figs. 3.3 and 3.4). It is an all stainless-steel bakeable UHV system, using copper gaskets with knife edge flanges.

The main experimental chamber (a) is mounted on the services well (b) and this arrangement is pumped by a Nitrogen trapped (c) oil diffusion pump (d). Both the Nitrogen trap (VG-CCt 100) and the four-stage oil diffusion pump (Edwards E106), have high pumping speeds of ~480L/S and 1350L/S respectively. In addition, the diffusion pump is charged with a special poly-phenyl fluid, which has an extremely low vapour pressure, making it ideal for clean UHV application. In fact, the manufacturers claim that for the above CCT100/E106 combination the carbon level increase in 48 hours is less than a monolayer.

There is also an additional pumping facility of the titanium

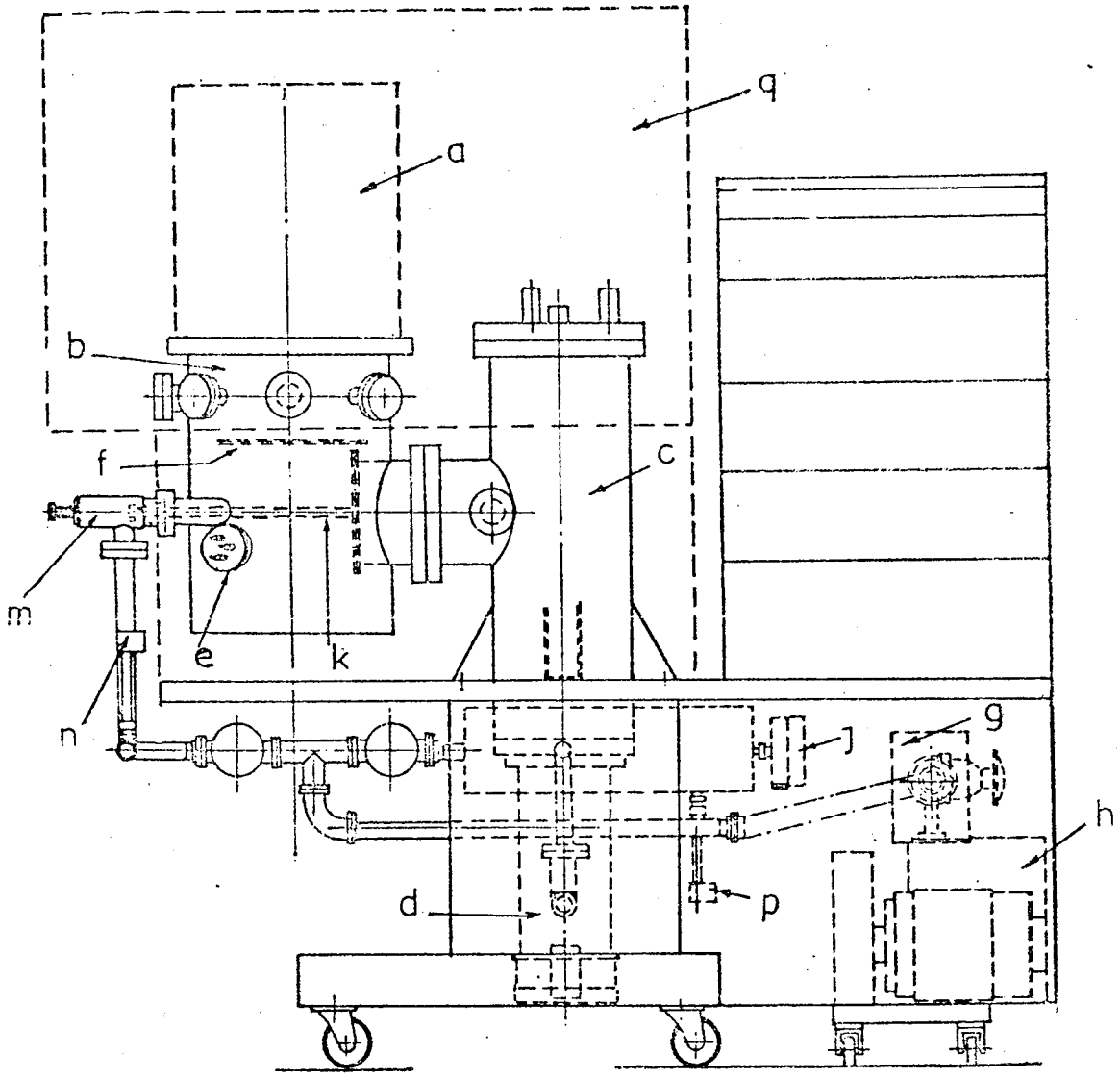

VACUUM SYSTEM

Figure 3.5

sublimation pump (e), fitted to the service well: its cartridge carries 3-(T_1/M_o) alloy filaments from which titanium may be evaporated onto the chamber walls and the sublimation shield (f); the clean titanium film reacts with the chemically active gases to form low vapour pressure solid compounds. Its pumping speed which depends on the area of the condensing surface at pressure below 10^{-7} torr and the rate of deposition at higher pressures can be quite high, up to $\sim$1000 ℓ/s, which makes it ideally suitable for when outgassing, for instance, i.e. heating of any component is undertaken, because the gases so produced can quickly be pumped away by the sublimation pump, while maintaining a constant background pressure with the diffusion pump.

The diffusion pump is backed via a sorption trap (g) by a two-stage gas ballasted rotary pump (h) with a pumping speed of 330 ℓ/s. The function of the foreline trap is to suppress any backstreaming hydrocarbon contamination from the rotary pump, reaching the diffusion pump. As a further safeguard against accidental failure and the system being contaminated with hydrocarbons from the diffusion pump, the backing line incorporates a ballast tank fitted with a pressure protection switch (j). There is also a thermal cut-off device fitted directly to the diffusion pump cooling system for the same purpose. In addition, to achieve a quick turn around system, the viton sealed isolation valve (k) (bakeable to 250°C when open) can be operated across the services well to maintain the nitrogen trap/diffusion pump arrangement under vacuum and the backing line directly used via the all metal isolation valve (m) to rough the experimental chamber.

The backing pressure is monitored by two Pirani gauge heads (n), (p), whilst the pressure in the chamber is measured by a nude ionization gauge. The ultimate pressure for the unbaked system is 2×10^{-8} Torr, but after baking the system to a temperature of $\sim$ 250°C

with the aid of the ovens (q), an ultimate pressure of $\backsim 5 \times 10^{-11}$ torr can be routinely achieved.

3.3.2 The Microparticle Facility

Full details of the construction, operation and performance characteristics of the microparticle facility and its associated systems are given in chapter 4.

3.3.3 Target Assembly

Figures 3.1, 3.2, and 3.6 show the arrangement and details of the specially designed, UHV, all stainless-steel/ceramtec construction (see section 4.2.1) target assembly. It is basically a multitarget turret system mounted on an externally adjustable universal motion drive manipulator i.e. a bellows mounted rotary drive giving accurate linear (up to 2mm), tilt and rotary movements for precision target positioning.

The multitarget turret consists of a main central spindle fitted with a number of (up to 8) spoke-like arms, each carrying a diamond polished target in its end mounted, bayonet type target holder. To satisfy the high voltage ($\geqslant$30Kv)/high temperature ($\geqslant 1000^{\circ}C$), insulation requirements of the individual target, each of the spoke-like arms incorporates a convoluted (to increase electric path length) ceramtec rod, one end of which is clamped in the main turret and into the other end is press fitted the stem (2mm diameter, thin walled stainless-steel tubing) of the bayonet type target holder, so that the targets when mounted, are carried at a radius of precisely 100mm, i.e. directly in line with 'test' and service facilities (see section 3.2.1). In addition, the design of the target holder and the targets (see below) offers a low thermal mass arrangement which minimises the heating/cooling times and heat energy requirements and hence the amount of outgassing produced when the targets are cleaned/annealed by electron beam heating.

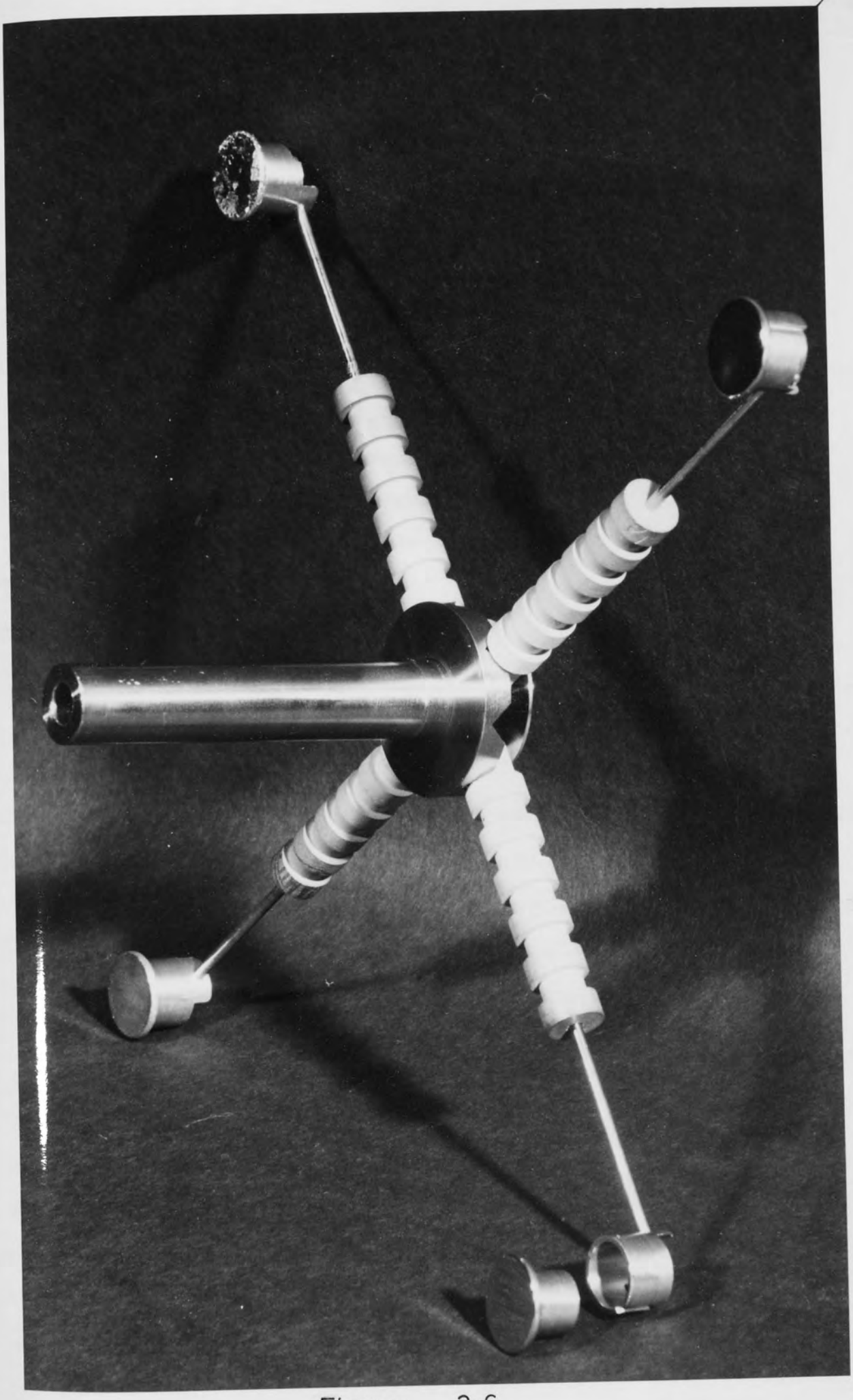

Figure 3·6

The target electrodes were made to specifically chosen profiles by machining from bulk materials e.g. OHFC copper, EN58 stainless-steel, commercial titanium, nickel and lead etc. with Harrison-profile (183) faces and the back ends to fit the bayonet type target holders - all surplus materials being removed to minimise their thermal mass. The 15mm diameter test area was mechanically polished (see section 2.15d) first with emery of successively finer grades and then to a mirror finish with diamond paste polishes down to $\frac{1}{4}\mu m$. They were then ultrasonically cleaned to remove loosely bound particles and finally boiled in isopropyl alcohol and passed through its vapour to remove all traces of grease.

3.3.4 Electron Gun

Atomically clean surfaces of metals can be generated by heating the desired material to high temperatures in vacuum. This method was pioneered by Langmuir and Villais (175) in their researches on tungsten. It is applicable only to those materials whose surface impurities possess higher vapour pressure than the base material or decompose at temperature below the melting point of base material.

The sectional view and the arrangement of the electron gun used for specimen heating to high temperatures ($\sim 1000^{\circ}C$) is shown in figures 3.1 and 3.7 respectively. This is basically, a triode design consisting of a resistively heated tungsten filament wound into a flat spiral (F) (perpendicular to the plane of diagram), a concentric grid (G) and an anode cylinder (C). An electromagnetic focussing lens (L), having maximum ampere-turn rating of 300, is mounted externally on an orientation-adjustable, Cardini ring system to enable the beam to be focussed to a 1-cm^2 spot and directed to the centre of the target.

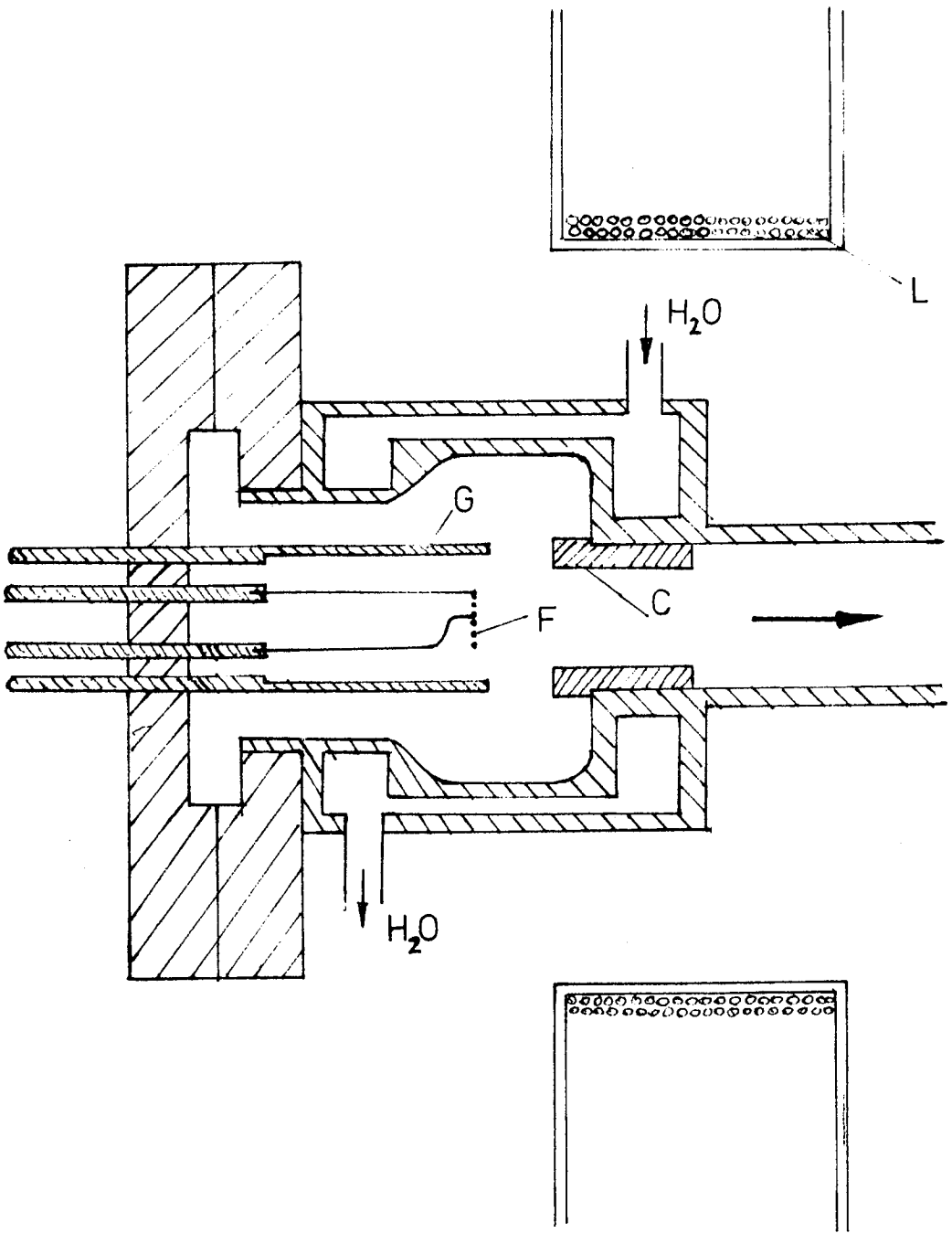

Figure 3.7 ELECTRON GUN

With the filament biased at 750V with respect to the earthed anode (the experimental chamber) the saturated emission current was found to be 75mA. The target potential was variable between 0-3kv, with maximum collected current of 8mA after focussing. Therefore, this gave maximum power dissipation of up to 225W. The target temperature was measured by means of an optical pyrometer.

3.3.5 Ion Gun

The erosion of surfaces which have been exposed to ion bombardment is a process which has been known to occur for many years (176). For example, Kingdon and Langmuir (177) investigated the removal of thorium from a thoriated tungsten filament which was subjected to ion-bombardment. More recently however, Farnsworth and co-Workers (178) (179) have developed a technique of ion-bombardment and annealing for producing atomically clean metal surfaces that show minimum amount of surface defects and a similar approach was adopted in the present work.

Figure 3.8, shows the sectional view and associated circuitary of the saddle-field ion source of spherical configuration used for surface cleaning of targets in this work. It is essentially a spherical ionization chamber (with a gas inlet) supporting an axially symmetrical electrostatic saddle-field by means of two hemispherical aluminium cathodes around a central stainless-steel annular anode. These electrodes are held in position and isolated with the aid of various ceramic insulators. A convenient approximation to the annular anode is achieved by employing a plate anode with a central aperture shielded either side by plates at cathode potential, the anode protruding beyond the shields into central region.

Due to the symmetry of the ion source, two ion beams emerge in diametrically opposite direction. One of these beams is used as a

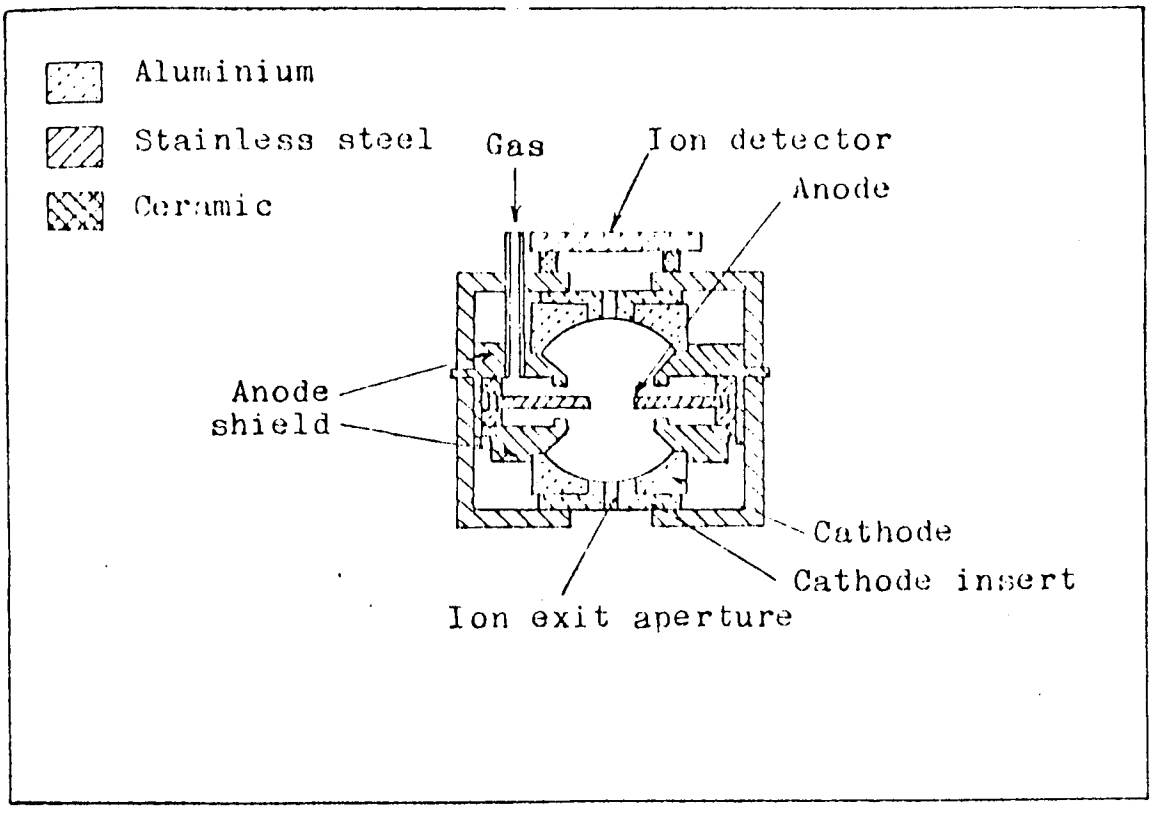

Figure 3.8 The spherical source.(182)

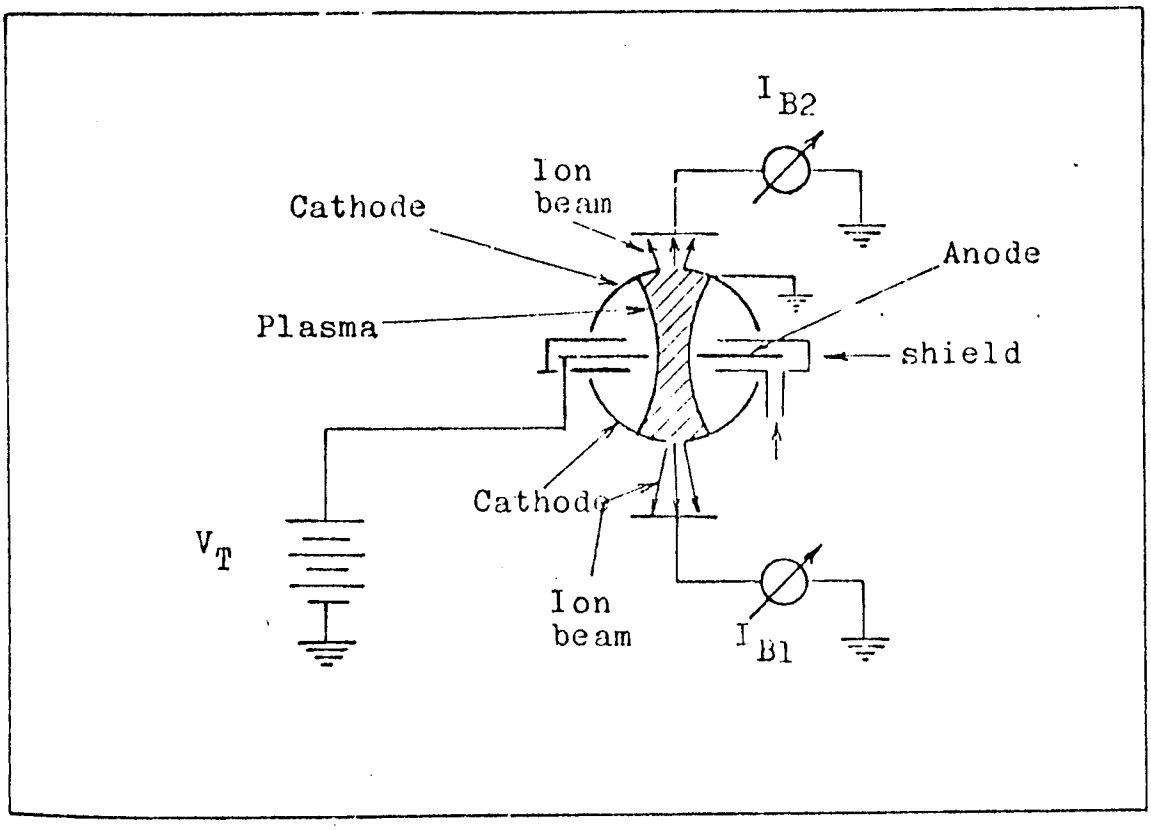

monitor, its current (I_b) being continuously measured by an ion-collector mounted on the source; whilst the other beam can be used for various application e.g. surface etching. Each cathode carried a replaceable aluminium ion exit so that tne beam diameter at the exit can be varied between 1.5 to 5mms.

The ion source preformance characteristics such as the out-put beam current, its profile and energy spread at a range of source voltages, currents and chamber pressures for Argon and Helium have been measured (182). It has been found to give an intense narrow ion-beam of low divergence and small energy spread with beam currents up to 100μA. For the present application however, the source was typically operated at the chamber pressures in the range (10^{-5} - 10^{-6}torr Argon), at 6 - 8kv and 1.2mA tube current, this gave low ion-beam currents of 20-30μA which were found quite adequate for generating atomically clean surfaces without causing any severe surface damage, i.e. pitting.

3.3.6 The Ellipsometer

The ellipsometer system was assembled on two triangular section optical benches, which were mounted on a pair of lockable swivel frames attached to the vacuum system chassis (see figs. 3.2, 3.3 and 3.9). Apart from enabling easy adjustment of the angle of incidence (see later), this set-up also permits the optical benches, together with their components to be moved out of the way for system bakeout.

The arrangement of the various components that make up the ellipsometer assembly is shown in figures 3.9-10. The light source (s), is a special 12V, 100W, tungsten filament projector lamp with a built-in concave mirror backing, operated from a 12V stabilised power supply. This mirror effectively focusses the light onto the pinhole

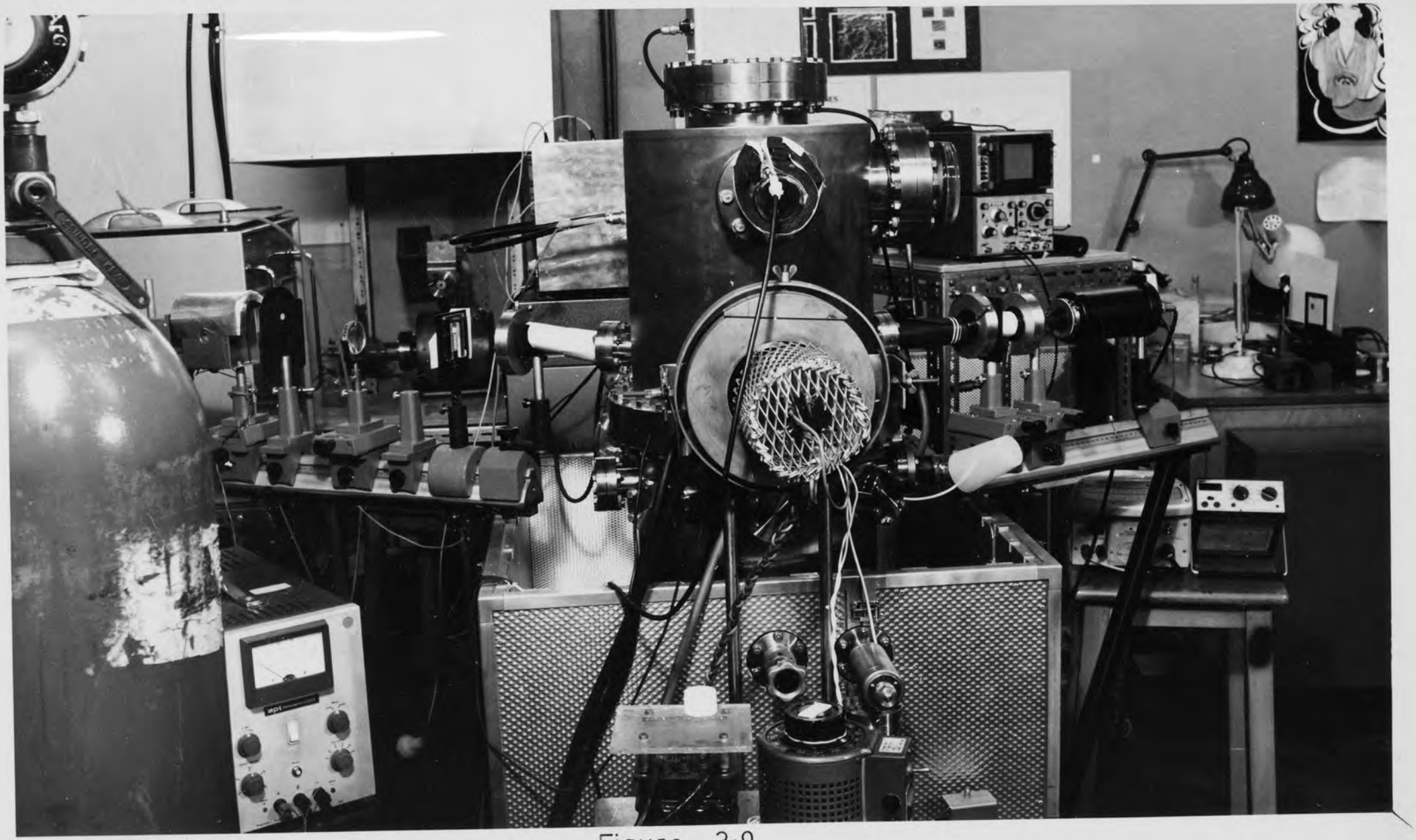

Figure 3·9

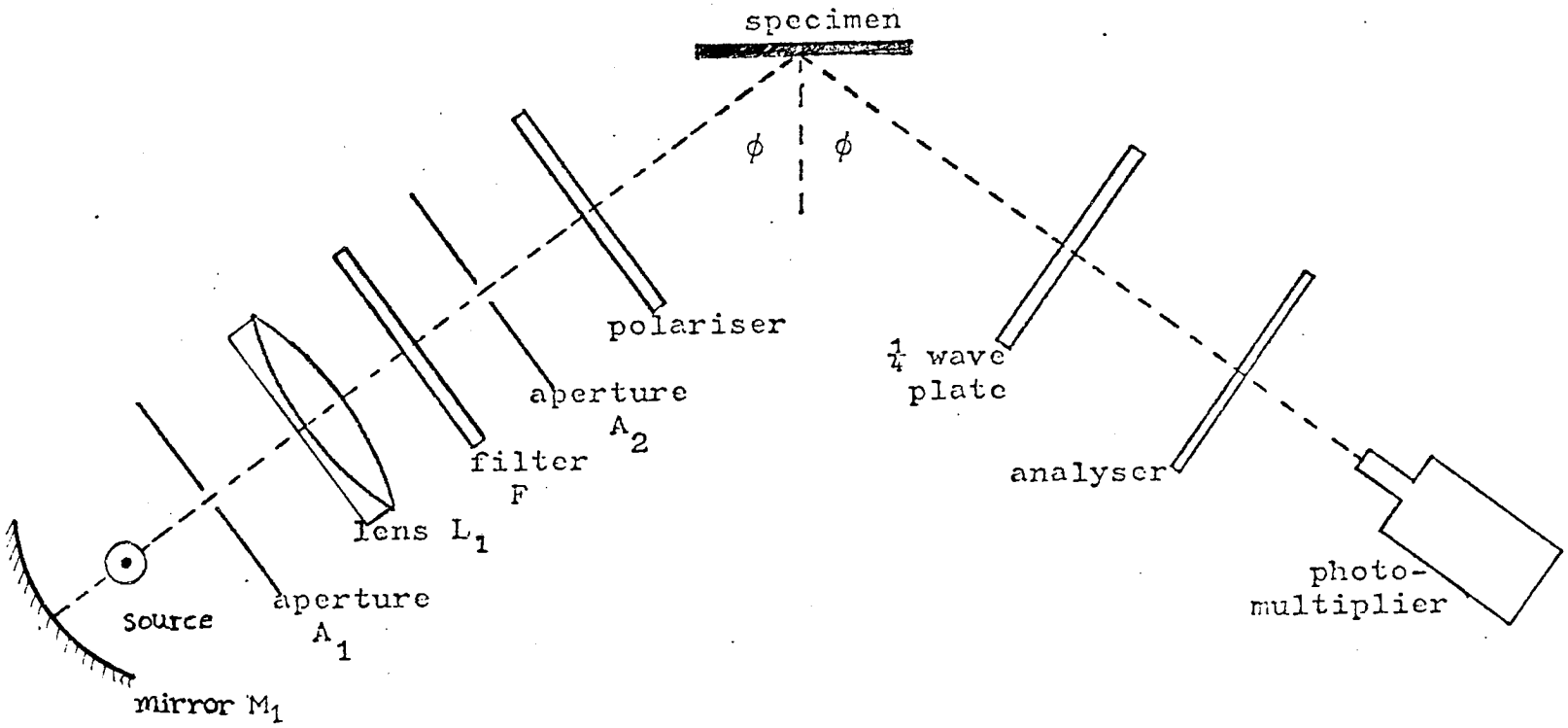

Figure 3.10. Arrangement of the ellipsometer components.

aperture (A), which is arranged to be at the focus of the aberration corrected lens (L). The wavelength of the parallel beam of light so formed is chosen by means of a Balzer interference filter (F), of wavelength 549nm, and beam spot size by the aperture A2. The beam then passes through the polariser and enters the vacuum space through optically flat kodial glass windows which are sufficiently transparent up to 2μm wavelength. After falling on the specimen at an angle approximately 63.5 degrees, the light is reflected out of the chamber, through the compensator and the analyser polaroids to the photomultiplier detector . The saddles that support the optical components have lateral and vertical adjustments to facilitate optical alignment. There is also adjustment of the specimen available (see section 3.3.3) for the same purpose. The angle of incidence was measured by the method described in section 3.4.2c.

3.3.6a Form of the ellipsometer used

The method of 'compensation' used is that due to Winterbottom (171) and is fully described in section 2.2.4. The polariser and the analyser consist of HN22 polaroid in graduated circular vernier scales. These were supplied by Precision Tool and Instruments and are accurate to within ±2 minutes of an angle.

The quarter wave plate is a mica sheet of a precise thickness mounted in an identical vernier scales. Its thickness was chosen such that at a wavelength of 549nm, it produces with the required accuracy a 90 degree phase difference between the ordinary and the extra-ordinary rays.

The light detector was a photomultiplier type 60948 supplied by E.M.I. enclosed in a specially made, light tight magnetic shield. It was used in conjunction with a 2.5Kv, Brandenburg stabilised power supply.

3.4 Experimental Procedure

3.4.1 Microparticle Impact Phenomena

The experimental procedures adopted for the measurements of the mechanical and electrical aspects of microparticle impact on oxided and atomically clean electrode surfaces are briefly outlined below. It being assumed that all the facilities on the experimental system are fitted, and operational, the microparticle gun cleaned and reloaded with a new charge of 'dried' carbonyl-iron powder and freshly polished/cleaned specimens mounted on the target holder. The system is brought under vacuum of $\leq 2\times10^{-10}$torr after following the usual pumping, bakeout and outgassing procedures but first having taken precautions to remove all the unbakeable items, before commencing system bakeout.

As detailed in section 3.1, the various physical aspects of microparticle impact are studied by firing single paraxial particles into high-field test gap and measuring the charges and velocities of the incident and reflected particles, which are displayed as two sequential trapezoidal pulses after passage through the drift tube particle detector. Depending on the measurement being undertaken $\sim$50-200 such consecutive bouncing events are recorded for each target.

For the 'charge' and 'momentum' reversal measurements on various diamond polished targets, the chosen specimen, mounted on the mulit-target holder, is rotated into the 'test' position, facing the grid electrode (see figure 3.2) and the grid/target interelectrode gap accurately set with the aid of a cathetometer by adjusting the UMD manipulator bellows. In this position the target also makes an external electrical contact with the EHT supply so that its potential V_t, may be varied between 0 to $\pm$ 15kv; to produce macroscopic fields up to $E_o \backsim 8\times10^6$ Vm^{-1} across the interelectrode gaps $2 < d < 5$mm. The

impact behaviour of diamond polished targets of different material is then compared by studying the ratio of initial to reversed charge on the particle $\bar{q}$ and the coefficient of restitution e as function of field E_o and impact velocity V_1.

For impact measurements on a chosen target but with different surface conditions, three sets of impact data were obtained for each target studied. These correspond to (i) the 'commercially polished' surface that exists after $\frac{1}{4}\mu$m diamond polishing and ultrasonic cleaning, (ii) an atomically clean surface, to define such a surface one can use the definition of Allen et al (174), which states the atomically clean surface is one free from all but a few per cent of a single monolayer of foreign atoms, either absorbed on or substitutionally replacing surface atom of parent lattice (iii) a surface that has been excessively oxidized. To obtain these three characteristics, a typical sequence of operations alternating between the 'service' and 'test' positions is outlined below.

(a) 'Service' position - for fine adjustment of the optical axes to match the target orientation, and for the ellipsometric characterization (see the following section of the 'commercially polished' surface.

(b) 'Test' position - for impact measurements.

(c) 'Service' position - the target is heated to $\geqslant 800^{o}C$ by electron bombardment ($\sim$50mA at 3kv) of its rear surface using electron gun (see section 3.3.4) this is continued for $\backsim$3 min until Ψ and Δ reach steady values.

(d) 'Service' position - the target surface is argon ion etched for $\sim$1h at a pressure of $\sim 10^{-6}$Torr with a current of $\sim 30\mu$A at 6kv, after which the polariser and analyser angles reach constant value of Ψ_o and Δ_o respectively, when it is assumed that the surface is atomically clean.

(e) 'Service' position - the target is heated to $\sim 300^{\circ}C$ by electron bombardment in air at a pressure $\sim 10^{-3}$ torr to obtain a surface with a thick oxide coverage, which is then characterised ellipsometrically.

(f) 'Test' position - the system is re-pumped to UHV, followed by the final set of charge reversal measurements.

In some cases, the operations (c) and (d), were interchanged, so that the ion etched surface could be annealed since it has been suggested (179) that ion bombardment of a surface can disrupt it greatly and introduce a large number of surface defects.

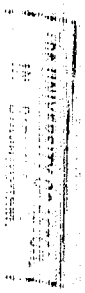

3.4.2 Ellipsometry Procedure

3.4.2a Determination of Reference Azimuths

In the compensator method (see section 2.2.4) the reference azimuths are taken as the polariser and analyser readings which correspond to the transmission axis of the polaroids being parallel and perpendicular to the plane of incidence. Assuming that the ellipsometer is aligned, approximate values are quickly obtained by removing each polaroid, in turn from the ellipsometer and arranging for light from a lamp to be reflected at approximately 56° from a glass plate, placed flat on the bench and to pass through the polaroid. Each polaroid in turn is rotated until minimum light is visible. As shown in figure 3.11, the transmission axis is then approximately vertical. When returning the polaroids to the ellipsometer, on which the plane of incidence is approximately horizontal, the transmission axis are set roughly perpendicular to the plane of incidence. The settings need not be accurate, as more precise settings are found later. The process, so far merely serves to distinguish between horizontal and vertical polarisation directions.

Next, the compensator is removed from the ellipsometer and with the light being reflected from a metal surface, the following procedure is adopted for the N22 polaroids. The polariser is rotated through 90° so that the transmission axis is parallel to the plane of incidence. The analyser is allowed to remain with its transmission axis perpendicular to the plane of incidence. With a small voltage applied to the photomultiplier, a slight adjustment of polariser and then analyser serves to reduce the signal to a minimum. The process is repeated, with the voltage steadily increasing, until optimum position of minimum transmitted light is obtained. The exact polariser and analyser azimuths for extinction are obtained by measuring the azimuths

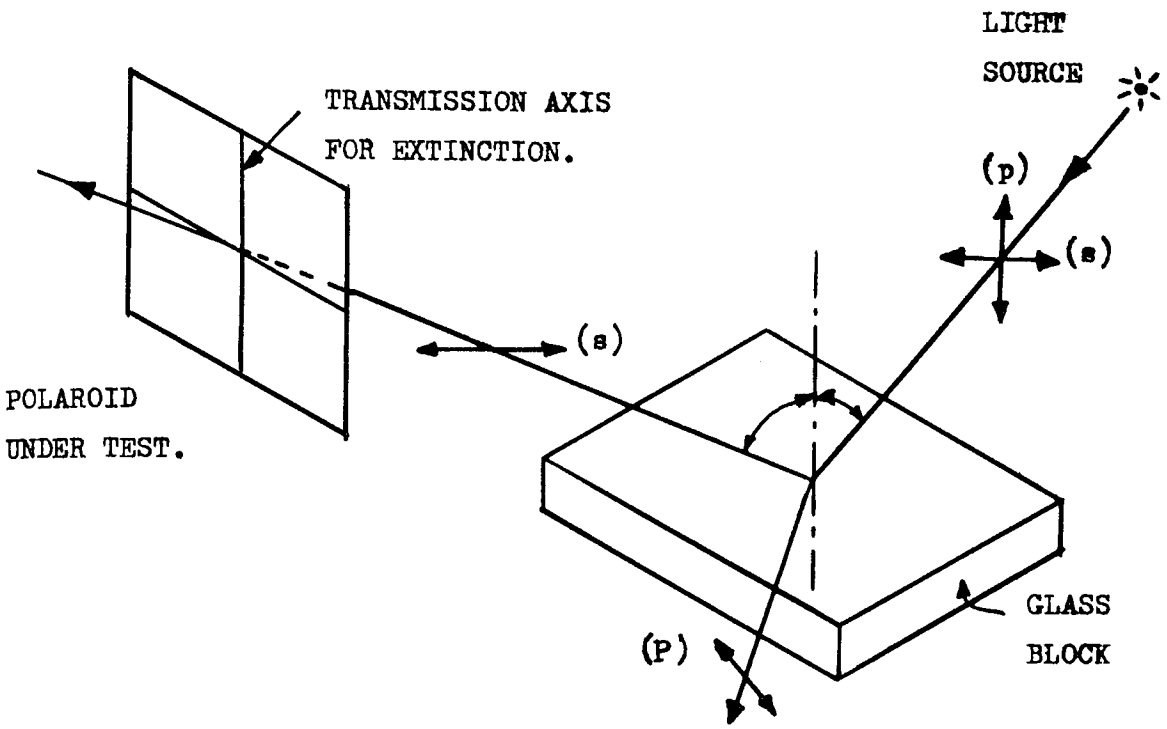

Determination of Reference Azimuths (Approx.)

Figure 3.11

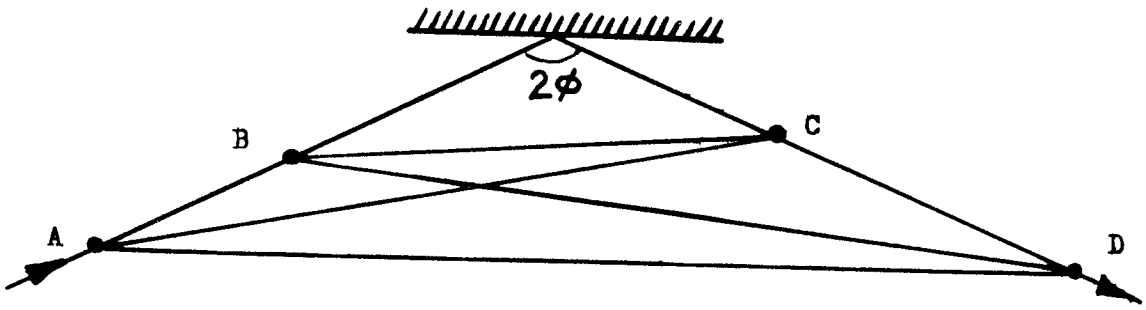

Measurement of Angle of Incidence.

Figure 3.12

at equal intensities on each side of the minimum i.e. by 'bracketing' It can be shown that the intensity of light received by the photo-multiplier is a function of the polariser azimuth and is symmetrical about its extinction position for any analyser setting; also if polariser is set to its extinction position, the intensity is a function of analyser setting and in turn is symmetrical about the analyser extinction position. A rotation of 5^{o} to 10^{o} being sufficient to attain the greatest accuracy. Referring to figure 2.23 the polariser and analyser azimuths correspond to π_p and α_s respectively. Both the polariser and analyser are then rotated through 90^{o} in the positive sense, i.e. anti-clockwise looking towards the on-coming light, and the entire procedure repeated. The new positions found correspond to the azimuths π_s and α_p should be exactly 90^{o} from the first position, for correctly aligned apparatus.

Finally, to obtain the compensator reference position, the polariser and analyser are set to a pair of related reference positions and the compensator returned to the ellipsometer, as shown in figure 3.9-10. By rotation of the compensator and 'bracketing' an exact reference position of the compensator azimuth is then obtained. This position corresponds to either the fast or slow axis of the compensator being parallel to the plane of incidence, because once again, it is only when the light incident on the compensator is plane polarised in a direction parallel to either the fast or slow axis that plane polarised light emerges through the compensator, enabling the analyser to produce extinction. The procedure is repeated for the alternative compensator position which is 90^{o} from the first position for correctly aligned apparatus.

3.4.2b Determination of Δ and ψ parameters

As discussed in section 2.2.4 the essential requirement of the compensator method is that the azimuth of the plane polarised light incident on the specimen is arranged so that the reflected light has equal components in the (p) and (s) directions, i.e. the reflected amplitude ratio $\frac{I_p}{I_s} = 1.0$. Because of the phase difference between these components, the reflected light will always be polarised with its major axis at 45° to the plane of incidence, and have an ellipticity which depends on Δ. If the compensator is set with its axis at 45° to the reference position, this ensures that the axis of the compensator coincides with the axis of the reflected ellipse. Light of any ellipticity is then compensated, i,e. converted to plane polarised light having an azimuth that depends on the ellipticity, and hence on Δ (see figure 2.23).

With the compensator locked at 45° to the reference position, the polariser and analyser are successively adjusted to give minimum light intensity and their extinction positions, say P_1 and Q_1, respectively found by 'bracketing'. The setting procedure is then for polariser azimuth in another quadrant, but not 180° (see section 2.2.4) giving readings P_2 and Q_2 for the polariser and analyser respectively. Two other polariser positions, P_3 and P_4 together with their corresponding analyser positions Q_3 and Q_4 are also measured. It is found that P_3 and P_4 are approximately 180° to P_1 and P_2, and also Q_1 and Q_2 respectively. Next, the compensator fast axis azimuth is set at -45° with respect to the plane of incidence and the whole procedure repeated. In some experiments, however, time did not allow for measurements in all four zones, and in those cases only two pairs of results designated 1 and 2 were recorded for each compensator setting. Finally, to arrive at the values for the parameter ψ and Δ, the polariser and analyser readings

respectively are used as follows. It has been shown in section 2.3.1, that P_1 and P_2 are symmetrically placed about π_p then $P_1 - \pi_p$ should equal $\pi_p - P_2$. In general, the average is taken and this gives the value for ψ :

$$\psi = \frac{P_1 - \pi_p + \pi_p - P_2}{2} \qquad \ldots\ldots\ldots \qquad (1)$$

Where tan (ψ) equals the relative amplitude reduction between (p) and (s) components by reflection from the specimen (see Appendix A).

(ii) It has been also shown in Appendix A that using the Poincare' sphere Q_1 and Q_2 are always separated by approximately 90°, therefore $\alpha_s - Q_1$ should equal $\alpha_p - Q_2$. In general, the average is taken as:

$$x = \frac{(\alpha_s - A_1) + (\alpha_p - A_2)}{2} \qquad \ldots\ldots\ldots \qquad (2)$$

Where the angle (2x - 90) degrees gives the relative phase retardation between the (p) and (s) components.

3.4.2c Determination of angle of incidence

The angle of incidence is determined after each alignment, by removing the detector and replacing it with a small telescope. Four saddles, each holding a sharp pointed spike were positioned on the ellipsometer benches, as shown in figure 3.12, were adjusted so that their points were all in line with the illuminated pin as seen through the telescope.

The distance between the points were measured as accurately as possible and the angle of incidence, ϕ , calculated by simple trigonometry. The possible error in ϕ, thus determined is estimated as $\pm$ 20 minutes of angle.

Chapter IV

MICROPARTICLE FACILITY

4.1 Introduction

The present chapter gives a full description of the specially designed microparticle facility used for studying high-field impact phenomena under UHV conditions. It is basically a low-velocity development of the dust source facility pioneered by Shelton et al (78). This latter design, which has been widely used (75)(76)(77)(84)(116)(95), employs the principle of high-field (electrostatic) contact charging and has proven to be very efficient for generating high velocity $\geqslant$500m/s microparticles with high charge to mass ratios $\geqslant$ 250C.kg^{-1}. However, from the point of view of present experimental requirement of particle velocities as low as $\sim$1ms^{-1}, the conventional design suffers from the serious disadvantage of having a minimum velocity threshold of $\sim$100m.s^{-1} for efficient single particle operation.

To remedy this situation, it has been necessary to introduce two important design modifications. Firstly, the particle charging has been improved so that it is possible to operate the gun at a lower charging/accelerating voltage; secondly, a combined electrostatic post deceleration and velocity-selective focusing element has been incorporated as an integral part of the gun. With these inovations this new source is capable of delivering a controllable paraxial flux of single, micron-sized particles having velocities $\sim$1ms^{-1} and charges of $\geqslant 0.5\times10^{-15}$C. As a further refinement over earlier microparticle guns the present version has been specifically designed for operation under ultra high vacuum conditions. Finally, in order to competently study the

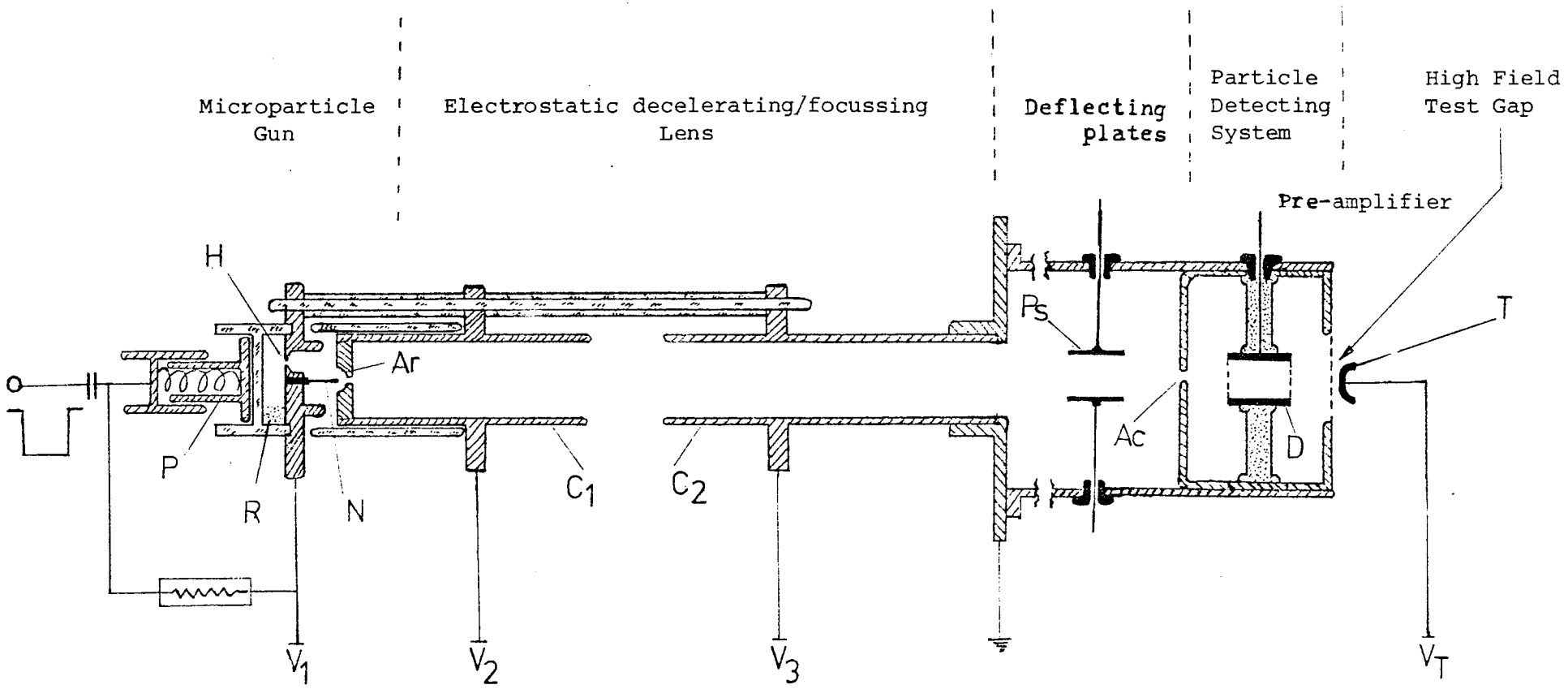

Figure 4.1 MICROPARTICLE FACILITY

phenomena of charge reversal during bouncing impact it has been necessary to improve the sensitivity of the particle detecting system: this arises because the 'reversed' charge on the reflected particle is generally much smaller than that carried by the incident particles emerging from the gun.

Use of this facility, to study the behaviour of micron-sized particles in a high field gap, is discussed in chapter 3. In this chapter, a detailed account is given of the construction, operation and performance characteristics of this new UHV low-velocity microparticle gun, its associated detecting system and the specially designed high field test-gap. In addition, a brief survey of the types of impact phenomena that can be studied with this new facility will also be included.

4.2 Experimental

Figures 4.1 - 4.4 show the layout and constructional details of the experimental assembly used for obtaining the performance data, on the micro-particle gun and for studying high field impact phenomena at normal incidence. The arrangement of this entire assembly, in the main UHV experimental chamber, is described in chapter 3.

It is an all stainless steel, clear-fused quartz (Vitreosil) construction, with only limited use of cremtec for electrically insulating parts requiring machining. These materials have been carefully chosen to satisfy a number of stringent requirements; low outgassing rate and bakeability (up to $\sim 300^{\circ}C$) for efficient UHV usage (230); good high voltage insulation, the metal as a high voltage electrode (see section 1.1.2) and the insulator as a dielectric (eg. $\geq$10kv per mm); low thermal expansion, to allow safe heating of carefully designed metal/insulator

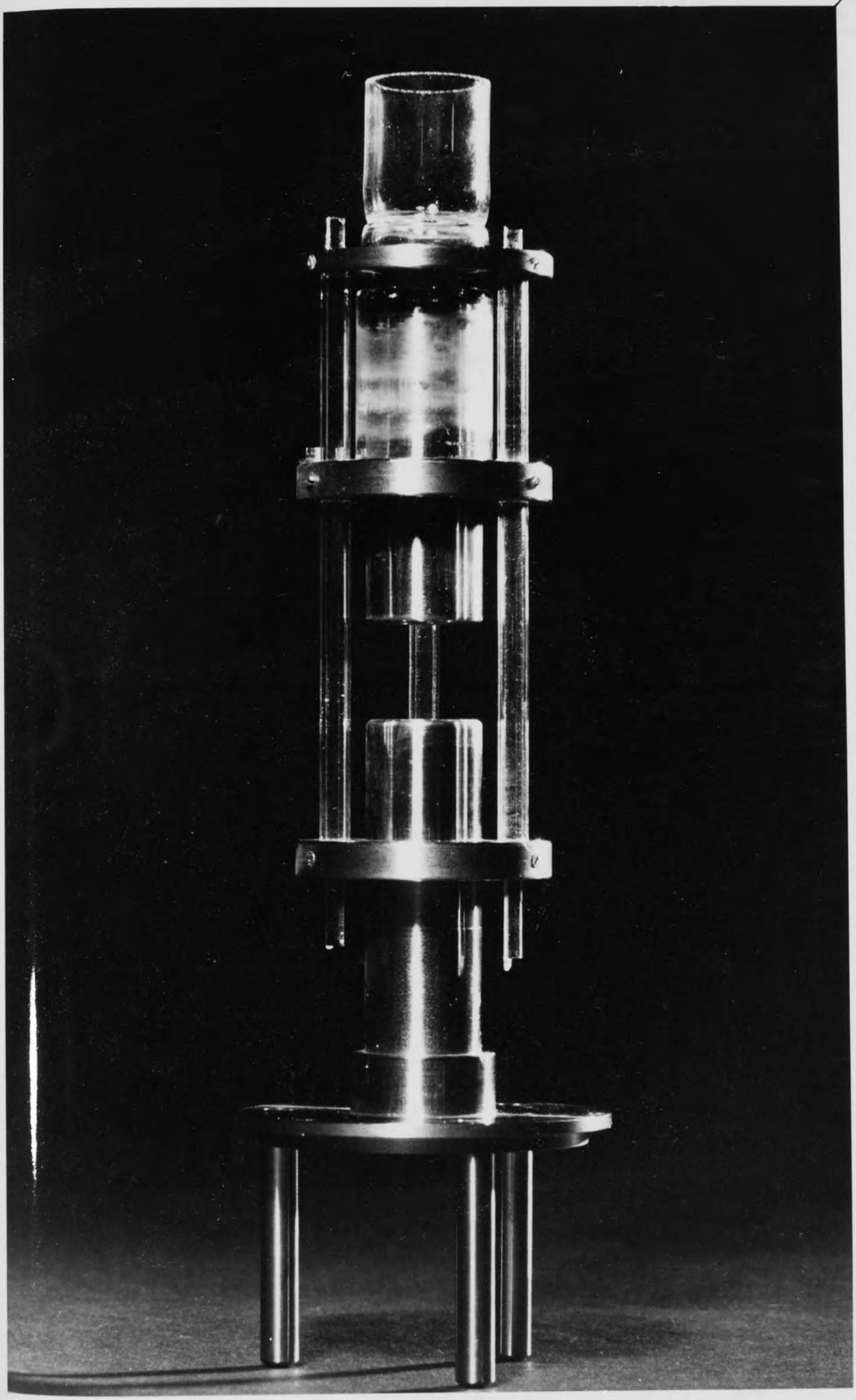

Figure 4·2

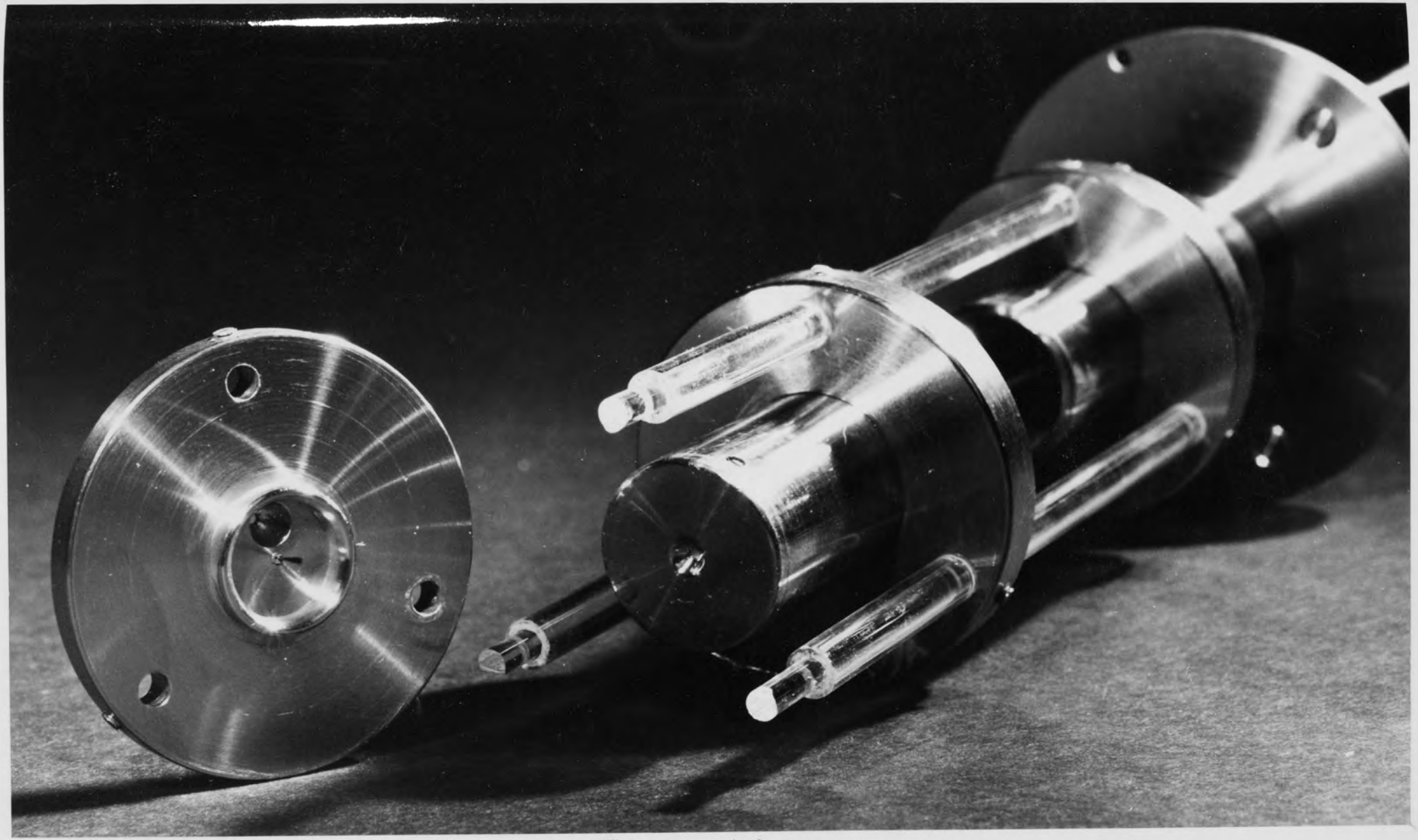

Figure 4·3

interfacing parts and finally, non-magnetic so as to avoid interference with the motion of charged (ferrous) particles for efficient gun operation. In addition, the optical transparency of vitreosil parts coupled with that of the outer pyrex envelope (see figure 4.4), makes the microparticle gun assembly into a semi-transparent system, allowing visual monitoring of some of its important functions, e.g. check on efficient powder agitation and powder level etc. (see later).

For further discussions, the total experimental facility will be conveniently broken down into its five constituent elements viz: (i) the microparticle gun (ii) the electrostatic decelerating lens (iii) the deflecting plates (iv) the microparticle charge and velocity detector and (v) the high field test gap.

4.2.1 The Microparticle Gun

Since the basic principle of this type of gun, has been adequately described in the original papers (78) (84), this account concentrates mainly on the design features of the new UHV, low-velocity version.

Referring to figure 4.1, the microparticle powder (186), consisting of carbonyl-iron spheres with diameters in the range of 0.5 - 5μm, is contained in a reservoir (R) formed by using a spring loaded plunger (P) to locate the "I"-shaped vitroesil cup in a groove machined in the back face of the charging electrode assembly. A small re-entrant "escape" hole (H) connects this reservoir with the high field region between the electrodes supporting the needle-like charging electrode (N) and the 1mm diameter radiused aperture (A_r) (see Fig4.3). Under UHV conditions ($\leq 10^{-9}$ torr), it has proven very important for this "escape" hole

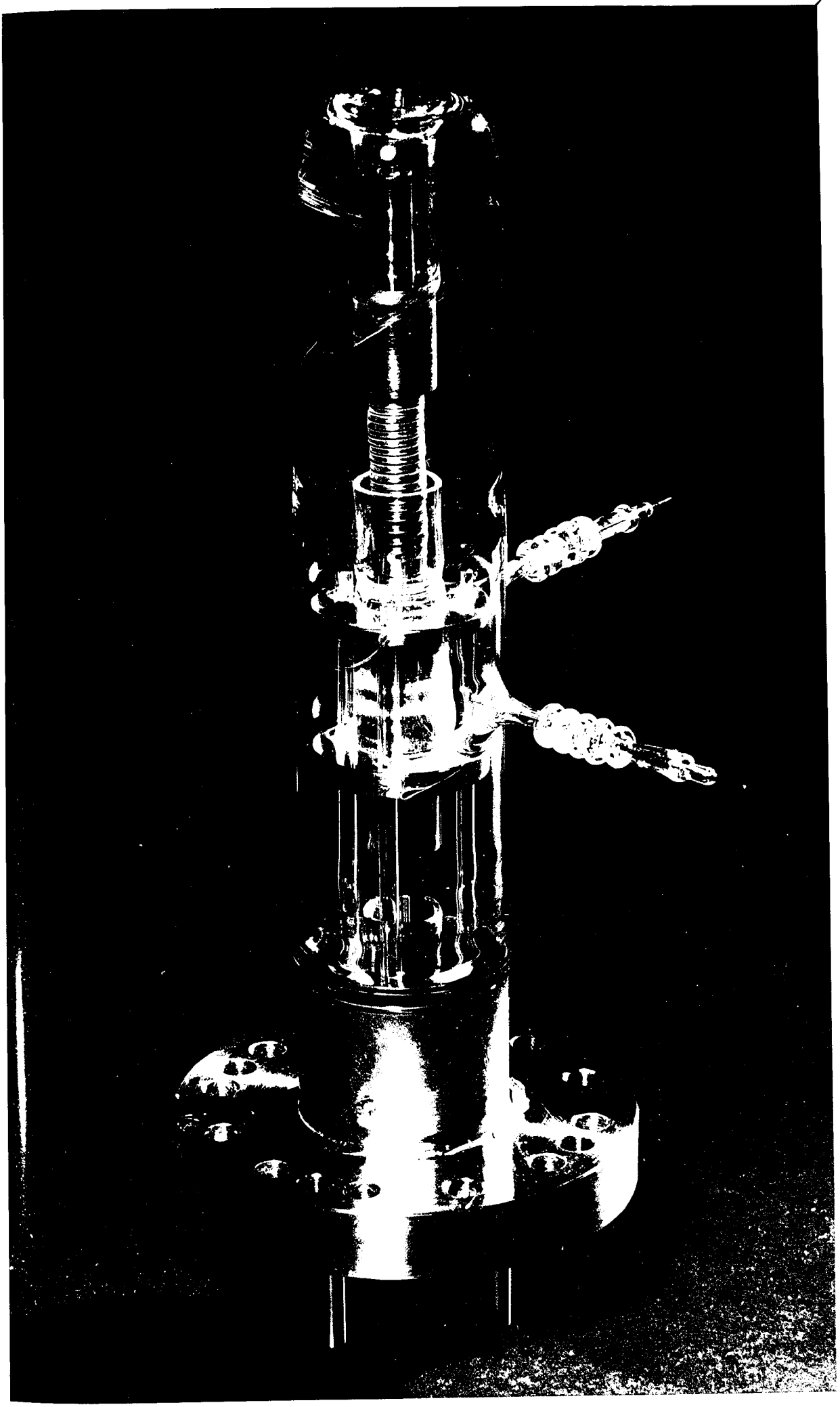

Figure 4·4

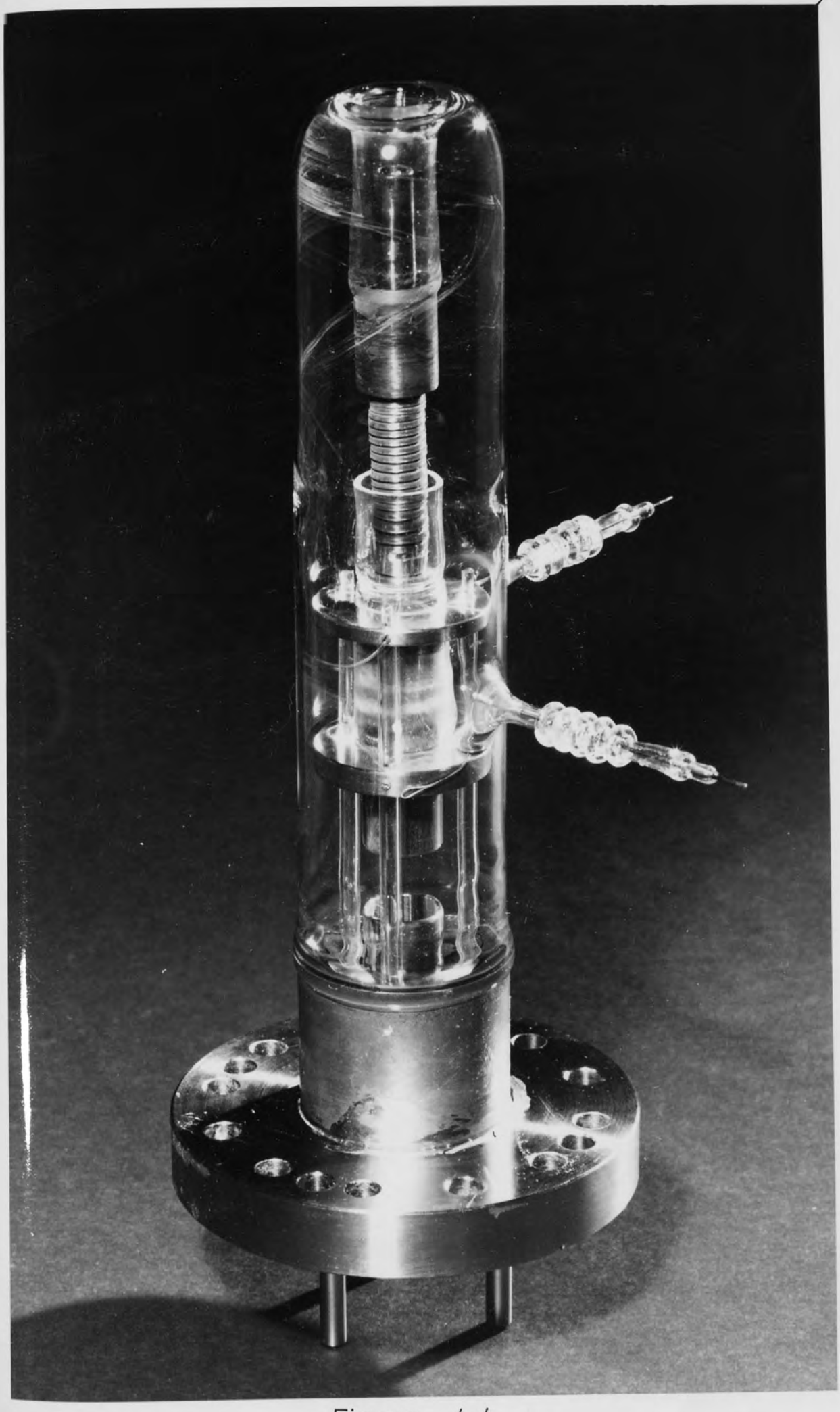

Figure 4·4

to be specially profiled and polished, such that its diameter can be made sufficiently small to minimise the wastage of powder and extend the life of a powder charge without the risk of blockage caused by particle aglomeration around the hole.

To understand the operating principle of this gun, consider the electrical circuitry in Fig.41. It is seen from this, that the back plunger electrode (P) is coupled to the charging electrode via a high voltage isolating capacitor arrangement. Hence when the microparticle gun is at "rest", the plunger and the charging electrode will be at the same potential, so that the powder in the reservoir is maintained in a field free region. To "fire" the gun a negative-going square voltage pulse (~8kV and 10-100ms long) is applied across the reservoir. This causes the microparticles to become charged by contact with the back metal face of the charging electrode assembly and hence explosively agitated by mutual repulsion. Some escape into the high field region where the combination of the gravitational and electric fields causes a few of them to impinge on the tip of the charging electrode and acquire a charge of the same polarity. As a result, they are acted upon by the approximately radial accelerating electric field existing between the tip and the radiused aperture, so that some can escape from the gun and are injected towards the subsequent experimental zones distributed within a narrow diverging axial pencil. The common charging/accelerating voltage shown as $V_2 - V_1$ in Fig.41, will subsequently be referred to as the gun voltage V_G.

The charge Q acquired by a microparticle during a glancing impact with the charging electrode will result from the quantum mechanical tunnelling mechanism of contact electrification (102).

Thus, although the magnitude of Q will be mainly determined by the particle dimensions and the locally enhanced electric field (E_T) at the tip of the charging electrode, it may also be influenced by the contact time, especially when insulating surface layers are present on one or both of the contacting surfaces.

If the charging electrode is represented by an idealised geometry in the form of a hemispherically capped cylinder of radius r in contact with the tip is given by(78),

$$Q = 2\pi^3 \frac{R^2}{R+r} E_T r^2 \quad \text{-------4·1.}$$

Thus, for $R \gg r$, and assuming $E_T \propto V_G$, it follows that

$$Q \propto V_G r^2 \quad \text{----------4·2}$$

for a given set of operating conditions, and explains the practical observation that larger particles acquire larger charges. This reasoning also explains the findings of several groups (75) (111), who have made unsuccessful attempts to operate the conventional gun design at lower accelerating voltages V_G with a view to obtaining a flux of lower velocity, single, micron-size particles; viz. that at these lower values of V_G(<8kV), only larger or aglomerated particles acquired sufficient charge ($\gtrsim 1 \times 10^{-15}$C) to be detectable.

This limitation was overcome in the present design by using a charging electrode whose geometry resulted in a greater field enhancement at its tip, so that an equivalent charging efficiency can be achieved at a lower gun voltage V_G. It was achieved in practice by replacing the conically-shaped conventional charging electrode (mechanically ground from a 1mm diameter tungsten rod to a tip radius of $\sim$50μm) by a cylindrically shaped carbon fibre of $\sim$7μm in diameter.

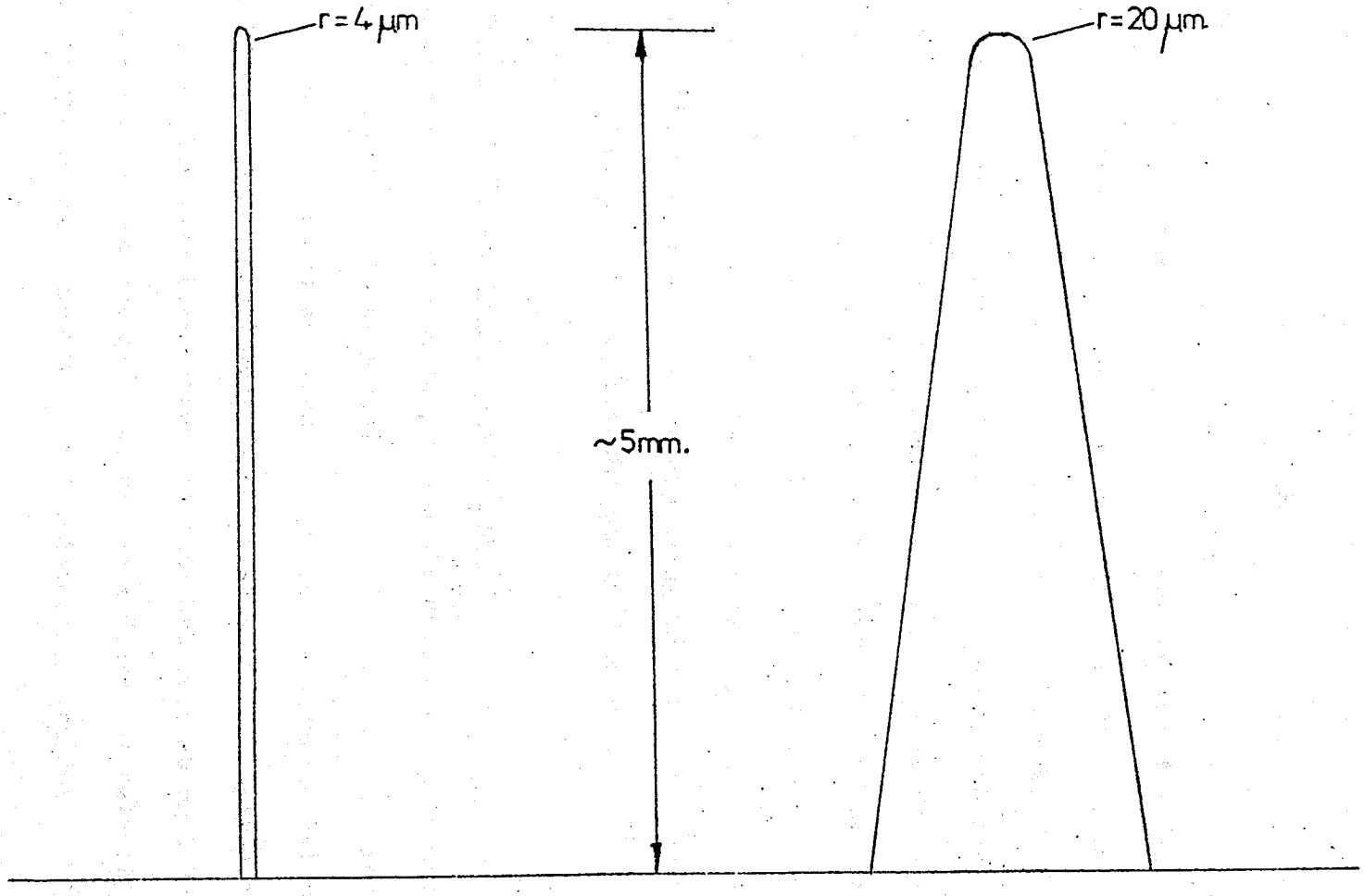

Figure 4-5

Thus comparing these alternative geometries, as represented diagramatically in Fig. 4.5, it can be shown from the computations of Rohrbach (63) and Vibrans (112) that the tip field enhancement has been increased by a factor of more than ten. The use of carbon as a charging electrode material has the additional advantage of being free of any electrically insulating oxide layers as are inevitably present on conventional metallic tips.

The simple comparison of field enhancement discussed above is not strictly true, since it has been found desireable to use a slightly splayed bunch of $\sim$10-15 fibres for the charging electrode. This of course involves some sacrifice of the gain in field enhancement, but is more than off-set by the advantages gained from a greatly increased particle charging probability. With this arrangement, it has been found that an adequate single particle charging efficiency can be achieved with $V_G \gtrsim 1kV$ compared with an equivalent operating threshold of $V_G \gtrsim 15kV$ in the conventional design. The corresponding reduction in the mean velocity of particles emerging from the gun is from $\sim 500\ m.s^{-1}$ to $\sim 10 ms^{-1}$

4.2.2 The Electrostatic Decelerating Element

This element was designed to perform the dual role of further reducing the particle velocities and, by its focusing action, increasing the flux of paraxial microparticles that reach the experimental zone. However, because it is effectively functioning as a wide apertured immersion lens, its associated spherical and chromatic aberration may be used to additional advantage in providing a degree of velocity selection at the entrance aperture of the detecting element.

Referring to Figure4.1, the decelerating element is in the form of a symmetric two-cylinder (C_1 and C_2) electrostatic lens that was constructed as an integral part of the gun using precision vitroesil rods to support and electrically insulate the constituent electrodes (also see Figure4.2). The lens parameters were based on the recent theoretical computations of Read et al. (114) such that the geometry of the cylinders was chosen to give a weak lens configuration, i.e. with their separation being set equal to their internal diameter, viz. 16mm. Thus, for the voltage ratio of~1 : 4.5, obtained by operating the gun with V_1 = + 550 volts V_2 = -1900 volts and V_3 = 0 Volts (see Fig.4.1), the lens element has a theoretical "paraxial" mid focal length of 65mm for particles entering it with an average velocity of $35ms^{-1}$ appropriate to the normal gun operating voltage of V_G= 2.5 kV (see later). Under these conditions, such a particle would be decelerated through~2 kV and brought to a focus in front of the 1.5mm diameter collimating aperture A_c at the entrance to the detecting element.

Although the focal length of an electrostatic lens is independent of the charge to mass ratio (Q/M) of the particles, it will however depend on the velocity with which they approach the lens. Hence, for the present application, where there is a considerable spread in the particle velocities emerging from the gun (arising from their differing Q/M), the lens will exhibit severe chromatic aberration with the lowest velocity particles being focussed nearest to the lens. However, by a suitable fine adjustment of the voltage ratio of the lens, this behaviour may be used to additional advantage in selecting a particular species of particle velocity to predominate in the beam transmitted by the collimating aperture A_c.

4.2.3 Deflecting Plates

A set of four deflecting plates, a pair of 'X' for horizontal and 'Y' for vertical displacement of the charged particles have also been incorporated in the microparticle facility to serve as a positioning element (see Fig. 4.1). These enable small adjustments to the particle trajectories, especially the vertical plates for gravity correcting of the very slow $< 5 ms^{-1}$ particles; making them move paraxialy so that they impact on the targets at normal incidence. This assembly is again a stainless steel/ceramtec, (UHV), construction consisting of four $1cm^2$ stainless steel plates with centrally welded 1mm diameter rods supports which are mounted in a mutually orthognal orientations into a ceramtec holder ring.

Considering the horizontal X-plates, the force (F_x) due to a uniform electric field (E_x) on a particle of mass m, charge Q_o and velocity u_1 moving across the plates is given by,

$$F_x = ma = E_x Q_o \qquad \text{-------} \qquad 4.3$$

and the time of flight $t = \frac{\ell}{u_1}$, where ℓ is the length of the plates. The resultant deflection of the particle then is,

$$\Delta x = \frac{1}{2}\left[\frac{E_x Q}{m}\right]\left[\frac{\ell^2}{u_1}\right] = \frac{E_x Q_o}{2m u_1^2} \qquad \text{-------} \qquad 4.4$$

For the case of vertical Y-plates, if a field E_y is applied between the plates and the acceleration due to gravity is g_o then the vertical deflection Δy within the length of the plates is given by

$$\Delta y = \frac{1}{2}\left[E_y \frac{Q_o}{m}\right] - \left[g_o\right]\left[\frac{\ell}{u_1}\right]^2 \qquad \text{------} \qquad 4.5$$

Therefore, to effectively correct for the downward deflection due to gravity, the field E_y is chosen so that the term $E_y \frac{Q_o}{m} \rightarrow g_o$, and $\Delta y \rightarrow 0$. It should however be mentioned, that

fields Ex and Ey between the x and y plates respectively are not strictly uniform because of 'end effects' i.e. due to finite lengths of the plates fringing is obtained at their ends. This causes the particles to be focussed (decelerated) at entry and defocussed (accelerated) at exit.

4.2.4 The micro-particle Charge and Velocity Detector

This is a time-of-flight device which directly measures the velocity (u) and charge (Q) of a particle. The particle mass (M) may then be indirectly determined from the energy conservation relation $\frac{1}{2}Mu^2 = QV_G$ and a knowledge of the accelerating voltage V_G. Although, this procedure also assumes a constant charge, e.g. that a particle suffers no in-flight charge losses, supporting experimental evidence will be presented to confirm the validity of this assumption. The device itself consists of a low capacitance electrostatically shielded, stainless steel drift tube (D) of known accurate length (50.00mm), mounted concentrically with the particle axis in a ceramtec insulator ring and directly connected to an external voltage-sensitive pre-amp via a glass to metal lead-through.

When a charged particle passes through the detector it induces an equal and opposite charge on the drift tube which is amplified and detected as a trapizoidal voltage-transient on a storage oscilloscope. The amplitude of this pulse is then directly proportional to the charge on the particle, and its length inversely proportional to the particle velocity. To sharpen the profile of these induced charge signals, the drift tube ends were faced by stainless steel grids having ~90% transparency to particles.

In order to achieve the maximum sensitivity for the voltage

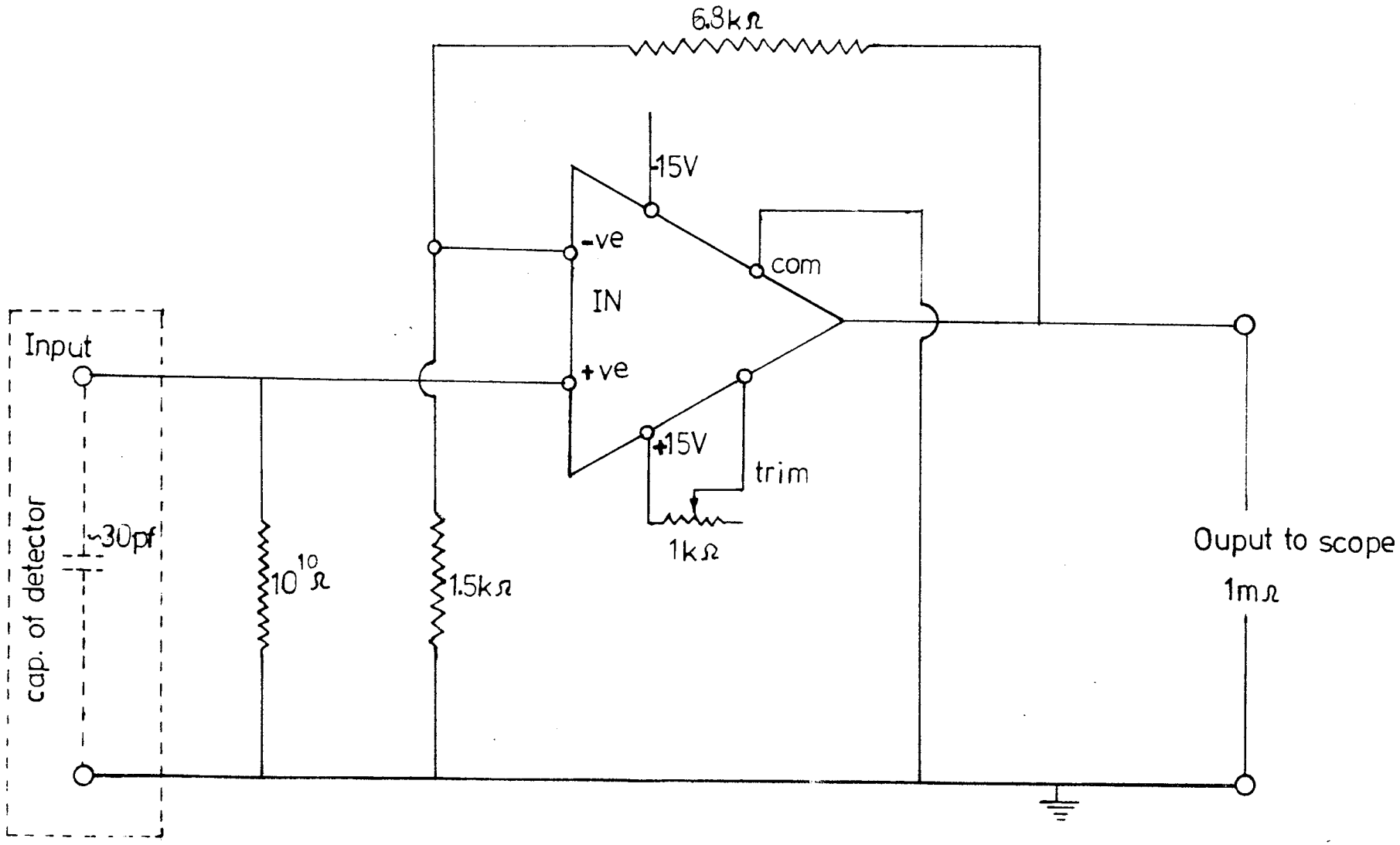

Figure 4.6 F.E.T. PREAMP.

sensitive pre-amplifier, it is essential to approach the following "ideal" design requirements: (i) It must have a low noise level. (ii) The effective input capacitance must be low as possible (i.e. to a few pF) in order to maximise the input voltage signal. (iii) A high input impedence is required to avoid excessive pulse differentiation (i.e. the input time constant must be large compared with the transit time of the microparticles through the drift tube). (iv) A wideband response is necessary, with a low frequency limit of $\sim$100Hz to cope with the transit times of the particles, and a high frequency limit of $>$ 5MHz to ensure that the rise and fall times of pulses are undistorted. (v) Finally, for efficient coupling of the pre-amp output signal to a suitable storage oscilloscope, its output impedance must match the input impedance requirements of the oscilloscope.

Such an amplifier was first demonstrated by Hansen (185) using discrete components, with maximum charge sensitivity of 1.0×10^{-15}. However, with the present day availability of integrated circuits it has been possible to make a simple low cost voltage-sensitive device using a commercially available F.E.T. input differential OP-AMP. This has a low noise (2mV noise voltage), high speed (minimum slew rate 75 v/ sec), a wideband response (unity gain bandwidth of 10MHz) with high input impedence ($> 10^{11}$ ohms) and low input capacitance (3pF). As an additional precaution it was constructed using low noise, high stability auxillary components in a simple non-inverting configuration (see figure 4.6). This arrangement gave a calibrated gain of $\sim$200, with an output noise corresponding to an improved charge detectability of $\leq 1 \times 10^{-16}$ Coulombs.

4.2.5 The High-Field Target Assembly

As explained previously, this microparticle gun facility was set up to investigate the electrical and mechanical aspects of low-velocity microparticle impact at normal incidence in a plane-parallel high voltage gap. It was therefore necessary to design a uniform field test gap that closely approximated to the real situation and which would allow the injection of low velocity microparticles. Referring to Fig. 4.1, this was achieved by using a 10mm and 15mm diameter Harrison-profiled (183) targets (T) (see section 333)in conjunction with an extended - area stainless steel grid, where the gap spacing was externally adjustable. By using a very fine stainless steel grid with a 0.5mm mesh of 0.015mm diameter wire, it was possible to achieve a transparency of 90% for the incident particles.

To determine the electric field distribution when a grid instead of a plane electrode is used opposite another plane electrode in a high-field gap. Consider first, the case of an array of parallel wires lying in a plane, the wires are infinitely long and equally spaced. Figure 4.7 schematically shows the equipotentials at various distances from such a grid (112). The electric field at large distances above the plane of wires is seen to be constant, just as though the charge were spread over a plane. However, at closer distances the field begins to deviate from uniform field, fluctuating in a periodic manner.

Now, any periodic quantity can be expressed in terms of Fourier series. For a grid lying in the xy plane with its wires along the y-direction (see figure 4.7), the potential is given by,

$$\phi(xz) = F_n(z) \cos \frac{2\pi n x}{a} \quad \text{-------- 4.6}$$

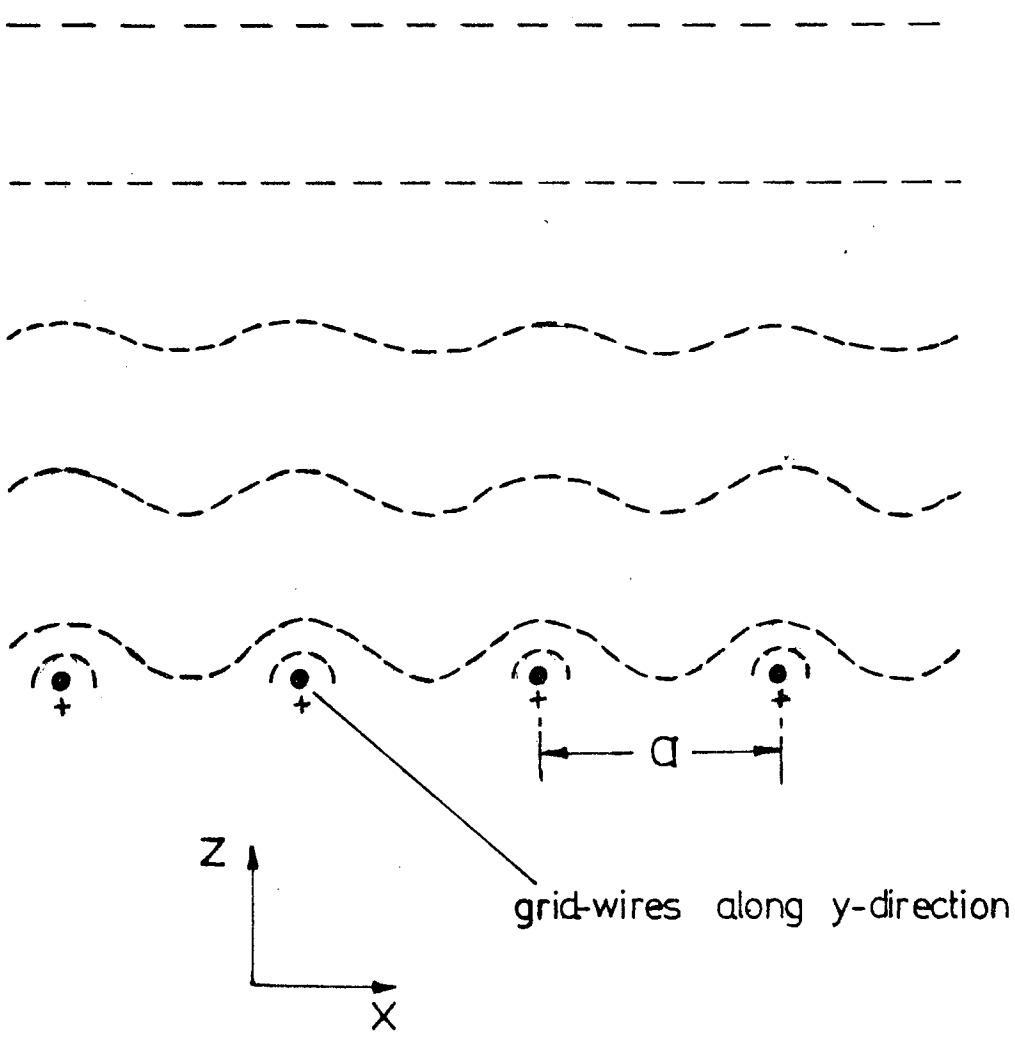

Figure 4·7

where (a) is the spacing of the wires and n(= 1,2,3.....) is the harmonic number. There should be no variation with y, since long wires in y-direction have been assumed.

If equation (4.6) is to be a valid potential, it must satisfy Laplace's equation in the region above the wire, where there are no charges. That is,

$$\frac{\partial^2 \phi}{\partial x^2} + \frac{\partial^2 \phi}{\partial z^2} = 0 \qquad \text{----------} \qquad 4.7$$

substituting for ϕ from eq (1), gives,

$$- \frac{4\pi^2 n^2}{a^2} Fn(Z) \cos \frac{2\pi nx}{a} + \frac{d^2 Fn}{dz^2} \cos \frac{2\pi nx}{a} = 0 \text{ --- } 4.8$$

or that Fn (z) must satisfy,

$$\frac{d^2 Fn}{dz^2} = \frac{4\pi^2 n^2}{a^2} Fn \qquad \text{---------} \qquad 4.9$$

Solutions for equation 4.9 are of the form,

$$Fn = \dot{A}_n e^{-z/z_o} \qquad \text{----------} \qquad 4.10$$

where,

$$Z_o = \frac{a}{2\pi n} \qquad \text{----------} \qquad 4.11$$

It can be clearly seen that, any Fourier components of field will decrease exponentially with the characteristic distance $z_o = \frac{a}{2\pi n}$. For the first harmonic n=1, the amplitude falls by the factor $e^{-2\pi}$, a large decrease, each time z is increased by spacing a . The other harmonics fall off even more rapidly. With the result that only at a few times the distance a_1, away from the grid, the field is very nearly uniform, i.e. the oscillating terms becoming negligible. There would, of course, always remain 'zero harmonics' field $E_o = \frac{\phi o}{z}$ to give a uniform field at large z.

Now for the case of a grid consisting of a fine mesh of x

d y wires, of the type used in the present experiments, it can reasonably assumed that the field distributions would be similarly not more uniform compared to the above arrangement of a single ray of x or y wires; since in this case there is a general increase the density of wires, approximating more of a plane electrode. So hat, when a plane electrode is placed at a distance where the quipotentials have sufficiently smoothed out, it will see a uniform harge distribution just as though it was facing another plane electrode hus, providing a grid/plane gap that can faithfully simulate a igh-field gap between two plane electrodes. For the present arrangement it can be seen from field plots in figure 4.7 , that were alculated using equation 4.10, that a uniform and well defined field n the $\backsim 5mm^2$ paraxial test region will be ensured, provided the nterelectrode separation are chosen to be $\gtrsim$ 2mm.

and y wires, of the type used in the present experiments, it can be reasonably assumed that the field distributions would be similarly if not more uniform compared to the above arrangement of a single array of x or y wires; since in this case there is a general increase in the density of wires, approximating more of a plane electrode. So that, when a plane electrode is placed at a distance where the equipotentials have sufficiently smoothed out, it will see a uniform charge distribution just as though it was facing another plane electrode Thus, providing a grid/plane gap that can faithfully simulate a high-field gap between two plane electrodes. For the present arrangement it can be seen from field plots in figure 4.7 , that were calculated using equation 4.10, that a uniform and well defined field in the $\backsim 5mm^2$ paraxial test region will be ensured, provided the interelectrode separation are chosen to be $\gtrsim$ 2mm.

nd y wires, of the type used in the present experiments, it can
e reasonably assumed that the field distributions would be similarly
f not more uniform compared to the above arrangement of a single
rray of x or y wires; since in this case there is a general increase
n the density of wires, approximating more of a plane electrode. So
hat, when a plane electrode is placed at a distance where the
quipotentials have sufficiently smoothed out, it will see a uniform
harge distribution just as though it was facing another plane electrode
hus, providing a grid/plane gap that can faithfully simulate a
igh-field gap between two plane electrodes. For the present arrange-
ent it can be seen from field plots in figure 4.7 , that were
alculated using equation 4.10, that a uniform and well defined field
n the $\backsim$ 5mm^2 paraxial test region will be ensured, provided the
nterelectrode separation are chosen to be $\geq$ 2mm.

nd y wires, of the type used in the pr
e reasonably assumed that the field dis
f not more uniform compared to the abo
rray of x or y wires; since in this ca
n the density of wires, approximating
hat, when a plane electrode is placed a
quipotentials have sufficiently smooth
harge distribution just as though it w
Thus, providing a grid/plane gap that c
igh-field gap between two plane electr
ment it can be seen from field plots in
calculated using equation 4.10, that a
in the $\sim 5mm^2$ paraxial test region will
interelectrode separation are chosen to

and y wires, of the type used in the present experiments, it can be reasonably assumed that the field distributions would be similarly if not more uniform compared to the above arrangement of a single array of x or y wires; since in this case there is a general increase in the density of wires, approximating more of a plane electrode. So that, when a plane electrode is placed at a distance where the equipotentials have sufficiently smoothed out, it will see a uniform charge distribution just as though it was facing another plane electrode Thus, providing a grid/plane gap that can faithfully simulate a high-field gap between two plane electrodes. For the present arrangement it can be seen from field plots in figure 4.7 , that were calculated using equation 4.10, that a uniform and well defined field in the $\backsim 5mm^2$ paraxial test region will be ensured, provided the interelectrode separation are chosen to be $\gtrsim$ 2mm.

and y wires, of the type used in the present experiments, it can be reasonably assumed that the field distributions would be similarly if not more uniform compared to the above arrangement of a single array of x or y wires; since in this case there is a general increase in the density of wires, approximating more of a plane electrode. So that, when a plane electrode is placed at a distance where the equipotentials have sufficiently smoothed out, it will see a uniform charge distribution just as though it was facing another plane electrode Thus, providing a grid/plane gap that can faithfully simulate a high-field gap between two plane electrodes. For the present arrangement it can be seen from field plots in figure 4.7 , that were calculated using equation 4.10, that a uniform and well defined field in the $\backsim$ 5mm^2 paraxial test region will be ensured, provided the interelectrode separation are chosen to be $\geq$ 2mm.

4.3 OBSERVATIONS

This section is principly concerned with the performance of the microparticle gun but also briefly surveys the types of microparticle impact phenomena that can occur at normal incidence in a high field gap.

4.3.1 The performance characteristics of the microparticle source

Depending on the polarity of V_2 and V_1 (see Fig. 4.1) it is possible to generate positive or negative particles as shown in Fig. 4.11 . However, owing to electron field emission from the carbon fibres, the negative function is intrinsically unstable. In fact there is an upper limit to the operating voltage $(V_2 - V_1)$ of 1.8KV beyond which the field emission currents become excessive and rapidly destroy the fibres. Accordingly, the gun is normally used to generate positively charged particles, and it is the operational characteristics of this function that are reported here.

There is also a choice of operating the gun facility in a fast or slow mode. Referring to Fig. 4.1, the fast mode corresponds to that used in the conventional design where $V_2 = V_3 = 0$ (earthed) so that the electrostatic lens is not employed. For the slow mode, V_1 and V_2 are independently adjusted to obtain the required values for the gun voltage $(V_G = V_1 - V_2)$ and the voltage ratio of the lens $\frac{V_1}{V_G}$.

Although, as stated previously, the gun can be operated with $V_G \ll 1kV$ if the slowest possible particles are required, it has been found more suitable for most investigations to set $V_G \cong 2.5kV$ in order to obtain a greater particle flux. To satisfy this requirement for the slow mode, whilst maintaining the lens voltage ratio of 1 : 4.5 necessary for focussing the particle

flux, the electrode voltages were adjusted to V_1 = + 600V V_2 = -1900V and V_3 = 0, corresponding to an effective particle accelerating potential of 600 V volts.

The operating characteristics of these modes are presented in terms of the distributions of velocity (u) and charge (Q) among samples of 200 consecutive paraxial particles that enter the detecting drift tube from the collimating aperture A_c. In order to isolate the influence of the electrostatic decelerating lens, the operating characteristics of the two modes have been compared using an identical gun voltage of V_G = 2.5kV, so that it may be assumed that the basic charging element is delivering an identical particle flux in each case.

Figure 4.10a shows a typical example of the single particle trapezoidal pulses from which the overall gun performance characteristics have been compiled. These signals are initially recorded on a Hewlett-Packard 180A storage oscilloscope, and subsequently photographed on a polaroid plate for presentation purposes. The charges are obtained directly from the height of the pulses and the sensitivity of the pre-amplifier, whilst the velocities are determined from the length of the pulses and detector drift tube. For the example shown, which was obtained with the gun operating in the slow mode, the particle charge and velocity are $\backsim 2.5 \times 10^{-15}$C and $\backsim 10 ms^{-1}$ respectively.

The above type of measurement has been used to compile the histograms of figures 4.8 and 4.9, which compare respectively the general character of the velocity and charge distribution for the two operating modes. Figure 4.8, clearly illustrates the decelerating action of the lens, where the mean particle velocity (u) has been reduced from $35 ms^{-1}$ to $12 ms^{-1}$; its velocity selectivity is demonstrated both by the greater


- Conventional Mode
- Slow Mode
N(u1)
60
50
40
30
20
10
0
10
20
30
40
50
60
70
80
90
100
110
120
u1 (V m-1)

Figure 4.8

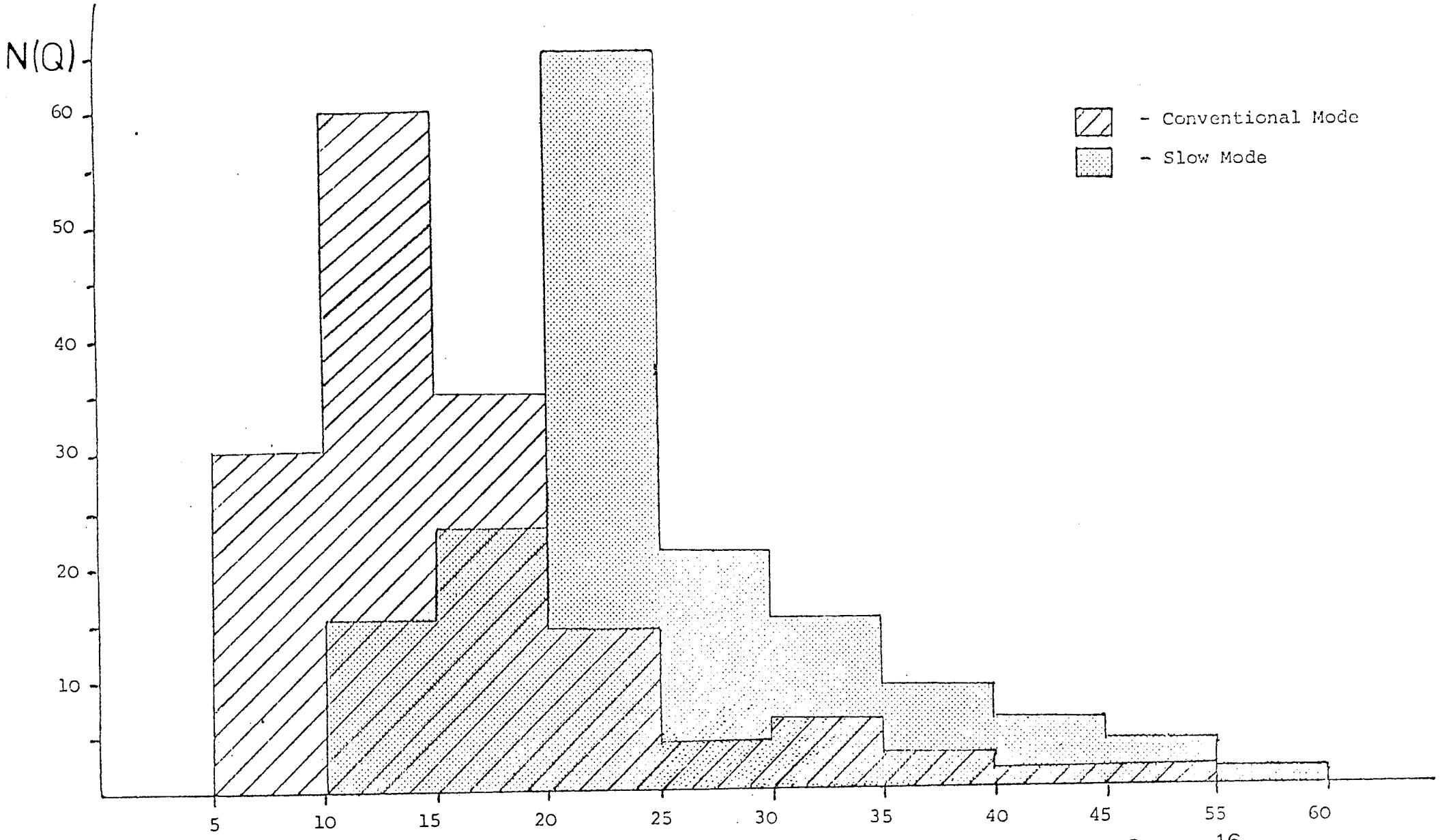
N(Q)
60
50
40
30
20
10
5
10
15
20
25
30
35
40
45
55
60
Q(×10^-16)
- Conventional Mode
- Slow Mode

Figure 4.9

symmetry of the slow mode distribution and the reduced spread of particle velocities, viz. from $\sim$110ms^{-1} to $\sim$20ms^{-1}. The corresponding accelerating voltage for calculating the Q/M ratios of particles are 2.5kV and 600V respectively for the fast and slow modes.

Figure 4.9, illustrates another important consequence of the velocity selecting action of the lens, whereby it is possible to have some control over the charge distribution among the transmitted particles: in the example shown, the mean charge $\bar{Q}$ has been doubled. This will however also be associated with a corresponding mass selection, since, as explained earlier, the effect arises from the gun. Depending upon which velocity species is selected from the conventional mode velocity distribution (Figure 4.8), it is possible to obtain either an increase or decrease in the average mass of the transmitted particles. The example of Figure 49 corresponds to a sample selected from the high velocity part of the distribution, so that doubling of Q is accompanied by a decrease in the mean particle mass. If a low particle flux is acceptable, the lens can be adjusted to select a velocity from the extreme of the distribution which could correspond to a four-fold increase of $\bar{Q}$.

The focussing action of the lens in the slow-mode operation has the further practical advantage of increasing the flux of paraxial particles entering the detector. Thus, whereas about five agitations of the powder reservoir are typically required for each detected particle with the conventional mode, that obtained with the slow mode is generally much lower, and can approach one particle for each agitating pulse.

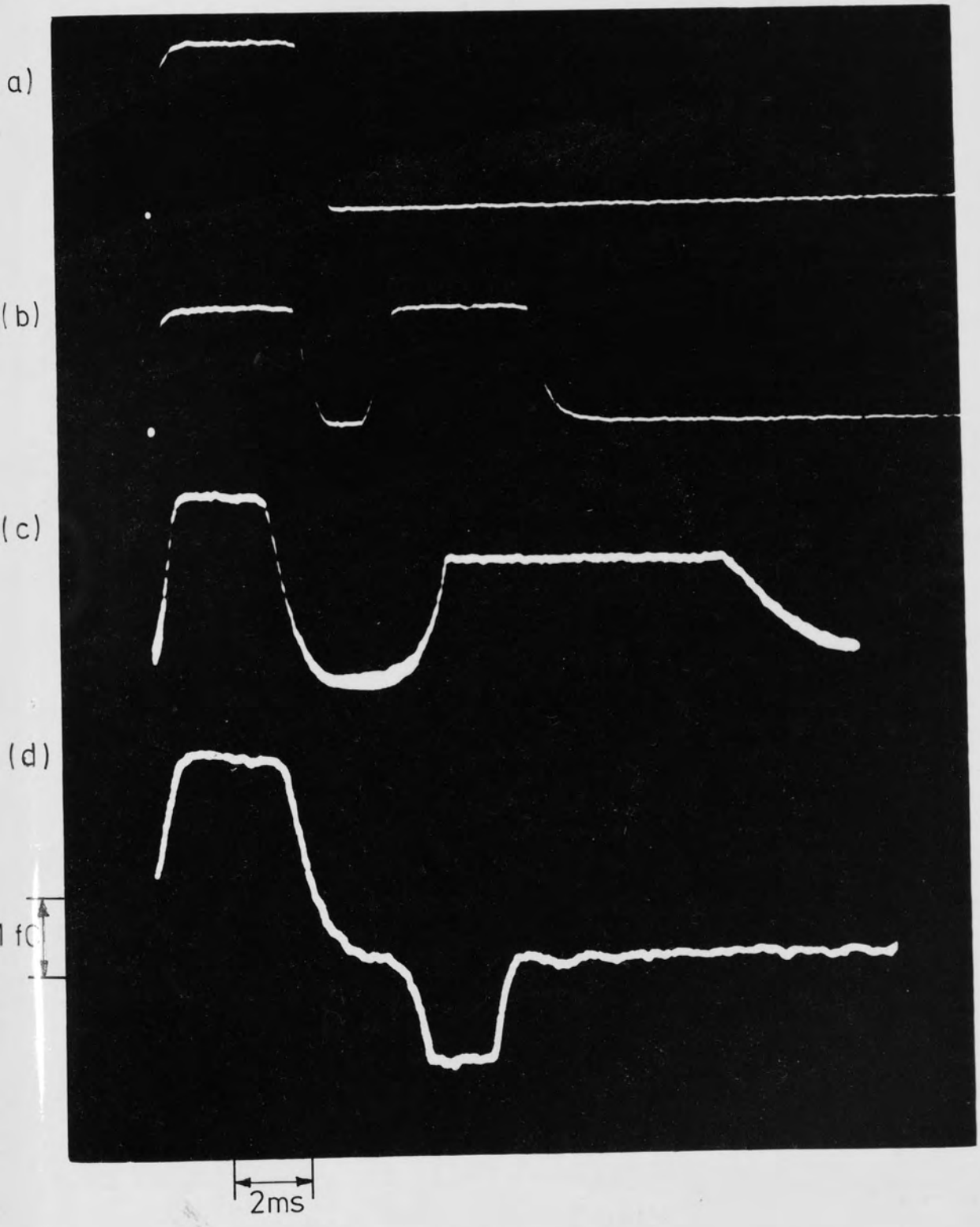

Figure 4·10

4.3.2 Microparticle 'reflection' phenomena at normal incidence

Depending on the target potential (V_T) relative to that of the charging electrode (V_1), three types of particle 'reflection' events can occur. They are observed for both positively and negatively charged particles, but as stated previously, only the observations with positive particles are reported.

(a) For $(V_T) > (V_1)$, a particle will be repelled by the target and brought to rest before impact. Consequently, there will be complete in-flight momentum reversal with conservation of charges as shown in Figure 4.10(b). The fact that one must always have $(V_T) \geq (V_1)$ to observe this type of event, is an experimental verification of the important assumption that particles suffer no significant in-flight loss of charge. It is evident that if this were not the case, momentum reversal would be expected to occur with $(V_T) < (V_1)$.

(b) For $0 < (V_T) < (V_1)$, the surface charge on the target still has the same sign as that on the incident particle, but impact with the target will occur. Under these circumstances, some degree of mementum reversal and charge modification (no change of sign) would be expected. An example of this type of event is shown in Figure 4.10(c) where the reflected particle has both a lower charge and velocity.

(c) For $(V) \leq 0$, the particle will be attracted to the target, the impact will occur following its acceleration across the gap. Since the target is negatively charged, there is the additional possibility in this case of the charge on the particle being reversed during impact, so that it will be further accelerated back across the gap. Figure -

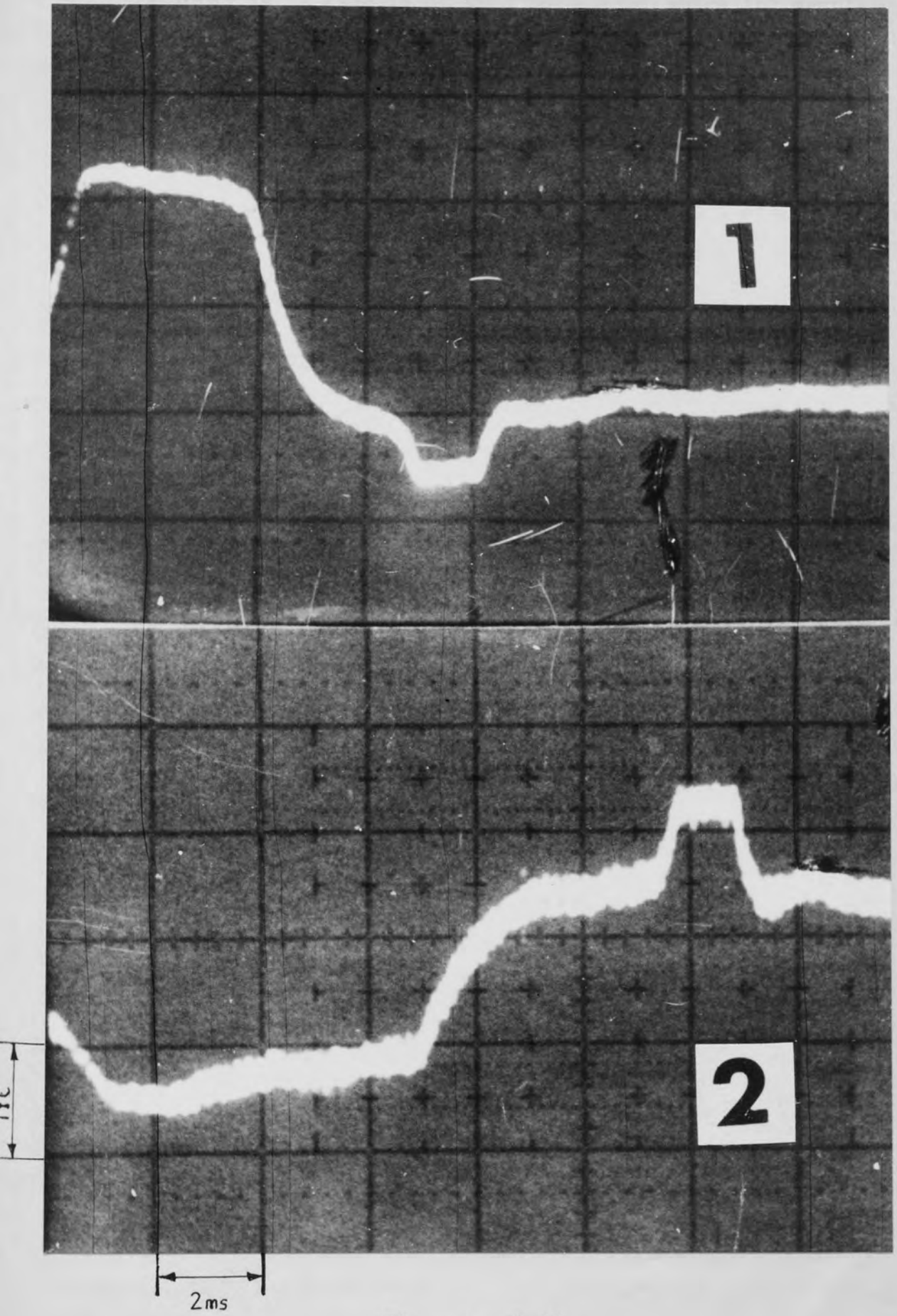

Figure 4·11

4.10(d) is an example of this phenomenon, where the magnitude of the charge on the particle has been reduced as a result of its bouncing impact with the target, although its final reversed velocity on leaving the test gap is greater than when initially entering it. Figure 4.11, traces 1 and 2, further show that this charge reversal phenomenon is equally possible with both positively and negatively charged initial particles impacting on negatively and positively biased targets respectively.

As explained previously, the physical aspects of microparticle impact are important for the problem of high voltage vacuum insulation, and the detailed observations from its study are presented in Chapter 5. Of particular significance in this investigation is the role of the target surface layers in controlling the efficiency of charge reversal during a bouncing impact.

CHAPTER V

RESULTS AND DISCUSSION

5.1 Introduction

As outlined in Chapter 3, a similar experimental procedure was followed for each target material or surface state studied. In this, $\sim$50 to 200 consecutive bouncing events were recorded, each represented by a twin trapezoidal pulse (see figure 3.1) for a given species of particle i.e. micron-submicron sized, positively charged, q_1 ($\sim$1 - 6fC) and u_1 ($\sim$1 - 500ms^{-1}). These sets of measurements were later digitized for computer analysis in terms of the ratio of initial to reversed charge $\bar{q}$, the impact velocity v_1, the rebound velocity u_2 and the coefficient of restitution e.

Using this technique, up to six different materials viz. copper, stainless-steel, titanium, lead, carbon and mica, representing a wide range of electrical and mechanical properties have been studied. This list is by no means exhaustive and is limited almost entirely by the time available to try different materials.

Since there is a general similarity in the character of the processed data for each target, only that belonging to copper and stainless-steel will be discussed in detail. These materials have been selected for representing both extremes of electrical stability (see section 1.1.2) and mechanical hardness, when used as high voltage electrodes. However, the data from other targets will also be included in averaged form for comparison of their respective electric and elastic properties and with any unusual or interesting behaviour by the targets being fully described.

5.2 Impact Results - Mechanical

Figures 5.1a and 5.1b illustrate respectively, the distributions of individual impact events from copper and stainless-steel targets in

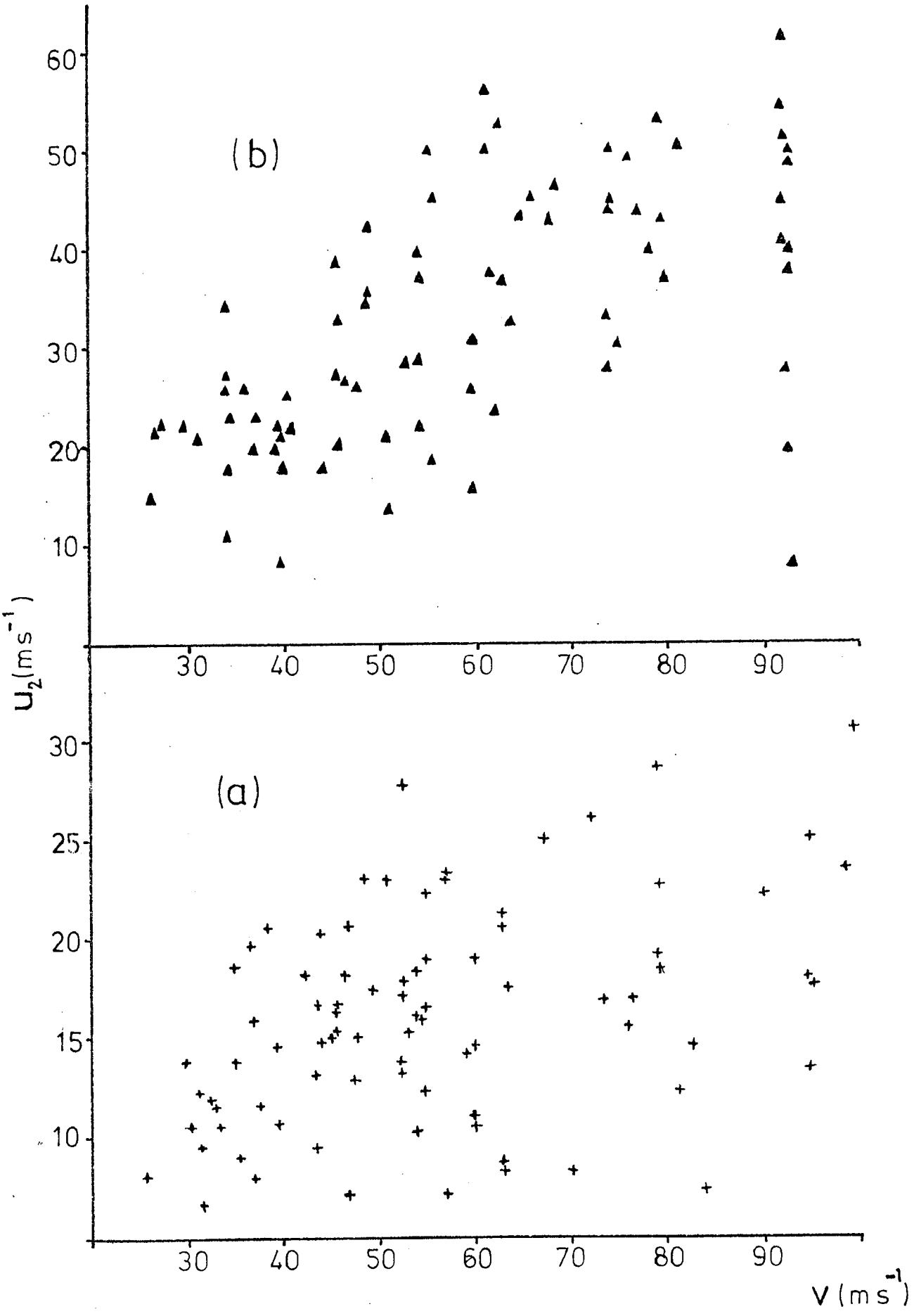

Figure 5.1

terms of the impact velocity v_1 and the rebound velocity v_2. In both cases, the impact data is seen to increase in scatter with increasing v_1. On replotting these data in the form of 'centroid' plots, in terms of the rebound to incident velocity ratio $\frac{u_2}{v_1}$ (=e, the coefficient of restitution) verses v_1, as illustrated in figure 5.2(a) and 5.2(b), respectively, it is seen that there is a general trend of e - decreasing with v_1 for both the metals, but this behaviour is accompanied by an increase in the uncertainty of e with increasing v_1. It can further be seen that e decreases with v_1 at a slightly higher rate for the copper than with the stainless-steel target.

Figures 5.3(a) and 5.3(b) show the histograms of the respective population distribution of the restitution measurements for the copper and stainless-steel targets. On comparison of the symmetry of these distributions and of the curves on figures 5.2a and 5.2b it is clearly seen that there is a marked difference in behaviour of these two metals: whereas stainless-steel shows widely ranging population distribution throughout range of e-values 0.1 - 1, copper is seen to exhibit a sharp cut-off for e-values greater than 0.5 .

The mean elastic data for <u>different surface conditions</u> obtained from the respective copper and stainless-steel targets is compared in figures 5.4 - 5.5, in terms of the coefficient of restitution-e verses the impact velocity (v). In each case, characteristics are given for target surfaces that are atomically clean (curve a), ambient oxidised (curve b) and excessively oxidised (curve c). Significant differences in the responses of different surface conditions can be clearly seen; the heavily oxidised surfaces promoting elastic impacts with higher e-values than the other two surface conditions and the atomically clean exhibiting the lowest e-values. This is not an entirely unexpected result (see later) since it is

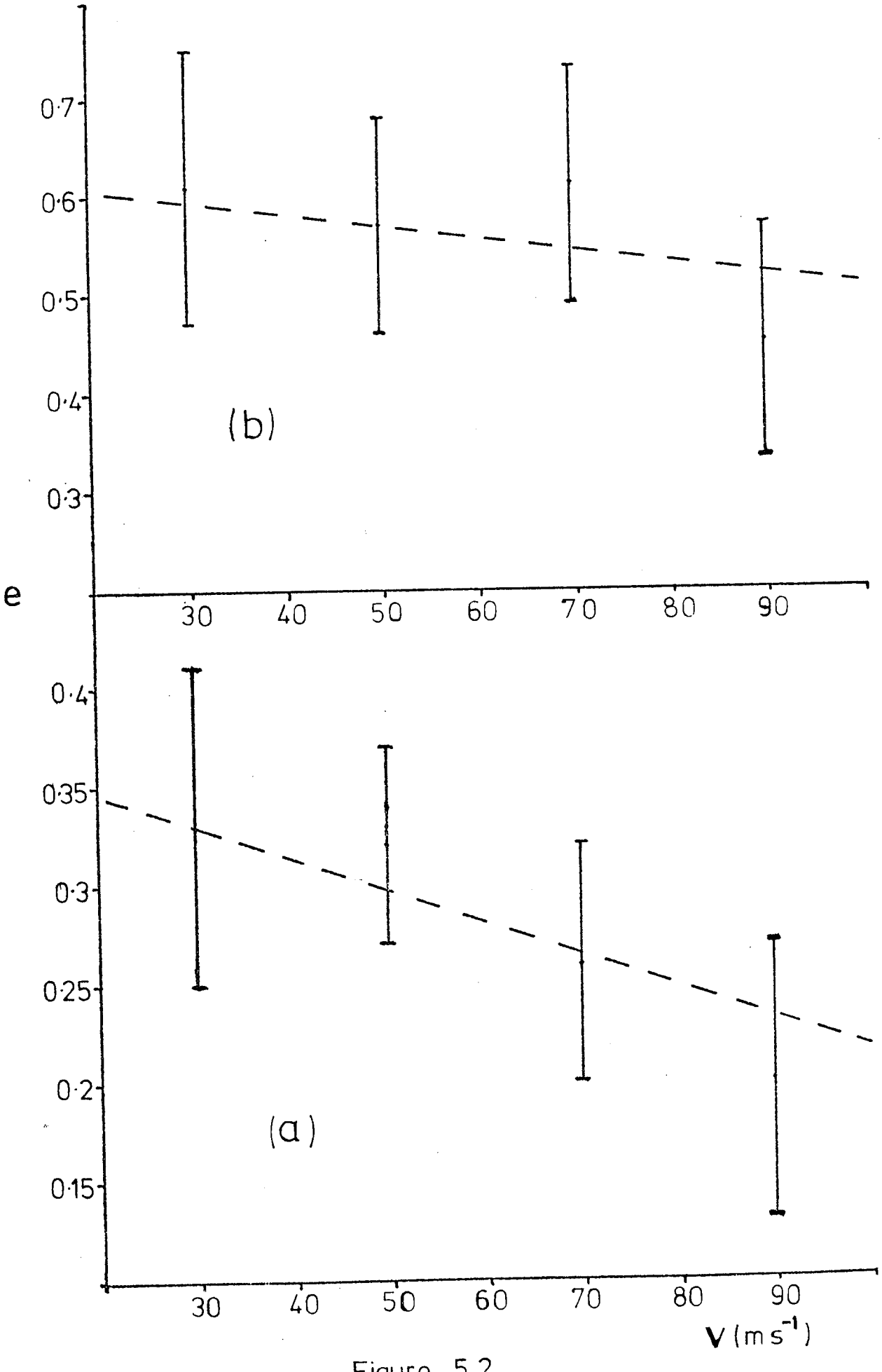
e
0·7
0·6
0·5
0·4
0·3
(b)
30
40
50
60
70
80
90
0·4
0·35
0·3
0·25
0·2
0·15
(a)
30
40
50
60
70
80
90
V (m s⁻¹)

Figure 5.2

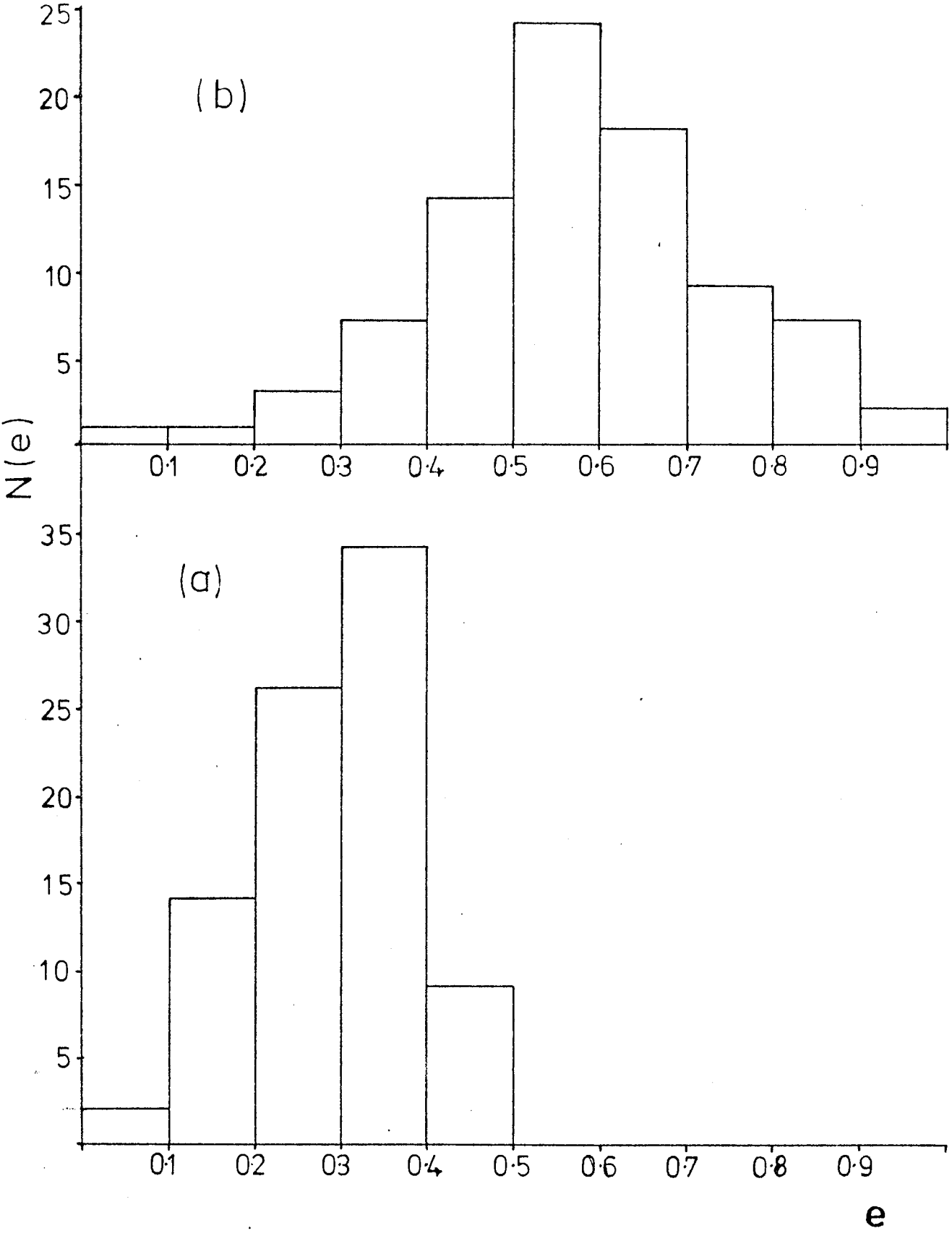
(b)
25
20
15
10
5
0·1
0·2
0·3
0·4
0·5
0·6
0·7
0·8
0·9
N(e)
(a)
35
30
25
20
15
10
5
0·1
0·2
0·3
0·4
0·5
0·6
0·7
0·8
0·9
e

Figure 5·3

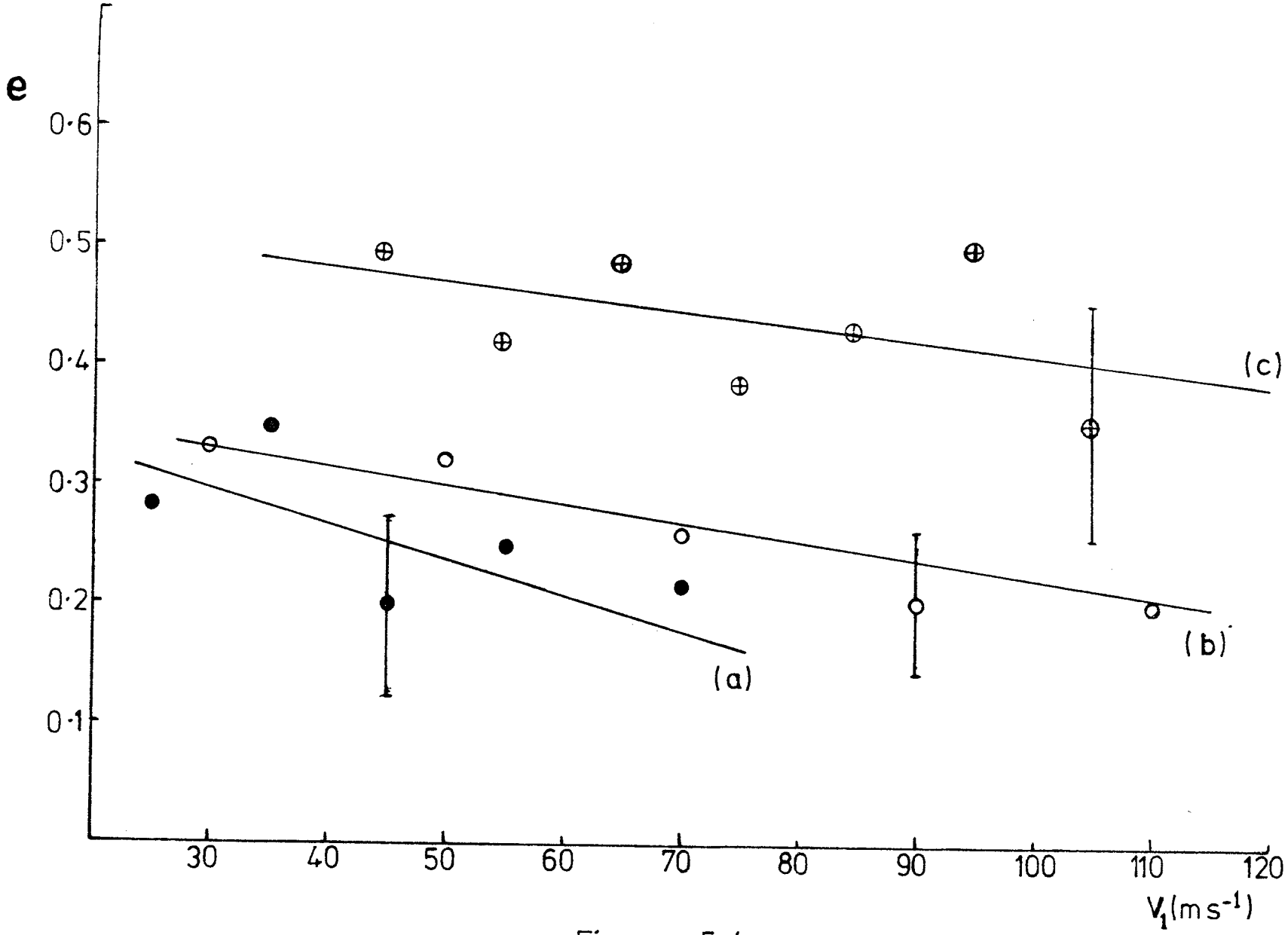

Figure 5·4

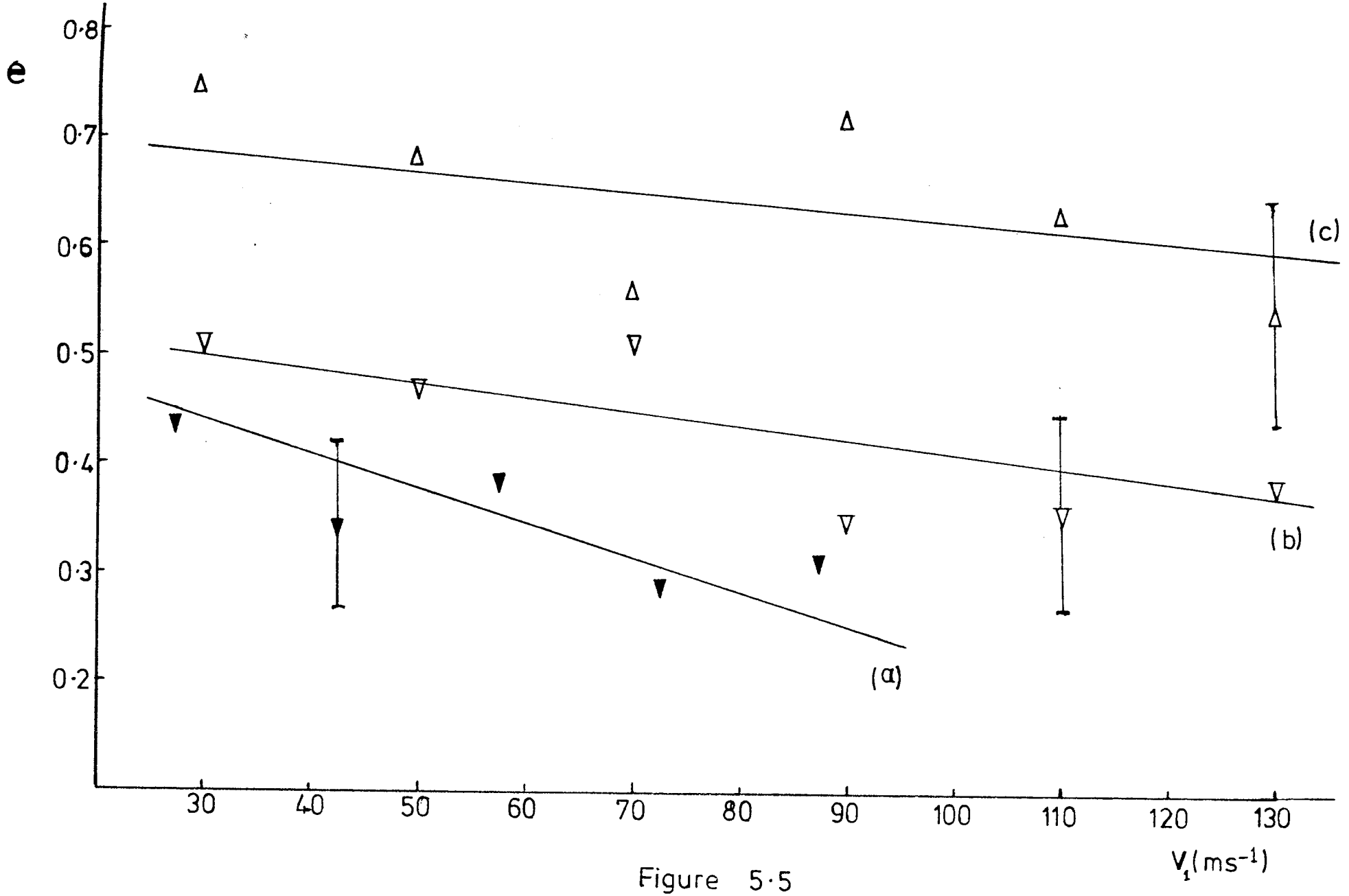

Figure 5·5

well known that metal oxides generally exhibit much harder surfaces than their respective bare metal substrates. Accordingly, such surfaces are likely to promote elastic reflections with higher coefficients of restitution. For instance, in experiments where copper and stainless-steel targets were faced with (5-50μm) mica films, a relatively hard material, rebounds with e-values almost approaching ($\backsim$ 1) were obtained, whereas in the case of atomically clean surfaces the lower e-value obtained can be attributed to annealing and absence of hard surface films.

To compare the elastic behaviour of all the target materials studied their mean e-values (as calculated from all impact events occurring within the velocity range 20-100 ms^{-1}) have firstly been plotted in figure 5.6 as a function of the 'hardness value' of each material as measured directly on the Vickers Scale, where the error bars associated with each point represent the variation of e over this velocity range; i.e. as determined from the linear plots of figure 5.2. In the second comparative plot of figure 5.7, the same e-values have been plotted as a function of the density of the target material. The physical significance of the linearity of these last two plots will be considered in the discussion section of this chapter.

Figures 5.8, micrographs a, b, and c illustrate various surface conditions of a copper target used for impact studies. They show the geometrical relation between an isolated microsphere of diameter .5μm and the typical microtopography of a diamond polished target surface which is characterised by a random mesh of scratch grooves, clusters of modular structures and deep pore-like holes: these latter features, which might be confused with indentation craters, are present on freshly polished surfaces (see figure 5.8b). In addition, the first micrograph (figure 5.8a) is of particular interest, since it

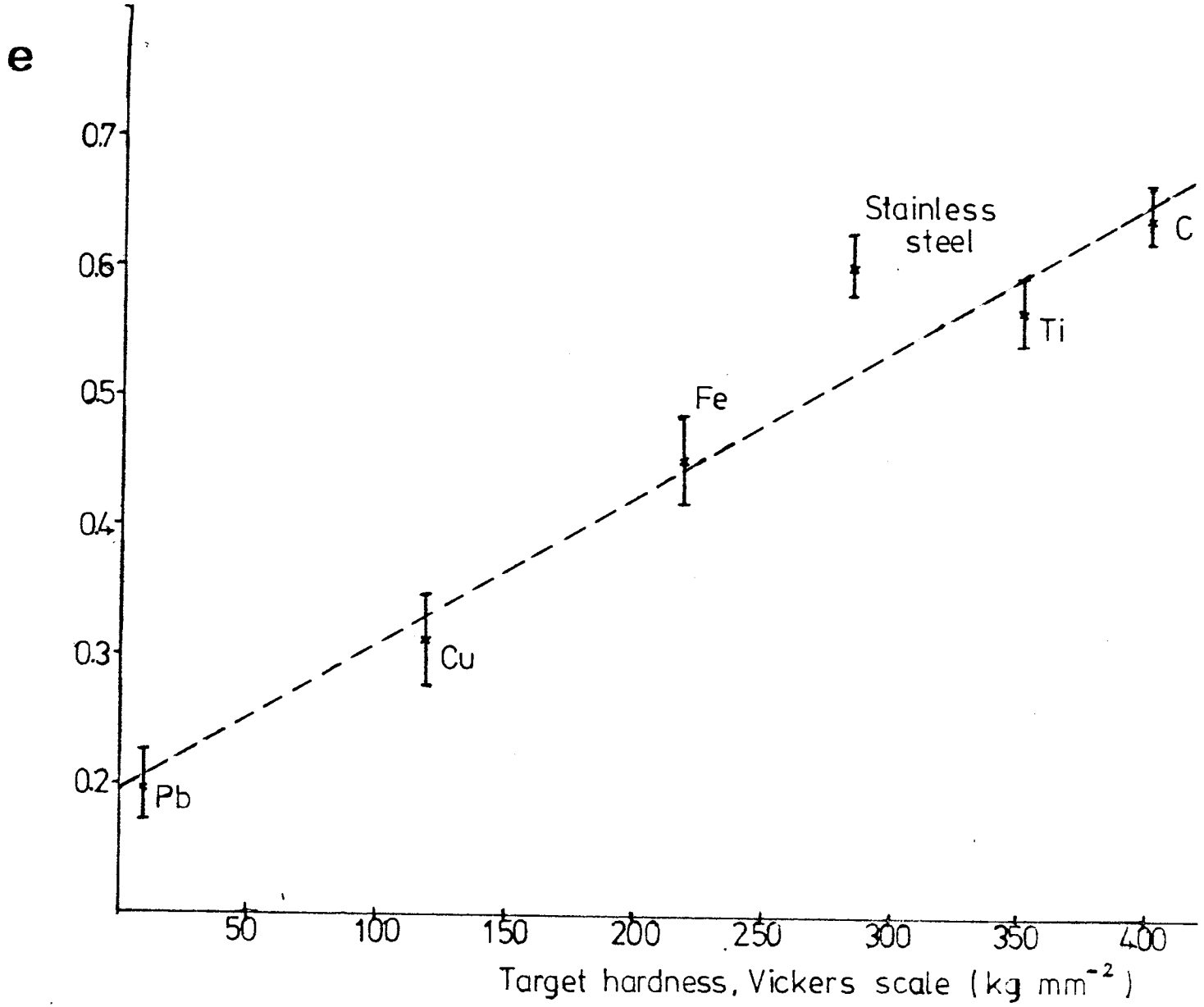
e
0.7
0.6
0.5
0.4
0.3
0.2
Stainless steel
C
Ti
Fe
Cu
Pb
50
100
150
200
250
300
350
400
Target hardness, Vickers scale (kg mm^{-2})

Figure 5.6

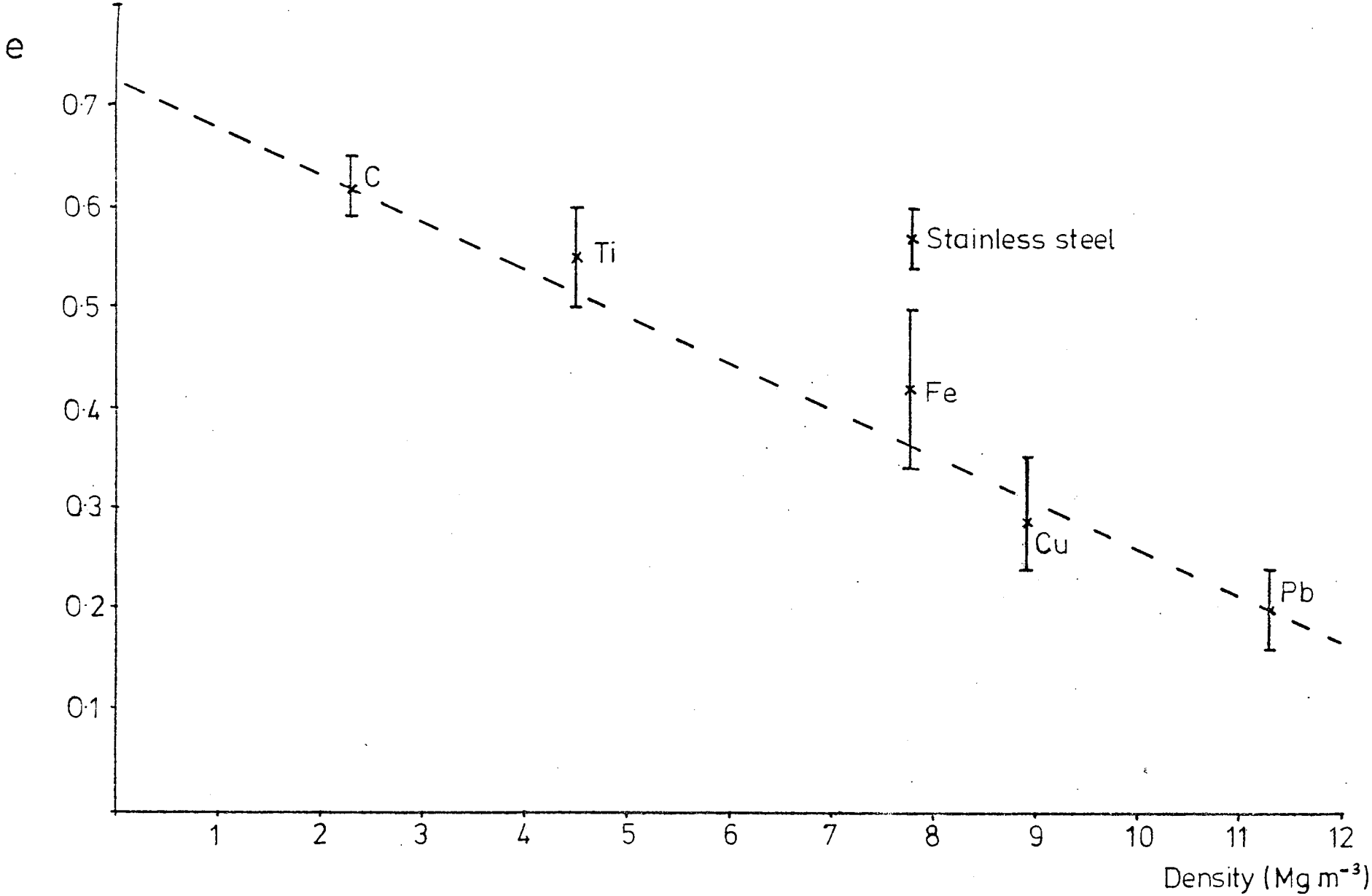
e
0·7
0·6
0·5
0·4
0·3
0·2
0·1
C
Ti
Stainless steel
Fe
Cu
Pb
1
2
3
4
5
6
7
8
9
10
11
12
Density (Mg m⁻³)

Figure 5.7

[a]

[b]

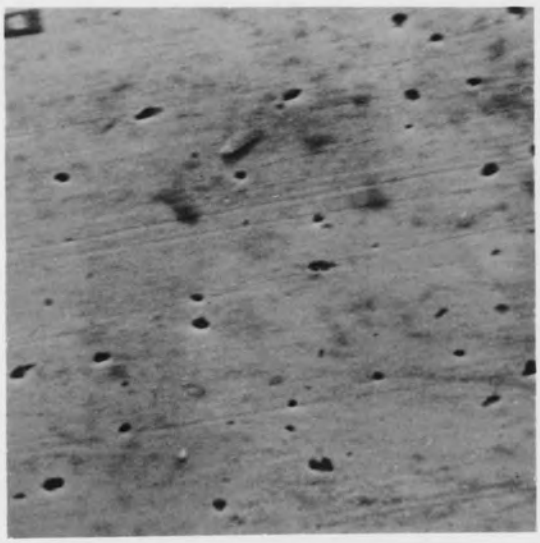

[c]

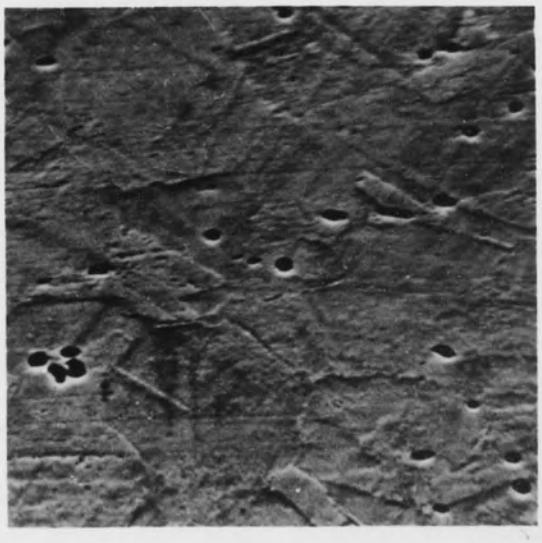

Figure 5·8

clearly shows how microspheres tend to become 'stuck' to the surface where they impact directly on a scratch groove. The second micrograph (figure 5.8b) shows the surface after high temperature heat cleaning by electron bombardment - no significant changes in surface micro-topography can be seen from its previous untreated state. Similarly, surfaces which were prepared by careful ion-beam etching again did not show any significant changes. However, in the third micrograph (figure 5.8c) it can be seen what happens when a sample is strongly ion-etched ; due to perferential etching the surface has become uneven and underlying grain structure has started to appear.

5.3 Charge Reversal Results

Since the bouncing mechanism, as shown above (also see section 5.5), depends on the unpredictable microscopic conditions at the point of impact (e.g. local field and surface conductivity) one finds in practice, a similar spread in the charge reversal measurements for a given set of external parameters. Accordingly, it has been necessary to adopt an averaging technique in presenting data such that each point plotted on the figures 5.9 - 5.11 below represents a mean of ten sample events and the spread in these observations being accounted for in the error bars.

The mean charge reversal data obtained from copper, stainless-steel and titanium targets has been collated in figure 5.9, traces (a), (b) and (c) respectively. These curves show how the ratio of incident to reverse charge $\bar{q}$ varies with the macroscopic field E_o. It can be seen that in all three cases this ratio decreases with E_o, in other words the charge reversal efficiency improves with the increasing applied field. It is further seen that there is a significant difference between the responses of the three metals for all values of E_o, with copper clearly promoting the charge reversal

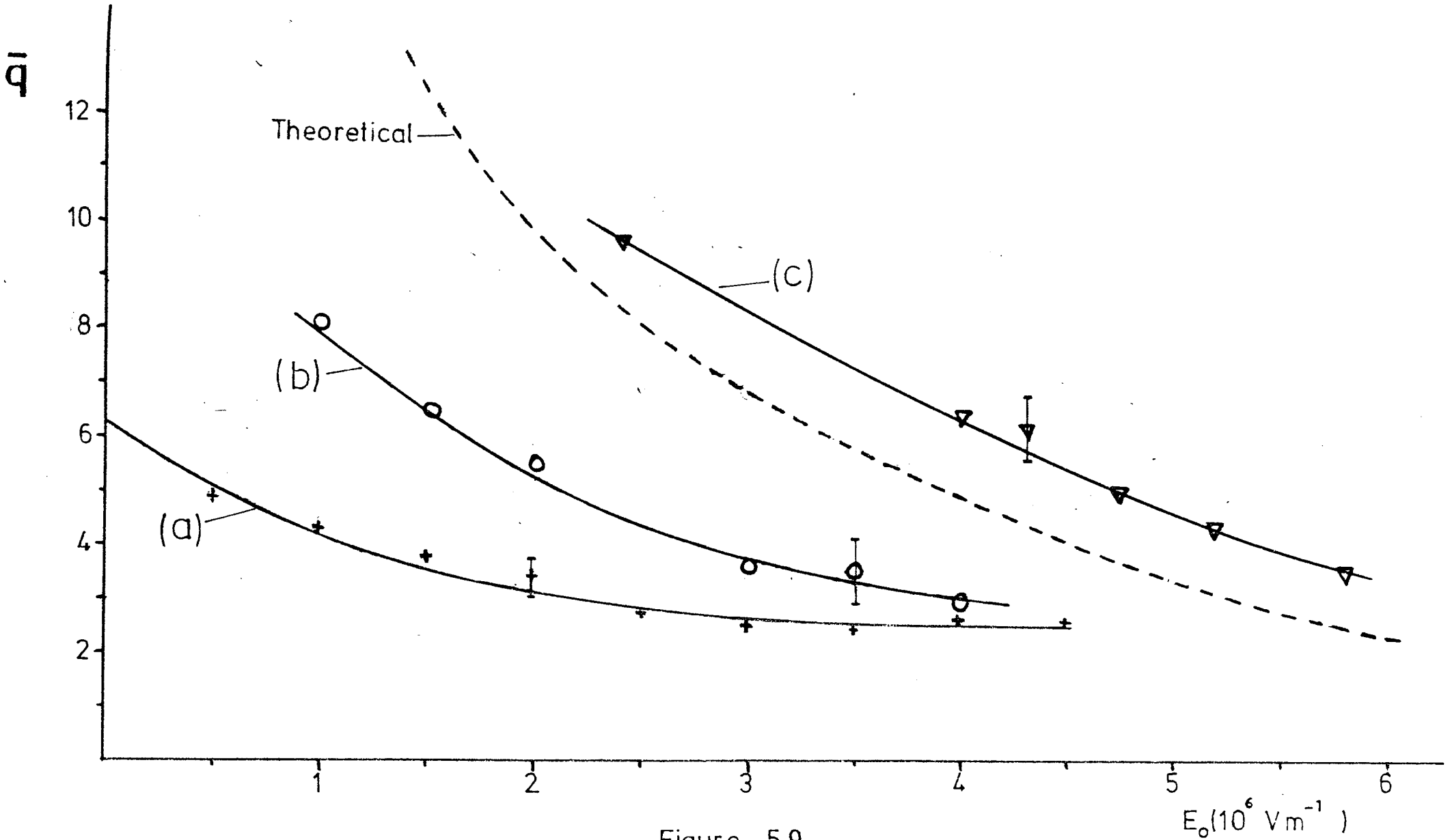

Figure 5.9

more effectively than stainless-steel and titanium quite unexpectedly (see later) even more effectively than copper. In fact, titanium can be seen to exhibit charge reversal even at zero applied field, this suggests that its remarkably high charge reversal efficiency may not just be the result of a more effective response to E_o, but is probably due to some form of extra intrinsic contribution (see section 5.6), which will be discussed later.

In experiments where either a copper or stainless-steel target was faced with thin (5 - 50μm), cleaved mica films; inspite of obtaining highly efficient ($e \rightarrow 1$) rebounds in majority of cases, no charge reversal events were however observed, even for the maximum safe-applied voltages. But instead, it was found that the microparticles tended to retain most of their original positive charge after undergoing an elastic rebound.

With the lead targets, it was found difficult to generate smooth mirror like surfaces (as typically obtained with most other metals) and so rather dull - rough looking surfaces, which appeared to be supporting a thick-oxide layer were obtained. Accordingly, at the low applied fields no charge reversal events were observed, and the particles were found to rebound retaining their original positive charges as in the above case of mica. Whereas, at high applied fields, although charge reversal was observed but the frequency of such events was very low. This, probably being due to those few particles impacting the target at the oxide free regions or the regions with thin oxide films as would be expected with the rather uneven type of oxide film found on most polycrystalline metals, especially the softer ones like lead which have undergone intensive mechanical polishing.

Finally, in the case of carbon, with the type of target used, it again proved difficult to obtain a smooth mirror-like surface by mechanical polishing, this time however it was mainly due to the rather granular under-

structure of these targets and consequently the number of charge reversal events observed were also quite small. From those events observed, the reversal efficiency was found to be much lower than with the metal targets, which is not entirely an unexpected result from a material with semi-conducting conductivity.

Figures 5.10 and 5.11 respectively illustrate the mean charge reversal behaviour for different surface conditions of copper and stainless-steel targets. In each case these plots show how the ratio of incident to reverse charge $\bar{q}$ varies with the macroscopic field E_o, for target surfaces that are atomically clean (curve A), ambient oxidised (curve B) and excessively oxidised (curve C). Because of the inherent spread in the experimental data, as mentioned above, it was not possible to distinguish between the responses of commercially polished surfaces and those that had been freshly oxidised in pure oxygen. Similarly, the responses from atomically clean surfaces produced by argon ion etching and electron bombardment heating were only slightly different with both target materials, it was found that atomically clean surfaces were associated with a greatly enhanced electron emission which had the effect of limiting the range of E_o for which measurements could be made if breakdown was to be avoided. The complementary ellipsometric data relating to the various target surfaces, together with the estimated thickness of oxide films, are presented in table 5.1, where the $\delta\psi$ and $\delta\Delta$ values are relative to the clean surface readings ψ_o and Δ_o. The uncertainty in the estimated film thicknesses arises from the difficulty in deciding upon the appropriate values for the optical constants of the oxide films: for copper the data of Roberts (202) was used, while for stainless-steel that of Hill and Weaver (187).

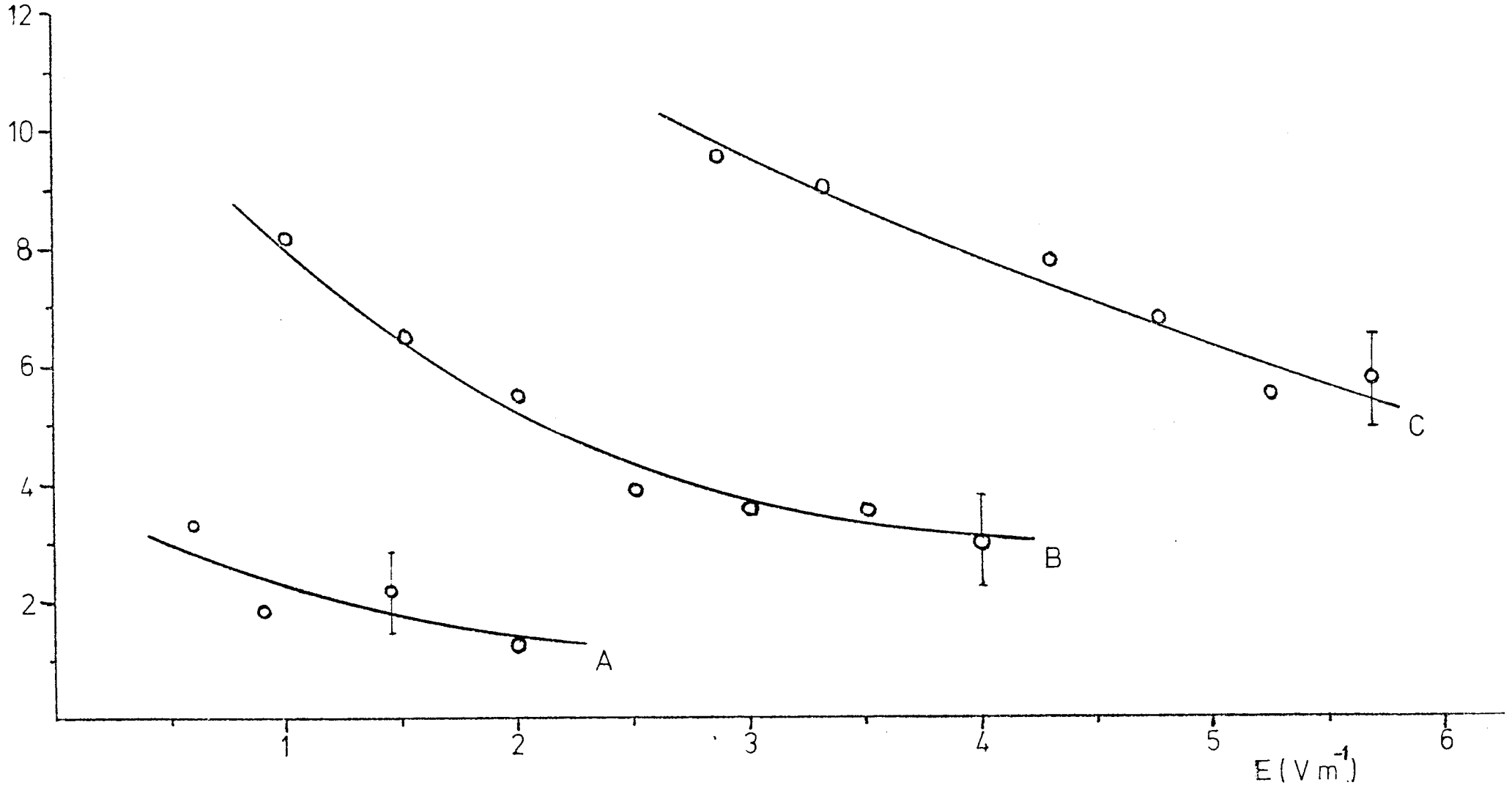

Figure 5.10

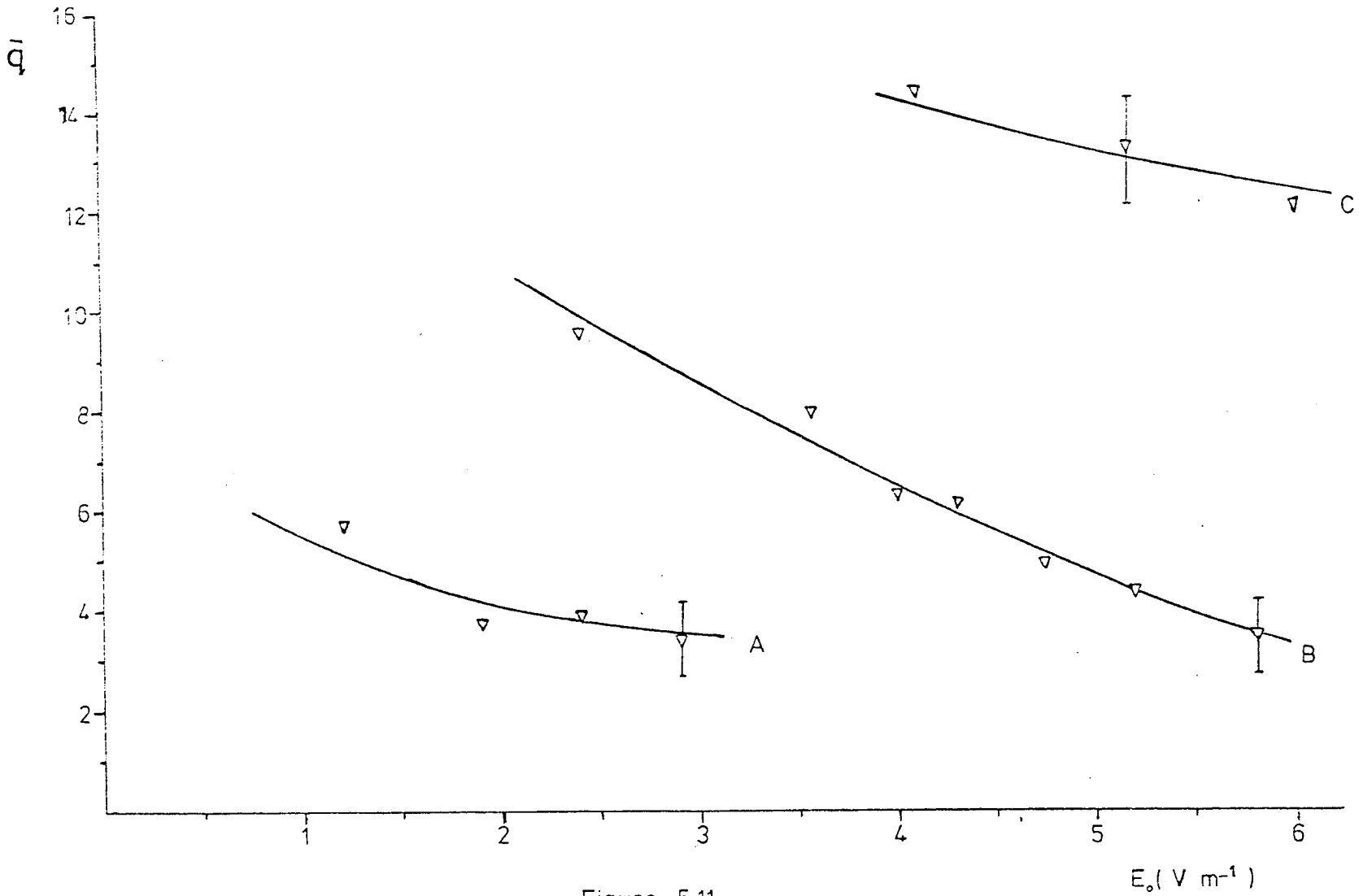

Figure 5.11

It will be seen from these plots (figures 5.10 and 5.11) that the level of surface oxidation has a very marked effect on the charge exchange process for both target materials. With the excessively oxidised stainless-steel target, it was only possible to observe charge reversal events for $E_o \gg 4x10^6 Vm^{-1}$, and even then only rarely as in the case of lead and carbon above: thus explaining the sparsity and relatively greater spread in the experimental points for this surface.

5.4 Interpretation of ellipsometric data

5.4.1 Copper Targets

From the ψ and Δ values given under item 4 of table 5.1, the optical constants of the clean metal substrate were calculated to be n=1.03 and k=3.43 respectively. These values compare favourably with other reported measurements on clean copper by Butcher et al (199) and, Hayfield and White (197) provided adequate allowances are made for differences in the angles of incidence and the wavelength of light used. When such a surface is exposed to air, it acquires an equilibrium oxide film with optical constants of n=2.75 and k=1.5; these values represent the average of the slightly varying published data (189) (197) (199) (202). These two sets of optical constants for the substrate and overlaying oxide may now be used to characterize the oxide film from the associated ellipsometric data of table 1: changes in Δ are used to calculate the film thickness, while changes in ψ indicate changes in the microstructure of a surface.

Thus, the thickness of the equilibrium oxide layer, corresponding to item 1 of table 1, was found to be 25 ± 5Å, which compares favourably with other reported values in the range of 20—40Å (191) (199) (202). This spread in experimental data has been accounted

for by both optical (189) and X-ray crystallographic (192) studies, which have shown that film thicknesses vary with the crystallographic orientation of the substrate. In addition, because such films are crystalline and highly orientated, they will be subject to large epitaxial stresses that result in an isotropy across the film and a consequent variation of the optical constants with thickness. The ellipsometric film thickness measurements on the polycrystalline surfaces of the present investigation must therefore be interpreted as an average value for the coverage on the crystallites included within a typical sampling area of $\backsim 10mm^2$. It should also be noted that since k is non-zero, the oxide film on copper is absorbing and hence semiconducting: a conclusion that is in agreement with the findings of Latham (81) using a direct measuring technique.

The ellipsometric readings of item 2 (table 5.1) correspond to the dynamic equilibrium existing between the oxide desorption and regrowth processes simultaneously occurring on the target surface following extended electron beam heating to a temperature of $\sim 800^{o}C$ at $\sim 5x10^{-6}$Torr. Thus, the presence of a 5Å thick residual oxide film indicates that the maximum attainable temperature is too low for the desorption mechanism to predominate. To remove this remaining oxide, the target was subjected to the successive ion bombardment treatments detailed in items 3 and 4 of table 5.1. The system pressure $\sim 6x10^{-6}$ Torr during these operations was almost entirely derived from the externally introduced argon; the partial pressure of oxygen remained $\sim 5x10^{-10}$Torr so that the oxide regrowth mechanism was effectively inhibited.

In considering the ellipsometer readings corresponding to the heavily oxidised surface (item 5 of table 5.1), it will be seen that while there has been an anticipated large change in Δ, there has also been a significantly larger change in ψ than was found for

Target Surface Treatment	System Pressure (Torr)	COPPER TARGET				STAINLESS-STEEL TARGET				Physical Implications
		ψ (deg)	Δ (deg)	$\delta\Delta$ (deg)	Film Thickness (A^{o})	ψ (deg)	Δ (deg)	$\delta\Delta$ (deg)	Film Thickness ($\mathring{A}$)	
Commercially polished-i.e. without any additional in-situ treatment.	8×10^{-10}	35.38	117.19	-4.81	$\sim 25\mathring{A}$	33.52	131.67	-7.17	$\sim 38\mathring{A}$	The presence of an equilibrium oxide film (visually transparent for both targets)
Electron bombarded for 6 min (Beam current ~5mA at 4kV)	5×10^{-6}	35.58	121.14	-0.86	$\sim 5\mathring{A}$	33.75	137.24	-1.60	$\sim 9\mathring{A}$	Progressive removal of the oxide film
Argon ion bombardment for 30 min (Ion current ~50 A at 6kV)	6×10^{-6}	35.76	121.82	-0.18	$\lesssim 1\mathring{A}$	34.01	138.63	0.21	$\sim 1\mathring{A}$	
Further ion bombardment for ~30min, when $\delta\Delta \rightarrow 0$	6×10^{-6}	35.81	122.00	0	$0\mathring{A}$	34.08	138.84	0	0	Atomically clean target surfaces
Heated in-situ to~500°C by electron bombardment at an increased pressure	$\sim 10^{-3}$	29.06	104.40	-17.60	$\gtrsim 150\mathring{A}$	28.10	119.64	-19.20	$\gtrsim 150\mathring{A}$	The growth of a thick oxide film (visually dark brown for both targets)

Table 5.1

items 1-4. The most likely explanation of this latter observation comes from the complementary evidence of a scanning-electron-microscopy examination of this heavily oxided surface which showed it to have undergone a marked textural change with the growth of close-packed, hemispherical oxide nodules of typical radii $\lesssim 0.05\mu m$. An additional contribution to the change in ψ would also be expected if the film was composed of the two oxide species Cu_2O and CuO having differing optical constants. However, the findings of similar oxidation investigations in air (199) and oxygen (191) indicate that this possibility is unlikely. Accordingly, the estimated film thickness of $\sim 150\text{Å}$ is based on the assumption that the oxide is composed entirely of the 'equilibrium' species having known optical constants; it also represents an average thickness which 'smooths-out' the material present in the surface nodules.

5.4.2 Stainless-steel Targets

Following the same procedure used with copper, the optical constants of atomically clean stainless-steel were computed to be n=2.35 and k=3.70. These values again compare favourably with an earlier measurement (98) if adequate allowances are made for differences in the angles of incidence and the wavelength of the light used.

Considering next the equilibrium oxide layer, it has been reported that stainless-steel surfaces that have not been subjected to prolonged heat treatment contain a high percentage of chromium (187) (201) whose optical constants are n=2.42 and k=0. When these two sets of constants are combined with the $\delta\Delta$ value given under item 1 of table 5.1, the thickness of the equilibrium layer is found to be $38\pm5\text{Å}$, which is also in good agreement with the earlier investigation (98). Unlike the oxide on copper, that on stainless-steel

is a good non-absorbing dielectric as evidenced by k=0: this observation is again supported by the direct electrical measurements (81).

The changes in ψ and Δ between items 1 and 2 of table 5.1 show the same general trends as those found with copper, and hence are interpreted in similar terms. There is however the possibility of the heat treatment leading to a depletion of the chromium oxide content in the film (201), and the consequent predominance of iron oxide which has the very similar optical constants of n=2.5 and k=0.3 (206). If the film thickness is now recalculated using these constants the potential error in the tabulated value is $< 10\%$ which is within the experimental error and whose presence therefore will not be detectable. The subsequent ion bombardment treatments have also led to changes in ψ and Δ that follow those for copper, although the magnitudes of the $\delta\psi$'s are somewhat greater with stainless-steel. This observation is attributed partly to changes in the surface microstructure following the annealing of the cold worked surface, but more likely due to the preferential etching of either the iron or chrome species in the surface.

Referring finally to the ellipsometric readings of item 5, which characterise the heavily oxidised stainless-steel surface, it will be seen that, as with copper, there have been significantly larger changes in both ψ and Δ . The film thickness of $\gtrsim 150\text{Å}$ has been calculated from $\delta\Delta$ on the assumption that the oxide is a single-species, homogenous chromium oxide film. Since however, there is a possibility of the film being composed of mixed species of iron and chromium oxides, the reliability of the tabulated thickness value is limited. As in the case of copper, the change in ψ is mainly attributed to the structural changes in the target surface following the nodular growth of a thick oxide film.

5.4.3 Titanium targets and carbonyl-iron microsphere

Although, in the present investigations detailed ellipsometric studies were not carried-out on the other target materials, such as titanium, mainly due to the time limitation; or as in the case of carbonyl-iron microspheres where measurements were not possible due to the small size of the specimen. However, a good idea of the structure and thickness of air formed oxides on these materials can be obtained from several other studies which have dealt primarily with this subject.

5.4.3a Titanium targets

Considerable investigations have been carried out on oxides that form on titanium (209) (210) (223) (224). It has been generally established that the protective crystalline oxide film which normally passivates titanium forms instantaneously on exposure to air to a thickness of ∽10-25Å but then only grows very slowly on further exposure. For example, according to Andreeva (209) the initial film is 12-16Å thick, after about 70 days it reaches ∽ 50Å and after 4 years it grows to about 250Å.

The structure of this passivating oxide film is quite complex, although it is generally believed that the air formed oxide is Rutile -TiO_2, the strongly insulating form, however, several more recent electron diffraction studies have shown that the air formed oxide does not correspond to any of the known single oxides. Tomashov et al (211) have reported that the composition of the film varies across its thickness: near the metal interface it consists of TiO and at the surface it is TiO_2, but in the interior it contains Ti_2O_3. In another study up to seven distinct phases of oxide have been reported (225).

5.4.3b Carbonyl-iron microsphere

Furthermore, the thickness of the equilibrium oxide film which forms on iron has been measured by gravimetric (204) (205), optical (206) (207), electrochemical (203) and electron diffraction methods (226). It is generally found that mean film thickness is of the order of 10 - 30Å, depending on surface pretreatment, oxygen pressure and the time of exposure.

Gravimetric experiments (204) on hydrogen reduced polycrystalline iron - indicate about 15Å of oxide following 6 minutes exposure to oxygen at 15 Torr pressure and exposure of such specimens of several days (205) resulted in some 29Å. These gravimetric results compare favourably with the ellipsometric studies of Winterbottom (206) on bright annealed carbonyl-iron. About 20Å of oxide was found after 1 hour air exposure, increasing to some 25-40Å after many days. Whilst such subsequent experiments (207) have shown 10-19Å of oxide on iron immediately after exposure to air at 40-45% humidity 25°C. This film increased to 15-23Å after 24 hours and remained constant for 3 days. By using an electrometric method to estimate the oxide film thickness on hydrogen reduced iron, an oxide film of 26Å was obtained after 48 hour air exposure. In a more recent electrometric and Electron diffraction study (226), besides measuring the film thickness, further information regarding the composition of oxide, its particle size and epitaxial relationship between oxide and metal has been obtained. The structure of oxide is found to vary from a Fe_3O_4 type material at the metal oxide/interface to a $\gamma - Fe_2O_3$ type material at the gas oxide/gaps interface. The detailed nature of this film varies with the crystallographic orientation of the iron substrate.

5.5 Discussion - Interpretation of experimental results - Mechanical

From the experimental results presented above, it can be seen that the 'average' impact behaviour of micron-submicron sized iron microspheres on various diamond polished targets exhibits a trend which agrees remarkably well with earlier observations on the impact of macrospheres on planar targets (117), (118), (119). However, a more closer examination shows that there are considerable differences in the threshold velocity for plastic deformation and the degree of scatter in the experimental data. For instance, in the case of centimetre-sized metal spheres it is generally known that limiting velocity for elastic impact is of the order of 0.1m/s. Whereas in the present investigation, no clear evidence of target indentation has been found for impact velocities $< 200ms^{-1}$ and as shown in section 2 this observation is strongly supported by several other impact studies (76), (77), (104), where under very similar experimental conditions it has been commonly established that the critical velocity heralding the onset of permanent elastic deformation is $<$ 500m/s. Although in these latter cases, particularly for the harder target materials it cannot be definitely concluded that only elastic impact strains were involved because when the impacting materials have similar elastic properties, the initial deformation can occur in the spherical projectile which is not examined. Nevertheless, the additional indirect experimental evidence of impact ionization (75) and theoretical predictions of Cook(120) further support the conclusion that $V_c \sim 100ms^{-1}$.

Furthermore, no simple theoretical explanation can be seen for this dependance of V_c on particle radius R, in terms of classical macroscopic Hertzian impact theory. In fact the analysis of Davies (130) clearly illustrates that V_c depends only on the bulk properties of the

impacting materials. Although this theory received support from his associated experimental observations on the impact of macrospheres, the findings cannot be regarded as generally conclusive as the range of sphere radii used was rather restricted (1.5-5mm). Which leads to the conclusion that for the present and previously cited micro-impact situations when the size of the micro-sphere is comparable or less than the grain size in the target surface, the predictions of the classical impact theory may no longer be regarded as strictly valid.

Nevertheless, a viable explanation of this anomaly in the responses of macro and micro-impact systems seems possible if one considers the differences in mechanical properties of very small volume of surface and that of a bulk solid: For example, (i) the intrinsic differences in the mechanical strength of a single crystal and a poly-crystalline sample; (ii) the extrinsic differences in the mechanical properties of a defect free atomically clean ideal planar surface and those of a non-ideal specimen as found in practice with surface films such as oxides, adsorbed gases and worked polish layer; (iii) as well as non-planar surface microtopography.

(i) It is well known that the mechanical strength of most poly-crystalline solids on a bulk scale is very much smaller than the theoretical strength of a perfect crystal. This results from the presence of defects such as dislocations and cracks within the crystal and on its surface. In fact, these defects form the basis of the bulk mechanical behaviour of solids and in the case of ductile metals the bulk strength is determined primarily by the generation and propagation of dislocations. Since these dislocations have a spacing which may be considerably larger than atomic dimensions ($\backsim$5000 atomic spacings apart in an annealed metal), the strength properties might be expected to depend on the scale of the experiment.

Experimental verification of this size effect has been established in several studies where measurements of the mechanical strength of metals on a small scale have all shown that there is an increase in strength with decrease in size. This appears to be true not only for crystals grown specially in a small form such as whiskers and evaporated thin films, but also in crystals prepared from the bulk. Schiichta (212) obtained considerable increases in strength of wires electro-polished down to 4μm diameter and subsequently Smith and Bowkett (216) have reported tensile strengths approaching the theoretical value in tungsten, aluminium and nickel with cross-sectional diameter down to 0.05μm. Whilst, Muller (213) has shown that stresses of the order of the theoretical strength are sustained in field emission tips during field emission experiments ; the stress in this case is produced by the electric field at the tip. These strengths have also been observed when the stress is applied by compression at an external surface. Gilman (220) found high strengths in lithium fluoride and Gane and Bowden (217) have observed strengths approaching the theoretical value in metals.

The latter experiments which took the form of sub-micrometre indentation hardness tests using field ion microscope tips as indenters have more recently been extended and refined (218) (219) to include the mechanical strength studies of annealed metals in four different types of experiments: (i) indentation of a soft metal surface with a hard stylus, (ii) blunting of a soft metal tip against a hard surface, (iii) compression of individual metal crystals and (iv) bending of thin filaments. It was found that mechanical strengths approaching the theoretical value could be achieved in the majority of cases but in compressive experiments ((i), (ii), and (iii) above), where the stress was applied to an external surface the hardness was strongly dependent on the conditions of the interface. The yield

pressure for example, that could be sustained by a region of perfect crystal in contact with hard metallic contact was found to be ∿5 times less than the theoretical value, however with the introduction of a polymeric or amorphous layer at the interface the strength was raised to the theoretical level. This, it was suggested resulted from the polymeric layer removing the high stress concentration which produce interfacial tractions that can lower the strength.

Thus, it can generally be concluded from above that large increases in strength are obtained at the submicrometer scale, these are not due to extrinsic effects such as surface contamination (see below) but are a real intrinsic effect associated with the difficulty of generating and moving dislocations in a very small volume.

(ii) For the type of metal surfaces found in practice however, apart from the differences in mechanical response due to the intrinsic size effects above, it also is important to consider extrinsic effects resulting from the presence of surface films such as oxides, adsorbed gases and worked polish layers. As shown above the presence of adsorbed polymeric films in the micro-hardness experiments (218), can have profound effect on the mechanical strength. Similarly, the presence of oxide films (as discussed in section 2.1.1) can increase the surface hardness by factors of 5 to 100 times the bare metal values, since metal oxides in general are known to have higher mechanical strengths than the corresponding parent metal. In the present work this behaviour is clearly demonstrated in figures 5.4 and 5.5 for copper and stainless-steel targets respectively. Where, for both the metals the hardness response of different surface conditions clearly shows that the oxide-carrying surfaces give higher coefficient of restitution values than atomically clean surfaces and the rebound efficiency increases with the thickness of oxide.

It is also important to note that at the micro-scale, the differently orientated micro-single crystals which make up the polycrystalline targets, apart from intrinsically exhibiting differing mechanical strengths, will acquire oxide films (see table 5.2) which may vary from grain to grain, because of orientation dependance of surface energies. In fact the grain boundaries themselves on the polycrystalline metal surface tend to interact strongly with oxygen because of higher surface energies in these regions.

Furthermore, as previously discussed in section 2.1.5d, the intensive mechanical polishing of a metal surface can profoundly effect the properties of its surface. It has been shown (107) (110), for example, in the case of diamond polished surfaces, changes of structure in form of a worked impurity layer are detectable to depths of many atomic radii. Where the polish layer usually consists of a fudge of metal, cold-worked metal, metal oxide and in some cases also the constituents from the polishing medium itself. Thus, such a mechanically polished surface will exhibit micro-regions with a variety of hardnesses and so are likely to produce a large scatter in coefficient of restitution measurements.

(iii) Finally, the microtopography of a $\frac{1}{4}\mu m$ diamond polished target surface (see figure 5) is characterised by a random array of grooves having typical dimensions $0.1\mu m$ and other irregular features of somewhat larger dimensions. Hence, for a field-free target space, it could be anticipated that a significant incidence of wide-angle particle scattering events would be observed. Even with the strong collimating effect of the high axial electric field associated with the present target assembly, some reflected particles could still acquire significant off-axis velocity components whose influence on the measured values of v_2 and hence e, must now be considered.

Referring to figure 3.1 (a), it will be seen that the collimating aperture immediately in front of the particle detecting tube will transmit only paraxial particles that will subsequently undergo impact events within a localized region at the centre of the target. However, as a result of wide-angle scattering from the target surface, it is possible for 'reflected' particles to have non-axial trajectories, where from the geometry of figure 3.1 (a), the finite aperture of the detecting tube will accept returning particles having an off-axis divergence.

$$\tan^{-1}\left[\frac{D}{2(L+I+d)}\right] \gtrsim 1 \qquad \ldots\ldots\ldots \qquad 5.1$$

This observation therefore implies that the measured 'axial' values of V_2 could be liable to an error $(1-\cos 11^{\circ})v_2$, with a corresponding error in e of $\backsim 2\%$. This, coupled with an overall measurement error of 5% is still too small to account for the observed 'spread' in e-values, but in any case, computations of the possible trajectories of typical particles within the high-field gap indicate that their final divergence would in fact be less than the above 11° limit. This conclusion has been confirmed experimentally by the rarity of observing 'reflected' particles that strike the detector tube.

Apart from the possibility of oblique reflection from a non-planar microfeature, it can be seen from figure 5.8 that the microtopography of a target surface will give rise to impact events where the microsphere makes simultaneous contact at two or more points. Consider for example the idealized symmetrical situations illustrated in figure 5.12 where e is the true coefficient of restitution for normal impact between a particle and a plane and e' is the apparent value as measured indirectly from V_2, i.e. e' = e for case (a). For the type of impact event of case (b), where an equipartition of impact momentum is assumed, it follows that e' will vary from e to $e/\sqrt{2}$ as angle θ,

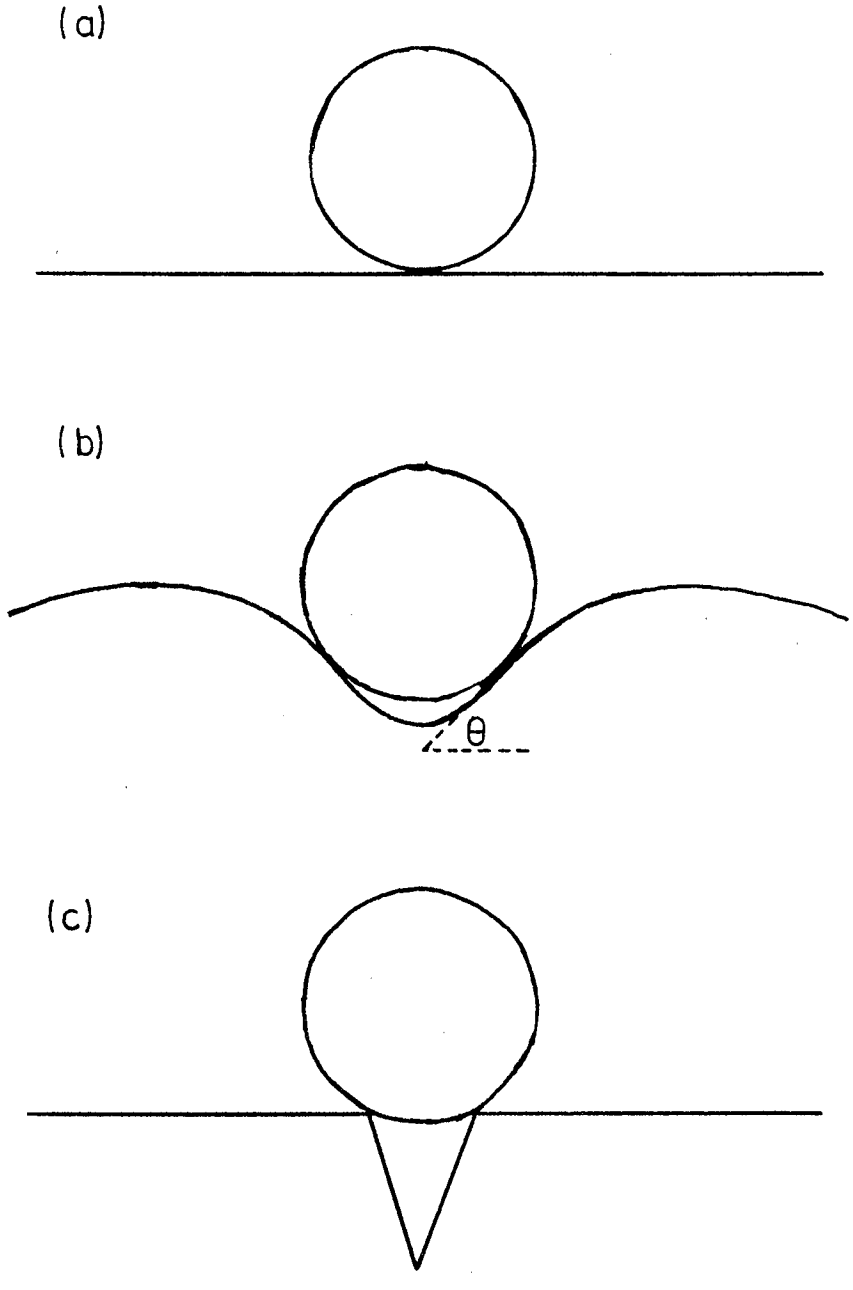

Figure 5·12

Different impact situations

varies from 0 to 45. In case (c), which corresponds to a microsphere straddling a polishing groove, the initial impact will be shared between two knife-edge contacts, which will give rise to greatly enhanced contact pressures and the likelihood of plastic deformation. Accordingly, such an impact event would be characterised by a reduction in e of up to $\backsim$60% (119). Alternatively, the particle may cold-weld to the edges of the groove as has evidently happened to the microspheres shown in figure 5.8a. Clearly then if all these factors which can produce an increase in the static yield strength are taken into account and if similar discrepancies are assumed for the dynamic yield strength Py then significantly higher critical impact velocities for the microsphere impact systems can be expected: For example, if V_c is taken as $\backsim 0.1 ms^{-1}$ for macrospheres, and it is assumed that $P_y \propto V_c^{2/5}$ (123), then using the above criteria (i.e. P_y micro $\backsim 20 \times P_y$ bulk), the value of V_c for microsphere impacts would be $\backsim 200 ms^{-1}$, which is in far better agreement with the micro-impact observations.

However, the possibility must also be considered that some of the higher velocity observations plotted in figures 5.2 and 5.3 will have resulted in some plastic flow of the impacting materials. Such events would be identified experimentally by a greatly reduced coefficient of restitution (119), so that this mechanism must be regarded as a possible contributary factor in accounting for the marked increase in the 'scatter' of experimental data with increasing impact velocity. But, as explained earlier, confirmatory target indentation evidence of such inelastic processes was found to be inconclusive.

It is now necessary to consider the physical implications of the linear dependencies of the 'averaged' values of the coefficient of restitution e on both hardness and density of the various studied.

5.5.1 Dependence of e on the target hardness (figure 5.6)

Although this linearity has been demonstrated in terms of the measured Vickers hardness numbers of the target materials, it can be assumed that a similar correlation would have been found if the more appropriate Shore solerscope dynamic method had been used: because the various hardness measuring scales are closely related. In this latter type of measurement, the hardness of a material is given in terms of the height of rebound of a standard sphere after falling through a fixed vertical distance onto a plane anvil of the material. Hard materials suffer less deformation, which consequently leads to a high recovery of energy from the elastic impact stresses: this therfore results in high rebound velocities which, by definition constitutes a high coefficient of restitution.

5.5.2 Dependence of $\bar{e}$ on target density (figure 5.7)

With the exception of the stainless-steel result, this approximately linear dependence may be explained qualitatively by reference to the work of Dietzel et al (77) who found that impact behaviour of similar microparticles depends on the characteristic product $B\rho$, where B is the shock parameter and ρ is the density of the target. This product is proportional to the fraction of the incident kinetic energy of the particle that is irreversibly lost during an impact; so that a target with a high B would be expected to have a low coefficient of restitution. However, since the tabulated values of B (77) show only a small variation among typical target materials, it follows that the target density will be the dominant parameter, with the coefficient of restitution $\bar{e}$ decreasing with increasing density as observed experimentally. In the absence of an alternative explanation, it is assumed that the non-linear behaviour of stainless-steel indicates that this

material has a significantly different B-value from the other target materials.

5.6 Interpretation of experimental results - electrical

From the theoretical considerations of Chapter II it clearly emerges that charge may in principle be exchanged between the particle and target either by direct ohmic conduction via the electrical contact formed or by close-proximity tunnelling.

In the special case where both surfaces are atomically clean, the charge exchange would only be limited by the constriction resistance of the two members (see section 2.11). This arises as a result of the actual contact area being very small but also because only a fraction of this contact area may be electrically conducting, so that the current lines are bent together through a narrow area causing an increase of resistance that is much higher than the case of fully conducting apparent contact surface. Nevertheless, depending on the electrical properties of the interacting materials, the charge exchange should be completed in times which are not too vastly different from the relaxation times τ of typical metals, where $\tau \sim 10^{-14}$ secs (230). Since, it has already been shown in section 2.15a, that for quasi-elastic impacts the contact time t_c is $\sim 10^{-8} - 10^{-9}$ secs, clearly then, $\tau \ll t_c$ and it follows that the reversed charge acquired by a particle should be the equilibrium value for a sphere in contact with plane as given by equation 2.1. Thus for the case of 1μm diameter microsphere and $E_o = 5\times10^{6}\,Vm^{-1}$ equation 2.1 predicts a reverse charge $q_{o2} \sim 2.5\times10^{-16}$C, whereas favourable experimental values for q_2 at this value of E_o can reach $\sim 2\times10^{-16}$C, which suggests that in these cases charge reversal has nearly been completed during the contact time t_c. In practice, q_{o2} is likely to

be somewhat greater than 2.5×10^{-16}C since the irregular microtopography of the target surface will lead to the localized enhancement of E_o. In addition, there will also be some positive or negative contribution to reverse charge as a result of differences in work functions of the two conductors (see later).

For the case where one or both the surfaces support thin oxide films an analysis by Holm (103) with crossed rod macrocontacts, between 2mm diameter cylinders for a range of materials has shown that both conduction mechanisms play a role but the tunnelling process tends to predominate. Since, in this type of contact a highly resistive path is formed between the two conductors due to the constriction and film resistances (see section 2.1.2), where in the latter case alone resistivity values can approach $\sim 10^{18} \Omega m$. Accordingly, in a micro-contact situation it seems even more likely that the tunnelling process would predominate, because the conduction paths will be much smaller and hence, highly resistive.

To quantitatively demonstrate this for the present micro-system, it is first necessary to establish the axial electric field E_g between the particle and the target as outlined in section (2.1.2). In general E_g is given by superposition of three charge contributions: (i) the initial charge on the particle, (ii) the charge which produces the macroscopic field intensity E_o residing of plane electrodes and (iii) the charge induced on the surface of the microsphere. The most rigorous and commonly used expression for E_g, which accounts for all these charge contributions has been derived by Martynov (79) (Equation 2.35), however in the present case it is more appropriate to use the slightly modified form,

$$E_g = \frac{V_p}{g} = \frac{\beta}{\epsilon} \left(2.6 \left(\frac{r}{g}\right)^{0.8} E_o\right) \quad \ldots\ldots \quad 5.2$$

Where from equation 2.41, $\bar{\epsilon} \backsim \frac{g}{t_v + \frac{\epsilon_s t_p + \epsilon_p t_s}{\epsilon_p \epsilon_s}}$ is the mean dielectric constant and β is the field enhancement factor which has been included to represent a more realistic surface microtopography. Also,

$$V_p = \frac{Q_t}{Cg\bar{\epsilon}} \qquad \ldots\ldots\ldots \qquad 5.3$$

where Q_t is the total charge on the microsphere and C is the sphere-plane capacitance (155) (156) (157).

In addition, if the two electrodes have significantly differing work functions there will be an extra field contribution due to the intrinsic field (see section 2.1.2) given by,

$$E_i = \frac{\phi_p - \phi_t}{eg} \qquad \ldots\ldots\ldots \qquad 5.4$$

where ϕ_p and ϕ_t are the particle and target work functions. These differences in the metal work functions which arise due to their intrinsic band structure can be seen in table 5.2. Additionally however, large differences in work function of a given material may be introduced by surface films such as oxides and adsorbed gases. The change in work function when a gas is chemisorbed on a metal depends upon the nature of the metal and of the chemisorbed adsorbate (109), (221). Atoms chemisorbed on the metal surface are transformed into ions which involves an electron transfer from adsorbed atom to the metal or from metal to the chemisorbed adsorbate. These processes result in decrease or increase in the work function respectively.

It is generally believed that the sign of surface potential $\Delta\phi$ of metal depends on the differences of its work function ϕ and on the electronegativity of the adsorbate e_n ,

$$\Delta\phi = \phi - e_n \quad \text{and} \quad e_n = \tfrac{1}{2}(I + \chi) \qquad \ldots\ldots \qquad 5.5$$

Where I, is the ionization potential and χ is the electron affinity. If e_n exceeds the work function the sign of $\Delta\phi$ is negative. In opposite case, the sign of the surface potential is positive and the latter corresponds to decrease in work function. For example, the effect of electronegative gases: oxygen, fluorine, chlorine and iodine adsorbed on iron (2 2 2) is as follows. At low temperatures, in the case of physical adsorption, the work function increases, however at room temperature, in case of chemisorption the work function decreases.

The three parameters above, namely E_g, E_i and V_p have been computed from equations 5.5, 5.6, and 5.11, using $\bar{\epsilon}$ = 1, 6 and 20 with $\phi_p - \phi_t$ = 1eV for a range of 'microgaps' (g) and are shown in figure 5.15. It is important to note that $E_g \leq 10^9 Vm^{-1}$ for all conditions, thus making it highly unlikely for any significant inflight emission (65) to have taken place from the cathode protrusions to the particle (see section 2.1.2) and also, since no conclusive experimental evidence was found that indicated the occurrence of this mechanism its effects will be ignored. But it is important to note that, depending on the differences in the particle and target work functions there can be significant changes in E_g due to the intrinsic field contribution E_i.

Before this data can be used to compare the relative quantities of charge transferred by the ohmic and tunnelling conduction mechanisms, it is necessary to make some realistic assumptions about the corresponding gap conductances. For the situation where each surface has its ambient oxide film present, the ohmic conductance will vary from zero at the instant of contact to a maximum of $\frac{1}{\bar{R}}$ at $t = \frac{t_c}{2}$, where from section 2.2.1 $\bar{R}$ is the total contact resistance given by,

$$\bar{R} \backsimeq \frac{1}{na}(\rho_p + \rho_t) + \frac{2}{na}\left[\frac{\rho_p \rho_t}{\rho_p + \rho_t}\right] \quad \ldots\ldots\ldots \quad 5.6$$

Here the first term gives the total constriction resistance and the

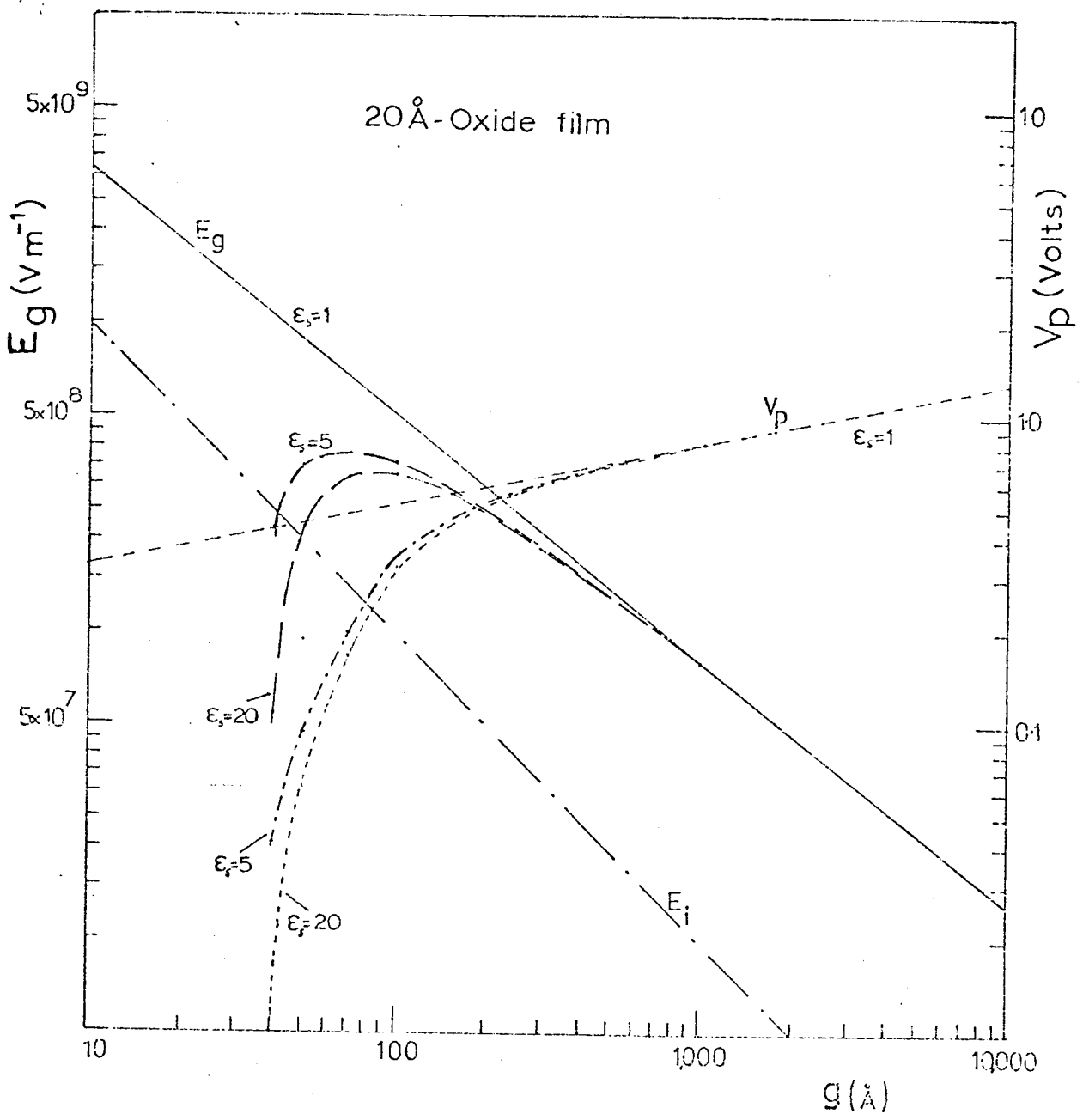
20 Å - Oxide film
E_g ($V m^{-1}$)
V_p (Volts)
5×10^9
5×10^8
5×10^7
10
1·0
0·1
E_g
$\varepsilon_s=1$
V_p
$\varepsilon_s=1$
$\varepsilon_s=5$
$\varepsilon_s=20$
$\varepsilon_s=5$
$\varepsilon_s=20$
E_i
10
100
1000
10000
g (Å)

Figure 5.15

second term the total film resistance; a is the contact area, s is the combined film thicknesses and n ($\backsim$2-5) is a constant dependant on the geometry and surface conditions of the two members; ς_p, ς_t, ρ_p and ρ_t are respectively the bulk and film resistances of the particle and target. This contact resistance and the sphere plane capacitance ($\bar{\epsilon}$ C) will thus control the discharge and charge rates (i.e. $\bar{\epsilon}$ C$\bar{R}$) of the particle to the target potential (see section 2.1.1.). Accordingly, in the absence of any other conduction mechanism, the decay of the particle potential will be given by,

$$V_p(t) = V_{op} \exp\left(-\frac{t}{\bar{\epsilon}C\bar{R}}\right) \qquad \ldots\ldots\ldots \qquad 5.7$$

where V_{op} is the particle potential at the instant of contact t = 0, i.e. as plotted in figure 5.15.

It then follows that the total charge transferred by conduction will be,

$$Q_c = \int_0^t \frac{V_p(t)}{\bar{R}}\, dt \qquad \ldots\ldots\ldots \qquad 5.8$$

which, after substitution from equations (5.6) and (5.7) and integration becomes,

$$Q_c = \bar{\epsilon}CV_{op}\left[1 - \exp\left(-\frac{t}{\bar{\epsilon}C\bar{R}}\right)\right] \qquad \ldots\ldots\ldots \qquad 5.9$$

This expression may now be evaluated by introducing appropriate values for the various electrical parameters involved. Although transition metal oxides are known to exhibit a wide range conductivity values varying from insulating, semi-conducting to metallic (233), (227), (228), however for the present approximate calculation and for the materials used, the resistivities may generally be taken as being considerably higher than corresponding bulk resistivities. For instance, in the case of iron particle, as shown in section (5.4.3b), the stable

phase of air-grown oxide is Fe_2O_3 and resistivity of pure oxide can be $\backsim 10^{11}\ \Omega$ m (196) as compared to the corresponding bulk metal resistance of $10^{-3}\ \Omega$ m: it is however possible that this value may be somewhat lower in practice due to the partial reduction of Fe_2O_3 to the semiconducting oxide Fe_3O_4 (198) during the low-temperature bakeout of the vacuum system. In the absence of detailed information, a typical value of $\epsilon_p \backsim 6$ will be assumed for the low-frequency dielectric constant of such an insulating oxide. The stable oxide on the copper target will again be the oxygen rich phase CuO (194) (195), (200). This is a semi-conducting oxide with a resistivity of $\backsim 10^{6}\ \Omega$ m (190) (193), (195); no specific value is available for its dielectric constant, but from a comparison with that of the other semi-conducting oxide Cu_2O a value of $\epsilon_T \backsim 6$ would again seem appropriate. Finally, the complex iron-chromium oxide on stainless-steel is known to be insulating from its non-corrosive properties and so a resistivity $\backsim 10^{14}\ \Omega$ m can be assumed: its dielectric constant has been measured (81) to be $\epsilon \backsim 5$.

These data together with that from fig. 5.15 may now be introduced into equation 5.9 to estimate Q_c. Thus, in the most favourable situation, where a 1μm diameter iron particle with an initial charge of 10^{-15}C impacts on an atomically clean target such that the charge transfer mechanism is only limited by the iron oxide film, it is found that $Q_c \ll 10^{-26}$C. If this value is compared with the corresponding measured charge transfer, which is typically $\backsim 10^{-15}$C, it can be concluded that the contribution from ohmic conduction can be ignored.

Alternatively, as shown in section 2.1.2 electrical conduction through thin dielectric films may take place by quantum mechanical tunnelling, where the tunnel effect furnishes currents which are independent of film resistivity ρ_f, even if ρ_f is infinite. Thus, under the low-bias conditions as operating in the present experimental regime

the convenient concept of tunnel resistivity σ ($\Omega\ m^2$) can be used, where

$$\sigma = V_p/J_T \qquad \ldots\ldots\ldots \qquad 5.10$$

and is very sensitive to the film thicknesses, its effective dielectric constant ϵ and the bias V_p existing across the film.

In the present experiments, the above steady-state model is complicated in two important respects. Firstly, the area of the tunnelling junction is changing continuously during contact, varying from zero at $t = 0$ to πa^2 at $t = t_c/2$ and finally returning to zero again at $t = t_c$. Secondly, $V_p(t)$ decreases continuously from its initial value V_{op} at $t = 0$ (as given by figure 5.1) to $(q_1 - q_{o2})/(q_1 + q_{o2})$ V_{op} at $t = t_c$ as the charge exchange process progresses: this therefore leads to the additional complication that the tunnel resistivity σ will increase continuously during contact. Hence, to apply existing steady-state theory to obtain an order-of-magnitude estimate of the charge exchange contribution from this transient tunnelling process, the following simplifying assumptions will be made.

(i) The effective contact area will be taken as constant and equal to its mean value of $\pi a^2/2$,

(ii) From the published low-bias data of Simmons (134), the tunnel resistivity may be approximated by the linear dependence

$$\lg \sigma \simeq \lg \sigma_o - KV_p(t) \qquad \ldots\ldots\ldots \qquad 5.11$$

where K is a constant that can be taken as independant of the insulating material, and σ_o is a constant that depends on the thickness, band-gap and dielectric properties of the film, together with the difference in work-function of the electrodes.

(iii) The time-decay of $V_p(t)$ - which, for a constant contact capacitance C (s) is proportional to the charge on the particle

$q(t)$ - can be taken as exponential with a time constant t_c: this is based upon an earlier observation that the process of charge-reversal as measured by the ratio $(q_1 + q_2)/(q_1 + q_{o2})$, is 0.8-0.9 completed during contact i.e.

$$V_p(t) = V_{op} \exp(-t/t_c). \quad \ldots\ldots\ldots \quad 5.12$$

With these assumptions, the total charge exchange by tunnelling Q_T will be given by,

$$Q_T = \frac{\pi a^2}{2} \int_0^{t_c} \frac{V_p(t)}{\sigma} dt \quad \ldots\ldots\ldots \quad 5.13$$

which after substituting from equations (5.11) and (5.12) and integrating becomes,

$$Q_T \approx \pi a^2 t_c \exp(KV_{op})/2\sigma_o K \quad \ldots\ldots\ldots \quad 5.14$$

Equation (5.14) may now be used to estimate the magnitude of Q_T for an equally 'favourable' experimental situation to that used for the earlier estimate of Q_c. Thus, from the published data of Simmons (134) for a 30Å thick insulating oxide film of dielectric constant 2 and having a band-gap of 1 eV, one finds $\sigma_o \sim 5\times10^{-2}\,\Omega\,m^2$ and $K \sim 2\ m^2V^{-1}$, which with $V_{op} \sim 7V$ from figure 5.15, leads to Q_T $5\times10^{-16}C$. Since this is in such close agreement with typical experimental values of $\sim 10^{-15}C$, it can be safely concluded that charge exchange in the present experiments is almost entirely confined to electron tunnelling through the oxide films.

Therefore, from these theoretical conclusions and of section 2.1.5, it follows that the dependence of the charge reversal efficiency ($\bar{q}$) on surface oxidation as illustrated by the differences in traces A and B, in either figures 5.10 or 5.11, must be interpreted in terms of a thickness dependence of the tunnelling resistivity of the oxide film. Similarly, the dependence of $\bar{q}$ on the nature of oxide film (as illustrated in figures 5.10 and 5.11 respectively for the oxides on copper and stainless-steel targets), on comparison of $\bar{q}$ for a given film thickness at a given gap field E_o, mainly reflects the dependence of σ_T on band gap of these surface oxides and to lesser extent on its dielectric constant.

The differing response from atomically clean surfaces of copper and stainless steel (curve A of figures 5.10 and 5.11) can be attributed partly to the differences in their surface microtopography as evidenced by higher field emission at a given field E_o from copper than stainless-steel, but to a greater extent to the differences in work functions of these materials with respect to the work function of the iron particle (see table 5.2), where the latter (see section 2.1.1b) can result in the particle/target exhibiting forward bias ($\phi_T > \phi_p$) as opposed to reverse bias ($\phi_T < \phi_p$) characteristics or simply alter the degree of a given bias condition.

Similarly, in the case of titanium target, its unusually high charge reversal efficiency with charge reversal even at zero applied field, as illustrated in figure 5.10, can only be interpreted in terms of some extra intrinsic charge contribution arising from significantly differing work functions of the two members (see table 5.2). So that, at zero applied bias, the reverse charge is purely the result of $\backsim$ 0.6V contact potential or $\backsim 10^8 Vm^{-1}$ axial field (across a $\backsim$ 40Å gap, corresponding to the combined thickness of oxide films on iron and titanium) giving rise to charge flow from the titanium target

Material	Property						
	(172)(214) Work function $\bar{\Phi}$ eV	(172) Bulk resistivity ρ $\mu\Omega$/cm	(226)(227)(228) Type of Oxide film	Film resistivity ρ_f Ω/cm	Band Gap eV	more recent (230) $\bar{\phi}$ eV	
Fe	4.4	~10	F_2O_3 Fe_3O_4	10^{3-5}	E_a=0.3-1.5	4.6	
Cu	4.4	~1.8	CuO Cu_2O	3×10^3 10^3	E_a=2.6	4.6 4.29 4.51	
Cr	4.38	~10	CrO	10^5	E_a=0.4 $\epsilon \sim 8$	4.19 4.44	
Ti	4.14	~50	TiO_2 TiO Ti_2O_3	10^8	E_g=3.6-6.7		
Pb	3.94	~20	PbO Pb_2O Pb			3.83	
C	4.81	~4300 -7500					

Table - 5.2

to the iron particle. When voltage is applied and the titanium electrode is negatively biased, then forward bias ($\phi_p > \phi_T$) behaviour is obtained. It is important to note the work function values used above are for atomically clean surfaces and can vary $\backsim \pm$ 0.2V in published values or more depending on the measurement technique used e.g. contact potential, thermionic emission or photoelectron. Similar variations in the work function values may simply be obtained over the different single crystal faces of a polycrystalline sample. Additionally, however, large changes in the work functions can result from surface contamination such as adsorption or chemisorbtion of foreign gas atoms. In the above case for instance, from equation 5.3.1 it follows that chemisorption of electronegative gases like O_2 will decrease the work function of both these metals.

Furthermore, this unusually efficient electrical conductivity through what is believed to be a protective - strongly insulating film (band gap $\backsim$ 3-6 eV) on Ti (which itself exhibits relatively high bulk resistivity $\backsim$50 $\mu\Omega$/cm c.f. 1.8 $\mu\Omega$/cm for copper), can only be explained in terms of the following alternatives. (i) As shown in section 5.4.3, TiO_2 is not the only species of the ambient oxide film on titanium, but that the oxide is combination of two or more oxides such as TiO, which has metallic conductivity (10^{-4} Ω cm), or Ti_2O_3, which exhibits semiconductor behaviour but is well known (223) (227) (228) to undergo semiconductor-to-metal transition at temperatures not much higher than room temperature. (ii) Because of the high fields that are produced at close approach $\backsim 10^9 Vm^{-1}$, breakdown of the highly insulating films like TiO_2 may be occurring, since the breakdown limit for this type of oxide is $\backsim 2 \times 10^7 Vm^{-1}$.

The exponential type of behaviour of $\bar{q}$ with E_o as exhibited by all surfaces (see figures 5.9.-11) indicates how the reverse charge progressively increases with E_o, towards its limiting maximum value. It can also be seen that there is a remarkable similarity between this experimental behaviour and the theoretical curve, which gives the dependence of $\bar{q}$ on E_o for a typical 1μm diameter particle with an initial charge q_1 of 10^{-15}C and rebound charge calculated from the equilibrium charge equation 2.1. It can further be seen in figure 5.9, that the stainless-steel curve lies well above and the copper and titanium curves lie well below the theoretical curve at low E_o values; with all the curves tending to somewhat merge at higher E_o values. This behaviour, clearly indicates that there is a modifying influence exerted by the intrinsically originating contact potential, which in the case of copper and titanium results in a forward bias behaviour and in case of stainless-steel a reverse bias behaviour. At higher applied fields, the apparent reduction in these intrinsic effects however can partly be attributed to the way the charge ratio's are plotted (i.e. a diminishing ratio with increasing E_o) and partly to the switching of the forward bais to reverse bias condition (see section 2.1.2), at some higher particle/plane voltage. It should however, be noted that when calculating this theoretical curve, additional field enhancement contributions due to the non-planar target surface microtopography typical of the diamond polished surface were not taken into account, and hence in order only to demonstrate the differing responses of the three materials comparison with standard diamond polished instead of atomically clean surfaces has been carried out. Presumably, if the field enhancement contributions are taken into account, then theoretical values which are closer to those from the atomically clean surfaces will be obtained but this should by no means influence the overall conclusions drawn above.

In order to compare the experimental with the theoretically predicted thickness - dependence of charge transfer, the tunnelling equation 5.18 above can be rewritten in its simplified approximate form,

$$Q_T \lessapprox \text{constant} \times \left[\exp(KV_{op})/\sigma_o \right] \quad \ldots\ldots\ldots \quad 5.15$$

since, as has been shown in section 2.1.5d, a and t_c are only slowly varying functions of the impact velocity. Hence, to a first approximation, the charge reversal behaviour can be interpreted in terms of σ_o and V_{op}, where values for σ_o can be extracted from the published data of Simmons (134) (assuming the electrical properties of the oxide discussed previously) and V_{op} may be calculated from equations (5.5) and (5.7) or directly from figure 5.15,for the 'typical' case of a 1μm microsphere carrying a charge of 10^{-15}C in a field of 5×10^{6}Vm^{-1}. Then, if $(Q_T)_1$ and $(Q_T)_2$ correspond to the charge exchanged with 30 and 80Å thick films respectively, the validity of equation (5.15) can be readily checked for the 'typical' event by comparing the experimental and theoretical values of the ratio $(Q_T)_1/(Q_T)_2$ for given target material. In fact, this calculation reveals a large discrepancy in the two ratios, with theory predicting a negligible charge transfer for oxide films $>$ 60Å thick. This discrepancy in the ratios can however be mainly attributed to the rather uneven nature of oxide films typically found on polycrystalline samples, especially those which may also have undergone extensive diamond polishing (see section 2.1.5d); in fact it is well known that thin oxide films $<$ 50Å appear in the discontinuous form of small islands (215) accordingly, the present experimental observations that $\leq$ 50% of incident particles undergo charge reversal for 30Å thick films and $\ll$10% for 70Å film can be cited in strong support of this proposal. It must also be recognised that the

non-uniform nature of these films can also result in quite large error in the thickness measurements by the ellipsometric technique (~1mm spot size), not to mention other errors being introduced by the use of approximate optical constants for atomically clean metal surfaces and for the oxide films, where these films may be a combination of two or more different species. The dependancies of the tunnel resistivity are complex and very sensitive to the physical parameters used in the model. Accordingly, since the magnitudes of most of these parameters are so ill-defined for the present system, it is questionable whether much reliance could be placed on computations that used this ideal theory in an attempt to discriminate between the present experimental regimes.

Lastly, it should be noted that the materials used in the present experiments were not of ultra-pure quality but commercial materials as in the case of titanium, copper, lead and iron, containing small amounts of impurities or alloys as in case of stainless steel. These impurities or the composition of the alloy can markedly affect the physical properties of these materials including the nature of oxide film that they may grow and thus significantly influence their electrical and mechanical responses under impact conditions.

5.7 Microparticle behaviour in a high voltage vacuum gap.

It now remains to discuss the implications of the above findings in connection with the multiple bouncing model for microparticle induced breakdown (55)(68)(72). For the mechanism to operate, it is essential that the kinetic energy of a microparticle is enhanced following each impact. Thus, from discussions in section 3.1 and assuming that the particle mass is conserved during impact, it follows that the condition

$$\frac{V_2}{U_1} > 1 \qquad \ldots\ldots\ldots \qquad 5.16$$

must be satisfied, or

$$\ldots\left[e^2 + \frac{1}{\bar{q}} \left[\frac{V_T}{V_0 + V_T} \right] \right]^{\frac{1}{2}} > 1 \qquad \ldots\ldots \quad 5.17$$

Then for the special case of $U_1 = 0$, corresponding to the real situation in a natural vacuum gap where the particle is initially at rest on its parent electrode, $V_0 = 0$ in the above equation, so that the breakdown criterian becomes,

$$e^2 + \frac{1}{\bar{q}} \geq 1 \qquad \ldots\ldots\ldots \qquad 5.18$$

It is clearly evident from this expression that both the mechanical and electrical aspects of microparticle impact behaviour, as respectively represented by e and $\bar{q}$, jointly govern the efficiency of the bouncing mechanism, with probably the electrical response playing a more dominant role since the mechanical coefficient ($e<1$) is squared. On the other hand, a survey of the present impact data indicates that the mechanical response will be more dominant, however a more detailed analysis taking into account some of the conditions actually existing in a "natural gap" e.g. higher fields/velocities and electrode originating particles etc., gives a remarkably good agreement with the predictions of eq. 5.18.

above as well as with the electrode material stability trends found in practice (see section 1.1.2).

This can be illustrated by first comparing the mechanical behaviour of carbonyl iron microspheres in a high voltage vacuum gap say for copper and stainless-steel electrodes, where from detailed data of figures 5.2a and 5.2b it is seen that only with stainless- steel are there occasional events where e approaches ~ 0.95, whereas with copper it never exceeds ~ 0.5. Which, respectively gives a breakdown probability of $e^2=0.9 : e^2=0.25$ or $\sim 3.6:1$ in favour of stainless-steel, this is completely the reverse to what is found in practice i.e. stainless-steel is a well known stable anode material outstanding in suppressing microcratering and has a breakdown voltage three times higher than copper. Secondly, if the charge reversal data from figures 5.10 and 5.11 respectively, is compared, say at a gap field $\sim 3 \times 10^6 Vm^{-1}$, one finds that the mean charge reversal response $(\frac{1}{\bar{q}})$ for copper is ~ 0.25 and stainless-steel ~ 0.12, giving a breakdown probability of $\sim 2:1$ in favour of copper, which is more in agreement with the electrode material stability trends. If now the respective e's and $\bar{q}$'s for the two materials are summed up according to eq.5.18; due to its dominant mechanical coefficient, stainless-steel is still $\sim 2:1$ more likely to breakdown than copper. However, in a real gap, since breakdown normally occurs at fields that are more than an order higher than those existing in the present studies, then the single transit particle velocities will be correspondingly higher so that impact behaviour is likely to be mainly inelastic and characterised for all materials by a low average e-value with large uncertainty. Whereas the charge reversal response $(1/\bar{q})$ is most likely to improve under these conditions. Finally if the case of titanium is considered, both from the point of view of its

mechanical ($e \sim 0.95$) and electrical ($\frac{1}{q} \sim 0.5$ at $3 \times 10^6 Vm^{-1}$) behaviour it appears to be the most favourable electrode material for initiating electrical breakdown by the multiple bouncing mechanism, this again is completely opposite to what is found in practice e.g. titanium is one of the highly ranked stable electrode materials with a breakdown voltage that is even higher than stainless-steel. But as mentioned in section 5.6 above, this highly efficient charge reversal response of Ti is only specific to the artificial situation of using carbonyl-iron microparticle which have significantly differing work functions to titanium and that the response of naturally occurring microparticle in a real gap situation may be quite different.

In conclusion therefore, the data currently available does not represent an exact simulation of a real gap, since in all cases 'foreign' particles are used whose mechanical and electrical properties are likely to differ markedly from microparticles composed of parent electrode material. Also, as seen from the above theoretical conclusions and those in chapter II, the picture is further complicated by the fact that in a real gap the situation is very complex, involving a multiplicity of factors which operating singly or accumulatively can influence the microparticle impact behaviour. But inspite of this, the present work has served to isolate various mechanical and electrical aspects of microparticle impact phenomena and so given a better insight into how the physical properties of high voltage electrodes can have a significant influence on the behaviour of trapped microparticles.

CHAPTER VI

CONCLUSION

6.1. Summary

A survey of the literature on vacuum insulation at the outset of this work indicated that electrical breakdown for small inter-electrode gaps ($\lesssim$1mm) is due to the field emission process and for large gaps ($\gtrsim$6mm) it is the result of the impact of high energy microparticles. Whereas for the intermediate range of gaps ($\sim$2-5mm) the picture is in some confusion, it would appear that since it is difficult to justify the high field enhancement factors necessary for a purely field emission induced breakdown, one must assume some form of microparticle induced breakdown as the only other alternative. In this case however, the single transit particle energies are too low to cause the formation of emission sites on the cathode or the vaporisation of the particle/target. Breakdown can be initiated by low energy particles by the trigger discharge process, but this mechanism requires large particles ($\gtrsim$50μm), such as are rarely observed in practice. Therefore, for the low-velocity micron submicron sized particles that have been commonly found to occur in large numbers, the initiation of breakdown can only be explained by postulating the existence of an intermediary energy enhancing mechanism. The most promising of these is the energy enhancement of a microparticle following a bouncing impact with efficient momentum and charge reversal. The aim of this work has been to carry out a detailed study of this proposed mechanism both experimentally and theoretically.

A sophisticated UHV experimental facility incoporating a specially designed low-velocity microparticle source with its associated in-flight velocity/charge detector and a simulated high field test gap has been developed to investigate the role of low-velocity microparticles in initiating breakdown in a high voltage vacuum gap.

This system is capable of delivering/detecting single, positively or negatively charged ($\sim 10^{-16}$-10^{-15}C), low-velocity ($\sim$1-500ms^{-1}), iron microspheres ($\sim$1-5μm) into the simulated(grid/plane target electrode) high field gap ($\sim$0-10^{7}Vm^{-1}) for normal incidence impact studies on a range of diamond polished electrode materials having oxidised or atomically clean target surfaces. Firstly, it has been demonstrated that bouncing impacts with efficient momentum and charge reversal can occur, which would represent an intermediary energy enhancing mechanism leading to breakdown in a high voltage gap. Secondly, from detailed comparative studies of the momentum and charge reversal efficiencies of different target materials a correlation with their mechanical and electrical properties has been demonstrated. Finally, from similar comparative studies of differing surface states such as ambient/heavily oxidised and atomically clean, the influence of the oxide-surface contamination films has also been established ; in situ argon ion etching and electron beam heating being used for target preparation and ellipsometry for its characterisation.

Theoretically, an associated sphere/plane model has been developed for detailed analysis of the many complex electrical and mechanical interactions that take place as a charged microparticle closely approaches, impacts and finally bounces off a plane electrode. The electrical phenomena considered include in-flight field emission, metal-insulator-metal tunnelling and Ohmic conduction. With a rigorous discussion on the theoretical computations of the electric field experienced by a charged microparticle in close-proximity to a plane electrode, dealing particularly with the previously neglected contributions arising from: (i) the presence of surface films in the form of oxides and adsorbed gases, (ii) the differences in the work functions of the materials under investigation.

The mechanical phenomena considered include, impact kinetics, surface damage, restitution factor, contact time and area. With detailed discussions in this case, on the differences in mechanical properties of a bulk material and a very small volume of surface. Moreover, in each instance the influence of a number of parameters such as, particle radius, impact velocity, particle/target surface field and surface condition has also been determined.

Results have been presented and compared on the mechanical and electrical aspects of microparticle impact behaviour in terms of the coefficient of restitution $\bar{e}$ and the ratio of the initial to reverse charge $\bar{q}$ respectively for six different target materials viz copper, stainless-steel, titanium, lead, carbon and mica - and for differing surface conditions such as ambient oxidised, heavily oxidised and atomically clean, in the case of Cu, stainless-steel and Ti electrodes.

It has been generally established that the "microscopic" mechanical behaviour of the materials studied follows the same general trend as found with corresponding macrosystems. However, there are considerable differences in the threshold velocity of plastic deformation and the amount of scatter obtained, that can reach up to $\backsim$50% at the higher impact velocities ($\gtrsim$100ms^{-1}). This observation has been interpreted as being mainly due to the differences in the mechanical properties of a very small localised volume of a surface and those of a bulk solid. These include, (i) the intrinsic differences in the mechanical strength of a single crystal and a polycrystalline sample and (ii) the extrinsic differences in the mechanical properties of a defect-free atomically clean, ideal planar surface and one with contamination films such as oxides, adsorbed gases and worked polish layers as well as non-planar surface microtopography.

The electrical behaviour has been shown to be predominantly controlled by electron tunnelling and that the mechanism is extremely

sensitive to the difference in work functions of the two interacting materials, the surface field and the thickness of the contamination films. From the comparison of Cu, stainless-steel and Ti electrodes, that are covered by similar thickness of films of their respective oxides, it has been further shown that the mechanism also depends on the properties of these films e.g. dielectric constant, band gap and conductivity etc.Furthermore, the experimental observation that the probability of an incident particle exhibiting charge reversal is ~10% for excessively oxidised electrodes is taken to indicate that the nature of surface oxidation on these polycrystalline electrodes, as typical of most transistion metals, is non-uniform and may vary in composition,i.e. the film grown is uneven in thickness and composes of two or more species of oxides with differing electrical and mechanical properties. So that, the data obtained relates only to impact events where local field oxidation conditions are particularly favourable.

Finally, the above findings have been shown to have important implications on the behaviour of naturally occurring microparticles in high voltage gaps formed between diamond polished electrodes. Whilst there are marked differences in the low-velocity impact behaviour among the target materials, there is a progressive overlap in the range of e-values found for the individual impact events at the higher fields. This suggests that the mechanical properties of electrodes are unlikely to play the dominant role in controlling the initiation of electrical breakdown resulting from multiple bouncing microparticle impact processes in high-field gaps. Instead the evidence suggests that it is the electrical properties of an electrode surface, through their controlling action on charge reversal mechanisms during the bouncing impact of a microparticle,that is the crucial factor.

6.2. Suggestions for future work.

It has clearly emerged from the work presented in this thesis that the microparticle impact phenomena is a highly complex process involving a variety of mechanical and electrical interactions which in practice are further complicated by use of non-ideal and improperly characterized surfaces. So that, whilst working with commercially used materials, as in the present experiments, may be justified for the first stage of studies when an immediate application is in mind and to gain a measure of the complexity of the problem. However, for the next stage of more refined fundamental work it is highly desireable to use better defined and more idealised situations. For instance: (i) The first and most obvious suggestion would be to use well characterised planar target surfaces such as single crystals of pure elements rather than diamond polished, commercial materials containing a high level of impurities. To assess the composition and structure, on the atomic scale, some of the more sophisticated techniques of surface physics should be employed. These will enable a quantitative correlation of the role of impurities, and surface contamination, such as oxidation and or adsorbed gases in various micro-impact processes. (ii) The range of materials investigated should be extended both in the types of powders used for microparticles and as planar targets; mainly in order to isolate the various factors involved. For example, to determine the influence of work functions use may be made of metal surfaces with vastly different work functions; to determine the effect of surface hardness materials with vastly differing mechanical properties could be employed and so on.

Theoretically, the improved field calculations developed in this work, which take into account the previously neglected effects due to differences in work functions of the interacting materials and the presence of surface contamination films, should be used to look again at processes like trigger discharge.

In addition, there are several modifications possible on the existing apparatus, one of these would be to incorporate an A/D converter with a microprocessor to output the "twin pulse" experimental data in a digitised form for convenient direct computor input. Thus, eliminating the laborious task of manually measuring each signal from the storage oscilloscope, at the same time improving the accuracy and speed of data aquisition and processing.

APPENDIX A

Poincare sphere

To represent elliptically polarised light, generally three parameters are required: (i) the ratio of minor to major axis, or ellipticity which is = b/a = tanβ; (ii) the azimuth of the major axis χ; and (iii), the rotation direction, conventionally positive if anti-clockwise looking towards the on-coming light.

Referring to the Poincaré sphere shown in figure A1, the longitude represents twice the azimuth, and the latitude represents twice the ellipticity. The factor 2 arises because rotation of a polaroid through 180 (i.e. 360 on the Poincaré sphere) results in an optically identical situation. The northern hemisphere represents clockwise rotations and the southern hemisphere, anti-clockwise rotations. The equator, β = zero, represents plane polarised light of variable azimuth. The poles, β = 45, represent circularly polarised light. Thus, it is deduced that any state of polarisation may be represented by a single point on the surface of the Poincaré sphere (P.S.).

In figure A2, the polariser and analyser scales are represented by π and α respectively. As usual (p) and (s) indicate the directions parallel and perpendicular to the plane of incidence. The dash notation represents the optically equivalent scale reading at 180.

If a plan of the Poincaré sphere, fig. A3 is considered, P_1 represents the plane polarised light falling on the specimen, having azimuth ψ (shown as longitude 2ψ on P.S.). Since in Fig.2.23 $\tan\psi = \frac{I_s}{I_p}$, then $\pi_p P_1$ represents Is and $\pi_s P_1$ represents Ip, the components perpendicular and parallel to the plane of incidence respectively. The relative amplitude reduction on reflection alters the ratio of these components to $\frac{\pi_p P_1}{\pi_s P_1}$.

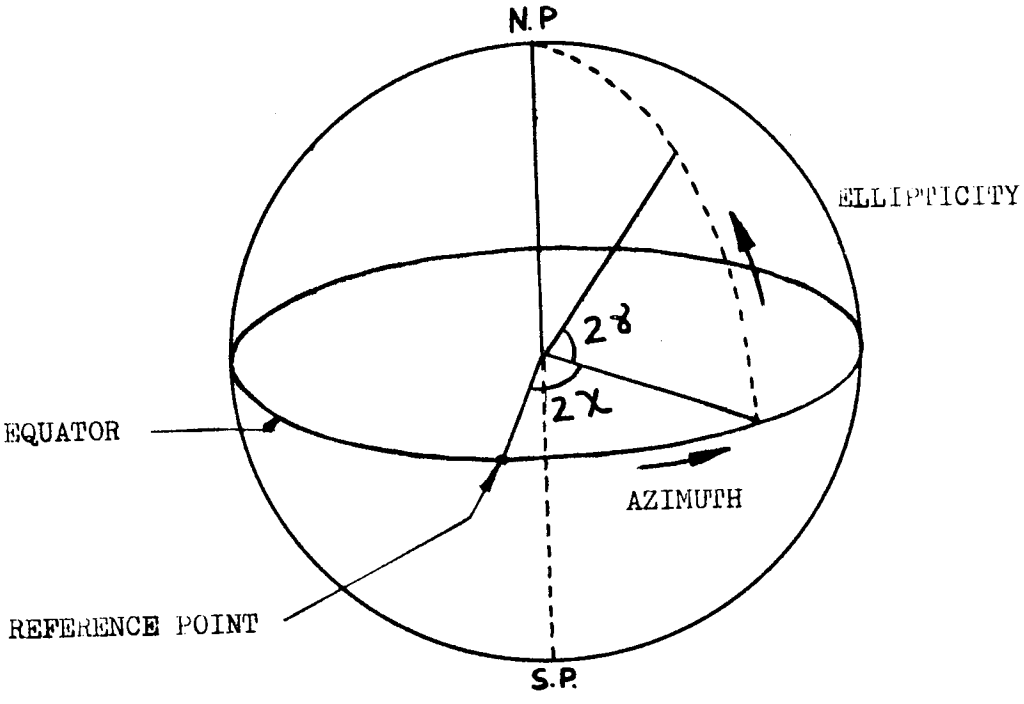

POINCARE SPHERE

Figure A1

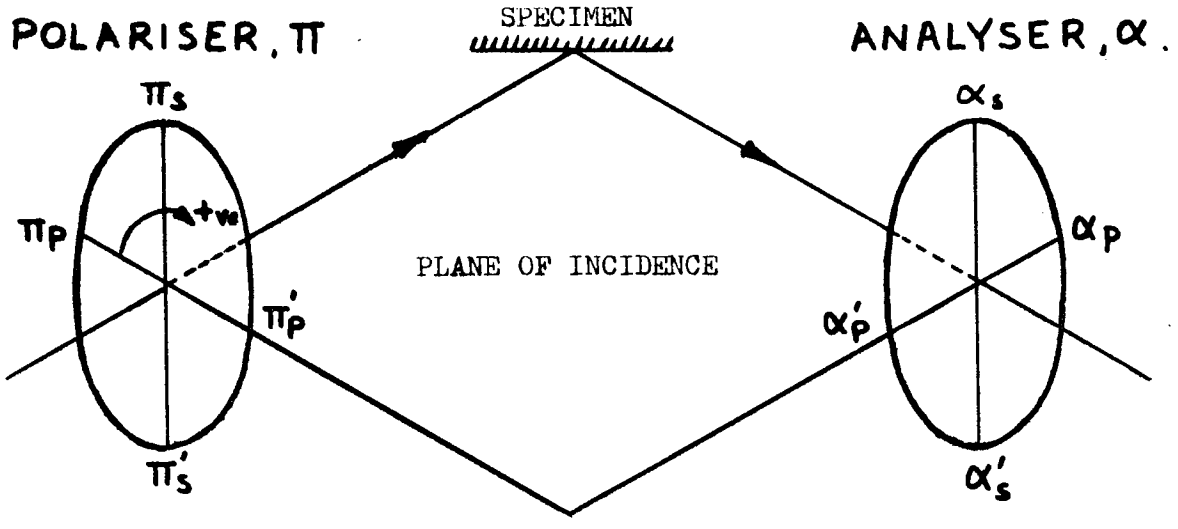

Figure A2

The azimuth of P_1 (i.e. the setting of the polariser) is adjusted until the components are equal after reflection and can be represented by the point P' on fig. A3. P_1 is therefore the polariser setting for extinction between πp and πs which are 90° apart, but shown as 180° on P.S.

Consider the relative phase retardation Δ, between the (p) and (s) components. The effect of the reflection from the specimen as regards phase is to convert the linear vibration P' to an elliptical vibration $\not\equiv$ by rotation about the axis πp πs, by an amount Δ . See fig. A4 (clockwise rotation as seen from the fast axis, say πs).

The effect of the compensator will now be considered. The compensator fast axis is locked at azimuth Q at 45 degrees to the plane of incidence as shown in fig. A5. Note that Q coincides with P'. The compensator introduces a relative retardation of 90° (i.e. one quarter wavelength) so that any elliptical vibration on the great circle Q'OP' is converted into a plane polarised vibration represented by a point on the equator. Therefore, the elliptically polarised light is converted to plane polarised light P" on the equator. During this rotation the angle remains constant. Finally, the plane polarised light P" passes to the analyser adjusted into the 'crossed' position, A_1 (A_1 is at 90° to P" but is shown as 180° on P.S.)

Referring to fig. A5 the relative phase retardation Δ may be calculated. If the analyser azimuth for extinction A_1 is at a measured angle x to $\propto s$ (shown as 2x on P.S), then

$$2x = 90 + \Delta$$

$$\Delta = 2x - 90$$

For convenience Δ has been shown less than 90° but the method

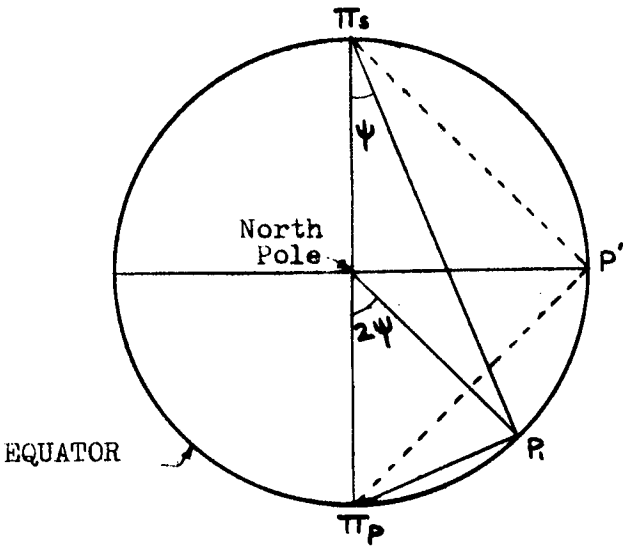

Plan of POINCARE SPHERE

Figure A3

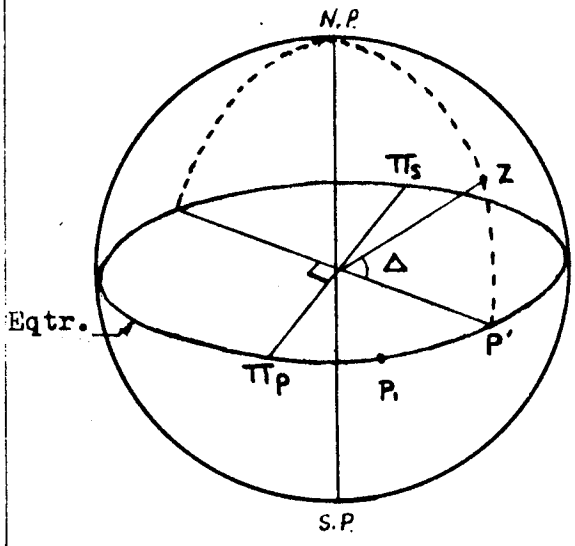

Reflected light is Elliptically Polarised and is represented by point Z.

Figure A4

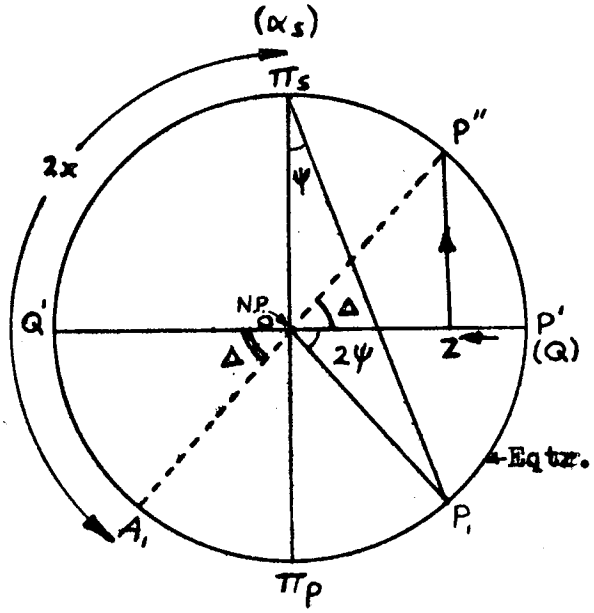

Figure A5

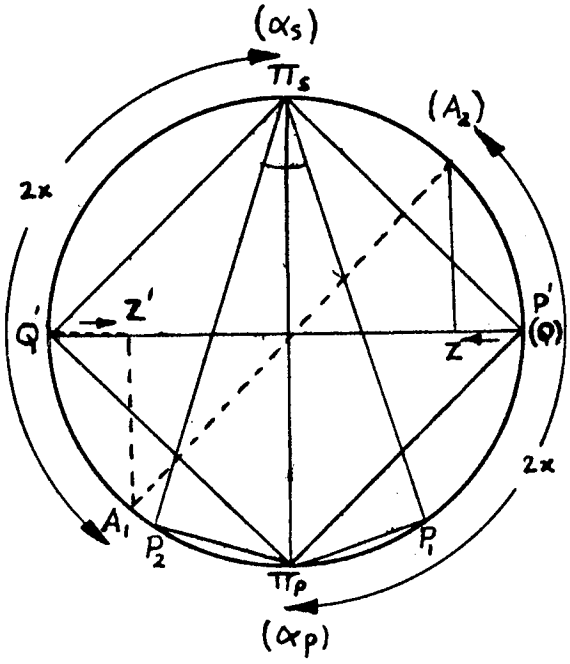

Figure A6

is still applicable if Δ is greater than 90°.

As well as the polariser position for extinction P_1, there is also a position P_2 which is symmetrically placed about πp. See fig. A6. There are also two non-significant positions at 180° to each other. Fig. A6, also shows the corresponding analyser extinction positions A_1 and A_2 which are seen to be perpendicular to each other (180° apart on P.S.). The southern hemisphere is represented by the dotted lines. The scheme that develops, then, is as follows: the two polariser positions for extinction, P_1 and P_2 are symmetrical about πp (the plane of incidence). The two corresponding analyser positions A_1 and A_2 are at right angles to each other, and are at an angle (x) from αs and αp respectively. Two more pairs of extinction position, designated 3 and 4, exist at 180° to all the above positions. Furthermore, compensation of the reflected light is also possible with the fast axis at an azimuth of -45°, i.e. with the compensator locked at 90° from its first position. In this case the compensation is affected by an anti-clockwise rotation of the point $\not\equiv$ about the axis Q'P' in fig. A5, instead of a clockwise rotation. The polariser extinction positions are unaffected but the analyser extinction positions occur at the same angle (χ) on the other sides of αs and αp. Four more pairs of extinction positions are thus produced, making a total of eight pairs, and all of these in turn have an equivalent position at 180° so that 16 pairs of measurements are possible. Finally, rotation of the compensator through 180° in both cases doubles the possible number of results, making 32 pairs in all.

REFERENCE

1. Wood, R.W., Phys. Rev., 5, 1 (1897)
2. Denholm, A.S., Trump J.G., and Gale, A.J., Prog. in Astronautics and Rocketry, 3 745 (1961)
3. Hawley, R., and Craik, R.L., Elect. Times, 143, 43 (1963)
4. Hawley, R., and Zaky, A.A., Prog in Dielectrics, 7, 115 (1967)
5. Arnal, R., C.R. Acad. Sci., 237, 308 (1953)
6. Bourne, H.C., J. Appl. Phys., 26, 625 (1955)
7. Millikan, R.A., and Sawyer, R.A., Phys. Rev. 12, 167 (1918)
8. Denholm, A.S., Canad. J. Phys., 36, 476 (1958)
9. Steib. G.F., and Moll, E., J Phys. D: Appl. Phys., 6, 243 (1973)
10. Bolin, P., Tse, F., Bell, W., and Mulchay, M., Ins. Ccts., 59 (1972)
11. Trump, J.G., Collog. Int. Cent. Nat. Rech. Sci., Grenoble (1960)
12. Hadden R.J.B., A.E.R.E. Report, G/M, 92 (1951)
13. Van Oostrom, A. Proc. 4th Int. Symp. on Disch. and Elec. Ins. in Vac. Waterloo, 1 (1970).
14. Donaldson, E.E., and Rabinowitz, M., M.I.T. - 22nd Ann. Conf. Phy. Elec. (1962)
15. Jedynak, L., Phd. Thesis, Mass. Ins. of Tech. (1962)
16. Rabinowitz, M., Phd. Thesis, Washington State Univ. (1963)
17. Slivkov, I.N., Sov. Phys. Tech. Phys., 3, 708 (1963)
18. Maitland, A., Brit. J. Appl. Phys., 13, 122 (1962)
19. Arnold, K.W., Britton, R.B., Zanon, S.C., and Denholm, A.S., Proc. 4th Int. Conf. Ionization Phenomenon on Gases, 2, 101 (1963)
20. Alpert. D., Lee, D.E., Lyman, E.M., and Tomaschke, H.E., J. Appl. Phys. 38, 880 (1967)
21. Farrel, G.A., J. Appl. Phys., 33, 96 (1962)

22. Wijiker, W.J., Appl. Sci. Res. 9, B, 1 (1961)

23. Halpern, J., Everhart, E., Rapuano, R.A., and Slater, J.C., Phys. Rev., 69, 688A (1964)

24. Rohrbach, F., Proc. 4th Int. Symp. on Disch. and Elec. Ins. in Vac. Waterloo 68 (1970)

25. van Atta, L.C., van de Graff, R.J., and Barton, H.A., Phys. Rev., 43, 158 (1933)

26. Ionov, N.I., Sov. Phys. - Tech. Phys., 5, 527 (1960)

27. Mansfield, W.K., Brit. J. Appl. Phys., 11, 454 (1960)

28. Arnal, R., Ann. Phys. 10, 830 (1955)

29. Tarasova, L.V., Proc. 3rd Int. Symp. on Disch. and Elec. Ins. in Vac. Boston (1968)

30. Trump, J.G., and van de Graff. R.J., J. Appl. Phys. 18, 327 (1974)

31. Pivovar, L.I., and Gordienko, V.I., Soviet Phys. Tech. Phys. 7, 908 (1963)

32. Germain, C., and Rohrbach, F., 2nd Int. Symp. on Ins. of High Voltages in Vac. Boston (1966)

33. Fowler, R.H., and Nordheim, N., Proc. Roy. Soc. A119, 173 (1928)

34. Dyke, W.T., and Trolan, J.K., Phys. Rev., 89, 799 (1953)

35. Little, R.P., and Whitney, W.T., J. Appl. Phys., 34, 2430 (1963)

36. Biradar, P.I., and Chatterton, P.A., Proc. 3rd Int. Symp. on Disch. and Elec. Ins. in Vac. Paris 35 (1968)

37. Fursei, G.N., and Vorontsov-Vel'yaminov, P.N., Soviet Phys. Tech. Phys., 12, 1370 (1968)

38. Alpert, D., Lee, D.A., Lyman, E.M., and Tomaschke, H., J. Vac. Sci. Tech., 1, 35 (1964)

39. Bennette, C.J., Swanson, L.W., and Charbonnier, F.M., J. Appl. Phys., 38, 634 (1967)

40. Davies, D.K., and Biondi, M.A., J. Appl. Phys., 39, 2979 (1968)

41. Kerner, K. and Raether, H., Z. angew. Phys., 6, 212 (1954)

42. Kerner, K., Z. angew. Phys. 8, 1 (1956)

43. Schottky, W., Z. Phys., 14, 63 (1923)

44. Morrant, M.J., Proc. Soc., 688, 513 (1955)

45. Chatterton, P.A., Proc. Phys. Soc., 88, 231 (1966)

46. Charbonnier, F.M., Bennette, C.J., and Swanson, L.W., J. Appl. Physl, 38, 627 (1967)

47. Utsumi, T., J. Appl. Phys., 38, 2989 (1967)

48. Nottingham, W.B., Phys. Rev., 59, 907 (1941)

49. Williams, D.W., and Williams, W.T., J. Phys. D: Appl. Phys. 5, 280 (1972)

50. Boyle, W.S., Kisiliuk, P. and Garner, L.H., J. Appl. Phys., 26, 720 (1955)

51. Little, R.P., and Smith, S.T., J. Appl. Phys., 36, 1502 (1965)

52. van Oostrum, A., Proc. 6th Int. Symp. on Disch. and Elec. Ins. in Vac. Swansea (1974)

53. Cranberg, L., J. Appl. Phys., 23, 518 (1952)

54. Latham, R.V., and Braun, E., J. Phys. D: Appl. Phys., 36, 1502 (1968)

55. Latham, R.V., and Braun, E., J. Phys. D. Appl. Phys., 3, 1663 (1970)

56. Heard, H.J., and Lauer, E.J., U.C.R.L. Report 1622 (1952)

57. Browne, P.F., Proc. Phys. Soc., 68B, 564 (1955)

58. Tarasova, L.V., and Razin, A.A., Sov. Phys.- Tech. Phys., 4, 879 (1960)

59. Schwabe, H., Z. Agn. Phys., 12, 244 (1960)

60. Hawley, R., and Walley, C.A., Nature 190, 252 (1960)

61. Rozanova, N.B., and Niziaev, V.I., Rad. Eng. and Elec. Phys., 5, 253 (1960)

62. Razin, A.A., Tarasova, L.V., and Tsukerman, V.A., Rad. 1. Elec. 5, 187 (1960)

63. Rohrbach, F., Cern Courier 9, 208 (1969)

64. Piuz, F., Cern Report TC-L/Int. 72 (1972)

65. Hurley, R.E., and Parnel, T.M., J. Phys. D. Appl. Phys., 2, 881 (1969)

66. Menon, M.M., and Srivastava, K.D., J. Appl. Phys., 45, 2094 (1974)

67. Buekema. G.P., J. Phys. D: Appl. Phys., 7, 1740 (1974)

68. Birdar, P.I., and Chatterton, P.A., S. Agn. Phys., 30, 163 (1970)

69. Boulloud, A., Le Vide 99 (1962)

70. Zeitoun-Fakiris, A., Goldman, M., C.R. Acad. Sci., Paris, Ser. B., 273, 521 (1971)

71. Rozanova, N.B., 12V. Akad Nauk s.s.s.R. sev F12. 26 1438 (1962)

72. Olendzkaya, N.S., Rad. Eng. and Elec., Phys. 8, 423 (1963)

73. Hurley, R.E., Vacuum 19, 283 (1969)

74. Cornish, J.C.L., Latham, R.V., and Braun, E., Proc. 4th Int. Symp. on Disch. and Elec. Ins. in Vac. Waterloo 28 (1970)

75. Smith, D., and Adams, N.G., J. Phys. D: Appl. Phys., 6, 700 (1973)

76. Auer, S., and Sitte, K., Earth and Plan. Sci. Lett. 4, 178 (1968)

77. Dietzel, H., Neukum, G., and Rauser, P., J. Geophys. Res. 77, 1375 (1972)

78. Shelton, H., Hendricks, C.D., and Wuerker, R.F., J. Appl. Phys., 31, 1243 (1960)

79. Martynov, E.P., Electronnya Tekhnika, Serio, 3 (1968)

80. Fabiniak, R.L., T.J., Dodd, R.A., and Jedynak. L., J. Appl. Phys., 42, 2231 (1971)

81. Latham, R.V., J. Phy. D. Appl. Phys., 5, 2044 (1972)

82. Udris, Y.Y., Int. Conf. on Gas Discharges. London 108 (1970)

83. Menon, M.M., and Srivastava, K.D., J. Appl. Phys., 45, 3832 (1974)

84. Slattery, I.C., Friichtenict, J.F., and Hansen, D.O., Appl. Phys. Letters, 7, 23 (1965)

85. Razanova, N.B., Bull. Acad. Sci. USSR. Phys. Sev., 26, 1462 (1962)

86. Udris, Y., Rad. Eng. and Elec. Phys., 5, 226 (1960)

87. Phoshekhonov, P.V., and Pogorelskii, M.M., Sov. Phys. Tech. Phys., 14, 811 (1969)

88. Martynov, E.P., and Ivanov, V.A., Rad. Eng. and Elec. Phys., 14, 1732 (1969)

89. Slivkov, I.N., Sov. Phys. Tech. Phys., 2, 1928 (1957)

90. Germain, C., and Rohrbach, F., Proc. Int. Conf. on Ionisation Phenomena in Gases, Paris, 111, (1963)

91. Slivkov, I.N., Sov. Phy. Tech. Phys., 15, 238 (1970)

92. Martynov, E.P., Sov. Phys. Tech., 16, 1364 (1972)

93. Chatterton, P.A. Menon, M.M. and Srivastava, K.D., J. Appl. Phys. 43, 4536 (1972)

94. Chakrabarti, A.K., Ph.D. Thesis University of Liverpool (1975)

95. Chakrabarti, A.K. and Chatterton, P.A., Proc. 6th Int. Conf. on Disch. and Elec. Ins. in Vac., Swansea 16 (1974)

96. Poshekhonov, P.V. and Solovyev, I.V., Rad. Eng. and Elec. Phys. 16 1545 (1971)

97. Latham, R.V. and Chapman, C.J.S., J. Phys. E: Sci. Instrum. 3 732 (1970).

98. Fane, R.W., Neal, W.E.J. and Latham, R.V., Phys., 44, 740 (1973)

99. Rohrback, F., Cern Report (1971)

100. Lebdev, N.N. and Skalskaya, I.P., Soviet Phys. Tech. Phys., 7, 268 (1962)

101. Frenkel, J., Phys. Rev., 36, 1604 (1930)

102. Harper, W.R., Contact and Frictional Electrification (London: Oxon U.P.)

103. Holm, R., Electric Contact Handbook, (Berlin: Springer) (1958)

104. Bjork, R.L., Proc. 6th Symp. on Hypervelocity Impact, (U.S. Dept. of Commerce Washington D.C.), 2, 1 (1963)

105. Hume-Rothery, W., in 'Solid State Surface Science' (M. Green, ed.) Vol. 1., p. 179, Dekker, New York, (1969)

106. Brunauer, S., The Adsorption of Gases and Vapours, (Princeton: Princeton V.P.) (1943)

107. Samuels, L.E., J. Instit. Metals, 51 (1956)

108 Latham R.V., Proc. 5th Int. Symp. on Disch. and Elec. Ins. in Vac., Poznan, 124 (1972)

109. de Boer, J.H., Advances in Catalysis, 8, 18 (1956)

110. Bowden, F.P. and Tabor, D., The Friction and Lubriaction of Solids (Lond: Oxford U.P.) (1964)

111. Bedford, D.K., J. Phys. A : Gen. Phys., 4, L14 (1971)

112. Feynman,R.P., Lieighton, R.B. and Sands, M., Feynman Lectures on Physics, (Massachusetts: Addison Wesley) 2, 710 (1970)

113. Vibrans, G., J. Appl. Phys., 35, 2855 (1964)

114. Read, F.H., Adams, A., and Soto-Montiel, J.R., J. Phy.E: Sci. Instrum., 4, 625 (1971)

115. Kinslow, R., ed., High Velocity Impact phenomena (N.Y.: Academic Press) (1970)

116. Rudolph, V. Z., Naturf., 24a, 326 (1969)

117. Tabor, D., Proc. R. Soc. A. 192, 247 (1948)

118. Andrews, J.P., Phil. Mag., 9, 593 (1930)

119. Taylor, G.I., J. Ins. C. Eng., 26, 486 (1946)

120. Cook, M.A., The Science of High Explosives. (N.Y.: Reinhold) (1958)

121. Goldsmith, R., The Theory and Physical Behaviour of Colliding Solids (Lond : Dover) (1962)

122. Hertz, H., J. Reine. Agnew, Math. 92, 56 (1889)

123. Tabor, D., The Hardness of Metals (Oxford : Clarendon Press) (1958)

124. Bowden, F.P., and Yoffe, A.D., Fast Reactions in Solids (Lond : Butterworth) (1958)

125. Bowden, F.P., and Perrson, P.A., Proc. Roy. Soc. A., 260, 433 (1961)

126. Danson, R., Pyrodynamics, 5, 39 (1967)

127. Powel, F., and Quince, B.W., J. Phys. D: Appl. Phys. 5 1540 (1972)

128. Beilby, G., Aggregation and Flow of Solids. (Lond: Macmillan) (1921)

129. Reather, H., Ergebn. exakt. Naturw., 24, 54 (1951)

130. Davies, R.M., Proc. Roy. Soc., A 197, 416 (1949)

131. Sommerfield, A., and Bethe, H., Handbuch der Physik, (Berlin: Springer Verlag), 24, 450 (1933)

132. Holm, R., and Miessner, W., Z, Physik, 74, 715 (1932)

133. Stratton, R., J. Phys. Chem. Solids, 23, 1177 (1963)

134. Simmons, J.G., J. Appl. Phys., 34, 1793 (1963)

135. Simmons, J.G., J. Appl. Phys., 34 2581 (1963)

136. Hartman, T.E., J. Appl. Phy., 35, 3283 (1964)

137. Mott, N.F. and Gurney, R.W., 'Electronic Processes in Ionic Crystals', (Lond: Oxford, U.P.) (1948)

138. Lamb, D.R., Electrical Conduction Mechanism in Thin Films (Lond: Methuen) (1967)

139. Schottky, W., Z. Physik, 113, 367 (1939)

140. Geppert, D.V., J. Appl. Phys. 34, 490 (1963)

141. Pittelli, E., Solid - State Electron., 6, 667 (1963)

142. Penley, J.C., Phys. Rev., 128, 596 (1962)

143. Schmidlin, F.W., J. Appl. Phys., 37, 2823 (1966)

144. Grundlock, K.H., and G. Heldmann, Phys. Solid State, 21, 575 (1967)

145. Schnup., Solid - State Electron., 10, 785 (1967)

146. Simmons, J.G., Brit. J. Appl. Phys. 18, 269 (1967)

147. Stratton, R., Phys. Rev., 90, 515 (1963)

148. Roy, D.K., Phys. Stat. Sol., 2, K241 (1970)

149. Pollack, S.R., and Morris, C.E., J. Appl. Phys., 35, 1503 (1964)

150. Hurst, H.G., and Ruppel, W., Naturforsch, Z., 19a, 573 (1964)

151. Pollack, S.R., and Morris, C.E., Trans. AIME, 233, 502 (1965)

152. Mirolyubov, N., Kostenko, M., V., Levnhshtein, M., L., and Tnxodeev, N.N., Metody Rasch. Elec. Polei. M. Vycshaya Shkola (1963)

153. Burgess, R.E., Kroemer, H., and Houston, J.M., Phys. Rev., 90, 515 (1953)

154. Jeans, J.H., The Mathematical Theory of Electricity and Magnetism, (Lond: Cambridge, U.P.) (1958)

155. Lorrain, P., and Corson, D.R., Electromagnetic Fields and Waves, (San Francisco: W.H. FREEMAN & Co.) 150 (1970)

156. Atkins R.H., Theoretical Electromagnetism, Lond: Heineman 1962

157. Morse, P.M. and Feshback, H., Methods of Theoretical Physics II (N.Y: McGraw Hill) 1300 (1953)

158. Tolansky, S., Surface Microtopography, (Lond: Interscience) (1960)

159. Dyson, J. and Hirst, W., Proc. Phy. Soc. Lond., 47, 309 (1954)

160. Cabrera, N. and Mott, N.F., Rep. Phys. Soc. (Progr. Phys.), 12, 163 (1948)

161. Bloomer, R.N., Brit., J. Appl. Phys., 8, 40 (1957)

162. Trapnell, B.M.W., Chemisorption (Lond: Butterworths) (1955)

163. Good, R.H., and Muller, E.W., Handb. d. Phys., (Berlin : Springer -Verlag), 21, 176 (1956)

164. Anderson, P.A., 1949, Phys. Rev., 59, 1034 (1941)

165. Davisson, C., and Germer, L.H., Phys. Rev., 30, 705 (1927)

166. Grigson, C.W.B., Rev. Sci. Instr., 36, 1587 (1965)

167. Vandeslice, T.A., and Whetten, N.R., J. Chem. Phys., 37, 535 (1962)

168. Hagstrum, H.D., Phys. Rev., 96, 336 (1954)

169. Ditchburn, R.W., J. Opt. Soc. Am. 45, 734 (1955)

170. Drude, P., Ann. Phys. Lpz. 34, 489 (1888)

171. Winterbottom, A.B., Optical Studies of Metal Surfaces (Trondheim : F. Bruns Bokhandel), (1955)

172. Weast, R.C., ed. Handbook of Chemistry and Physics (C.R.C) (1974)

173. McCrackin, F.L., Passaglia, E., Stromberg, R.R., and Steinberg, H.L., J. Res. N.B.S., 674,(1963)

174. Allen, F.G., Eisinger, J., Hagstrum, H.D., and Law, J.T., J. Appl. Phys., 30, 1563 (1959)

175. Langmuir, I., and Villars, D.S., J. Amer. Chem. Soc., 53, 2186 (1931)

176. Wehner, G.K., Advanc. Electron. Electron Phys., 7, 239 (1923)

177. Kingdon, K.H., and Langmuir, I., Phys. Rev., 22, 148 (1923)

178. Fansworth, H.E., Ann. N.Y. Acad. Sci., 101, 658 (1963)

179. Fansworth, H.E., and Tuul, J., J. Phys. Chem. Solids, 9, 48 (1958)

180. Young, F.W.Jr. and Gwathmey, A.T., J. Appl. Phys., 31, 225 (1960)

181. Boulloud, A., Proc 3rd Int. Symp. on Disch and Elec. Ins in vac., Paris. 77 (1968)

182. Franks, J., and Ghander, A.M., Vacuum 24, No. 10, 489 (1975)

183. Harrison, J.A., Brit. J. Appl. Phys., 18, 1617 (1967)

184. Llewellyn-Jones, F., and Morgan, C.G., Proc. Roy. Soc. 218, A.88 (1953)

185. Hansen, D.O., and Roy, N.L., Nucl. Instr. and Meth., 40, 209 (1966)

186. Smith, D., and Adams, N.G., and Khan, H.A., Nature, 252, 101 (1974)

187. Hill, R.M., and Weaver, C., Trans. Faraday Soc. 54, 1140 (1958)

188. Archer, R.J., J. Opt. Soc. Am. 52, 970 (1962)

189. Cathcart, J.V., Epperson, J.E., and Peterson, C.F., Acta Metallurg. 10, 699 (1962)

190. Zuev, K.P., and Dolgintsev, V.D., Izv. Akad. Nauk SSSR, Neorg. Mater. 4, 1498 (1968)

191. Dettore, J.F., Knorr, T.G., and Vaughan, D.A., Ellipsometry in the Measurement of Surfaces and Thin Films ed. E. Passaglia (Washington: NBS) 245 (1964)

192. Boris, B.S., and Sparks, C.J., Acta Crystallogr. 14, 569 (1961)

193. Battacharyga, D.P., and Mukherjee, P.N., J. Appl. Chem. Biotechnd. 22, 889 (1972)

194. Anderson, J.S., and Greenwood, N.N., Proc. R. Soc., A 215, 353 (1952)

195. Bloem, B.S., and Sparks, C.J., Acta Crystallogr. 14, 569 (1961)

196. Verwey, E.J.W., Haaijman, P.W., Romeijn, F.C., and Oosterhout, G.W., Philips. Res. Rep. 5, 173 (1950)

197. Hayfield, P.C.S., and White, G.W.T., Ellipsometry in the Measurement of Surfaces and Thin Films. ed. E. Passaglia (Washington : NBS) 245, (1964)

198. Feng, J.S-Y., Pashley, R.D., and Nicolet, M.A., J. Phys. C: Solid St. Phys. 8, 1010 (1975)

199. Butcher, E.C., Dyer, A.J., and Gilbert, W.E., J. Phys. D: Appl. Phys. 1, 1673 (1968)

200. Blankenburg, G., Ann. Phys. 14, 308 (1954)

201. Park, R.L., Houston, J.F., and Schreiber, D.G., J. Vac. Sci. Technol. 9, 1023 (1972)

202. Roberts, S., Phys. Rev. 118, 1509 (1960)

203. Hancock, P. and Mayne, J.E.O., J. Chem. Soc., 4167 (1958)

204. Gulbransen, E.A., Trans Electrochem. Soc., 81, 327 (1942)

205. Gulbransen, E.A., ibid., 82, 375 (1942)

206. Winterbottom, A.B., J. Iron. Steel Inst. Lond., 156, 9, (1950)

207. Andreeva, V.V., Trudy Inst. Fiz-Khim. Akad. Nauk. Novye Metody Fiz-Khim. Issledovanii, No. 2, 79 (1957)

208. Andreeva, V.V., and Alekseeva, E.A., Doki., (Proc.) Acad. Sci. U.S.S.R. Phys. Chem. Sect. 134, 106 (1960)

209. Menard, C., J. Opt. Soc. Am. 52, 427 (1962)

210. Johnson, D.L., and Tao, L.C., Surf. Sci. 16, 396 (1969)

211. Tomashov, N.D., Alkovskii, R.M., and Tabushnerev, M., Dokl. Akad. Nauk. (USSR), Tom. 141. 2, (1961)

212. Schlichta, P.J., Growth and Perfection of Crystals, (Lond: Chapman and Hall) 214, (1958)

213. Muller, E., Structure and Properties of Thin Films, (N.Y. and Lond: J. Wiley), 147, (1959)

214. Samsanov, G.V., ed., Handbook of Thermionic Properties (N.Y: Plenum Press) (1968)

215. Haase, O., Z. Naturforsch, 11a, 46 (1956)

216. Smith, D.A., and Bowkett, K.M., 4th Euro. Conf. on Elec. M.C., Rome, 1, 261 (1968)

217. Gane, N. and Bowden, F.P., J. Appl. Phys. 39, 1432 (1968)

218. Gane, N., Proc. Roy. Soc. A, 317, 367 (1970)

219. Gane, N., and Cox, J.M., Phil. Mag., 22, 881 (1970)

220. Gilman, J.J., J. Appl. Phys. 30, 1584. (1959)

221. Culver, R.V., and Tompkins, E.C., Advances in Catalysis., 11, 67 (1959)

222. Burstein, R.C., and Shurmorkaya, N.A., Surface Science, 2, 2102 (1964)

223. Yahia, J., Phys. Rev., 130, 1711 (1963)

224. Hollox, G.E., and Smallman, R.F., Phil. Mag., 13, 11, (1966)

225. Walbeck, P.G., and Gilles. P.W.J., J. Ann. Ceramic, Soc. 49, 180 (1966)

226. Sewell, P.B., Stockbridge, C.D., and Cohen, M., J. Electro. Chem. Soc. 109, 928 (1963)

227. Adler, D., Solid State Phys., Eds. Seitz, F., Turnbull, D., and Ehrenreich, H., 21, 1 (1968)

228. Howe, A.T., and Fensham, P.J., Quart. Rev. (Chem. Soc. London), 21, 507 (1967)

229. Dekker, A.J., Solid State Physics, (New York: Prentice Hall) (1957)

230. RIVIÈRE, J.C., in 'Solid State Surface Science' (M. Green, ed.) volume 1, p. 179. Dekker, New York, 1969.

AKNOWLEDGEMENTS

It is a pleasure to thank the following people all of whom have contributed in some way or other in making this work possible.

My supervisor Dr. R.V. Latham for his interest and advice throughout the course of this project and for criticism of the manuscript.

Drs. D. Smith and N.G. Adams for their help when initially setting up the prototype microparticle gun and for many subsequent helpful discussions.

Drs. W.E.J. Neal and R.W. Fane for their valuable advice on the ellipsometry system.

Dr. R.K. Fitch and students for their assistance with some of the target microtopography studies and for loan of the Ion gun.

Professor T. Mulvey for useful suggestions on the design of the electrostatic lenses.

Professor E. Braun for assistance in supervision and Professor S.E. Hunt for use of the departmental facilities.

All the technical staff, notably Mr. F. Lane and Mr. M. Khalid for their help in building and maintenance of the experimental apparatus.

Dr. R.G. Forbes, Mr. L. Verdi and colleagues for their help and encouragement.

Finally, my wife and family for their unending patience and moral support at all times.

These studies were made possible by financial support from the Science Research Council and a Research Scholarship from the University of Aston.

Pages removed due to Confidentiality reasons

Pages	L109 - L111

Pages removed due to Confidentiality reasons

Pages 119 - 123

Pages removed due to Confidentiality reasons

Pages 139 -167